DETECTION AND ELIMINATION OF DEFECTS DURING MANUFACTURE OF HIGH-TEMPERATURE POLYMER ELECTROLYTE MEMBRANES

A Dissertation
Presented
To The Academic Faculty

By

Kanthi Latha Bhamidipati

In Partial Fulfillment
of the Requirements for the Degree
Doctor of Philosophy in the
School of George W. Woodruff School of Mechanical Engineering

Georgia Institute of Technology
May, 2011

DETECTION AND ELIMINATION OF DEFECTS DURING MANUFACTURE OF HIGH-TEMPERATURE POLYMER ELECTROLYTE MEMBRANES

Approved by:

Dr. Tequila A. L. Harris, Advisor
George W. Woodruff School of
Mechanical Engineering
Georgia Institute of Technology

Dr. Jonathan S. Colton
George W. Woodruff School of
Mechanical Engineering
Georgia Institute of Technology

Dr. Marc K. Smith
George W. Woodruff School of
Mechanical Engineering
Georgia Institute of Technology

Dr. Comas Haynes
Georgia Tech Research Institute
Georgia Institute of Technology

Dr. J. Carson Meredith
School of Chemical and
Biomolecular Engineering
Georgia Institute of Technology

Date Approved: February 15, 2011

This thesis is dedicated to the
‘Divine Power’ driving this world,
my parents (Srinivasa Murthy Bhamidipati and Lakshmi Bhamidipati),
my sister (Anitha Bhamidipati) and
my husband (Raghuram Tadimalla).

ACKNOWLEDGMENTS

First and foremost, I would like to thank the Divine power inside me that leads me towards making the right decisions, achieving the goals and guiding through the path chosen. I owe all my accomplishments thus far to my parents, my sister and my husband, whose encouragement, efforts and sacrifices got me this far.

I will always be very thankful to my advisor, Dr. Tequila A. L. Harris, who trusted me and gave me the wonderful opportunity to work with her on my doctoral program. She is an excellent advisor who led me through the doctoral process by her mentorship, advice and guidance, while giving me the freedom to make decisions pertaining to research. I learnt a lot of great things from her, both at a personal and professional level.

I am grateful to my committee members, Dr. Marc K. Smith, Dr. Jonathan S. Colton, Dr. Comas Haynes and Dr. J. Carson Meredith for agreeing to be on the committee. Dr. Smith gave me useful insights into the three-dimensional nature of the air entrainment phenomenon that helped to improve the quality of the research. The discussions with Dr. Colton directed me to study the correlation between the fluid properties and the air entrainment phenomenon, which proved to be very valuable. Dr. Haynes' suggestion about plotting the coating window data in a non-dimensional form assisted in finding the actual parameters influencing the coating process. His immense assistance during all phases of my doctoral process is greatly appreciated. Dr. Meredith's suggestions on methods to explore defects in thin films paved the path to a successful study.

I want to sincerely show my appreciation for all the valuable suggestions made by Dr. Cyrus Aidun, whose great background in related work helped me tremendously during the research.

I want to sincerely thank BASF, GmBH, for their support during the early phase of this research, by supplying samples of their PPA/PBI solution.

I want to thank each and every member of the DaMES laboratory for assisting me throughout my curriculum at Georgia Institute of Technology. My special thanks to Jay Johnson, Xiao Ding and Zak Ahmad for their assistance in setting up the experimental setup and all the useful discussions and suggestions pertaining to the research. I would also like to especially acknowledge the assistance of Sima Didari with the fluid property measurements, experiments and simulations. Terry Caston was a great officemate with whom I had great discussions on research and other aspects. Outside of research, I had the opportunity to learn about various cultures due to the cultural diversity present in the DaMES laboratory, which is greatly appreciated.

I want to thank all other students at Georgia Tech, outside of DaMES laboratory, who helped me immensely throughout the research process. My special thanks to Marmar Mehrabadi, whose valuable suggestions pertaining to the volume-of-fluid model is greatly appreciated.

I would like to thank all other technical and administrative staff at Georgia Tech, who helped me immensely with all my needs. The assistance provided by Mr. Louis Boulanger with machining the shims at a short notice, and Mr. Kyle French and Mr. Ahn Nguyen with the encoder is truly appreciated. Ms. Wanda Joefield Branch, Ms. Joi

Outlaw, Ms. Melinda Raine, Ms. Glenda Johnson, Ms. Terry Keita and Ms. Trudy Allen have greatly assisted with all the administrative needs.

My family and friends have all been very supportive of my work and assisted enormously towards my personal, professional and spiritual development. My mother (Lakshmi Bhamidipati), and my father (Srinivasa Murthy Bhamidipati) have been instrumental in shaping my career. They always went out of their way to bring about professional and personal success in my life. They are also assisting me in taking care of my adorable, toddler daughter, Dhruthi Tadimalla, without which my doctoral process would not have been smooth. I can never appreciate my sister (Anitha Bhamidipati) enough for her encouragement and support throughout my life. Another person that inspires me and is making a big impact in my life is my husband (Raghuram Tadimalla), who has been very patient and encouraging throughout my doctoral program.

TABLE OF CONTENTS

LIST OF TABLES

LIST OF FIGURES

NOMENCLATURE

Dimensions

M’	Mass
L’	Length
T’	Time

Roman Alphabets

Bo	Bond number
Ca	Capillary number
$\boldsymbol{D}$	Rate-of-deformation tensor, 1/s
F	Force, N
Fr	Froude number
f	Function of any variable
G	Gibbs free energy, J
g	Gravity, m/s^2
h	Wet thickness, mm
H	Coating gap or Stand-off height, mm
I	Current density, A/cm^2
k	Consistency index, Pa-s^n
L	Coating bead length, mm
m	Number of parameters
n	Power-law index
P	Pressure, Pa

Q	Flow rate, mm^3/s
Q'	Flow rate per unit slot die width, mm^3/mm-s
R	any parameter
Re	Reynolds number
r	Distance from the contact line, mm
St	Stokes number
T	Temperature, °C
t	Time, s
u	x-velocity, mm/s
V	Voltage, V
v	y-velocity, mm/s
W	Slot gap, mm
We	Weber number
x	Space variable in the horizontal direction
y	Space variable in the vertical direction

Greek Symbols

α	Volume fraction
η	Apparent viscosity, Pa-s
$\dot{\gamma}$	Shear rate, 1/s
κ	Curvature of the interface surface, 1/mm
μ	Dynamic viscosity, Pa-s
Π	Dimensionless term

ϕ	Angle made by the sawtooth structures with horizontal, °
σ	Surface tension, N/m
$\boldsymbol{\tau}$	Shear stress tensor, Pa
θ	Contact angle, °

Other Symbols

$\mathcal{F}$	Faraday's constant
$\mathcal{L}$	Length, mm
ℓ	Characteristic length, mm
$\mathscr{n}$	Index for time step
$\hat{\boldsymbol{n}}$	Unit normal vector
φ	Fluid property, kg/m^3 for density, or Pa-s for viscosity
$\boldsymbol{\mathfrak{T}}$	Stress tensor, Pa
$\boldsymbol{\mathcal{T}}$	Normal stress tensor, Pa
$\hat{\boldsymbol{t}}$	Unit tangent vector
$\mathcal{U}$	Volume flux based on normal velocity, mm^3/s
$\mathscr{u}$	Velocity, mm/s
$\mathcal{V}$	Volume, mm^3
$\mho$	Characteristic velocity, mm/s
$\mathcal{W}$	Width, mm

Subscripts

a	Apparent
air	Air
c	Contact line
cs	Casting/coating solution
d	Dynamic
dj	Disjoining
f	Film
$\mathscr{f}$	Face of a computational cell
g	Gauge
i	Index
if	Interface
in	Inlet
j	Index
l	Die lip
max	Maximum
min	Minimum
nd	Non-dimensional
OCV	Open circuit voltage
PET	PET (substrate)
s	Static
st	Sawteeth
sd	Slot die

s	Source
w	Wall

Superscripts

a	power
b	power
c	power

SUMMARY

Defect generation and propagation in thin films, such as separation membranes, can lead to premature or catastrophic failure of devices such as polymer electrolyte membrane fuel cells (PEMFC). It is hypothesized that defects (e.g., air bubbles, pin-holes, and holes) originate during the manufacturing stage if precise control is not maintained over the coating process, and they propagate during operation. The manufacturing process used for this dissertation is slot die coating, which involves the wetting of a substrate by displacing the air between the die gap and the substrate. The primary objectives are to establish the upper and lower processing boundaries or coating window for relatively high-viscosity (> 1 Pa-s), shear-thinning solutions and to understand the mechanism(s) by which defects ensue at or along the dynamic contact line. Simulations and experiments were used to meet these objectives for a range of materials. To capture the two-phase flow field of the coating process, numerical simulations were made using a volume-of-fluid (VOF) multiphase method, available in FLUENT 6.3.26. To validate the numerical model and to investigate the mechanism(s) that causes defects, a customized roll-feed imaging system was used. The effect of coating gap, slot gap, solution viscosity, and surface tension were investigated to understand their impact on the size of the coating window and defects. A semi-empirical model correlating the maximum coating speed to a solution's material properties, geometric parameters and processing conditions was developed. Such a predictive model will enable engineers to determine the maximum coating boundary for shear-thinning and Newtonian solutions within certain constraints.

1. INTRODUCTION

1.1 Need for Alternate Energy & Use of Polymer Electrolyte Membrane Fuel Cells in Transportation

The world's increasing dependence on fossil fuels such as petroleum, coal, and natural gas, is resulting in energy insecurity [1, 2] and exponential increase in emissions [3, 4]. Consumption of liquid fuel in the United States (US) is projected to increase significantly by the year 2035 [5] as shown in Figure 1.1. The fuel consumption for the transportation sector in 2008 was 13.88 million barrels per day; by 2035 it is projected to rise to 16.38 million barrels per day, while other sectors are projected to remain relatively constant. Ultimately, the transportation sector is projected to account for 74% of liquid fuel consumption in 2035, while it accounted for 71% of the consumption in 2008 [5].

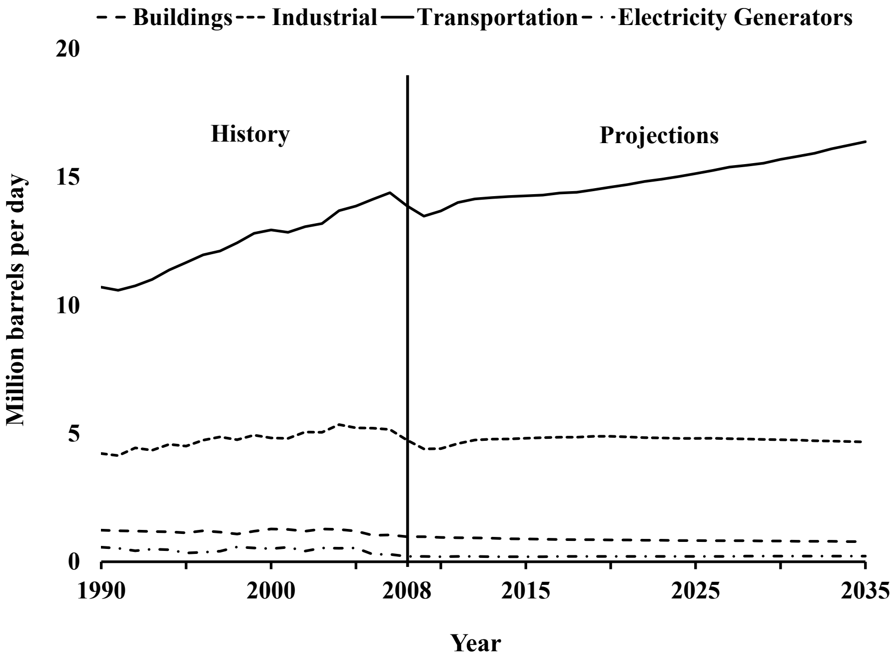

Figure 1.1: Liquid fuel consumption for the US (Re-plotted using data from [6]).

On the other hand, the combined oil production in the United States is not expected to increase at the rate of consumption as shown in Figure 1.2 [5]. For instance, the total oil production is projected to be less than 50% of the expected consumption by 2035. In addition, the production of oil both onshore and offshore is sensitive to world oil prices and technological advances. Due to the high costs required for offshore oil production, it is economically competitive only when the world oil prices are high, unless technological advances can result in low-cost production.

In order to bridge the gap between the production and the consumption, the US has to rely on foreign imports for oil. With the growing demand for oil globally, higher oil prices and consumption rates are imminent. Considering the finite oil supply and a depressed economy, such concerns are a matter of national security for the US [7].

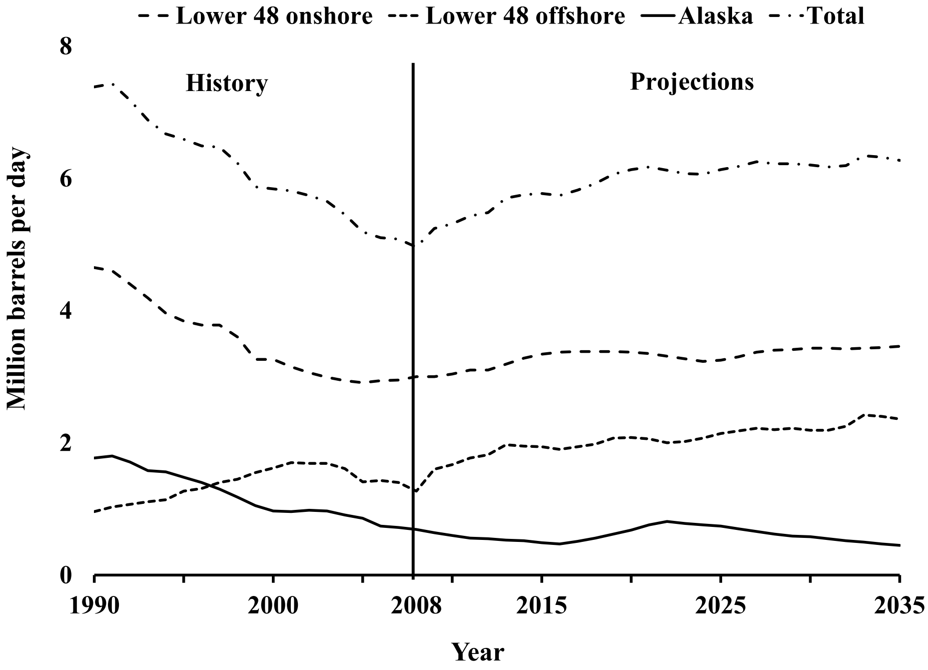

Figure 1.2: Domestic crude oil production (Re-plotted using data from [8]).

A major disadvantage in using fossil fuel, in addition to its finite generation, is the emission of carbon dioxide (CO_2), a greenhouse gas. In spite of stringent emission requirements that are in place, as shown in Figure 1.3, the total CO_2 emissions in 2035 are projected to increase by 9%, to 6,320 million metric tons, compared to emissions in 2008 [5].

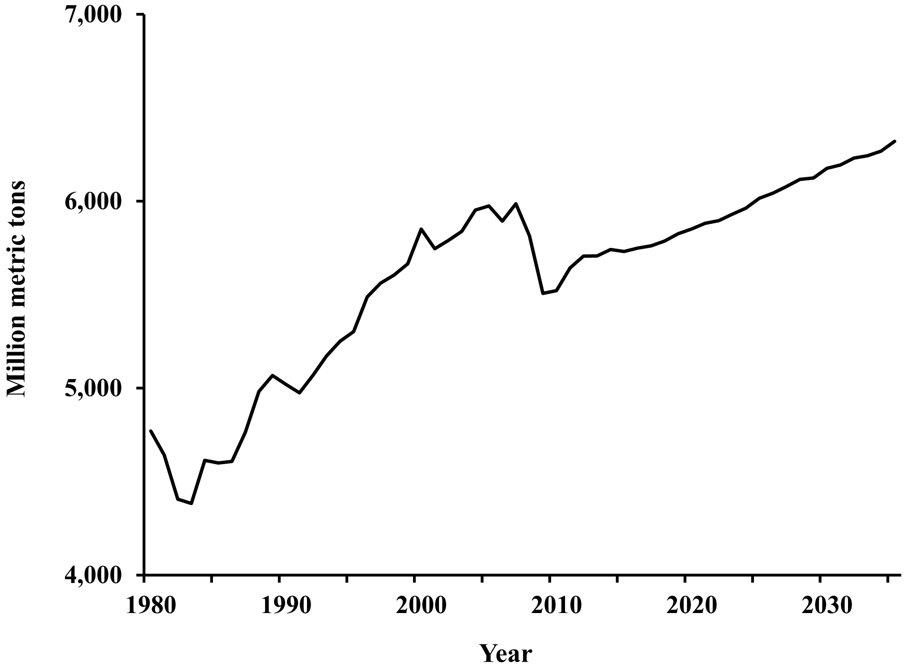

Figure 1.3: Total carbon dioxide emissions (Re-plotted using data from [9]).

The transportation sector remains the second largest contributor of carbon dioxide emissions, with petroleum accounting for 42% of emissions in 2008 and 41% of emissions in 2035 [5] as presented in Figure 1.4. It is strongly believed that increased dependence on fossil fuels have led to increase in greenhouse gas emissions such as CO_2, resulting in modern day global warming [10-12].

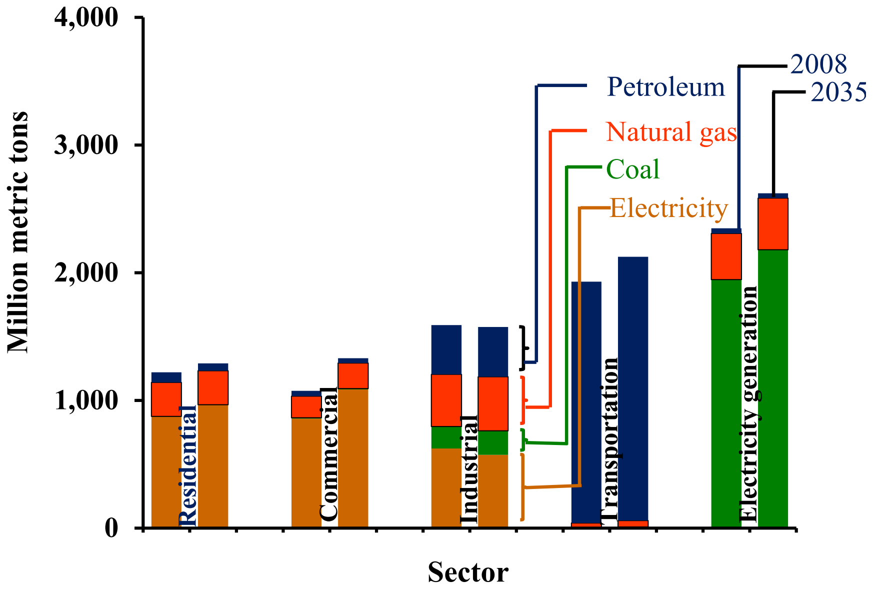

Figure 1.4: Carbon dioxide emissions by sector and fuel, 2008 and 2035 (Re-plotted using data from [9]).

In order to combat the issues with fossil fuels, alternative energy forms (such as wind, solar, hydrogen, etc.) have emerged. The polymer electrolyte membrane fuel cell (PEMFC) technology is typically a hydrogen based energy converter that serves as a great alternative to conventional fossil-fuel based engines in particular, and stationary and portable applications in general. A PEMFC uses hydrogen as the main anode side reactant, which allows for fuel-independence, because hydrogen can be produced independent of geographical location (for e.g., hydrogen can be produced by electrolysis). When pure hydrogen and oxygen are used as the reactants on the anode and cathode side respectively, the only byproduct is water thereby ensuring emission-free operation [13]. In addition, as a PEMFC fosters electrochemical reactions, the theoretical efficiencies at 25°C and atmospheric pressure can be as high as 83% [14, 15].

1.2 Working Principle of Polymer Electrolyte Membrane Fuel Cells

The working principle of a PEMFC is illustrated in Figure 1.5. The polymer electrolyte membrane (PEM), which is the heart of the fuel cell, separates the anode and cathode sides. The fuel, typically humidified hydrogen, enters the fuel cell through the anode-side bipolar plate. It then passes through the porous gas diffusion layer (GDL), which causes uniform distribution of the reactant at the electrode interface. The GDL combined with an electrode is referred to as a gas diffusion electrode (GDE). The electrode is loaded with platinum (Pt) as the catalyst. The anode half-cell reaction as represented by Equation (1.1) takes place at the triple-phase boundary, the area where the electrode, the membrane material, and fuel meet. During this reaction, hydrogen splits into protons and electrons. Protons are conducted by the membrane, while electrons flow through the external circuit onto the cathode-side. Similarly, humidified oxygen or air flows from the cathode-side bipolar plate, gets uniformly distributed at the cathode-side GDE and combines with electrons and protons forming water as described by Equation (1.2). Therefore, electricity and water are produced through the electrochemical reaction and the losses manifest as heat. The complete reaction is given by Equation (1.3).

$$H_2 \rightarrow 2H^+ + 2e^- \tag{1.1}$$

$$2H^+ + 2e^- + 0.5\ O_2 \rightarrow H_2O \tag{1.2}$$

$$H_2 + 0.5\ O_2 \rightarrow H_2O \tag{1.3}$$

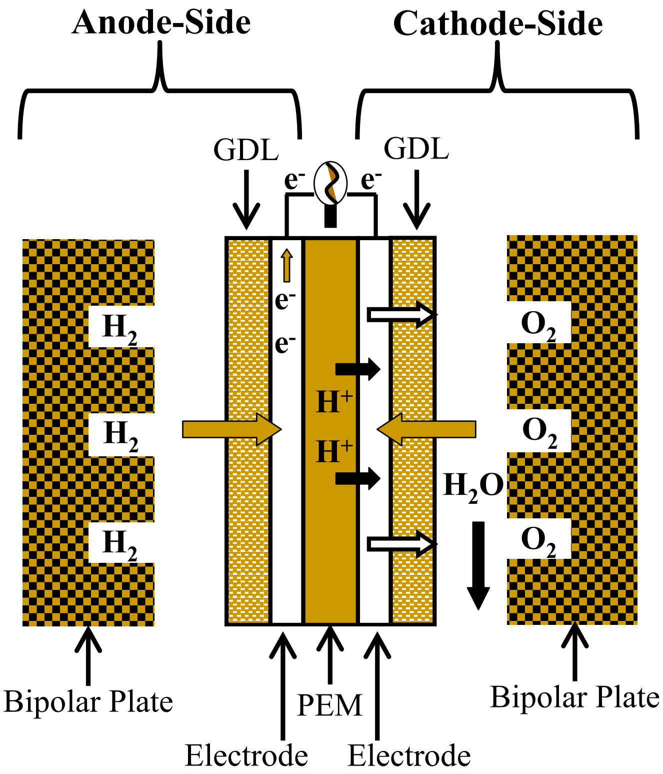

Figure 1.5: Illustration of polymer electrolyte membrane fuel cell.

1.3 Polymer Electrolyte Membranes

For PEM fuel cells, there are two classes of membranes: low temperature and high temperature. Each has its own advantages and disadvantages. However, PEMs generally should have the following characteristics:

- Conduct protons from anode side to the cathode side;
- Prevent electrons from passing through the membrane as this would result in internal current; and
- Prevent fuel crossover from one side to the other.

Internal currents and fuel crossover would result in a significant drop in the open circuit voltage (OCV) of the fuel cell, thus lowering its efficiency [15]. When fuel crossover occurs, hydrogen directly reacts with oxygen in the presence of catalyst instead of combining electrochemically, thus producing no current. Fuel crossover is a major problem if very thin or damaged membranes, which have cracks or pinholes [16], are used.

The operating temperature of the membrane determines the working conditions of fuel cells. The conventional low temperature PEMs (LT-PEMs) are sulfonated tetrafluoroethylene, such as Nafion™, which restrict the operating temperature of PEM fuel cells below 100°C. The low-temperature operation causes many disadvantages including water mis-management, slower reaction rates, carbon monoxide poisoning of the platinum catalyst and thermal mis-management.

Water mis-management: The PEM needs to be sufficiently hydrated at all times to effectively conduct protons [15, 17]. For this reason, the fuel and oxidant are humidified before passing through the fuel cell. However, too much water can block the GDL pores limiting the motion of fuel and oxidant to their respective active sites, where reactions take place [18-20].

Slower reaction rates: The reversible OCV, V_{OCV}, for a PEM (hydrogen) fuel cell is given by Equation (1.4) [15]:

$$V_{OCV} = \frac{-\Delta G}{2\mathcal{F}} \tag{1.4}$$

where ΔG is the Gibbs free energy and $\mathcal{F}$ is the Faraday's constant. The negative sign is used because the reaction is exothermic. As the operating temperature increases, ΔG reduces, reducing the reversible OCV in turn. This might suggest that lower operating temperatures are better. However, lower temperatures cause reduced reaction rates and slower kinetics [21-23], which would more than offset the advantage of achieving the higher reversible OCV obtained at lower temperatures.

Carbon monoxide (CO) poisoning of the platinum (Pt) catalyst: Hydrogen is the actual fuel participating in the fuel cell reaction; however, in a lot of cases, hydrocarbons are externally reformed to produce hydrogen. Traces of CO present in the fuel poisons the Pt catalyst at low temperatures [24-26], however, this problem is relieved as the temperature increases.

Thermal mis-management/Low-quality heat: The PEM needs to be sufficiently hydrated in order to effectively conduct protons. However, the fuel cell inefficiencies manifest as heat, which increases its temperature. This causes membrane dehydration, thus increasing resistance to proton transfer [27]. The heat can be ideally used for powering other auxillary devices, thereby improving the overall efficiency. For PEM fuel cells, the heat is released at relatively low temperature, limiting its applicability to other areas.

In order to overcome the disadvantages associated with low temperature PEMs (LT-PEM) such as Nafion™, research [28-31] has led to the development of high temperature PEMs (HT-PEM) such as the phosphoric acid doped polybenzamidazole (PA/PBI) membranes. Although HT-PEMs overcome the disadvantages of LT-PEMs, they suffer from some challenges associated with operation (due to the relatively longer times needed for start-up of HT-PEMs compared to LT-PEMs) and manufacturing.

1.3.1 High Temperature-PEM Manufacturing

Several manufacturing methods for making HT-PEMs [28, 29, 32-37] exist in the literature. The most common methods are solution casting of polyphosphoric acid doped polybenzamidazole (PPA/PBI) solution, which is later hydrolyzed to form PA/PBI membrane, and chemical bath immersion (where PBI membrane film is doped with phosphoric acid via a chemical bath) [28, 29, 32, 34, 37]. Harris and Walczyk [36] showed that traditional techniques, such as stencil printing, doctor blade extrusion, and nip-roller extrusion, were unsuitable for casting highly viscous, non-Newtonian solutions, such as PPA/PBI. In addition, these techniques are laboratory techniques, which are unsuitable for mass production. On the other hand, they found that slot die casting produced more uniform films with fewer defects. In a study conducted by Xiao et al., [35, 38] it was found that membranes produced using the slot die casting versus other fabrication methods possessed higher proton conductivity and superior mechanical properties at high temperatures. This was attributed to better retention of phosphoric acid in the final sol-gel membrane obtained through the slot die casting/hydrolysis process. Despite the advantages associated with the slot die casting technique for making PA/PBI membranes, defects can form in the membranes if proper processing conditions are not maintained. The working principle of slot die casting along with the nature of defects pertaining to such manufacturing process is explained in the next chapter.

1.4 Research Motivation

During the fuel cell operation, the membrane is primarily subjected to three failure modes:

Chemical degradation: The carbon support on the Pt catalyst is subjected to corrosion and dissolution/sintering of Pt catalyst occurs in an acid medium [39-42]. At high temperatures, leaching of phosphoric acid [41, 42] occurs due to the transition of phosphoric acid to less conductive pyrophosphoric acid [43-45].

Mechanical degradation: The presence of excess acid/water causes membrane swelling, facilitating gas-crossover resulting from increased permeability [28]. Mechanical and thermal stresses that arise during fuel cell operation result in pinhole/crack formation [42, 46-49]. Also, highly compressive strains induce creep in the membrane [50].

Thermal degradation: Membrane failure occurs as it is subjected to severe temperature gradients during fuel cell operation [40, 42, 51].

Research [52-54] has shown that defects originating in the membrane during manufacturing are further amplified during fuel cell operation, forming pinholes and cracks. As a result, the membrane can no longer prevent mixing of the reactants resulting in the degradation of fuel cell performance. For example, Lu et al. [55] compared the performance of hydrogen-air PEMFC when the membrane is defect-free and when a pinhole is present in the membrane. The comparison is shown in Figure 1.6 using a polarization curve for the PEMFC operated at 0.3 MPa, 60 °C and stoichiometric ratios of 1.75 and 2.5 for hydrogen and air respectively. It can be seen that there is a significant drop in the voltage, V for a given current density, I, when a pinhole is present. The effect is higher at larger current densities. Lu et al. also tested the durability of the PEMFC with and without pinhole by monitoring the variation in the cell voltage over a 40 hour period.

They found that when the pinhole is present, the performance of the fuel cell degraded rapidly after the first 20 hours.

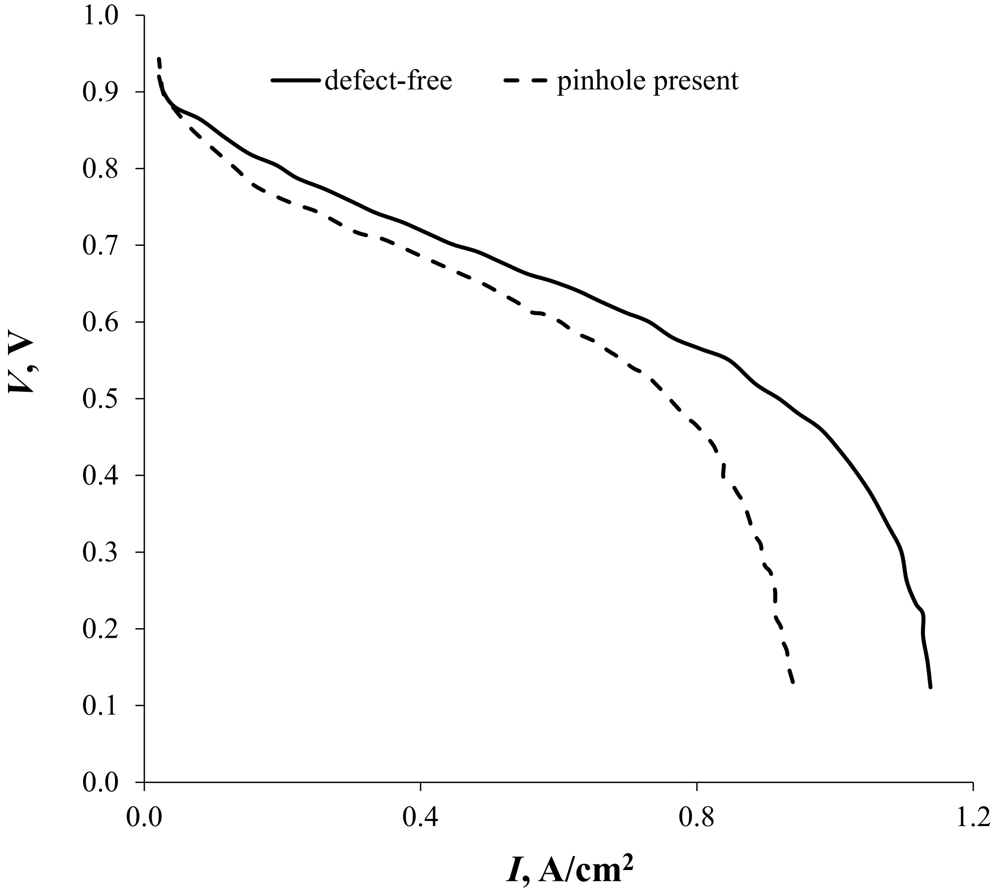

Figure 1.6: Polarization curves for H_2-Air PEMFC without pinhole and with pinhole (Re-plotted using data from [55]).

This work is one of the attempts to eliminate the defects originating in the PEM membrane during the manufacturing process, which will enhance the durability of PEMFCs.

1.5 Research Objectives

The primary objective of the current study is to improve the durability of HT-PEM by discovering the “coating window” for creating defect-free membranes and investigating the physical underpinnings of various defects. The methodology chosen to attain this objective pertains to identifying the defects occurring during the membrane manufacturing process and finding the optimum manufacturing conditions where defect-free membranes can be obtained (coating window). The reasoning behind this methodology relates to eliminating defects prior to their final end use. In order to obtain this main objective, the following subtasks as depicted in Figure 1.7 are implemented:

1. Obtain coating windows for the PPA/PBI solutions and identify the specific conditions limiting the range of processing parameters within specified constraints.
2. Detect and analyze various defects occurring during casting of thin films and identify the nature of defects and the relevant causes.
3. Obtain experimentally validated numerical model that can predict the coating windows and overall wetting phenomena.
4. Understand the air entrainment phenomenon, since it acts as a limiting factor on attaining higher coating speeds.
5. Find optimum processing conditions required to manufacture membranes with a wide range of thicknesses. A wide range of membrane thicknesses would ensure versatility.

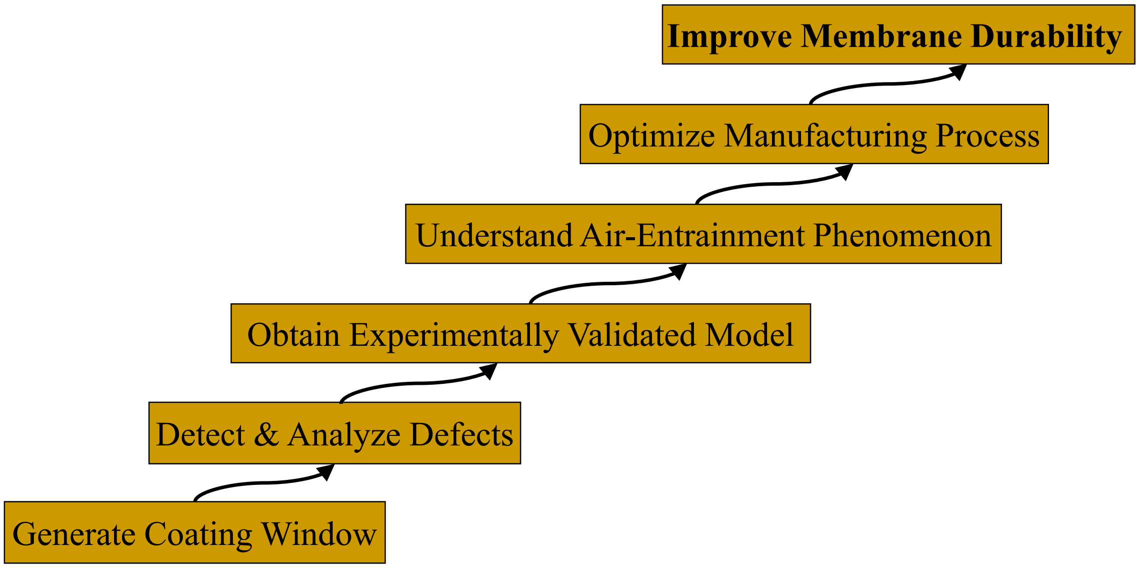

Figure 1.7: Research objectives.

1.6 Thesis Layout

This thesis is aimed at understanding the type and nature of defects originating during the manufacture of HT-PEMs. In Chapter 2, the relevant literature on coating processes (primarily emphasizing slot die coating), the concept of coating window, the common defects induced in the coated membranes, and the factors contributing to the defects are presented. In Chapter 3, the focus of the current study and the tools utilized in performing the research along with their limitations are outlined. In Chapter 4, details on the properties of coating solutions used and the instrumentation and procedures employed in obtaining the properties are provided. In Chapter 5, the experimental setup, experimental procedure, constraints on geometric and processing conditions employed in the experiments, and experimental uncertainty analysis are presented. In Chapter 6, the numerical methodology, the relevant boundary conditions, the sensitivity of the solution to various numerical parameters used, and the validation of the numerical model with experimental studies are explained. In Chapter 7, the air-entrainment and bubble breakup mechanism in addition to the effects of various parameters on air entrainment are discussed. In Chapter 8, the effect of geometric and processing parameters on the slot die coating process of HT-PEM is investigated. In Chapter 9, the important conclusions and findings from the present study in addition to the contributions of the current study are stated. In Chapter 10, a discussion on how the current study can be further extended in the future is provided.

1.7 Summary

Depleting fossil fuels combined with the need for curbing global warming have led to the emergence of alternative energy devices such as fuel cells. PEM fuel cells, which are especially suited for automotive applications traditionally use sulfonic acid based membranes, such as Nafion™. The disadvantages associated with such LT-PEMs such as water management and low reaction kinetics, have led to the emergence of relatively high-temperature PA/PBI membranes. Earlier research has shown that slot die casting is the best manufacturing technique for making such membranes due to their better proton conductivity and durability. However, the optimum geometric and processing conditions to make defect-free membranes using slot die coating have not been determined, hence the motivation of this work. In the next chapter, a review of existing literature on coating processes and the details of slot die coating are presented.

2. BACKGROUND REVIEW OF COATING PROCESSES AND DEFECTS

As discussed in the previous chapter, slot die casting/coating has been found to be best suited for manufacturing HT-PEMs. There exist similar coating processes from operational and functionality stand-points. The similarity lies with the coating fluid wetting a moving substrate. Therefore, regardless of the coating method or the coating solution, the overall wetting phenomenon and nature of defects are similar. In this chapter, a review of the important coating processes and their characteristics are discussed while emphasis is placed on the slot die coating.

Coating processes have been in use for fabricating thin films or membranes since the 1850s [56]. The coating processes can be mainly classified as pre-metered coating processes and non-pre-metered coating processes. The characteristic of a pre-metered coating process is that for a given die/substrate geometry, the final desired thickness of the coating can be obtained from the flow rate of the solution through the die and the substrate speed, based on mass conservation. Pre-metered coating assists in manufacturing thin films at relatively uniform thicknesses and faster rates. Examples of pre-metered coating processes are slot die coating, slide coating, and curtain coating, as shown in Figures 2.1 (a)-(c) respectively. On the other hand, the thickness of the final coated film cannot be predetermined when non-pre-metered coating processes are used. Plunging tape, wetted roll, and blade coating (Figures 2.1 (d)-(f) respectively) are examples of non-pre-metered coating processes. However, in both cases, during coating, the solution to be coated displaces air and wets the substrate, which is referred to as dynamic wetting. The line along which fluid contacts the substrate is termed the dynamic contact line (DCL).

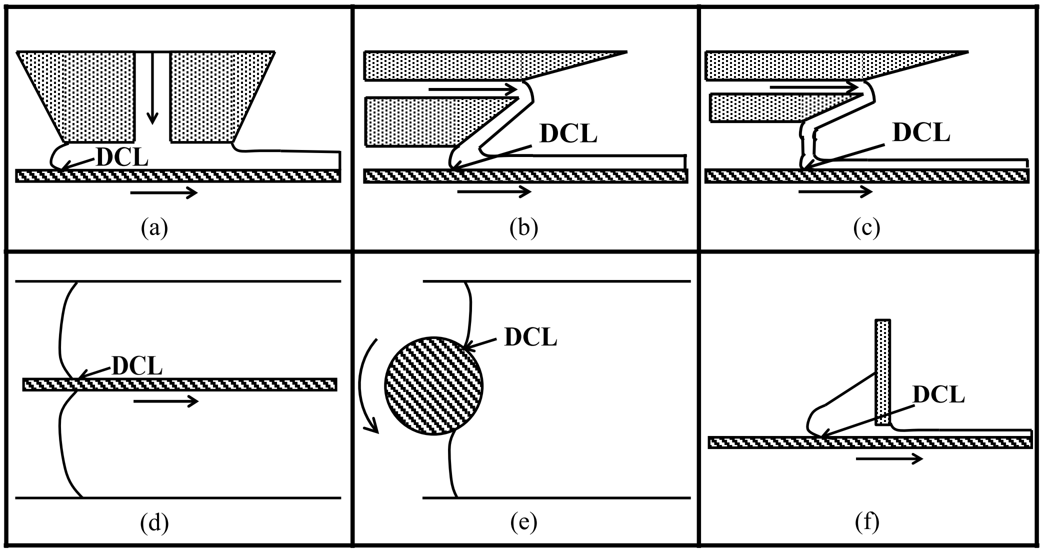

(a) (b) (c) (d) (e) (f)

Figure 2.1: Typical coating processes. (a) Slot die coating, (b) Slide coating, (c) Curtain coating, (d) Plunging tape, (e) Wetted roll, (f) Blade coating.

2.1 Slot Die Coating

Slot die coating or slot die casting is a pre-metered manufacturing technique, first introduced by Beguin [57] in 1954 for making photographic films. Slot die coating/casting involves suspending a solution from a slot die at a predetermined flow rate, Q_{in}, onto a substrate moving at speed, u_w. The difference between coating and casting is that the substrate remains an integral part of the final product in the case of coating, while the coated film is stripped off the substrate in the casting process. As the current research involves studying the quality of the film while it still remains on the substrate, the terms coating and casting will be used interchangeably. Slot die coating is successfully being used to make adhesive tapes, packaging materials, papers, and optical films for liquid crystal displays (LCD). The technique can be used to make films as thin as 15 μm [58], which matches with the lower limit of membrane thickness. As shown in Figure 2.2, the slot die consists of an upstream die and downstream die between which the coating liquid flows. The region bound by the inner walls of the upstream and downstream dies is termed the slot gap, *W*. The region bound between the die and the substrate is the coating gap, also termed as the stand-off height, *H*.

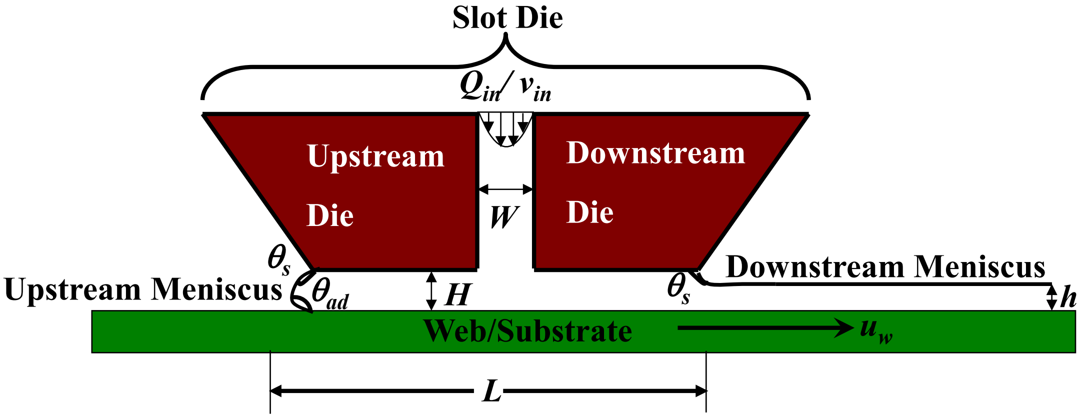

W – Slot Gap
H – Coating Gap/Stand-off Height
h – Wet Thickness
L – Coating Bead Length
u_w – Substrate Speed

Q_{in} – Volumetric Flow Rate
v_{in} – Inlet Velocity
θ_s – Static Contact Angle
θ_{ad} – Apparent Dynamic Contact Angle

Figure 2.2: Illustration of a slot die coating process.

The coated film forms upstream and downstream menisci with the die lips (the bottom most edges of the slot die). The distance between the two menisci is called the coating bead length denoted by *L* as coined by Higgins and Scriven [59]. The coated film attains a constant thickness downstream of the die, which is called the wet thickness, *h*. When viewed from inside the fluid, the upstream meniscus can have a convex or a concave shape depending on the nature of solution used as shown in Figures 2.3 (a) and

2.3 (b) respectively. The contact angles made by the fluid/air interface with the die and substrate materials determine the shape of the upstream and downstream menisci. In the case of forced wetting of the solid by the fluid, which occurs on the substrate side during slot die coating, the contact angle is referred to as the dynamic contact angle (DCA). However, the relevant parameter at macroscopic scale is the apparent dynamic contact angle, θ_{ad}, which is the angle made by the fluid with the solid as the eye perceives it. As the slot die is stationary, the contact angle made by the coating solution with the die lip is the static contact angle (SCA), θ_s.

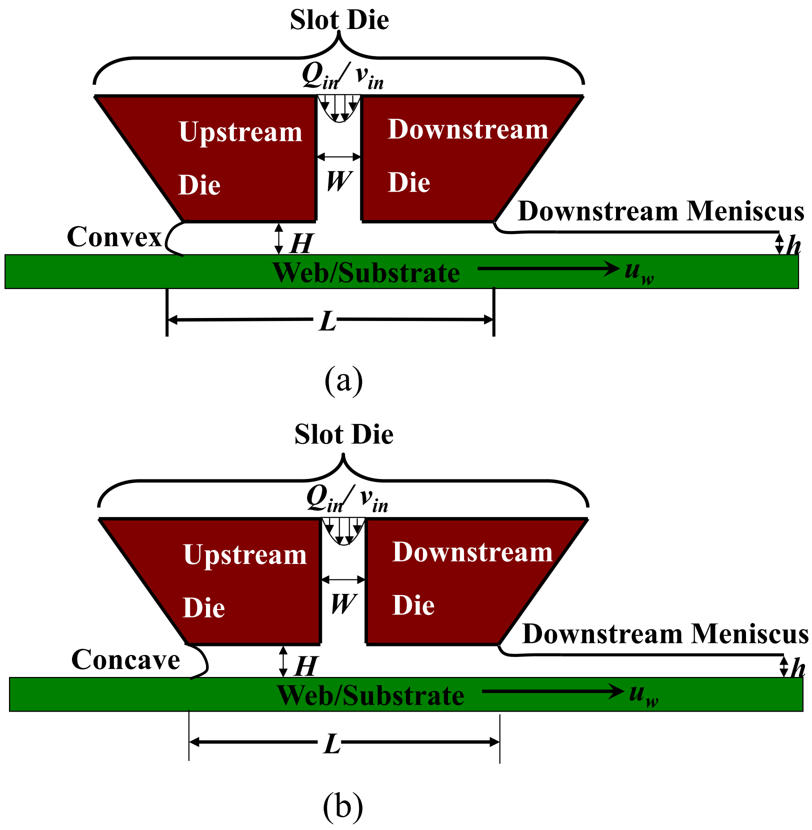

(a)

(b)

Figure 2.3: (a) Illustration of a convex upstream meniscus in a slot die coating process, (b) Illustration of a concave upstream meniscus in a slot die coating process.

2.2 Coating Window

Ruschak [60] was instrumental in quantifying the pre-metered coating process. He performed a theoretical study based on Landau and Levitch's [61] film coating theory. He showed that the upstream and downstream menisci can form various curvatures for a given substrate speed resulting in defect-free film of varying thicknesses within a limited region called the "coating window". Outside the window, steady-state ceases to exist and various defects will ensue. In order to attain a stable coating, the pressure difference across the length (L) of the coating bead has to be within certain bounds. Figure 2.4 (a) illustrates the general idea of a coating window, which is the region represented by the shaded area. The actual shape and width of the coating window can vary significantly from what is illustrated in the figure, depending on the properties of the coated solution and the operating conditions. The flow rate, Q_{in} (or pressure drop, P), or the flow rate per unit slot die width, Q', through the slot die is plotted on the y-axis and the coating/substrate speed, u_w, is plotted on the x-axis. It is desirable that the coating window be as large as possible to generate films with a range of thicknesses and to manufacture membranes at a faster rate, as these are the necessary features for mass production. It can be seen that there are bounds on the coating speed, which correspond to a given flow rate, and bounds on flow rate for any given coating speed to produce films with a wide range of wet thicknesses. The left most boundary on the coating window can be close to the origin as dictated by the solution rheology or constraints on the processing conditions. From mass conservation, if $\mathcal{W}_f$ is the width of the film, the wet thickness is given by Equation 2.1:

$$h = \frac{Q_{in}}{u_w \mathcal{W}_f} \tag{2.1}$$

For a given flow rate, the defect-free film has maximum wet thickness, h_{max}, at minimum substrate speed, $u_{w,min}$. As the coating speed is increased, both the upstream and downstream menisci move closer to the slot die exit and the thickness of the cast film decreases until the thinnest defect-free film is obtained at maximum coating speed, $u_{w,max}$. This smallest thickness is referred to as the minimum wet thickness denoted by h_{min} and corresponds to the low-flow limit condition. However, the usage of low-flow limit was disputed by Carvalho and Kheshgi [62] and Romero et al. [63, 64] when vacuum is not applied at the upstream end. According to them, low-flow limit refers to the condition where upstream meniscus is held away from the slot die exit by application of vacuum and only pulling of downstream meniscus towards slot die exit resulted in coating bead instability. Another form of representing the coating window is by plotting the minimum wet thickness, h_{min}, as a function of coating speed, u_w, as shown in Figure 2.4 (b). From Figure 2.4 (a), it can be seen that u_w increases as Q_{in} increases. So, the actual shape of the h_{min} versus u_w curve can differ based on the relative changes in Q_{in} versus u_w.

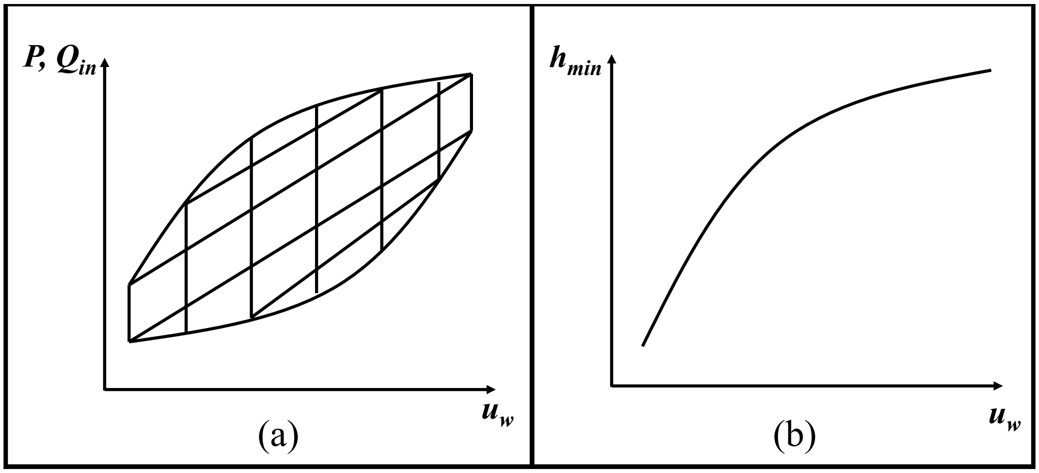

Figure 2.4: Illustration of a slot die casting window. (a) Pressure, P or flow rate, Q_{in} versus substrate speed, u_w, (b) Minimum wet thickness, h_{min} versus substrate speed, u_w.

Ruschak did not consider the viscous effects and predicted the coating limits accounting for capillary pressure alone. Also, the study assumed that the menisci remained pinned to the slot die lip edges. These assumptions hold only when the die lips are short and substrate speeds are low enough that viscous stresses do not have significant impact on the coating bead. However, these conditions do not hold in numerous practical situations. Higgins and Scriven [59] extended Ruschak's work by including viscous effects and allowing for the upstream meniscus to move. Studies [64, 65] have shown that the coating bead stability is dictated primarily by four forces; inertia of the fluid, viscous forces, gravitational force, and surface tension forces.

When homogenous solutions (not dispersions or suspensions) were used, the width of the coating window decreased as the solution viscosity increased [65-69]. On the contrary, studies performed on particle dispersions in solutions by Chu et al. [70], Yamamura et al. [71], and Lin et al. [72] showed that until an optimum particle concentration is reached, increasing viscosity of the dispersion delayed air entrainment causing wider coating windows. Similarly, tests performed by Chu et al. [73] with aqueous poly (vinyl alcohol) (PVA) solutions showed that the coating window expanded when high-viscosity PVA solutions were used.

Gutoff and Kendrick [68] performed experiments using non-Newtonian PVA solutions and found that when compared to coating windows obtained using Newtonian solutions, the maximum coating speed increased significantly for non-Newtonian solutions thus increasing the coating window substantially. They attributed the increase to elongational viscosity characteristics of the polymer. Studies performed by Ning et al. [74] showed that there exists an optimum polymer concentration in glycerin-water solutions at which the highest coating speeds for a solution can be achieved. On the other hand, experiments and simulations performed by Romero et al. [63] on high molecular weight polymers in dilute solutions showed that as the extensional viscosity of the coated liquid increased, the width of the coating window decreased. In another study, Romero et al. [64] discovered that when small viscoelastic stresses were present, the coating windows developed for mildly viscoelastic fluids are wider than those for Newtonian solutions characterized by the same capillary number.

The effect of surface tension on coating windows is inconclusive, due to contradicting findings by various researchers. Gutoff and Kendrick [68] found that surface tension does not play a significant role on the coating window and it only impacts the shape of the coating bead. According to Hamers et al. [75], solutions with lower surface tension assisted in widening the coating window. A study performed by Tiu et al. [76] found the exact opposite trend; that is, high surface tension solutions form more stable coating beads which extended the coating window. By performing tests with TiO_2

and SiO_2 particle suspensions in aqueous PVA solutions, Liu et al. [77] found that wider coating windows were obtained when higher surface tension solutions were used. Chu et al. [70] used the same solutions and found that porous particle suspensions can attain higher coating speeds compared to hard particles. This was attributed to an increase in surface tension due to the availability of larger surface area for porous particles. The study even found that the effect of surface tension dominates the effect of viscosity.

Other studies focused on understanding the effect of geometric parameters such as slot gap and coating gap on coating window size. Lee et al. [69] showed that processing at smaller coating gaps is advantageous as higher coating speeds can be attained. On the other hand, they found that the slot gap had negligible effect. The plots presented by Chang et al. [65] showed that for solutions with viscosities of 0.075 Pa-s and 0.2 Pa-s, smaller minimum wet thickness values were attainable if smaller coating gaps were used. This means smaller coating gaps were advantageous because higher coating speeds can be reached. However, the effect of coating gap was insignificant for much lower solution viscosities, i.e., 0.003 Pa-s. At low substrate speeds, it was shown that the coating speed reduces with slot gap, for such low viscosity solutions.

2.3 Coating/Casting Defects

As explained in Section 2.2, the left most boundary of the coating window is usually dictated by the minimum processing conditions that can be set due to the constraints on the experimental setup. Generally, that boundary is left open. The other boundaries of coating windows are dictated by defects such as dripping, air entrainment, break lines, ribbing and additional defects not of interest to this work.

Dripping: Dripping corresponds to the top most boundary of the coating window as shown by the dotted line in Figure 2.5 (a). Dripping occurs when the flow rate is too high relative to the substrate speed causing the cast solution to collect behind the upstream die, as shown in Figure 2.5 (b). The solution that creeps up the outer wall of the upstream die gets dragged down by gravity. When dripping occurs, the pre-metering characteristic of the slot die is lost as the process becomes unsteady and the thickness of the film can no longer be controlled. In some cases, dripping is seen along with air bubble entrainment in the coated film as shown in Figure 2.5 (c).

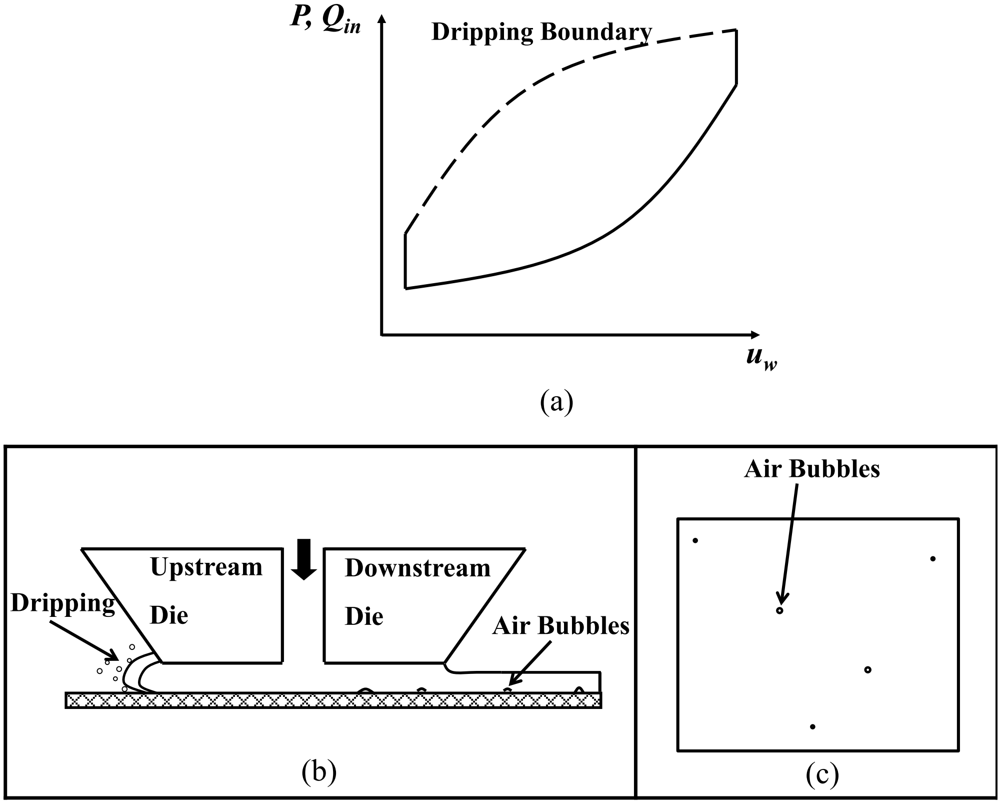

(a)

(b)

(c)

Figure 2.5: (a) Illustration of dripping boundary on the slot die coating window, (b) Solution dripping from the rear end of upstream die, (c) Coated film when air bubbles are also present.

Air Entrainment: On the coating window, the air entrainment is represented by the bottom most boundary indicated by the dotted line in Figure 2.6 (a). At this boundary of the coating window, as shown in Figure 2.6 (b), the originally two-dimensional flow field becomes three-dimensional (the solid line is the outer most section, while the dashed line represents a section in the interior) and air bubbles get entrained between the substrate and the liquid film intermittently. The upstream meniscus of the coating bead has a convex shape with the dynamic contact angle approaching 180° (indicated by the dashed line in Figure 2.6 (b)) prior to air entrainment. Air bubbles entrained in the final cast film are shown in Figure 2.6 (c). Air entrainment is the primary reason restricting processing of the membranes at higher coating speeds. In some cases, the air bubble is restricted to only a fraction of the total film thickness while in other cases; the bubble extends all the way to the top of the film resulting in a hole. This causes non-uniformity in the thickness of the cast film, which would compromise the film's performance to act as a separation barrier. The detailed physics behind air entrainment is explained in the next sub-section.

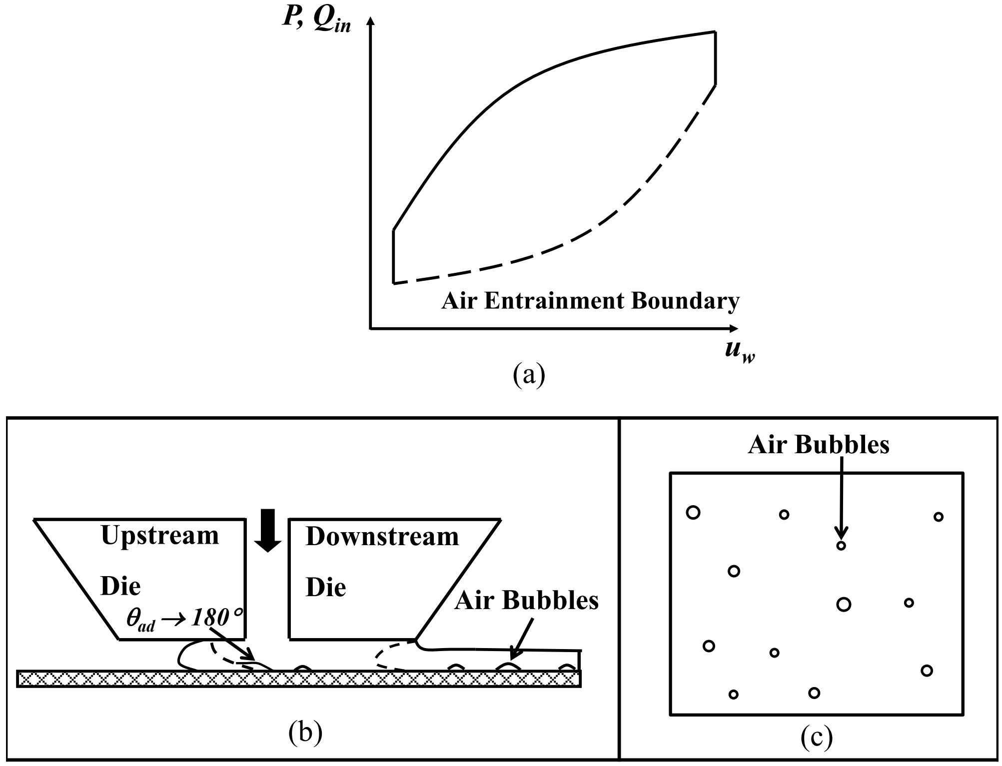

Figure 2.6: (a) Illustration of air entrainment boundary on the slot die coating window, (b) Three-dimensional flow field, upstream contact angle of the dashed line approaching 180°, (c) Coated film with entrained air bubbles.

Ribbing: Similar to air entrainment, ribbing occurs at the bottom most boundary of the coating window as shown in Figure 2.7 (a). However, the difference between the two lies in the shape of the upstream meniscus, which is concave in case of ribbing as shown in Figure 2.7 (b). Ribbing is associated with the appearance of a wavy structure on the surface of the film as shown in Figure 2.7 (c) and there exists non-uniformity in the thickness across the film.

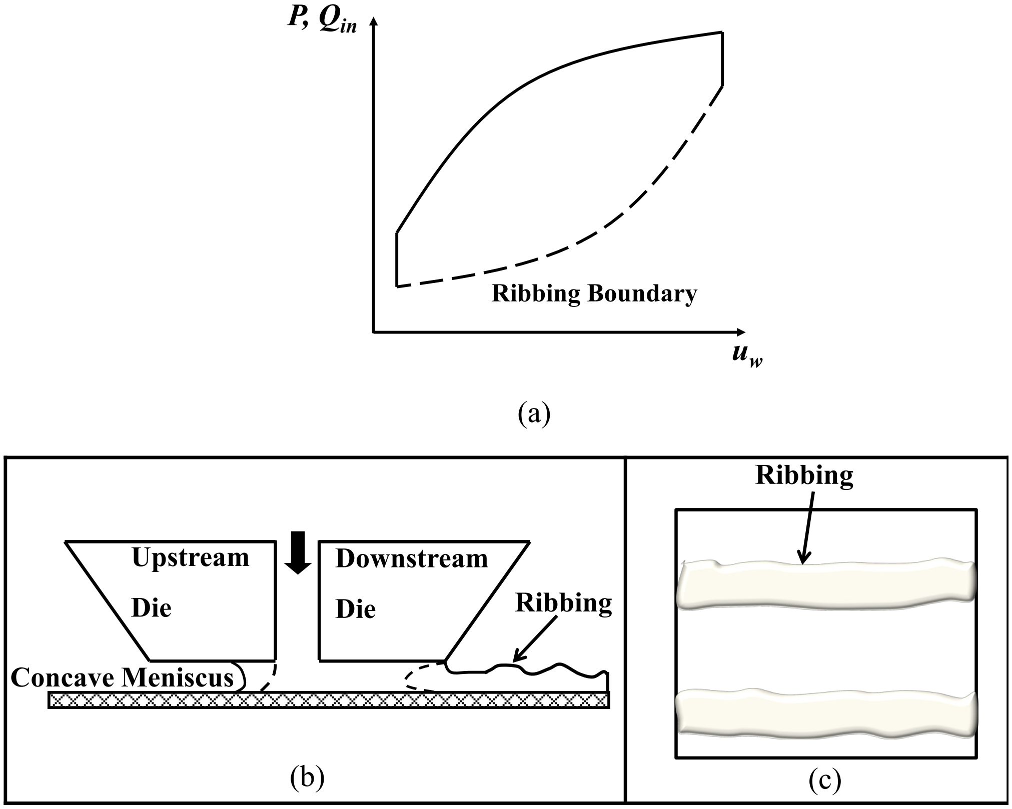

Figure 2.7: (a) Illustration of ribbing boundary on the slot die coating window, (b) Three-dimensional flow field, upstream meniscus has a concave shape, (c) Coated film with ribs.

Break lines or Complete Air Entrainment: The right most boundary of the coating window indicated by the dashed line as shown in Figure 2.8 (a) could either be dictated by break lines or complete air entrainment. In case of break lines, when the substrate speeds are very high corresponding to a given flow rate, the upstream meniscus cannot bridge the coating gap as illustrated in Figure 2.8 (b) and excessive air entrainment occurs, causing streaks and void spaces in the film. The break lines can occur in any direction as depicted in Figure 2.8 (c). Such films are totally unusable and are discarded resulting in material waste. In other cases, for any given flow rate, air gets entrained in the coated film for all substrate speeds and flow rates beyond the point of dripping leaving no room for good coating.

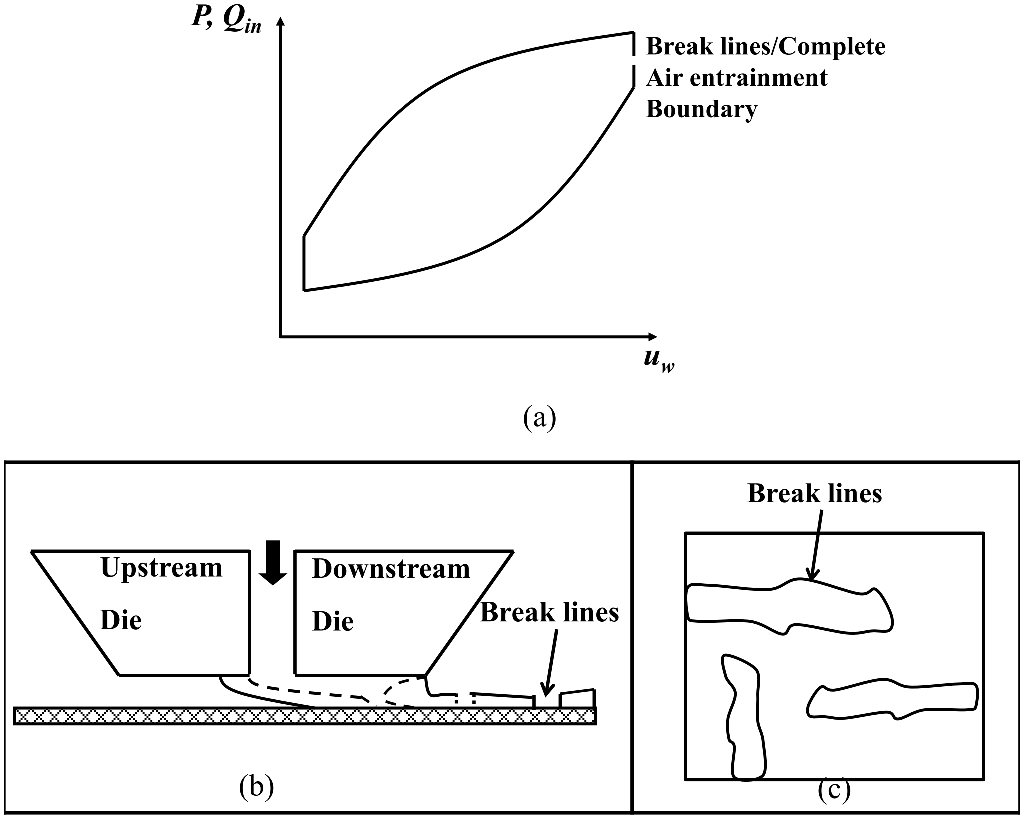

(a)

(b)

(c)

Figure 2.8: (a) Illustration of break lines boundary on the slot die coating window, (b) Three-dimensional flow field (upstream meniscus cannot bridge the coating gap), (c) Coated film with break lines.

Several researchers have noticed all of these defects during thin film/membrane processing [67, 74, 78]. Experimental studies on slot-coating performed by Chang et al. [65] showed that at the maximum coating speeds, ribbing occurred for low-viscosity solutions with upstream apparent dynamic contact angle less than 180°, while air entrainment occurred for high-viscosity solutions as the upstream contact angle approaches 180°. Chu et al. [70] also captured dripping, air entrainment in the form of bubbles and break lines experimentally.

In addition to the defects presented, there are other kinds of defects that are more specific to a particular property of a solution; for example another defect called “rough surfaces,” which are assumed to occur due to the elasticity of the fluid being cast. However, for this work, other defects will not be considered since their effect on the class of solutions used in this study is negligible.

As air entrainment is the major defect encountered by high-viscosity solutions (capillary number > 0.1 [78]), it is important to understand the factors driving it. This is because of the limitation posed by air entrainment on the speed of coating, which is an important factor in improving the production rates of the thin film, thereby reducing the turnaround times. A thorough understanding of the physics leading to the air entrainment and its effect on the film quality will allow for techniques to avoid it.

2.4 Air Entrainment and Sawteeth-Structures

Air entrainment during thin-film coating occurs at two levels; the microscopic level and the macroscopic level. The mechanisms driving air entrainment differ between the two levels.

Microscopic air entrainment: Air entrainment at the microscopic level, with the bubble sizes ranging in the order of a micron was studied by Miyamoto and Scriven [79]. The following is the theory behind the breakup of a thin air-film between the substrate and the coating liquid into small bubbles as explained by Miyamoto and Scriven.

Based on the work conducted by Miyamoto and Scriven, it was found that for very thin air-films corresponding to the critical air-side capillary number, $Ca_{air} > 10^{-5}$, the film breakup was driven by conjoining pressure instability. For their work, Ca_{air}, was estimated based on the theory developed by Teletzke et al. [80] and mathematically defined by Equation 2.2 as:

$$Ca_{air} = \frac{\mu_{air}\, u_w}{\sigma} \tag{2.2}$$

where μ_{air} is the dynamic viscosity of air and σ is the surface tension.

Conjoining pressure is the opposite of disjoining pressure, P_{dj} (typically indicated by symbol Π_d), introduced by Deryagin and Kusakov [81]. Disjoining pressure is instrumental in providing stability to the wetting film. The basis for disjoining pressure arises from the fact that compared to the bulk of the fluid, the molecular interaction energies in the fluid film are different. The pressure in the fluid film, P_f, is greater than the pressure in the bulk of the fluid, P_b, by a value equal to the disjoining pressure, as shown in Figure 2.9 and expressed by $P_{dj} = P_f - P_b$. Mathematically, the negative derivative of free energy with respect to the film thickness, dP_{dj}/dh, determines the fluid wettability of a surface [82]. The fluid can effectively wet the surface, when $dP_{dj}/dh < 0$, and de-wet the surface, when $dP_{dj}/dh > 0$. The disjoining (conjoining) pressure arises from the sum total of three different components [83]:

- The pressure component of the van der Waals forces between the fluid film and the substrate;

- The polar or electronic interactions between molecules; and
- The differences in the molecular structure of the fluid film compared to the bulk of the fluid.

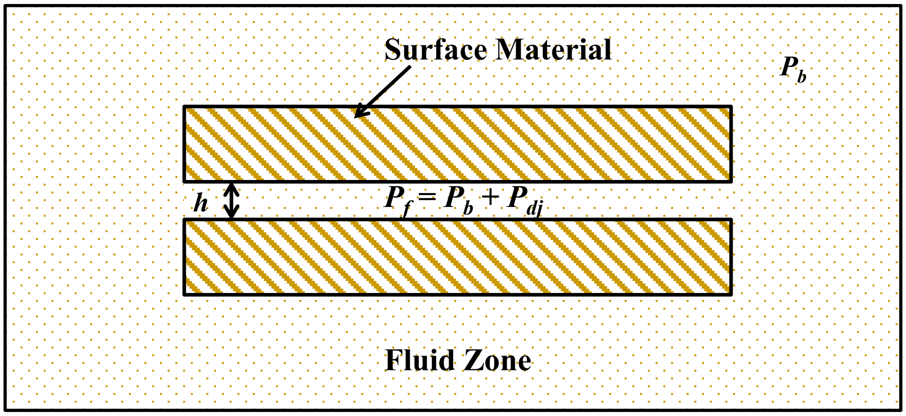

Figure 2.9: Illustration of effect of disjoining pressure on fluid film pressure, P_f = pressure in the fluid film, P_b = pressure in the bulk fluid and P_{dj} = disjoining pressure.

Miyamoto and Scriven found that for air films with thicknesses greater than 0.3 μm, the breakup mechanism was caused by electrostatic forces alone, while van der Waals forces were only significant in films that were much thinner than 0.3 μm. Near the inner region of the upstream meniscus (this region is less than 20 μm thick [84] and is invisible to the naked eye) next to the substrate, conjoining pressure forces and air viscosity became more important, especially at high substrate speeds. A 2D, Galerkin/Finite Element method was used to understand the rate at which the air film collapsed under conjoining pressure. They found that at low air-side capillary numbers, the film was continuously broken down under conjoining pressure to the adsorbed layer. At moderate air-side capillary numbers, the film again broke down under conjoining pressure into invisible bubbles that eventually dissolved. Relatively thicker films corresponding to $Ca_{air} >> 10^{-5}$ broke down due to Kelvin-Helmholtz instabilities and the bubbles remain entrained in the film. These findings were confirmed experimentally by Miyamoto [85].

Macroscopic air entrainment: This is a more common form of entrainment where air bubbles that are a few tens to hundreds of microns in size get entrained in the film. The focus of the current study will be on macroscopic air entrainment. Ablett [86], while performing dip-coating experiments was the first person to notice that the apparent dynamic contact angle approached 180° during air entrainment. Deryagin and Levi [87] also observed that as the coating speed increased, the apparent dynamic contact angle moved from nearly 0° to approximately 180° (Figure 2.10 (a)). As the apparent dynamic contact angle changed, the originally straight contact line broke into "vee" structures also termed as sawteeth pattern and triangular air pockets, as shown in Figure 2.10 (b). In this thesis, the terms "sawtooth" and "sawteeth" will be used. Deryagin and Levi performed tests by coating an emulsion onto a flexible substrate moving under a roller immersed in a coating hopper, and captured the DCL by observing the contrast in the illumination. The shaded area in the figure shows the liquid coated region. This marks the transition from the two-dimensional to the three-dimensional flow-field. The phenomenon was found to occur regardless of the coating solution used, however, the sizes of the sawteeth length and width varied with the properties of the solution. Figure 2.10 (c) depicts the length, $\mathcal{L}_{st}$, and width, $\mathcal{W}_{st}$, of a typical sawtooth. The terms “sawtooth tip” and “sawtooth base” are used by Veverka and Aidun [88] and Veverka [56].

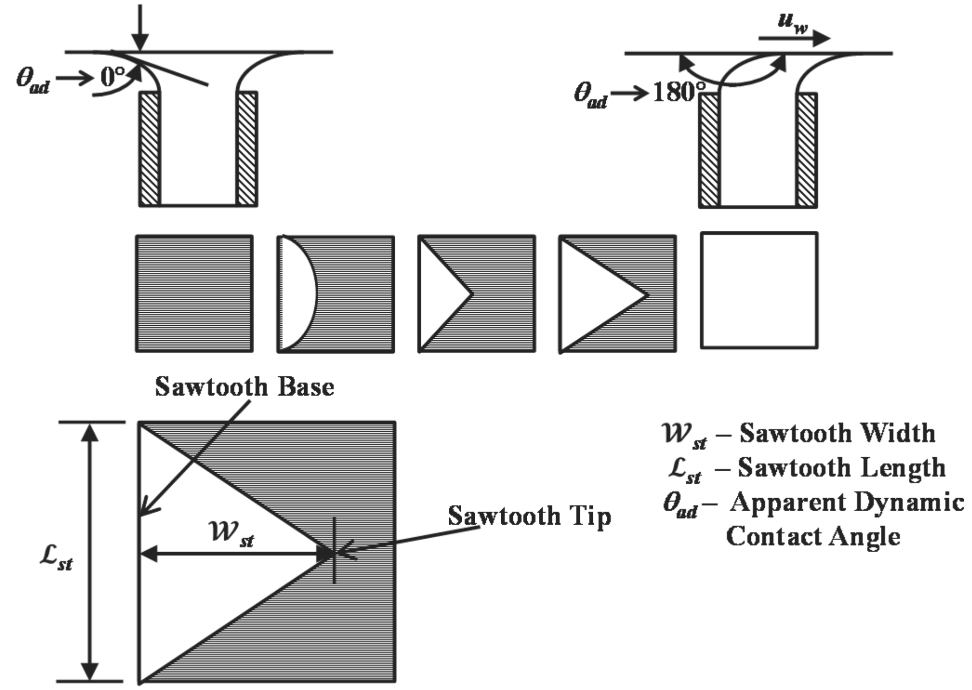

Figure 2.10: (a) Sectional view of the changing apparent dynamic contact angle as substrate speed increases, (b) Top view illustrating breaking of straight contact line into sawtooth structure (Re-drawn from [87]), (c) Features of a sawtooth.

Experiments were performed using a continuously moving tape in a fluid bath by Burley and Kennedy [89], to understand the effects of viscous and surface tension forces on air entrainment. They used different fluids and different tape (substrate) materials with dynamic viscosity and surface tension values ranging between 0.0059 Pa-s to 1.9335 Pa-s and 0.025 N/m to 0.065 N/m respectively. They made an important observation about the nature of sawteeth structures as a function of viscosity (Figure 2.11). The width and the length of the sawteeth structures decreased as the solution viscosity increased. This in-turn led to smaller air bubbles for high-viscosity solutions [89, 90]. Furthermore, there were more sawteeth structures per unit width of the tape for high-viscosity solutions. Burley and Kennedy found that the air bubbles broke off the tip of the “vee” structures, and the bubble breakup occurred more easily for low surface tension solutions. This was further supported by the fact that for a given viscosity, they noticed that the air entrainment velocity shifted to lower values when the surface tension was reduced. However, a study performed by Veverka [56] for a side driven free surface cavity setup, showed that at high-viscosity, lowering the surface tension delayed the air entrainment.

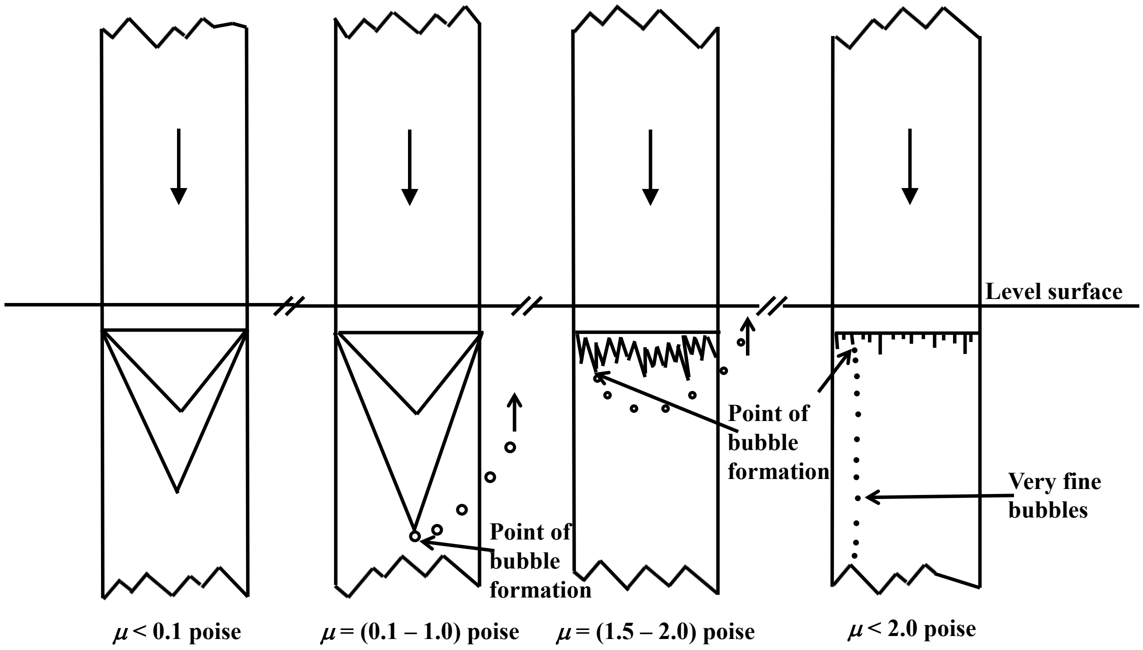

Figure 2.11: Sawteeth and air bubble sizes as a function of viscosity (Re-drawn from [89]).

To understand the reason for the sawtooth shape of the contact line, Blake and Ruschak [91] performed experiments with a plunging tape. They made an important observation that for any given system, the wetting line or contact line cannot move beyond a certain maximum speed perpendicular to itself. At low substrate speeds, the contact line was found to remain straight. As the substrate speed increased, the dynamic contact angle made by the upstream meniscus with the substrate increased until it approached 180°. This caused the straight contact line to break into multiple straight lines forming angle ϕ with the horizontal (perpendicular to the direction of substrate motion). The magnitude of ϕ adjusted such that at any location along the contact line, the velocity perpendicular to itself did not exceed the maximum speed of wetting, $u_{w,max}$. Veverka [56], however, identified two critical velocities pertaining to air entrainment, when the ratio of air to liquid viscosity was greater than 2×10^{-4} and capillary number was less than 1. The first critical velocity corresponded to the breaking of the DCL into multiple sawteeth structures without any air entrainment. The second critical velocity occurred when the triangular air film represented by the sawtooth structure became unstable and air bubbles were entrained. The second critical velocity is what was referred to as the air entrainment velocity, $u_{w,max}$.

Gutoff and Kendrick [92] developed an empirical relationship between the air entrainment velocity, $u_{w,max}$ and the viscosity of the coating solution, μ, using plunging tape experiments for Newtonian solutions as given by Equation 2.3:

$$u_{w,max} = 5.11\mu^{-0.67} \tag{2.3}$$

A study performed by Cohu and Benkreira [93, 94] showed that the air entrainment velocity for non-Newtonian solutions obtained by dissolving a polymer in a solvent was mostly a function of the solvent rheology and independent of bulk rheology.

Benkreira and Khan [95] performed dip coating experiments under reduced air pressures to understand the effect of air viscosity on air entrainment. They found that as the air pressure was reduced from atmospheric value to around 2000 Pa, the air entrainment velocity nearly doubled. Benkreira and Khan also found that as the air viscosity reduced due to decreasing air pressures, the size of the sawteeth structures decreased, while the total number of sawteeth increased resulting in a delayed air entrainment. They extended the study to include other gases (CO_2 and helium) [96] and found similar trends. Another important finding from their studies is that at low pressures, low-viscosity solutions encountered air entrainment sooner than high-viscosity solutions, which is contrary to the outcomes at atmospheric pressure.

Veverka [97] and Veverka & Aidun [88, 98] first documented the visible air entrainment mechanism at the macroscopic scale. The air entrainment mechanism followed a cycle as shown in Figure 2.12. They showed that the air bubbles nucleated from the side of the sawtooth and broke off the tip of the sawtooth. Severtson and Aidun [99] used long-wave stability analysis to explain the air entrainment mechanism. They found that the flow remained unstable at the side of the sawtooth air pocket causing nucleation of air bubbles, while the flow in the middle was stable. In addition, they found that the air entrainment mechanism occurred due to interfacial instability (resulting from viscosity and density stratification) alone and Kelvin-Helmholtz type of instabilities had no impact when the air was bounded by a solid surface on one side.

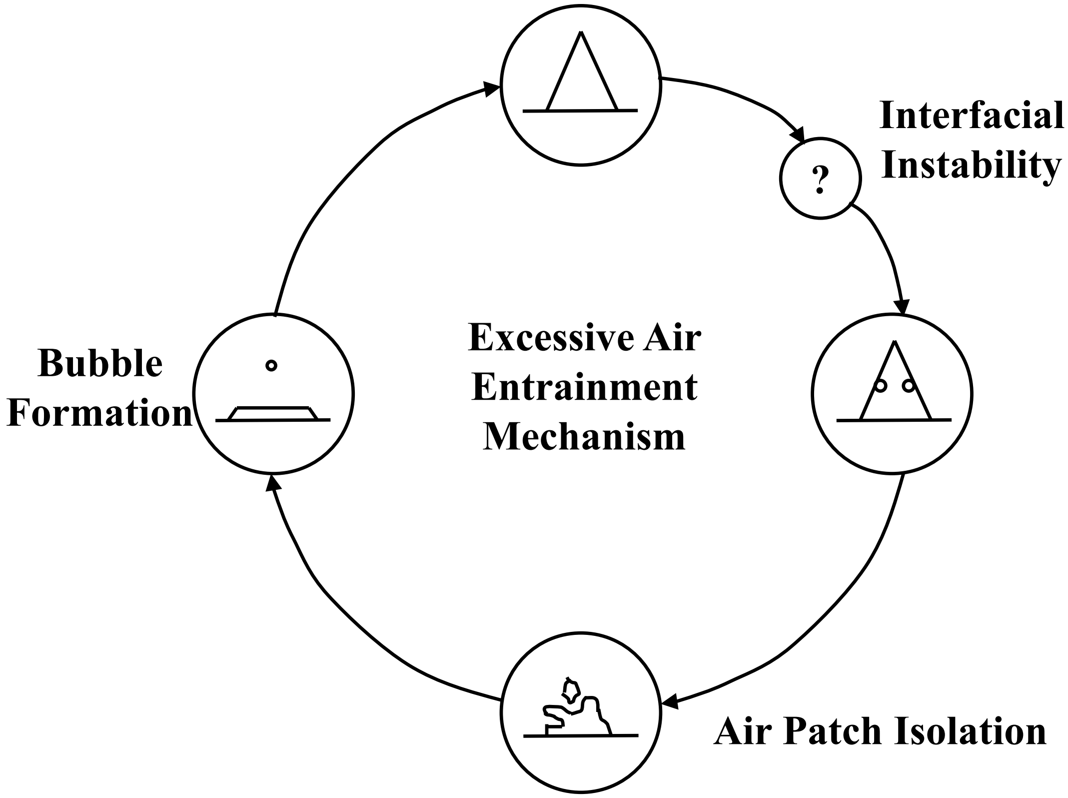

Figure 2.12: Air entrainment mechanism as observed by Veverka [97] and Veverka & Aidun [88, 98] (Re-drawn from [56]).

2.5 Three Minimum Wet Thickness Regions

Another very important and relevant topic in the field of slot die coating is the concept of the three minimum wet thickness regions. Lee et al. [69] performed slot die coating tests using glycerin-water solutions and silicone oils, which are Newtonian solutions. By plotting the dimensionless minimum wet thickness, $h_{nd,min}$ (= h/H), as a function of capillary number, Ca (= $\mu u_{w,\ max}/\sigma$ for Newtonian solutions), they made an interesting observation. Similar to dip coating, the dimensionless minimum wet thickness increased with capillary number (Region I) until a critical capillary number, Ca^*, was reached. Beyond the critical capillary number, the dimensionless minimum wet thickness was only a function of coating gap and was independent of capillary number (Region II) as is the case with blade coating. He noticed that the critical capillary number was reached when the dimensionless minimum wet thickness was between 0.6 and 0.7. Also, the critical capillary number was found to increase with the coating gap. Carvalho and Kheshgi [62] found another region (Region III) at high capillary and Reynolds numbers where the dimensionless minimum wet thickness decreased with capillary number. An illustration of the three regions is shown in Figure 2.13. It is customary to present the non-dimensional plot using logarithmic scale.

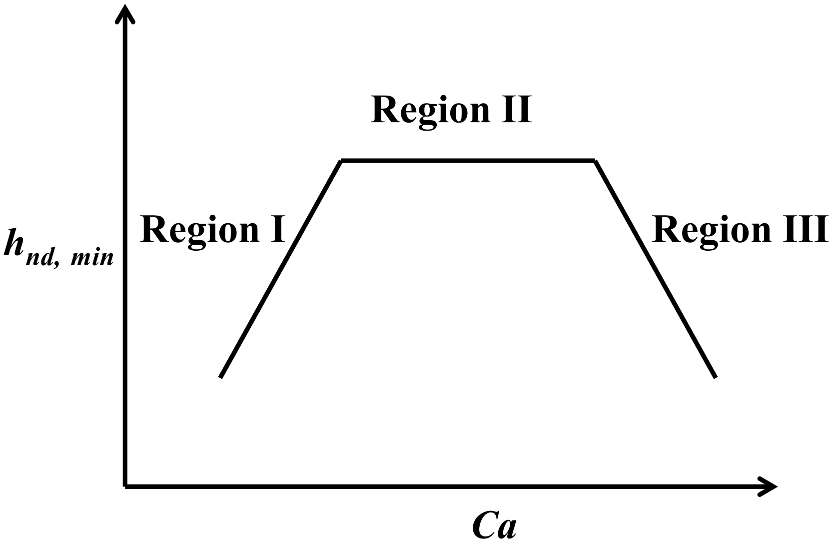

Figure 2.13: Illustration of three minimum wet thickness regions.

Chang et al. [100] correlated the location of the downstream meniscus at the onset of air entrainment to the minimum wet thickness regions. As shown in Figure 2.14 (a), if the location of downstream meniscus, as indicated by letter A, was beyond the edge of downstream die lip denoted by letter B, the dimensionless minimum wet thickness followed Region I. If the downstream meniscus, A was at or close to the edge of the downstream die lip, B, then the dimensionless minimum wet thickness followed Region II as seen in Figure 2.14 (b). If, however, the downstream meniscus, A was between the length of the die lip (between locations B and G), then the dimensionless minimum wet thickness followed Region III as shown in Figure 2.14 (c).

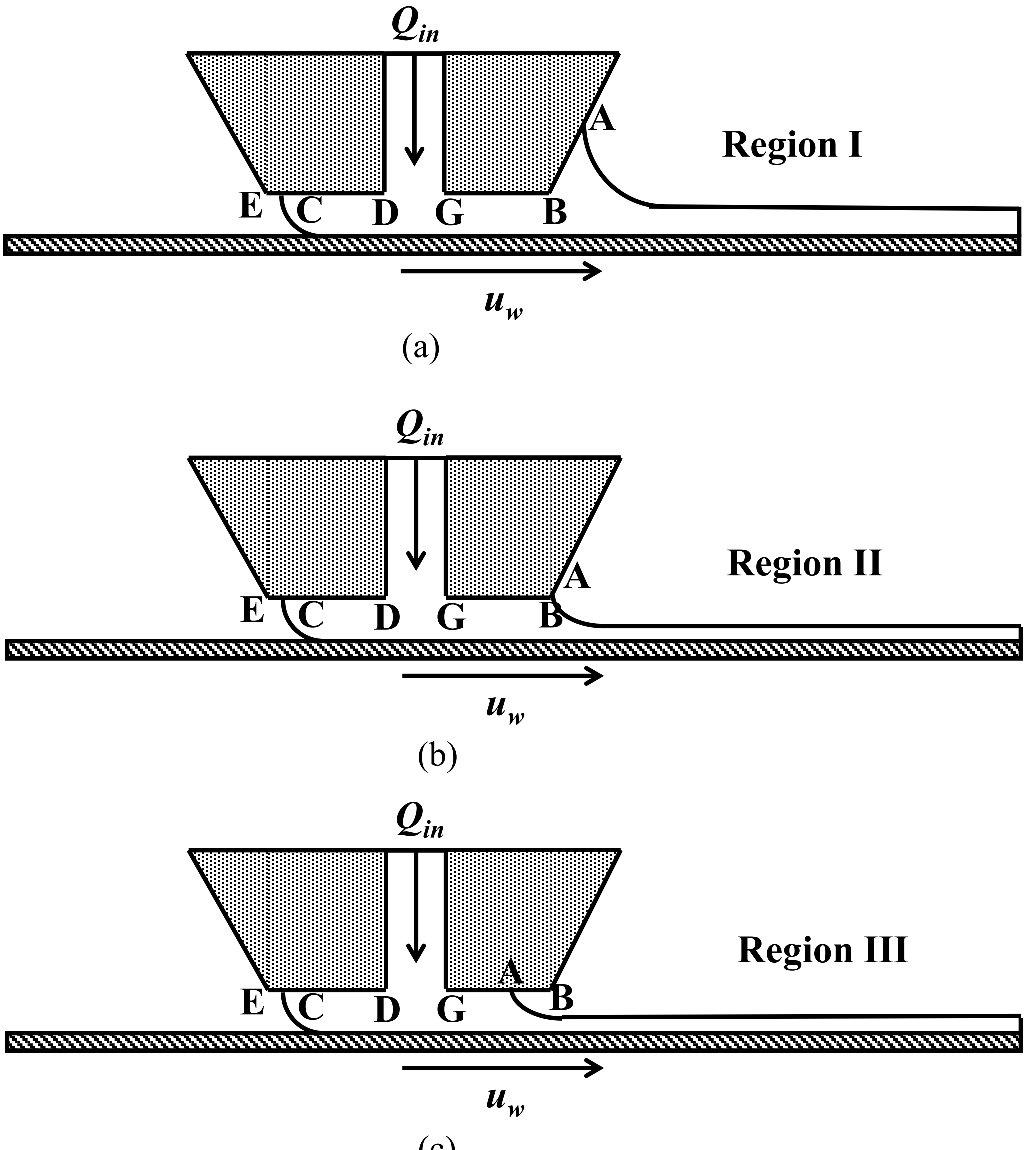

(a)

(b)

(c)

Figure 2.14: (a) Downstream meniscus location in Region I, (b) Downstream meniscus location in Region II, (c) Downstream meniscus location in Region III.

Similarly, the dimensionless minimum wet thickness was plotted against several other dimensionless numbers, such as Reynolds number, Stokes number, and Froude number, as discussed by Chang et al. [65]. Experiments performed by Chang et al. [100] show that the transition from Region I to Region II occurred near Re = 1, and the transition from Region II to Region III occurred near Re = 20. Furthermore, while moderate and high-viscosity fluids followed Regions I and II, low viscosity solutions followed Regions II and III. A list of other dimensionless parameters considered in various other studies is presented in Table 2.1 of Veverka's thesis [56].

As explained by Chang et al. [101], Region I was primarily dominated by viscous and surface tension forces. The transition from Region I to Region II had competing viscous and inertial forces, while Region II was influenced predominantly by inertial forces. The inertial forces grew significantly from Region II to Region III, such that the fluid exiting the slot die resembled a jet impinging on a moving substrate.

2.6 Methods to Extend Coating/Casting Windows

Researchers have come up with several methods to delay the air entrainment in order to extend the maximum coating speed. The most common methods have been summarized by Yamamura [102]. A few methods of interest are discussed including applying vacuum, finding optimum geometric/processing parameters, and applying electric field. Beguin [57] conceived the idea of applying vacuum at the upstream meniscus to further delay the air entrainment, thereby achieving higher coating speeds. Romero et al. [63, 64, 103, 104] also applied vacuum to extend the coating windows for Newtonian and non-Newtonian solutions. They found that as the substrate speed increased, the upstream and downstream menisci were pulled closer to the slot die (in

Figure 2.14, C approaches D and A approaches G) causing defects in the coating bead. Chang et al. [65] also noticed that the length of the coating bead decreased due to the upstream and downstream menisci being pulled closer to the slot exit. By applying vacuum, the upstream meniscus was prevented from getting pulled towards the slot die exit, resulting in higher coating speeds before air entrainment occurred.

Blake and Ruschak [91] found that angling the tape further delayed the air entrainment, by shifting $u_{w,\ max}$ to higher values. This observation was confirmed by Cohu and Benkreira's experiments using angled-dip coating [93, 94] and Benkreira and Cohu's experiments using angled-die coating [105]. Chang et al. [65] also studied the effect of orientation of slot die and substrate with respect to gravity on the size of coating window. They studied two configurations; vertical coating and horizontal coating. In the case of vertical coating, the direction of flow through the slot die was in the direction of gravity (Figure 2.15 (a)), while for horizontal coating, the substrate moved opposite to the direction of gravity (Figure 2.15 (b)). They found that vertical coating produces much wider coating windows compared to horizontal coating for low-viscosity solutions, however, as the viscosity increased; the difference between the two configurations became insignificant. Further, they found that stable coating beads were produced for low viscosity solutions when a vertical coating configuration was employed, whereas high-viscosity solutions produced more stable beads when a horizontal configuration was employed as it allowed for delayed air entrainment due to the pulling effect of gravity on upstream meniscus.

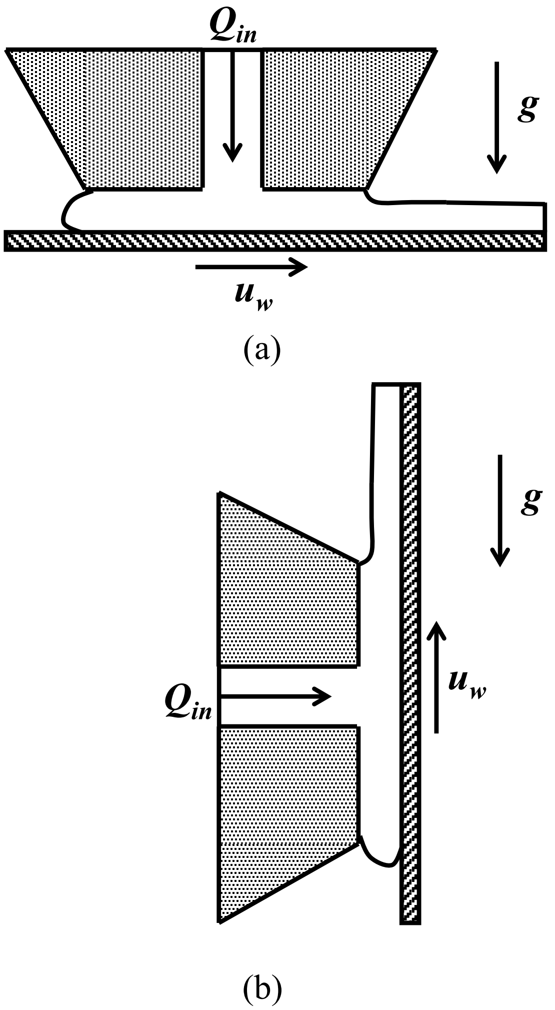

Figure 2.15: (a) Vertical coating, (b) Horizontal coating.

Yang et al. [78] showed that the coating speed can be extended when polymer additives were added to the solution, if air entrainment was the issue. However, polymer additives have no impact on the coating window when the coating speed was limited by ribbing defects.

Studies performed by Scriven [106] and Buonoplane et al. [107] showed that substrate roughness increased the air entrainment velocity thus facilitating higher coating speeds. However, Benkreira [108] showed that surface roughness can increase or decrease the air entrainment velocity depending on the solution viscosity. Thus, the surface roughness was found to have a positive effect on delaying air entrainment only beyond a critical viscosity.

Blake et al. [109, 110] experimentally and theoretically showed that the air entrainment can be delayed by forcing the liquid onto the moving substrate at high speeds in curtain coating. This phenomenon is termed hydrodynamic assist wetting and occurs due to the inertia of the fluid flowing onto the substrate. However, they found that too low or too high flow rates had no impact on the air entrainment velocity. Flow rates on either extreme will nullify the impact of inertia on the contact line.

Another technique to delay air entrainment includes applying an electric field across the substrate. Tests performed on curtain coating [111, 112] and slot coating [113] have shown that as the voltage increased, the dynamic contact angle made by upstream meniscus with the substrate decreased causing no air entrainment.

The list of studies discussed in this section to delay air entrainment is only a small sample of possible techniques and is by no means exhaustive.

2.7 Summary

A background review of different coating methods, the concept of coating window and the common coating defects were presented in this chapter. The differences between microscopic and macroscopic forms of air entrainment and the relevant physics were discussed. The chapter covered the three minimum wet thickness regions and their dependence on the location of the downstream meniscus. Finally, some of the methods reported in literature to delay air entrainment were outlined. In the next chapter, a discussion is presented on how the existing studies will be extended by performing the current research.

3. RESEARCH FOCUS

As discussed in the previous chapter, coating windows have been obtained by several researchers for a wide range of solutions. Some of the recent studies pertaining to coating windows for slot die coatings including the current study (highlighted in bold font) are summarized in Table 3.1. The type of tests performed, the nature of solutions used, the dynamic viscosity ranges of the test solutions, and the range of coating speeds obtained are also presented in Table 3.1. The maximum dynamic viscosity of the solutions used in previous studies has been limited to 1 Pa-s. As, the viscosities of the solutions used in the current work varies between 1 Pa-s and 40 Pa-s, understanding how the high-viscosity impacts the coating window and the nature of coating defects is of interest. In addition, understanding the impact of the shear-thinning nature of the relatively high-viscosity solutions on the slot die coating process is of importance. Although the results from the dimensionless coating window can be extended to a wide range of solutions, and processing and geometric parameters, if one carefully examines the results pertaining to dimensionless coating windows obtained in the previous studies (as discussed in Section 2.5), the coating windows do not overlap even for solutions with viscosities that have the same order of magnitude (which can be seen in Figure 16 in [65], and Figure 12 and Figure 13 in [100]). In this study, an understanding of whether previously developed dimensionless analysis can be extended to solutions whose viscosities are more than two to three orders of magnitude higher than those previously reported will be obtained.

Table 3.1: Slot die coating parameters used and coating speed ranges obtained in literature

Authors	**Type of tests**	**Solution type**	**Viscosity range, Pa-s**	**u_w range, m/s**
Iuliano (2004) [114]	Numerical & Experimental	Non-Newtonian	0.006 – 0.09	0.2 – 2.0
Romero et al. (2004) [63]	Numerical & Experimental	Non-Newtonian	0.017 – 0.084	0.2 – 2.8
Yang et al. (2004) [78]	Experimental	Newtonian & Non-Newtonian	0.013 – 0.35	0.08 – 0.7
Chu et al. (2006) [70]	Numerical & Experimental	Newtonian & Non-Newtonian	0.012 – 0.027	1 – 10
Chang et al. (2007) [100]	Experimental	Newtonian	0.0012 – 0.05	N/A
Chang et al. (2007) [65]	Experimental	Newtonian	0.003 – 0.3	0.25 – 8.2
Romero & Carvalho (2008) [103]	Numerical	Newtonian	0.01 – 1	0.1 – 5
Lin et al. (2008) [58]	Mathematical	Newtonian	0.007 – 0.014	0.033 – 0.17
Lin et al. (2010) [67]	Numerical & Experimental	Newtonian	0.003 – 0.2	? – 0.78
Chin et al. (2010) [66]	Experimental	Slightly non-Newtonian	0.01 – 0.15	0 – 0.33
Current Study	**Numerical & Experimental**	**Non-Newtonian**	**1 – 40**	**Presented in Chapters 6 through 8**

The current study will also shed light on air entrainment mechanisms observed when such high-viscosity solutions are coated using the slot die coating process, which has not been done to date. The effect of various fluid properties, geometric parameters, and processing parameters on the sizes of sawteeth and bubbles will be investigated in a qualitative manner. As per the author's knowledge, previous studies focused on understanding the effects of geometric parameters on the coating window only and their influence on air entrainment has not been explored.

3.1 Research Tools

Experiments and numerical simulations are implemented to conduct this research for the purpose of generating coating windows and capturing air entrainment, which can be used by the manufacturing industry to make membranes or other thin films. However, each has its own advantages and disadvantages. Experiments are crucial for this study as they are not only used to validate the numerical model, but are preferred over numerical simulations when time is of importance. For example, in order to obtain 10 data points on a coating window using an existing experimental setup, the experiments take about 4 hours, however to obtain each data point by running simulations on 8 parallel nodes; it takes about 3 to 10 hours depending on the rheology of the solution. Conversely, the experimental setup is expensive and tedious to build. Also the solutions to be cast may not be readily available and/or may be costly, which is the case for the present PPA/PBI solution study. Because the PPA/PBI solution (a small sample of PPA/PBI solution, which is prepared at BASF using a proprietary method, is used in the current study to make one set of experiments) is not readily available, experiments were primarily conducted with analogous solutions, which are henceforth referred to as the test solutions.

These solutions are selected such that they encompass the entire viscosity range of PPA/PBI solutions and are shear-thinning. The simulations and experiments are implemented with the test solutions under exactly the same conditions to obtain a validated numerical model. Once the validation is performed, the coating windows for PPA/PBI solutions are obtained numerically and semi-empirical relations are found. This semi-empirical data is finally validated with one set of experiments performed on a sample of PPA/PBI solution obtained from BASF, GmBH.

3.2 Relevant Non-Dimensional Variables for Dimensionless Coating Window

The relevant non-dimensional variables identified for the current study are listed in Table 3.2. These variables are obtained for power-law shear-thinning fluids using a vertical slot die configuration, as explained in Section 2.6. There are a total of six variables identified based on all combinations of any two forces among the four forces acting on the coating bead: inertia force, viscous force, surface tension force, and gravity. As the dimensionless minimum wet thickness (obtained at maximum coating speed) is plotted as a function of a given dimensionless number, the coating speed used in the dimensionless number definition is the maximum coating speed, $u_{w,max}$. The derivation of these dimensionless variables for the power-law fluids used in slot-die coating is presented in Appendix A.

Table 3.2: Relevant dimensionless numbers

Non-Dimensional Number	**Physical Significance**	**Vertical Coating**
Ca	Ratio of viscous and surface tension forces	$\boldsymbol{Ca = \frac{k\left(\frac{u_{w,max}}{H}\right)^{n-1} u_{w,max}}{\sigma}}$
Re	Ratio of inertia and viscous forces	$\boldsymbol{Re = \frac{\rho v_{in}^2 H^n}{k u_{w,max}^n}}$
St	Ratio of gravitational and viscous forces	$\boldsymbol{St = \frac{\rho g H^{n+1}}{k u_{w,max}^n}}$
We	Ratio of inertia and surface tension forces	$\boldsymbol{We = \frac{\rho v_{in}^2 H}{\sigma}}$
Fr	Ratio of inertia and gravitational forces	$\boldsymbol{Fr = \frac{v_{in}^2}{gH}}$
Bo	Ratio of gravitational and surface tension forces	$\boldsymbol{Bo = \frac{\rho g H^2}{\sigma}}$

3.3 Summary

This chapter began by explaining the motivation behind performing the study, in lieu of existing non-dimensional coating window data. The tools used for performing the research were introduced by discussing the advantages and disadvantages of each. Finally, the relevant dimensionless numbers that will be used in the study were presented. In the following chapter, the material properties of the solutions used in the current study are presented.

4. MATERIAL PROPERTIES

In this chapter, the properties of all the solutions used in the current study are presented along with the methodology used for obtaining the properties. PPA/PBI solutions are extremely viscous at room temperature (the solutions do not flow at room temperature) and hence are typically processed above 120 °C [115]. To this end, the PPA/PBI solutions will be evaluated at 120 °C, 140 °C and 160 °C. The PPA/PBI solutions are referred to as "actual solutions" in the current study. The "test solutions" (viscosity range: 1 Pa-s to 40 Pa-s) used in this study are blackstrap molasses (BSM), dilute blackstrap molasses (DBSM) obtained by mixing 10 parts of BSM with 1 part of water by volume, and diluted Poly (1-vinylpyrrolidone-co-2-dimethylaminoethyl methacrylate), which has seven parts of Poly (1-vinylpyrrolidone-co-2-dimethylaminoethyl methacrylate) and one part of water by volume. The last test solution will be henceforth referred to as "Polymer Solution". Due to the colorless nature of the Polymer Solution, a red dye is added and all the properties are evaluated in the dyed condition. A list of the actual solutions and test solutions is given in Table 4.1.

Table 4.1: Actual and test solutions

Actual Solutions	**Test Solutions**
PPA/PBI solution at 120° C	Diluted Poly (1-vinylpyrrolidone-co-2-dimethylaminoethyl methacrylate) [Polymer Solution]
PPA/PBI solution at 140° C	Blackstrap molasses [BSM]
PPA/PBI solution at 160° C	Dilute blackstrap molasses [DBSM]

The density, the rheology and the surface tension/contact angle properties of the test solutions, i.e., BSM, DBSM and Polymer Solution were measured in-house at room temperature. The properties of the PPA/PBI solutions were measured at elevated temperatures under controlled relative humidity conditions. Due to the limitations of the instrumentation available in-house, which is incapable of measuring the properties at elevated temperatures and controlled humidity conditions, tests for the PPA/PBI solutions were outsourced to Augustine Scientific laboratory in Newbury, Ohio. Unfortunately, different instrumentation (available in-house) was used to measure the properties of the test solutions than those used at Augustine Scientific, as explained in the following sections.

4.1 Density Measurements

The densities of the test solutions and the actual solutions were obtained using in-house and outsourced capabilities, respectively. A consolidated list of the results is listed in Table 4.2.

4.1.1 Test Solutions

The densities of the test solutions were obtained by measuring the weight of a known volume of the solution. The density was then obtained by dividing the weight of the solution by its volume. Each test was performed five times and the densities were averaged to obtain the final densities as presented in Table 4.2. The differences in the five measurements are within ±1% of the mean value.

4.1.2 PPA/PBI Solutions

The density data for the PPA/PBI samples were determined by the quartz rod displacement method on a Kruss Processor Tensiometer K100 (accurate to 4-signifcant figures). The tests were all conducted at a relative humidity of 55% and at three temperatures; 120 °C, 140 °C and 160 °C. The values were measured five times and averaged. The averaged density values are listed in Table 4.2. The differences in the five measurements are within ±0.05% of the mean value.

Table 4.2: Density of actual and test solutions

Solution	**Density, ρ, kg/m^3**
PPA/PBI solution at 120° C	1952.70
PPA/PBI solution at 140° C	1947.50
PPA/PBI solution at 160° C	1942.10
Polymer Solution	1041.13
BSM	1452.54
DBSM	1411.52

4.2 Viscosity Measurements

The viscosity of the test solution and the actual solutions were obtained using in-house and outsourced facilities, respectively. The consolidated results are presented in Figure 4.1.

4.2.1 Test Solutions

The viscosity measurements of the test solutions were performed using an Advanced Rheometric Expansion System (ARES), which is suitable for measuring high-viscosity solutions. A parallel-plate configuration was used to conduct "Steady Rate Sweep" tests. The following steps were followed during testing:

1. The plates were thoroughly cleaned prior to every test with distilled water and wiped completely, ensuring there were no traces of water.
2. The motor was set in the steady mode.
3. Before loading the sample, the torque and force were offset to zero and the gap between the plates was set to zero.
4. The final gap between the plates was set to the desired value. The desired gap is dependent upon the material properties of the solution.
5. The gap was set such that both plates were in contact with the sample and there was a small bulge of the sample outside the plate circumference. Therefore, the gap increased as the viscosity increased.
6. The sample was then loaded on the lower plate and another value for the gap (0.05 mm higher than the desired gap) was entered to allow for slow controlled contact with the sample.

Every run was performed twice to ensure repeatability. The final viscosity value is the average of the two runs. The averaged viscosity data for the three test solutions are shown in Figure 4.1 using open symbols. The differences in the two measurements are within ±7% of the mean value. Notice that some of the viscosity measurements could not be made at lower shear rates due to the large errors in viscosity values. A power-law curve is fitted to each curve to obtain the consistency-index, *k*, and the power-law index, *n*, values.

4.2.2 PPA/PBI Solutions

The viscosity measurements for all the PPA/PBI solutions were made using a Brookfield LV Viscometer with a small volume UL Accessory. The shear rates were varied from 1.3 s^{-1} to 132.0 s^{-1}. The tests were performed at temperatures 120 °C, 140 °C and 160 °C in a 55% RH environment. The variation in temperature readings was +/- 0.5°C. All the tests were repeated twice and the final viscosity values were obtained by averaging. The averaged viscosity data obtained at the three different temperatures are presented in Figure 4.1, using solid symbols. The differences in the two measurements are within ±1% of the mean value.

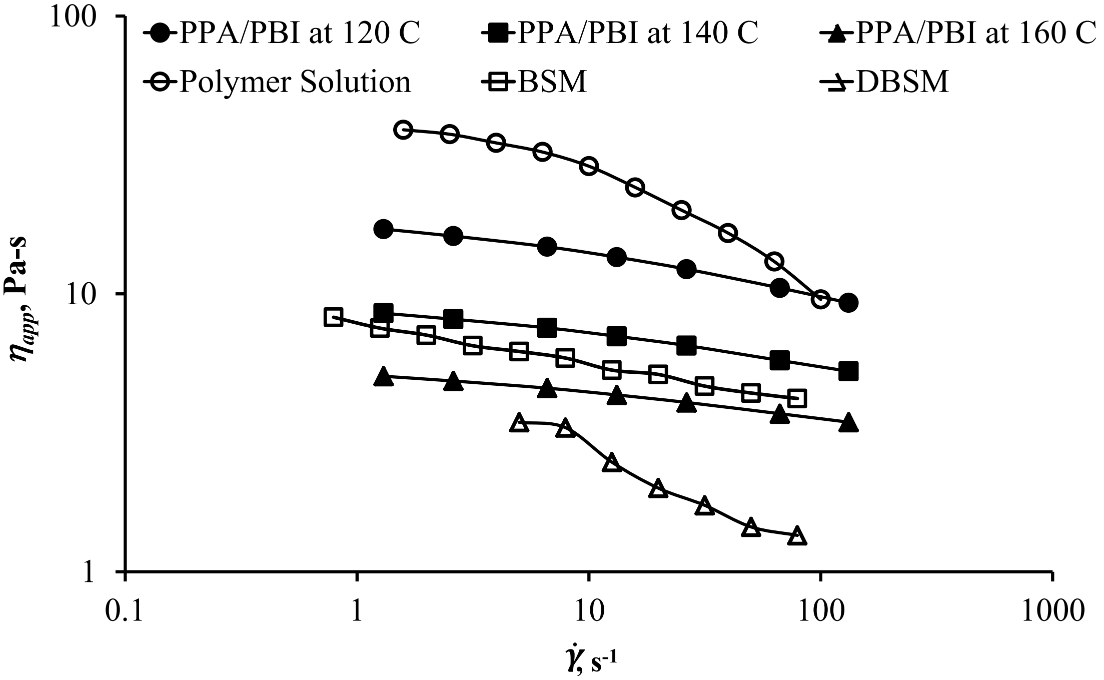

Figure 4.1: Apparent viscosity of the actual solutions and the test solutions.

It is evident from the viscosity curves that the solutions are shear-thinning. Also, the test solutions are chosen such that they encompass the entire range of viscosity values traced by the PPA/PBI solutions. Therefore, once a validated numerical model is obtained by performing and comparing simulations and experiments using test solutions, the numerical model can be used for predicting the coating window trends of the PPA/PBI solution.

4.3 Surface Tension Measurements

The surface tension of test solutions was obtained using the pendant drop method, whereas the surface tension measurements for PPA/PBI solutions were made using Wilhelmy plate method. Different methods were used due to the differences in the test conditions required for the solutions. A consolidated list of the results is provided in Table 4.3.

4.3.1 Test Solutions

The surface tension of the test solutions was measured using the pendant drop method employing a Ramé-hart Model 250 Standard Goniometer as described in the tutorial [116]. The main components of the instrumentation are: Ramé-hart Model 250 Standard Goniometer with DROPimage Advanced (p/n 250-F1), a Microsyringe (p/n 100-10-20, included with Model 250) and 22g Stainless Steel Straight Needle (p/n 100-10-12-22, included with Model 250). The DROPimage Advanced software uses a proprietary technology to trace the edges of the drop and calculates the surface tension using the Young-Laplace equation. The surface tension measurements were made at ambient conditions. The following steps were used to obtain the surface tension:

1. The microsyringe was filled with the sample liquid and the straight needle was attached to the syringe firmly.
2. Any air present was removed by turning the dispensing knob on the microsyringe.
3. The microsyringe was attached to a fixture such that the tip of the needle was visible in the center of the DROPimage live image window.
4. The environmental conditions and input parameters were set. The solution was dispensed such that it appears as a stable bead at the tip of the needle. The lighting was adjusted so that the background was white and the drop was black. The crosshairs in the graphical user interface (GUI) was aligned such that the horizontal line was set at the interface of the needle and the drop. The vertical line was aligned so that it passes through the center of the needle and the drop.
5. The experiment was performed.

The experiments were repeated twice and the surface tension values were averaged. The differences in the two measurements are within ±2% of the mean value. The averaged values are presented in Table 4.3.

4.3.2 PPA/PBI Solutions

The overall surface tension of the sample was measured in a controlled cyclic ramped temperature using Wilhelmy plate type surface tension on a Kruss Processor Tensiometer K100. The relative humidity over the sample during the experiment was controlled at 55% RH in inert argon during the surface tension experiment. This was done using a Vaisala X025004 humidity sensor in combination with a Hiden IGAsorp flow through RH control system. Temperatures were detected right at the surface of the sample with a laser thermometer during measurements. The surface tension measurements were performed at 120 °C, 140 °C and 160 °C. All surface tension tests were performed twice and the values were averaged. The differences in the two measurements are within ±0.1% of the mean value. The surface tension values had a weak dependence on the temperature (Table 4.3).

The averaged surface tension values for the PPA/PBI solutions and for all the test solutions are presented in Table 4.3.

Table 4.3: Surface tension of actual and test solutions

Solution	**Surface tension, σ, N/m**
PPA/PBI solution at 120° C	0.0475
PPA/PBI solution at 140° C	0.0467
PPA/PBI solution at 160° C	0.0461
Polymer Solution	0.060
BSM	0.047
DBSM	0.049

4.4 Contact Angle Measurements

The contact angle measurements were made using the sessile drop method for both the PPA/PBI solutions and the test solutions. However, the instrumentation used is different for the two types of solutions. The contact angles were measured on the slot die and substrate materials. The slot die is made of 316 stainless steel (SS 316) and the substrate is made of poly (ethylene terephthalate) commonly known as PET. The choice of these materials is explained in Chapter 5.

4.4.1 Test Solutions

The contact angles of the test solutions were measured using the sessile drop method. For this purpose, again a Ramé-hart Model 250 Standard Goniometer was used. The entire instrumentation used all the components required for surface tension measurements in addition to the desired substrate on which the contact angle was measured. The substrate (SS 316 or PET) was clamped to a stage, which was free to move vertically and horizontally. The measurement procedure is as follows:

1. The goniometer, DROPimage software, the light source and the camera were all setup for use.
2. The needle attached to the syringe was adjusted and centered such that the bottom of the needle appears at about a quarter of the total distance when measured from the top of the GUI live screen.
3. The plate clamped to the stage was adjusted such that it was just below the midpoint of the GUI screen.
4. Two microliters of solution was forced through the tip of the needle.
5. The needle was slowly lowered until the drop comes in contact with the substrate. Then slowly the needle was moved away from the plate so that the drop was separated from the needle and the needle disappears from the GUI screen.
6. A picture of the drop resting on the plate was taken using the camera.
7. The contact angle measurements were then made. The angle made by the tangent to the droplet with the plate, when measured inside the liquid phase gave the contact angle. Each measurement is repeated twice and the values are averaged.

The differences in the two measurements are within ±5% of the mean value. The averaged contact angles are listed in Table 4.4.

4.4.2 PPA/PBI Solutions

The contact angle measurements made by the PPA/PBI solution on SS 316 and PET were performed using the sessile drop method on a Kruss Drop Shape Analysis System (DSA) 100 under a controlled environment, i.e., 55% RH. For each test, two microliter drops of solution were dispensed on the substrate. In order to obtain the contact angle values at 120 °C, 140 °C and 160 °C, the drop and the substrate were heated to the desired temperature, while the contact angle was monitored. Tests were repeated and the final values of contact angle listed in Table 4.4 were obtained by averaging. The differences in the two measurements are within ±2% of the mean value.

The contact angles for the PPA/PBI solutions and the test solutions on SS 316 and PET are shown in Table 4.4. Notice that all the angles are static contact angles.

Table 4.4: Contact angles of actual and test solutions

Solution	Contact angle on SS 316, °	Contact angle on PET, °
PPA/PBI solution at 120° C	33.2	92.3
PPA/PBI solution at 140° C	31.6	91.5
PPA/PBI solution at 160° C	30.5	90.9
Polymer Solution	45.0	65.0
BSM	70.0	62.0
DBSM	68.5	74.0

4.5 Summary

This section summarized the material properties of the solutions used in this study and the instrumentation used for measuring the fluid properties. Specifically, the density, rheological properties, surface tension, and contact angle values were presented. The data on the fluid properties of the test solutions is presented in Appendix B. In the next chapter, the details of the experimental study are discussed.

5. EXPERIMENTAL STUDY

The thin films are experimentally cast and analyzed for defects. The experimental setup, procedure and the limitations on the processing and geometric parameters are explained in this section.

5.1 Experimental-Setup

In order to understand and analyze the defects generated during casting of high-viscosity, shear-thinning fluids, experiments are carried out using a custom designed, roll-feed imaging system (RFIS). A schematic of the RFIS system and the important dimensions of the system are shown in Figures 5.1 (a) and 5.1 (b) respectively. The main components of the RFIS system are the die, roll-feed/web control, heating/temperature control, and visualization/inspection systems. The overall frame of the experimental setup is built from components obtained from 80/20 Inc. A detailed description of each of these components is explained in the following subsections.

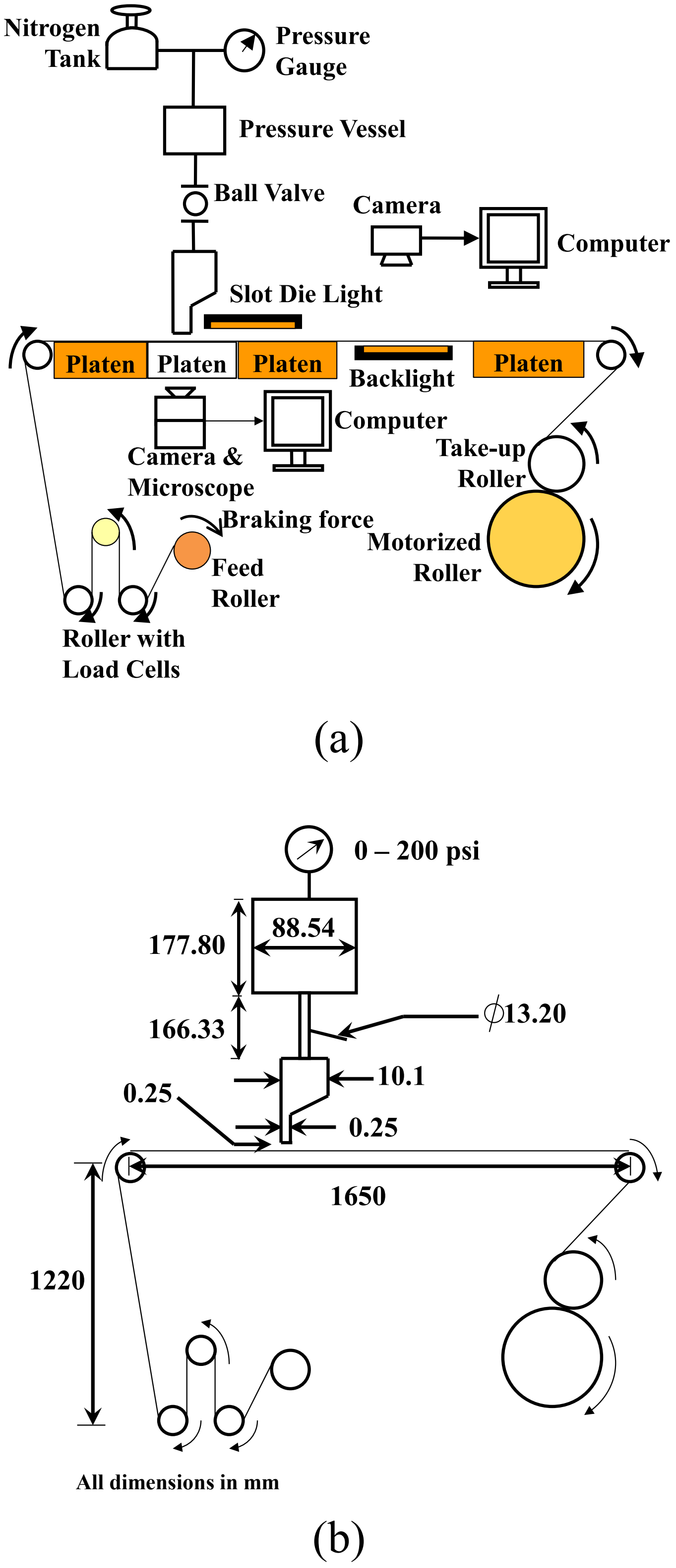

Figure 5.1: (a) Schematic of the roll-feed imaging system (RFIS), (b) Important dimensions of the RFIS system.

5.1.1 Roll-Feed/Web Control System

The substrate/web used in the experiments is made of PET due to its corrosion resistant nature and high-temperature operation [115]. A PET roll which is 0.1 mm thick and 60 mm wide is mounted onto a feed roller. As shown in Figure 5.2, the PET film moves over several other rollers, stretched along a horizontal plane underneath the slot die and rolled onto a take-up roller on the other side of the frame. The take-up roller is connected such that it is in contact with a motorized roller placed underneath. A Tesson Direct Current (DC) motor controls the speed of the motorized roller, which in-turn rotates the take-up roller. The rotation of the take-up roller causes the PET film to move from the feed roller, along the horizontal plane to the take-up roller, where it is wound. The horizontal plane, along which the PET film moves, is formed by several individual platens, which can be separately moved/adjusted. The individual platens consist of cast aluminum heated platens and a non-heated, Plexiglas transparent platen, as shown in Figure 5.2. The platens act as rigid supports on which the PET film rests. The heated platens allow for raising the temperature of PET film to the solution temperature during high-temperature coating. The transparent platen facilitates monitoring of the solution wetting process by a camera/microscope system as the solution is extruded from the slot die. The translational speed of the PET on the horizontal plane can be varied from 0 mm/s to 250 mm/s. However, the speeds are restricted between 1 mm/s and 15 mm/s in the experiments. At speeds below 1 mm/s, the errors are much higher than ± 20 %, which is not acceptable for obtaining controlled repeatable results. At speeds higher than 15 mm/s, the system is subjected to vibrations resulting in external noise factors, which were found to induce film thickness variations [103]. A BEI Technologies EX11 series miniature incremental rotary encoder installed on the motorized roller is used to determine the web speed.

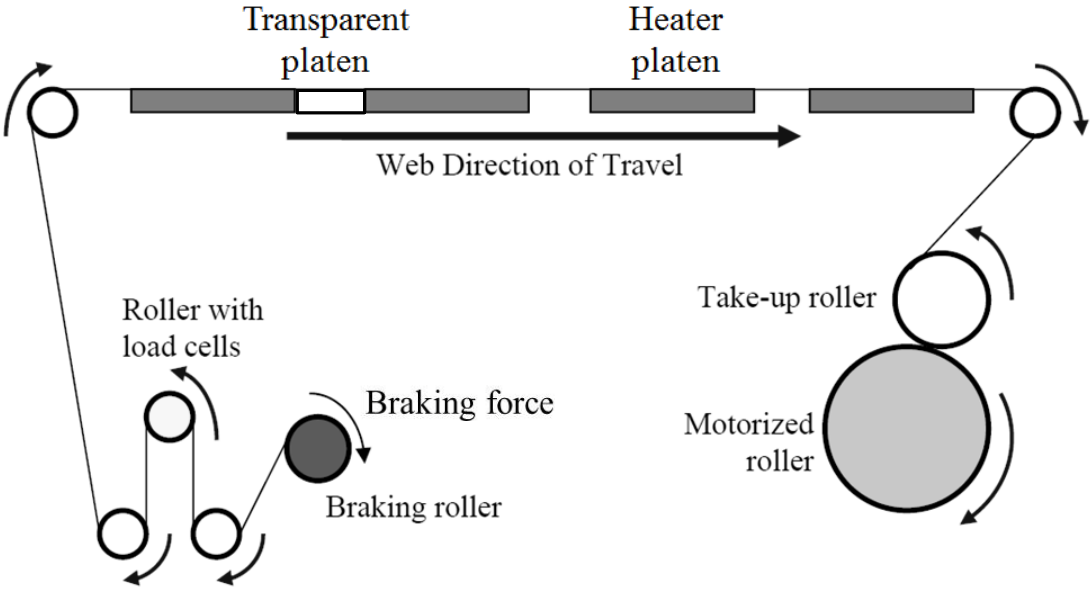

Figure 5.2: Schematic of the roll-feed web control system (made slight modifications to figure from [117]).

The PET substrate is held under tension to avoid out-of-plane vibrations and deflections that cause non-uniformity in the cast film. A Cleveland Motion Controls brake mounted on the feed roller controls the PET tension at the desired value by varying the voltage with a 1000 W pulse width modulated (PWM) signal. The tension is adjusted by passing a signal from a National Instruments LabVIEW [118] program onto a NI PXI-1010 DAQ card that is connected to a NI PXI-8186 Embedded Controller with a SCB-68 I/O board. The feedback control system for the web tension is provided by using Ultra Cartridge Transducer load cells. More details on the web tensioning and web speed control can be found in Johnson’s thesis [117]. In addition, similar to the procedure followed by other researchers [107, 119], the PET substrate is grounded to eliminate any static charges, which are known to skew the results. Hartman [120] showed with the help of curtain coating that air entrainment velocity could be significantly increased, when electrostatic charges are present.

5.1.2 Die System

A T-shaped slot die (Figure 5.3), made of SS 316, is chosen based on the experiments performed by Harris et al. [115] to cast the solutions, which was found to be best suited for casting highly-viscous, non-Newtonian solutions. The slot die has an upstream half and a downstream half, and a shim placed between them. The shim is selected such that its thickness is equal to the slot gap thickness, W. The width of the shim opening equals the width of the slot die opening, $\mathcal{W}_{sd}$. For all the experiments performed in the current study, the width of the slot die opening is set at 50 mm. In order to overcome the issues investigated by Romero and Carvalho [103] due to improper alignment of the die's components, the die's two halves and the shim are carefully aligned and clamped with nuts and bolts. The slot die is equipped with heater cartridges on the top surface and a thermocouple is placed in the bottom surface close to the slot die exit, to provide temperature control.

Depending on the casting temperature required, the fluid to be cast is heated to the desired temperature in a vacuum oven and then poured into a pressure vessel placed above the die as shown in Figure 5.1. The pressure vessel is connected to a Nitrogen tank, which assists in pressurizing the casting fluid. The pressure is set to the desired value using a pressure gauge (0 to 345,000 Pa for DBSM and BSM & 0 to 1, 380, 000 Pa for others) connected between the Nitrogen tank and the pressure vessel. The temperature of the pressure vessel is monitored using a thermocouple attached to the lid of the pressure vessel. A ball valve connected to a pipe fitting is placed between the pressure vessel and the slot die to allow for opening or closing of the die system, which is originally kept in a closed position, until experiments are performed.

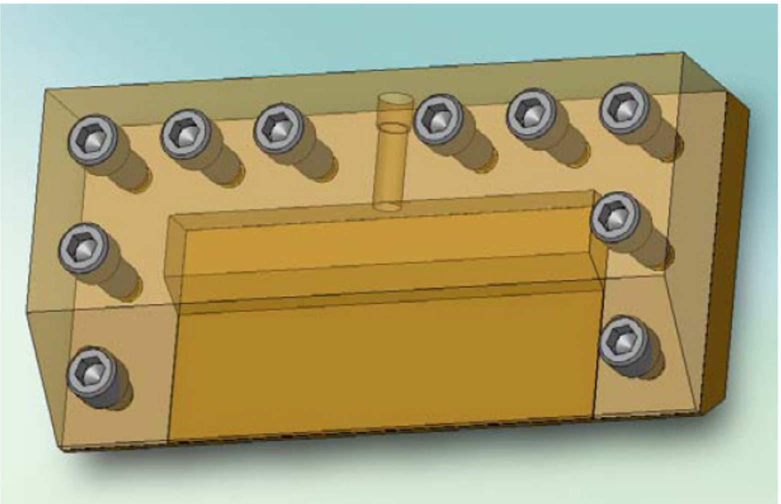

Figure 5.3: T-shaped slot die (figure taken from [117]).

Before every experiment, the perfectly cleaned slot die is connected to the pipe fitting containing the ball valve and mounted onto the vertical rail system of the mainframe using plastic linear bushings. Then, the pressure vessel is connected to the slot die through the pipe fitting. The stand-off height or the coating gap (the distance between the slot die and the substrate/web), *H*, is set by using a feeler gauge, which has a thickness equal to the desired coating gap. The height of the die from the substrate is adjusted by moving each side of the vertical rail system independently with worm gears connected to the rail guide blocks. Once the stand-off height is adjusted, solution is poured into the pressure vessel.

5.1.3 Heating/Temperature Control System

While the BSM, DBSM and Polymer Solutions are cast at room temperature, PPA/PBI solution is heated to temperatures equal to or greater than 120° to obtain viscosities low enough for the solution to flow. Prior to casting the PPA/PBI solution, it is heated in a vacuum oven to the desired temperature. Nearly, total vacuum conditions are maintained in the oven to prevent degradation of the solution, while heating. Before transferring the solution to the RFIS, the pressure tank, slot die and two platens over which the PET moves along the horizontal plane are all heated to the same temperature as the solution.

Two 800 W Watlow band heaters wrapped around the pressure vessel are used to heat it, while the slot die is heated using two 400 W Watlow cartridge heaters inserted in the top of the upstream plate of the slot die. The platens are 6500 W, cast aluminum heaters, custom built by Star Electric, Inc. that served to maintain the temperature of the moving substrate equal to the solution temperature so as to avoid rapid cooling and gelling of the cast solution. The platens are cut to a flatness of 0.001" to provide a flat surface under the substrate. The temperatures of the platens are monitored using bayonet thermocouple tubes that are placed at the center of the blocks. The thermocouple attached to the lid of the pressure vessel is placed about 1.5 mm from the bottom of the pressure vessel and is in contact with the inner wall of the pressure vessel. Another thermocouple is placed on the die's outer surface to measure its temperature. The temperatures measured by the thermocouples on the pressure vessel, slot die and the two platens are displayed on a heater control station (Figure 5.4) placed on the front of the frame. These temperatures are continuously monitored to ensure that the temperatures do not go above the set values, as higher temperatures would lead to changes in the chemical structure of the cast solution. To minimize heat loss from the die system to the outside and to ensure temperature uniformity, all the components of the die system are thermally insulated using fiber glass fabric with Velcro attachments.

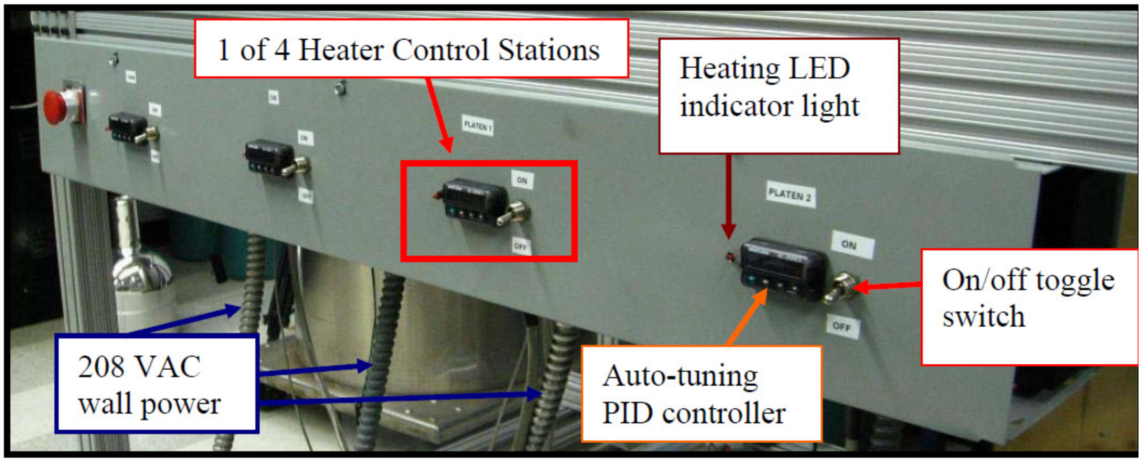

Figure 5.4: The heater control station (figure taken from [117]).

The power to the heaters is provided through a 208 VAC power supply. Due to the higher amperage of current required for the heaters (15 A for two systems and 40 A for the other two systems), each outlet has its own circuit breaker in the event of a short circuit. The grounds from all the heaters are earthed. While supplying power to the heaters, a Watlow EZ-ZONE PID auto-tuning controller is also powered using a parallel circuit. These controllers are connected to both the thermocouples and solid state relays (SSRs). By receiving a 5V control signal from the controllers, the power to the heaters is turned on or off depending on whether the temperature is going below or above the set temperature respectively. Additionally, the power to the heaters can be individually turned on or off using a toggle switch as shown in Figure 5.4. Four LEDs attached to the four controllers show the state of power to the slot die, the pressure vessel and the two platens.

5.1.4 Visualization/Inspection Systems

In order to understand the factors influencing defect generation, capturing of images of the cast solution during the casting process is important. For this purpose, a microscope (Olympus Zoom Stereo Microscope-model SZ61TR) attached to a camera (Olympus SIS-UC30) and another overhead camera (Lumenera LM135M) are used. The microscope is placed close to the slot die exit to capture the mechanism of casting solution wetting, while the overhead camera is placed significantly downstream of the slot die (distance) to capture the images of the film post-casting. The cameras are connected to a computer, which is loaded with Olympus Stream Application software that analyzes the images fed from the camera to the computer.

The microscope/camera system is placed under the transparent platen and serves the purpose of capturing the contact line location, the sawtooth structures formation and the air bubble breakup mechanism while casting the test solutions. For this purpose, the transparent PET film is placed on the transparent block as described in section 5.1.1. In the case of PPA/PBI solution experiments, due to the heating requirements of the PET film, the transparent block is not used and the PET film rests on the cast aluminum platens. Therefore, for the PPA/PBI solution, the images of the cast film are only taken by the downstream overhead camera and the actual bubble breakup mechanism is not captured. As such, the current study does not provide the location and shape of the DCL while coating PPA/PBI solutions.

The overhead camera placed further downstream of the casting process captures the images of the cast film and feeds it back to the computer. The type of defects are detected and classified using an in-house neural network program written in MATLAB 6.3 [121].

5.2 Experimental Procedure

Experiments are performed to obtain two sets of data:

1. The flow rate values corresponding to the set pressure from the Nitrogen tank, and
2. The coating windows for the solutions for different geometric conditions.

The flow rate values are needed for every pressure considered during experiments due to their use in numerical simulations. The simulation is more stable when the velocity condition obtained from the mass/volumetric flow rates are imposed at the slot die parallel plate inlet. Also, as the entire slot die is not modeled and the computational domain consists of only the downstream section of the die, specifying variables such as mass or volumetric flow rates or velocity is more appropriate and accurate. In addition, the pressure data are not known for the computational domain considered.

5.2.1. Pressure, *P* versus Volumetric Flow Rate per Unit Width, *Q'*

In order to obtain the pressure versus flow rate curves, two different methods were used depending on the solutions used for casting. The PPA/PBI solution forms a sol-gel after the casting process as it rests on the PET substrate, while BSM, DBSM and the Polymer Solutions remain as solutions. Hence, for PPA/PBI solution, the volumetric flow rate is calculated using Method 1, while for the remaining solutions, Method 2 is used. The details of the two methods follow:

Method 1: The pressure is set at the desired value, *P*, and noted from the pressure gauge fixed on the Nitrogen tank. The PPA/PBI solution is cast into a sol-gel film at a given substrate speed, u_w. For a defect-free film, the thickness of the sol-gel film is obtained by measuring and averaging the film thickness at five different locations of the film. The thickness uniformity is maintained and within ±6% of the average thickness. Also, the width of the film is measured. The width of the film is within ±2% of the slot die width. The flow rate per unit width, *Q'*, is then obtained from the product of average film thickness, h, and the substrate speed, u_w. The process is repeated for several other pressure values and corresponding volumetric flow rates per unit width are calculated by Equation 5.1:

$$Q' = v_{in} W = u_w h \tag{5.1}$$

Once all the *P* and *Q'* values are obtained, they are plotted in an Excel sheet, a linear curve is fitted, and an empirical relation between *P* and *Q'* is obtained. The *P* versus *Q'* curves along with the empirical relationship are presented in Appendix C. In the current study, both the experimental and numerical results are presented in terms of flow rate per unit width.

Method 2: Due to the inability of BSM, DBSM, and Polymer Solutions to gel, an alternate method is used to obtain the relation between *P* and *Q'*. In this method, after the pressure *P*, and the substrate speed, u_w, are set to the desired values, a known length, L_f, of the coated PET is weighed and the weight, m_f, is recorded. The mass of dry PET, m_{PET}, is recorded after it is cleaned and dried. The total time, t_f, required to coat the known length of PET, L_f, is obtained by dividing L_f by u_w. The volumetric flow rate per unit width, Q', is then obtained by Equation 5.2:

$$Q' = \frac{(m_f - m_{PET})}{\mathcal{W}_f t_f \rho_{cs}} \tag{5.2}$$

where the casting solution density is given by ρ_{cs} and $\mathcal{W}_f$ is the width of the film.

5.2.2. Procedure for Obtaining Coating Window

If the solution is cast at an elevated temperature, the solution is first heated in a vacuum oven. Once the solution is placed in the vacuum oven, the desired temperature is set and the pressure is adjusted to a pressure nearly equal to absolute zero (total vacuum) to prevent any contamination of solution. As the solution heats up, the slot die, pressure vessel and the two platens are heated to the same final temperature. After the solution and the components reach the final temperatures, the solution is transferred into the pressure vessel and the solution is purged with Nitrogen. The solution is allowed to sit in the pressure vessel for some time until it reaches thermal equilibrium with the pressure vessel. For solutions cast at room temperature, the solution is poured into the pressure vessel, the lid is replaced and the solution is purged.

The pressure is set at the desired value by adjusting the valve on the Nitrogen tank. The pressure reading is noted from the pressure gauge. Then the ball valve is opened allowing the solution to flow through the die and onto the substrate. The substrate speed is set by adjusting the power to the motorized roller, which in-turn imparts motion to the PET substrate. The value of the substrate speed that corresponds to the dripping condition is recorded as the minimum substrate speeds, $u_{w,min}$, for that corresponding pressure. Keeping the pressure at the same value, the substrate speed is gradually increased until the first set of air bubbles is noticed. This substrate speed is then documented as the maximum substrate speed, $u_{w,max}$. Both the dripping and air entrainment conditions are monitored using the image relayed by the microscope/camera system placed under the transparent platen. For PPA/PBI solution, air entrainment is recorded when bubbles are seen in the coated film, while dripping is recorded by visual inspection. The minimum and maximum substrate speed for that particular pressure forms the first set of points on the casting window. The minimum and maximum substrate speeds for a particular pressure are identified in the depiction of coating window by the horizontal solid line as seen in Figure 5.5. Then, the pressure is set to another value and the process is repeated until either the maximum limitation on the substrate speed (i.e., 15 mm/s) is reached as set by the system configuration or for a given pressure, a good coating can no longer be produced for any of the coating speeds. Alternatively, the upper (P_{max}, Q'_{max}) and lower (P_{min}, Q'_{min}) coating window points can be obtained by setting the substrate speed constant and gradually changing the pressure until defects are found as seen in Figure 5.5. For all the experiments and simulations performed in this study, the first method is implemented, wherein the pressure is set at a fixed value and the corresponding minimum and maximum substrate speeds are found.

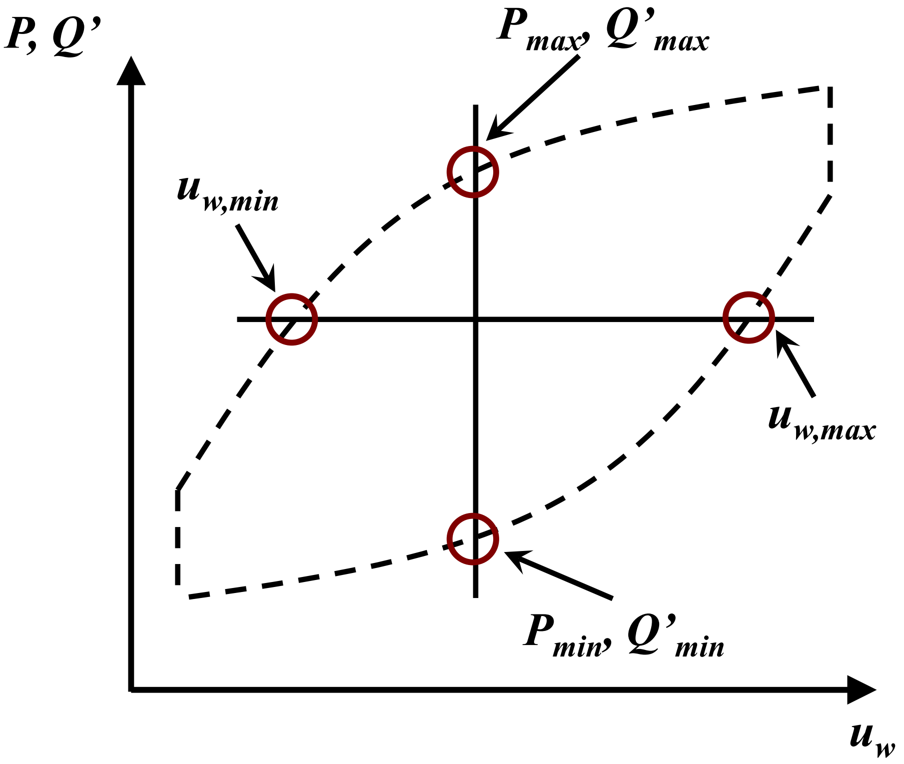

Figure 5.5: Illustration of upper and lower coating window points.

The images are carefully captured by the imaging systems and fed to the computer. At the end of a complete run, all the images are rendered using the Olympus Stream Application software and analyzed.

5.3 Uncertainty Analysis

During all the experiments, uncertainty arises in the measured values due to the slight fluctuations in the measured parameters. The uncertainties are not errors; rather they represent deviations in in the measured values due to the noise or random effects. Uncertainty not only applies to the independent parameters that are directly obtained from the read-out devices, but they are extended to other parameters, whose values are calculated from the independent parameters.

For a dependent parameter, R, that is a function of 'm' dependent or independent variables (R_1, R_2, R_3, …,R_m) as given by Equation 5.3:

$$R = f\,(R_1, R_2, R_3, \ldots, R_m) \tag{5.3}$$

If the uncertainties in R_1, R_2, R_3, …,R_m are δR_1, δR_2, δR_3, …, δR_m respectively, then the total uncertainty in R, given by δR, is expressed as given by equation 5.4:

$$\delta R = [(R_{1+\delta R1} - R_1)^2 + (R_{2+\delta R2} - R_2)^2 + (R_{3+\delta R3} - R_3)^2 + \ldots + (R_{m+\delta Rm} - R_m)^2]^{0.5} \tag{5.4}$$

Based on the uncertainty analysis, the parameter, R, lies within an uncertainty of δR at 95% confident level [122].

In the experiments used in the current study, the uncertainty in the coating speed is ± 0.20 mm/s, while the uncertainty in the pressure reading is ± 1720 Pa. For the experimental coating window plots presented in the current study, uncertainty limits on the flow rate per unit width, Q', and the coating speed, u_w, are presented using error bars. As the actual values recorded in the experiments are pressures applied by the nitrogen tank, P, and the coating speed, the uncertainty on the coating speed is obtained directly, while the uncertainty in Q' for a given solution is obtained by applying Equation 5.4 on the empirical relation between P and Q' for that solution as presented in Appendix C.

5.4 Summary

In this chapter, the experimental setup and procedure were discussed. The four individual subsystems; die, roll-feed/web control, heating/temperature control, and visualization/inspection systems that form the experimental setup were explained in detail. The experimental procedure and the methodology followed to obtain the coating window and the pressure versus flow rate (per unit width) plots were also explained. Finally, the uncertainty limits on the processing parameters were presented. In the next chapter, the details of the numerical model are presented.

6. COMPUTATIONAL STUDY

Several numerical studies exist to predict coating windows and air entrainment mechanism in thin films. In this chapter, a detailed review of several theoretical studies and their drawbacks is presented. Then, the numerical methodology used for the current study and its significance are discussed in detail.

6.1 Review of Existing Numerical Studies on Predicting Coating Windows

Some of the first theoretical studies predicting coating windows for pre-metered coating processes were by Ruschak [60] and Higgins and Scriven [59]. They assumed that the flow-field is steady and completely two-dimensional.

Saito & Scriven [123] used a steady, 2D finite element method to study slot coating of Newtonian solutions. Later, Carvalho & Kheshgi [62] performed 2D numerical simulations to predict coating windows for Newtonian solutions using both Galerkin/finite element methods and the long-wave expansion method developed by Kheshgi [124]. Romero et al. [63, 64, 103, 104] used a similar model to predict coating windows for Newtonian and mildly viscoelastic fluids, and high molecular weight polymer solutions. Based on the findings by Carvalho and Kheshgi [62] that the presence of parallel slot gap and the upstream region does not impact the operating conditions at low capillary and Reynolds numbers, the computational domain considered for some of these studies [63, 64, 104] was simplified by discarding the parallel-plate region of the slot die and the upstream die lip. So, neither the dynamic contact line nor the upstream meniscus was captured in these studies. Furthermore, these and other studies [125, 126] assumed that the downstream meniscus was pinned to the die lip. However, this restriction on the downstream meniscus movement is not realistic, because in reality the downstream meniscus is free to be within the die lip region or move beyond the die lip [65, 67, 70, 100]. Also, from the discussion in Section 2.5, the location of the downstream meniscus plays a major role in determining the three minimum wet thickness regions. A similar methodology was employed by Lee et al. [127], who used a pseudo-solid domain mapping technique coupled with the discrete elastic viscous stress (DEVSS) finite element formulation for solving 2D, steady, elastic, free surface problems in slot die coating.

Chu et al. [70] performed 2D simulations using Flow-3D software and predicted the maximum coating speed based on the contact angle made by the upstream meniscus with the substrate. A similar theoretical 2D model was employed by Chang et al. [101] using Flow 3D software to predict the time taken for the upstream and downstream menisci to reach their final steady state positions. In these studies, the meniscus shape was solved using force balance, but the actual air entrainment or ribbing effect was not captured.

Other models have been used to predict coating windows or air entrainment velocity, such as the one-dimensional lubrication model [71] and the coating model available in TopCoat software (Rheologic [128]) by Iuliano [114], however these models produced unsatisfactory results.

None of the aforementioned models solved the multiphase equations, which is a requirement to capture the air entrainment in the form of bubbles in the coated film. Instead, they based their predictions on the magnitude of the contact angles made by the upstream meniscus with the substrate (defects were assumed to occur when the angle made by upstream meniscus with the substrate ≈ 180°) [70] or the downstream meniscus with the downstream die lip (defects were assumed to occur when the angle made by downstream meniscus with the die lip ≈ 10°) [63, 64]. The majority of these models are steady state models, while the actual air entrainment mechanism is unsteady.

Hirt & Richardson [129] effectively used a 3D, transient, volume-of-fluid (VOF) model to predict air entrainment in slide coating. Harris & Bhamidipati [130] and Bhamidipati & Harris [131-133] showed that the 2D, transient, VOF model with Geo-Reconstruct scheme, available in FLUENT software can be successfully used to predict the air bubble entrainment in the coated film. The diameter of the bubbles however cannot be predicted with the 2D VOF model. Although another higher-order VOF method [133], CICSAM, successfully predicted the coating windows, it failed to predict the discrete bubble generation. Instead the air entrainment is depicted as a continuous sheet next to the substrate. Lin et al. [67] also used 2D VOF model available in Flow 3D to predict coating defects, but they could not capture the actual air bubbles.

Due to its effectiveness, the VOF model available in FLUENT 6.3.26 version is used in the current study to theoretically predict coating windows and defects. The details of the model will be discussed in the following subsections.

6.2 Popular Methods for Solving Free Surface Flows

Several numerical approaches exist to solve the free surface problems such as Lagrangian [134-136], Eulerian [137-140], Arbitrary Lagrange-Eulerian [141-146], and front tracking [147, 148] methods. The most common approaches are Lagrangian and Eulerian approaches. In the Lagrangian approach, every individual particle in the computational domain is tracked. The mesh moves with the fluid particle and hence is free to deform so as to align with the fluid particles. Therefore, when solving free surface problems, it offers the advantage of matching the boundary of the computational domain with the free surface. These methods have been employed to solve numerous problems such as droplet breakup [149], deformation of bubbles [150], multiple particle motion [151, 152], and wall-drop collision [153]. However, the mesh can be severely distorted when the interface suffers large deformation causing numerical instability [154]. Additionally, it can be very cumbersome to track and store information on all particles.

Eulerian approaches are based on using a relatively fixed mesh through which the fluid moves. These approaches therefore do not suffer from mesh deformation. In these methods, either the fluid volumes are tracked using volume tracking methods or interfaces are tracked. One such volume tracking method is the VOF method.

6.3 VOF Model

The VOF method was introduced by Hirt & Nichols [140] in 1979 for tracking interfaces between fluids. The method overcame the disadvantages of earlier methods such as height functions, line segments, and marker particles, which were either incapable of capturing large slopes at the interface or computationally very expensive [140].

The basic principle of VOF is to track a volume fraction scalar, α, in every fluid element, whose value can be zero, one, or any fraction between zero and one. As the name suggests, the volume fraction is the fraction of the total volume occupied by a given fluid. A volume fraction of one refers to a condition where the total volume is filled by the given fluid and a volume fraction of zero means that the volume is completely devoid of that fluid. At the interface between the two fluids, the volume fraction is a value between zero and one.

When the interface is captured between two fluids, as is the case in the current study (the two fluids are air and coating solution), a single governing equation is solved to compute the volume fraction of the coating solution (Equation 6.1):

$$\frac{\partial \alpha_{cs}}{\partial t} + \boldsymbol{u}.\nabla \alpha_{cs} = 0 \tag{6.1}$$

where t is time, α_{cs} is the volume fraction of the coating solution, and $\boldsymbol{u}$ is the velocity vector. As the sum total of volume fractions for the two phases should add up to 1 in a two-phase flow, the volume fraction of air in the computational domain is given by Equation 6.2:

$$\alpha_{air} = 1 - \alpha_{cs} \tag{6.2}$$

Once the volume fractions are calculated, the interface needs to be reconstructed. The reconstructed interface then provides the required boundary conditions. The geometric reconstruction (Geo-Reconstruct) method developed by Youngs [155], which is a piecewise-linear interface construction (PLIC) scheme is used in this study to construct the interface as it is the most accurate model available in FLUENT 6.3.26 [156].

The Geo-Reconstruction scheme requires explicit formulation of the VOF model. By applying explicit discretization in time and rewriting the advection term in terms of fluxes through the faces, Equation 6.1 can be rewritten as Equation 6.3:

$$\frac{\alpha_{cs}^{n+1} - \alpha_{cs}^{n}}{\Delta t}\mathcal{V} + \sum_{f}\left(\mathcal{U}_{f}^{n}\alpha_{cs,f}^{n}\right) = 0 \tag{6.3}$$

where $n + 1$= index for current time step, n = index for previous time step, $\alpha_{cs,f}$ = face value of the coating solution’s volume fraction, $\mathcal{V}$ = volume of computational cell, and $\mathcal{U}_{f}$= volume flux through the face, based on normal velocity. The Courant number is set at 0.1 for solving the VOF equation, because the smaller the Courant number, the smaller the time step and the more accurate is the solution. The second term on the left-hand side of Equation 6.3 is computed using the third order, Van Leer method [155] after constructing the interface. A third order method is used to minimize artificial diffusion and dispersion, while the Van Leer treatment [157] eliminates any non-physical behavior. The interface is constructed using the following steps:

1. The slope of the interface between the two fluids, A and B, in any given cell is computed using the volume fractions from the surrounding 8 cells (Figure 8.1) and the volume fraction (volume fraction pertaining to fluid A) of the cell itself.

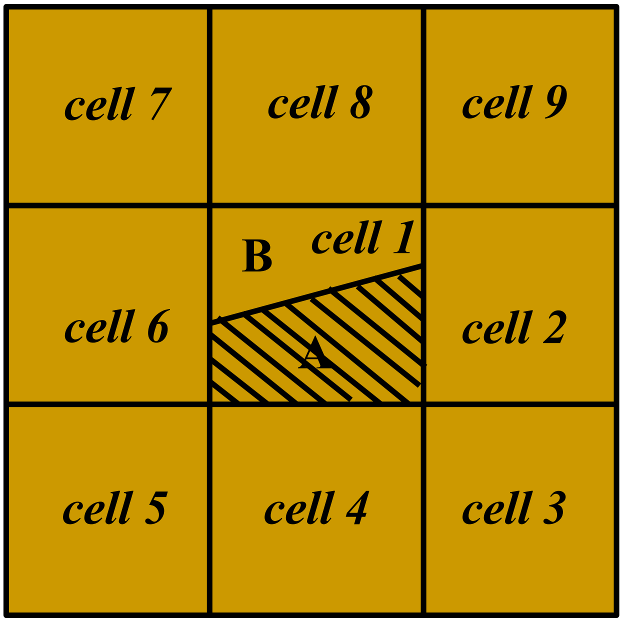

Figure 6.1: Cells considered in interface calculation.

2. The volume fractions at the four faces of *cell 1* are then computed (blown up view of *cell 1* is shown in Figure 6.2 (a)) using a linear interpolation between *cell 1* and each of the other four cells (*cells 2, 4, 6 and 8*), which share a face with *cell 1*.The interpolation between *cell 1* and *cell 6* is illustrated in Figure 6.2 (b). Similar procedure is followed with the remaining three adjacent cells.

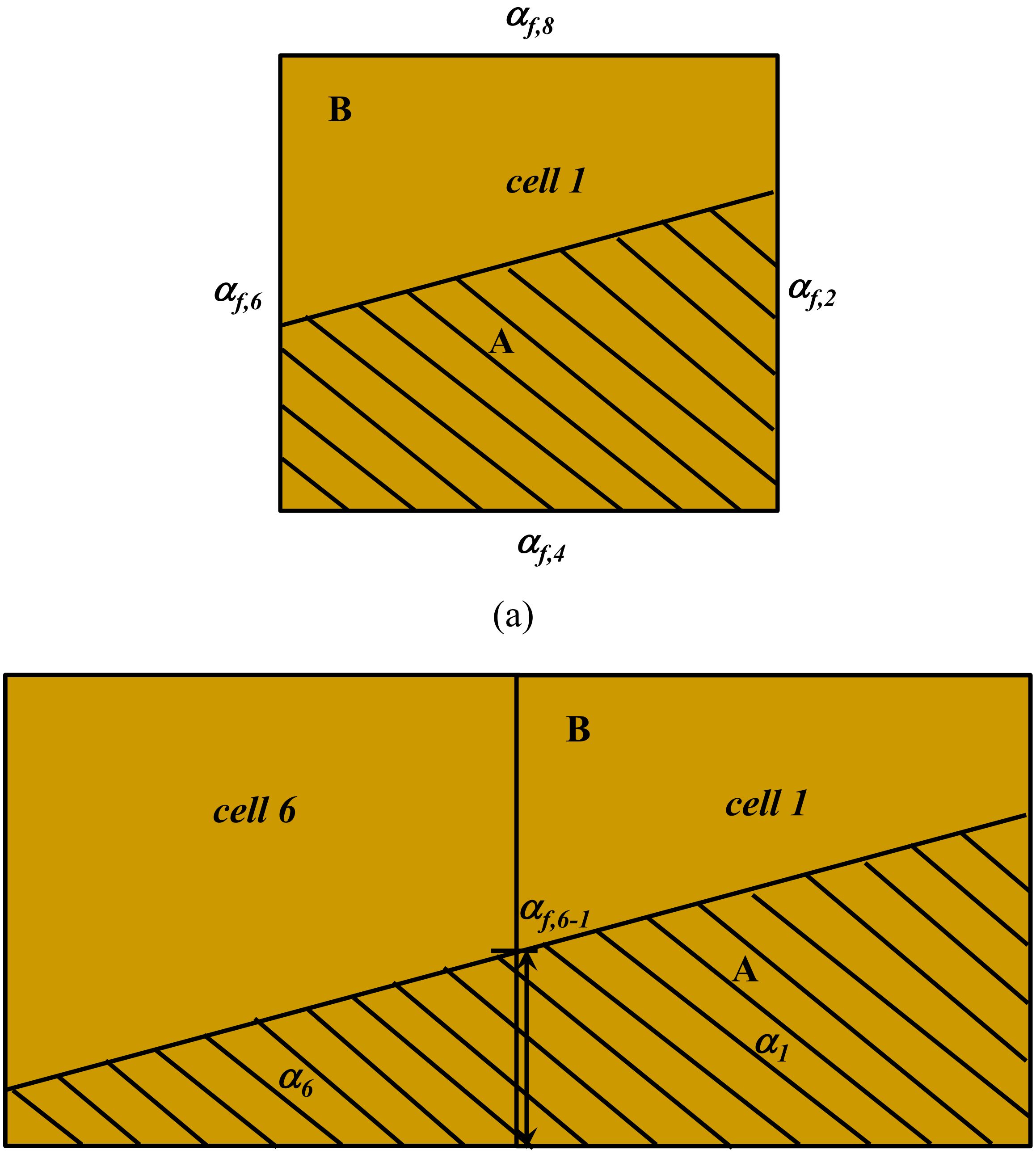

(a)

(b)

Figure 6.2: (a) Volume fractions at the four bounding faces of the cell, (b) Volume fraction at the face obtained from interpolation of cell volume fractions of adjacent cells.

3. Once the volume fractions are obtained on the bounding faces, the slope of the interface in *cell 1* is calculated using the four face volume fractions, $\alpha_{f,2}$, $\alpha_{f,4}$, $\alpha_{f,6}$ and $\alpha_{f,8}$ as illustrated in Figure 6.3.

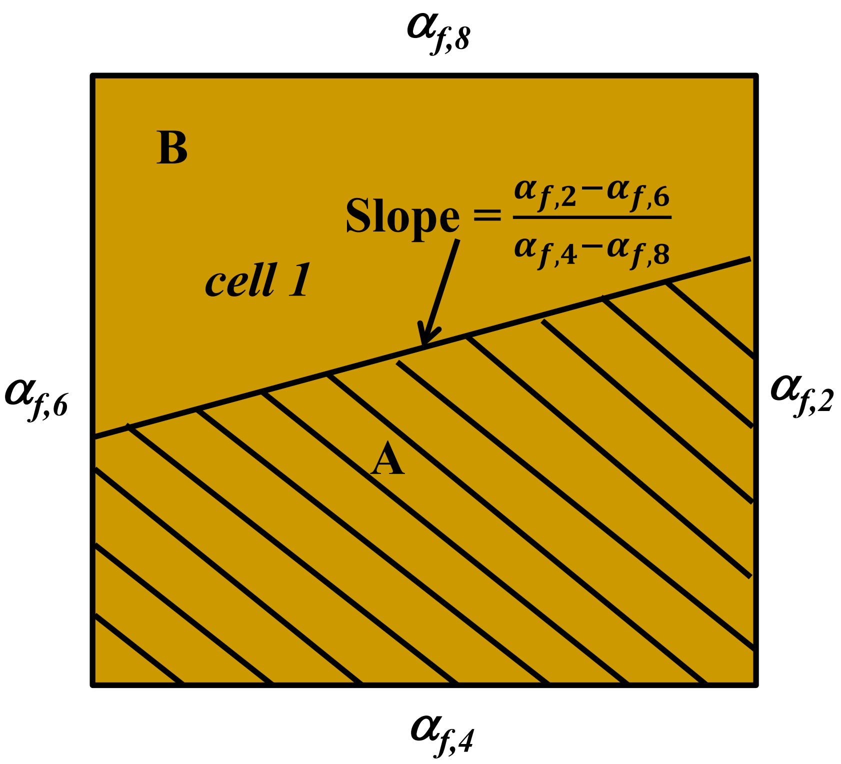

Figure 6.3: Calculation of the slope of the interface.

4. The interface is adjusted such that the ratio of volume occupied by fluid A, $\mathcal{V}_A$, to the total volume is equal to the volume fraction for fluid A of *cell 1*, α_1 (Figure 6.4).

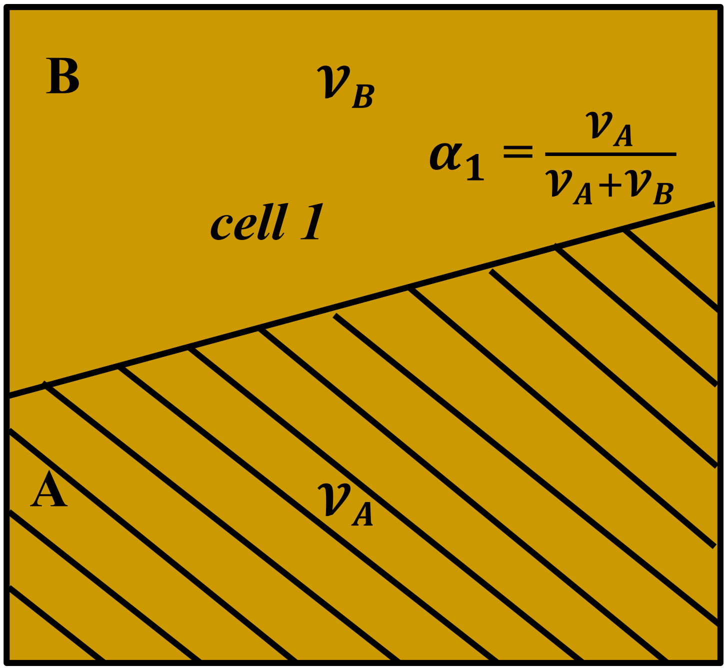

Figure 6.4: Interface adjustment to match with the volume fraction.

In order to obtain the velocity field required in the advective flux calculation of the volume fraction, the continuity equation described by Equation 6.4 and a single momentum equation in the x, y and z directions as given by Equation 6.5 are solved.

$$\frac{\partial \rho}{\partial t} + \nabla.(\rho \boldsymbol{u}) = 0 \tag{6.4}$$

$$\frac{\partial (\rho \boldsymbol{u})}{\partial t} + \nabla.(\rho \boldsymbol{u}\boldsymbol{u}) = -\nabla P + \nabla.\boldsymbol{\mathfrak{T}} + \rho \boldsymbol{g} + \boldsymbol{F}_s \tag{6.5}$$

where $\boldsymbol{u}$ is the velocity vector, $\boldsymbol{\mathfrak{T}}$ is the stress tensor, P is the pressure, $\boldsymbol{g}$ is acceleration due to gravity and $\boldsymbol{F}_s$ is a momentum source term. Within the FLUENT 6.3.26 software, PRESTO is chosen as the interpolation scheme for the pressure term. Body-forceweighted (BFW) scheme is the other pressure interpolation scheme available under the VOF model in FLUENT. However, the BFW scheme led to divergence of the solution and hence was not chosen. For pressure-velocity coupling, the Pressure-Implicit with Splitting of Operators (PISO) scheme with neighbor correction is used. This scheme belongs to the Semi-Implicit Method for the Pressure-Linked Equations (SIMPLE) algorithm family, however, PISO has the advantage of significantly reducing the total number of iterations required for convergence compared to SIMPLE and SIMPLE-Consistent (SIMPLEC) [156], when neighbor correction is used. The second order upwind discretization scheme is used for the momentum equation.

Properties such as viscosity and density indicated by φ, which are used in the continuity and momentum equations are averaged using Equation 6.6:

$$\varphi = \alpha_{cs}\,\varphi_{cs} + (1 - \alpha_{cs})\varphi_{air} \tag{6.6}$$

The velocity at the interface, $\boldsymbol{u}$ is computed using Equation 6.7:

$$\boldsymbol{u} = \frac{\alpha_{air}\,\rho_{air}\,\boldsymbol{u}_{air} + \alpha_{cs}\rho_{cs}\boldsymbol{u}_{cs}}{\alpha_{air}\,\rho_{air} + \alpha_{cs}\rho_{cs}} \tag{6.7}$$

6.3.1 Surface Tension

Fluids are subjected to inward forces at the interface resulting from an imbalance in the intermolecular forces. A given fluid molecule in the interior of the fluid is subjected to forces exerted by other molecules of the same fluid (cohesive forces). As the interior molecule is subjected to the same amount of force from all the directions, the net force experienced by the molecule is zero. However, the molecules on the surface of the fluid are in contact with other molecules of the same fluid on one side of the interface and molecules of a second fluid on the other side. This results in a net inward force, which is termed as surface tension. Surface tension force minimizes the surface energy by reducing the area of the interface. The effects of surface tension force become significant when the capillary number, Ca, is not much greater than one for creeping flows, or when the Weber number is not significantly greater than 1 for high Reynolds number (Re) flows. The flow-field in the current study falls under the creeping flow regime as the Reynolds number varies between 10^{-5} to 10^{-2}. So, the significance of surface tension effects in the current study depends on the range of capillary numbers obtained in the study. The capillary number for a power-law fluid is defined by Equation 6.8:

$$Ca = \frac{k\left(\frac{u_w}{H}\right)^{n-1} u_w}{\sigma} \tag{6.8}$$

For the fluids used in the current study, the capillary number ranges between 0.15 and 1.2. Therefore, surface tension effects are included in the momentum equation using the continuum surface force model (CSF) introduced by Brackbill [158].

The CSF model does not account for the surface tension force as a boundary condition; instead it is treated as a three-dimensional effect across the interface. Therefore, the surface tension force is modeled as a body force and is accounted for in the momentum equation using the source term, $\boldsymbol{F_s}$, from Equation 6.5. The source term, $\boldsymbol{F_s}$, is defined by Equation 6.9:

$$\boldsymbol{F_s} = \sum_{\text{pairs } ij, i<j} \sigma_{ij} \frac{\alpha_i \rho_i \kappa_j \nabla \alpha_j + \alpha_j \rho_j \kappa_i \nabla \alpha_i}{0.5(\rho_i + \rho_j)} \tag{6.9}$$

where i and j are the indices used to define the phases and κ is the curvature of the surface at the interface. Due to the fact that the surface tension is modeled as a body force, the discontinuous interface is approximated as a continuous function, which causes the surface tension to act everywhere along the smeared interface. In a two-phase flow field, $\kappa_i = -\kappa_j$ and $\nabla \alpha_i = -\nabla \alpha_j$ and Equation 6.9 transforms to Equation 6.10:

$$F_s = \sigma_{12} \frac{\alpha_1 \rho_1 \kappa_2 \nabla \alpha_2 + \alpha_2 \rho_2 \kappa_2 \nabla \alpha_2}{0.5(\rho_1 + \rho_2)} = \sigma_{12} \frac{\kappa_2 \nabla \alpha_2 (\alpha_1 \rho_1 + \alpha_2 \rho_2)}{0.5(\rho_1 + \rho_2)} \tag{6.10}$$

where the subscripts 1 and 2 in the current study correspond to air and coating solution respectively.

The curvature κ is represented as divergence of the unit normal at the interface, $\boldsymbol{\hat{n}_{if}}$ as given by Equation 6.11:

$$\kappa = \nabla . \boldsymbol{\hat{n}_{if}} \tag{6.11}$$

where the unit normal to the interface is given by Equation 6.12:

$$\nabla . \hat{n}_{if} = \frac{\nabla \alpha_{cs}}{|\nabla \alpha_{cs}|} \tag{6.12}$$

6.3.2 Viscosity of the Coating Solution

The apparent viscosity of the coating solution presented in Chapter 4 is specified using the power-law model available in FLUENT 6.3.26. The apparent viscosity, η, is a function of shear rate, $\dot{\gamma}$, consistency index, k and power-law index, n, as given by Equation 6.13:

$$\eta = k\dot{\gamma}^{\,n-1} \tag{6.13}$$

where $\dot{\gamma}$ is related to the second invariant of the rate-of-deformation tensor, $\boldsymbol{D}$, as defined by Equation 6.14:

$$\dot{\gamma} = \sqrt{\frac{1}{2}\boldsymbol{D}:\boldsymbol{D}} \tag{6.14}$$

where the rate-of-deformation tensor, $\boldsymbol{D}$ is given by Equation 6.15:

$$\boldsymbol{D} = \left(\frac{\partial u_i}{\partial x_j} + \frac{\partial u_j}{\partial x_i}\right) \tag{6.15}$$

6.4 Computational Domain

The computational domain is bounded by the downstream section of the slot die, the substrate surface, and the region between the slot die and the substrate. However, the slot die and substrate materials are not modeled because isothermal conditions exist. Only the fluid domain is considered in the study. The domain is extended on either side to ensure fully-developed conditions exist at the end of the domain. The sectional view of the computational domain along with the dimensions is shown in Figure 6.5. The entire geometric specifications for the die are based on the dimensions of the die used in the experiments. As the effects of slot gap, *W*, and coating gap, *H*, are analyzed in the current study, a value is not specified for *W* and *H* in Figure 6.5.

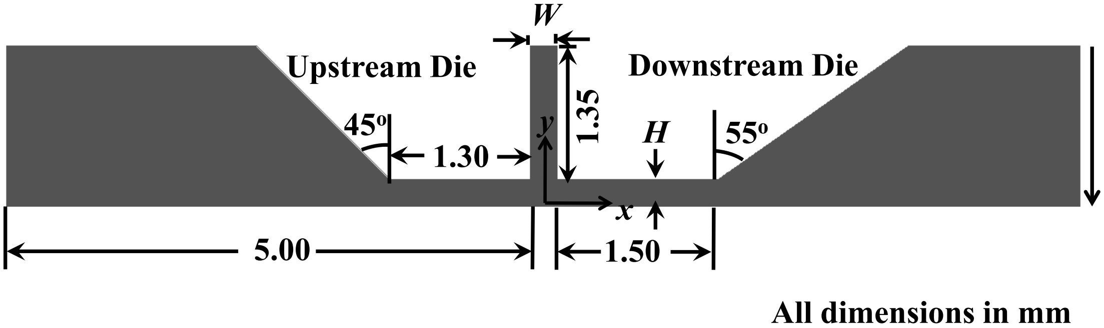

Figure 6.5: Dimensions of the computational domain.

Both two-dimensional and three-dimensional studies are performed. It is important to note that the actual slot die width used in the experiments is 50 mm, which is more than two orders greater than the slot gap and coating gap. The width of the computational domain in the three-dimensional study perpendicular to the page is chosen as 5 mm. To model the entire width would require excessive computational memory and time. The width of the domain is chosen based on the size of the defects observed during the experiments. Periodic boundary conditions are specified at the extreme boundaries.

6.5 Boundary Conditions

The locations where the boundary conditions are specified on the computational domain are represented in Figure 6.6.

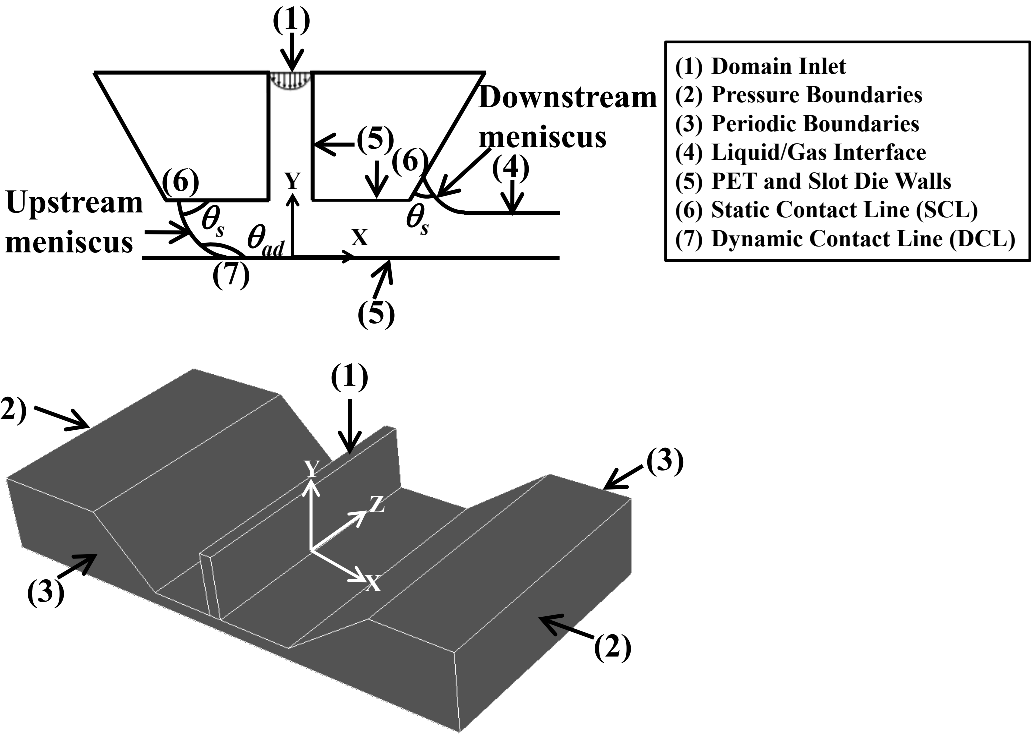

Figure 6.6: Locations of the specified boundary conditions on the computational domain.

Domain inlet (1): The total length of the slot die parallel plate region is about two orders higher than the slot gap. As the slot width is also about two orders of magnitude wider than the slot gap, fully developed conditions are expected to exist at the downstream region of slot die where the inlet condition is specified. The fully developed velocity profile pertaining to a fluid between parallel plate region is derived using a differential fluid element flowing between infinitely long plates as shown in Figure 6.7 (a). The forces acting on the fluid element is depicted in Figure 6.7 (b):

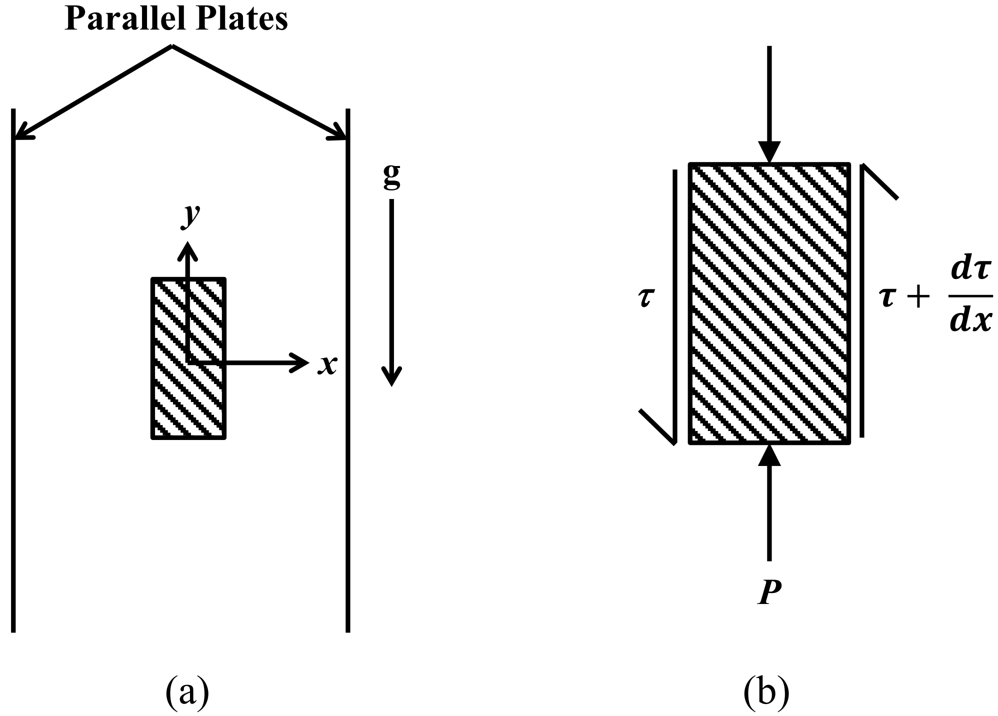

Figure 6.7: (a) Fluid element within the parallel plate region represented by shaded region, (b) Blown-up view of the fluid element with the forces acting on it.

When fully developed conditions exist, the pressure gradient across the fluid element in the flow direction is balanced by the shear stress gradient experienced by the element as given by Equation 6.16. The pressure term, *P*, in equation 6.16 accounts for both applied pressure and hydrostatic pressure.

$$-\frac{dP}{dy}=\frac{d\tau}{dx} \tag{6.16}$$

The shear stress for a power-law fluid at fully-developed conditions is given by Equation 6.17:

$$\tau = k\left(-\frac{dv}{dx}\right)^n \tag{6.17}$$

For simplicity, the negative of pressure gradient is represented by P' as shown in Equation 6.18:

$$P' = -\frac{dP}{dy} \tag{6.18}$$

Then, Equation 6.16 can be rewritten as Equation 6.19:

$$\frac{d\tau}{dx} = P' \tag{6.19}$$

Combining Equations 6.17 and 6.19, integrating once with respect to x and rearranging terms, Equations 6.20 through 6.22 are obtained, respectively:

$$\frac{d}{dx}\left[k\left(-\frac{dv}{dx}\right)^n\right] = P' \tag{6.20}$$

$$k\left(-\frac{dv}{dx}\right)^n = P'x + C_1 \tag{6.21}$$

$$\frac{dv}{dx} = -\left\{\frac{P'x + C_1}{k}\right\}^{1/n} \tag{6.22}$$

At the symmetry boundary ($x = 0$), gradient of 'v' with respect to 'x' would be zero, yielding the first integration constant, C_1, to be zero and Equation 6.22 is reduced to Equation 6.23:

$$\frac{dv}{dx} = -\left\{\frac{P' x}{k}\right\}^{1/n} \tag{6.23}$$

Integrating 'v' with respect to 'x' again and applying the boundary condition that at $x = W/2$, $v = 0$, Equations 6.24 and 6.25 are obtained respectively:

$$v(x) = -\frac{n}{n+1}\left\{\frac{P'}{k}\right\}^{1/n} x^{(n+1)/n} + C_2 \tag{6.24}$$

$$v(x) = \frac{n}{n+1}\left\{\frac{P'}{k}\right\}^{1/n} \left(\frac{W}{2}\right)^{(n+1)/n} \left\{1 - \left(\frac{2x}{W}\right)^{(n+1)/n}\right\} \tag{6.25}$$

The differential flow rate, dQ, as a function of 'x' is given by Equation 6.26:

$$dQ = 2v(x)dxW_{sd} \tag{6.26}$$

Combining Equations 6.25 and 6.26, Equation 6.27 is obtained:

$$dQ = \frac{2n}{n+1}\left\{\frac{P'}{k}\right\}^{1/n} \left(\frac{W}{2}\right)^{(n+1)/n} \left\{1 - \left(\frac{2x}{W}\right)^{(n+1)/n}\right\} dxW_{sd} \tag{6.27}$$

Integrating between limits 0 to *W*/2 gives:

$$Q = \mathcal{W}_{sd} \frac{n}{2n+1} W \left\{\frac{P'}{k}\right\}^{1/n} \left(\frac{W}{2}\right)^{(n+1)/n} \tag{6.28}$$

Combining Equations (6.25) and (6.28), *v* is obtained in terms of flow rate, *Q* as:

$$v(x) = \frac{2n+1}{n+1}\left\{1 - \left(\frac{2x}{W}\right)^{(n+1)/n}\right\}\frac{Q}{W\mathcal{W}_{sd}} \tag{6.29}$$

Pressure boundaries (2): The extreme boundaries of the upstream and downstream regions and top surfaces are specified as pressure boundaries with gauge pressure set equal to zero.

$$P_g = 0 \tag{6.30}$$

Periodic boundaries (3): The extreme x-y planes in the computational domain defined by $z = 2.5$ mm and $z = -2.5$ mm are modeled as periodic boundaries.

Liquid/Gas Interface (4): At the liquid/gas interface, the normal stress in the coating solution, $\mathcal{T}_{cs}$, is balanced by the sum total of capillary pressure and hydrostatic pressure on the air side, P_{air}. Therefore, in the direction normal to the interface, Equation 6.31 has to be satisfied:

$$\boldsymbol{\mathcal{T}}_{\boldsymbol{cs}} = \frac{1}{Ca}\hat{\boldsymbol{n}}\nabla.\hat{\boldsymbol{n}} - \hat{\boldsymbol{n}}P_{air} \tag{6.31}$$

In addition, there cannot be any mass transfer across the interface as given by Equation 6.32:

$$\hat{\boldsymbol{n}}.\boldsymbol{u} = 0 \tag{6.32}$$

PET and Slot die walls (5): On all the PET and slot die walls, the no-slip condition is specified everywhere except at the static and dynamic contact lines indicated by locations (6) and (7) respectively in Figure 6.6.

$$\boldsymbol{u} = \boldsymbol{u_w} \tag{6.33}$$

For the validation study, the numerical model is compared with experiments. Hence, similar to the experiments, all the simulations in the current study are limited to a maximum coating (substrate) speed of 15 mm/s. This implies that even if the maximum coating speed, as dictated by the air entrainment boundary, exceeds 15 mm/s, those simulations are not performed. Therefore, a clear boundary will exist on the extreme right of the coating window for simulations and experiments performed on solutions that have the maximum coating speed within 15 mm/s. However, for the cases that exceed 15 mm/s, the coating window will remain open on the extreme right.

Contact Lines (6 and 7): The solution adheres to the slot die wall upstream of the static contact line (6) where the viscous nature of the solution causes shear stress. On the other hand, the gas exerts negligible shear stress on the solution along the gas-liquid interface, subjecting the coating solution to acceleration around that region. Researchers [159-161] have shown that this results in a stress singularity at the static contact line, when the no-slip boundary condition is specified. The stress is proportional to $1/r$, where r is the distance from the static contact line to any point in the fluid. Therefore, as presented in [162], for Newtonian solutions, as the contact line is approached ($r \to 0$), the shear stress approaches infinity resulting in a mathematical singularity. Regardless of the nature of the solution used, the shear stress is integrable at a static contact line. Hence, Kistler [163] suggested that a no-slip condition is valid at the static contact line.

The wetting dynamics are further complicated at the dynamic contact line (7). The moving substrate transmits the shear stress to the impinging solution, which causes it to accelerate in the boundary layer. In the case of a dynamic contact line, the stress singularity is non-integrable, which causes an infinite force at the moving substrate. This is a physically impossible condition. In order to overcome this limitation, Dussan and Davis [164], Dussan [165, 166], Kafka and Dussan [167], Silliman [168], Lowndes [169], de Gennes [170], Cox [171], Thompon and Robbins [172], Brochard and de Gennes [173], Renardy et al. [174] and others have applied slip condition at the dynamic contact line. However, when a shear-thinning fluid is used, Rosenblat and Davis, and Weidner and Schwartz [175] showed that the stress singularity can be integrated resulting in a finite force on the wall. As shear-thinning solutions are used in the current study, the issue with the infinite force does not arise. But another issue needs to be resolved at the dynamic contact line. As forced wetting causes the dynamic contact line to move with respect to the substrate, the velocity at the dynamic contact line differs from the substrate velocity. Then a valid question to be answered is whether the fluid particles attain the substrate velocity or the contact line velocity. Huh and Scriven [160] suggested that a discontinuity in the velocity should be introduced at the moving wall by introducing slip, such that the fluid reaches the velocity of the dynamic contact line, u_c and not of the substrate, u_w.

Based on the aforementioned discussion, the boundary conditions at the walls including the contact lines can be combined into one equation as represented by Equation 6.33 for the slot die walls and Equation 6.34 for the PET wall. The boundary condition for the PET wall is based on the slip formulation by Kistler [163].

$$u = f(x)u_c + [1 - f(x)]u_w \quad \text{for PET walls} \tag{6.34}$$

In Equation 6.34, $f(x)$ is a function of x, where, 'x' is the distance from the contact line. $f(x)$ is defined such that, for any slip length, Δx:

$$f(0) = 1 \tag{6.35}$$

$$f(x) = 0 \quad \text{for } x \geq \Delta x \tag{6.36}$$

The contact line velocity, u_c is specified in FLUENT by identifying the contact line region on the PET wall through a User-Defined-Function (UDF) and setting the velocity of the contact line equal to the velocity in the first cell centroid above the contact line.

The other boundary conditions relevant at the contact lines are the contact angles. The measured static contact angles presented in Chapter 4 are specified at the static contact lines as specified by Equation 6.37:

$$\theta = \theta_s \tag{6.37}$$

At the dynamic contact line, the most appropriate condition to be specified is the dynamic contact angle [176]. There is a disagreement on the value of the dynamic contact angle. While the dynamic contact angle is widely believed to be a function of the capillary number, Lowndes [169], Hocking [177, 178], and Hocking and Rivers [179] postulate that the contact angle is expected to be a constant and is equal to its static value throughout the motion. This idea is also supported by Huh and Mason [180] and Silliman and Scriven [181] for low capillary number flows. On the other hand, Benny and Timson [182] hypothesized that in any forced wetting process, the actual contact angle at the microscopic length next to the substrate is always 180° and therefore the stress singularity is not an issue.

In order to understand the differences in the coating window predictions when static and dynamic contact angles are specified at the dynamic contact line, computations are performed using BSM. Due to the limitation of the instrumentation available at the Georgia Tech facility, dynamic contact angle measurements could not be made. Instead, the dynamic contact angle is defined using the popular molecular kinetic theory (MKT) introduced by Blake and Haynes [183]. According to MKT, the dynamic contact angle, θ_d, is a function of static contact angle, θ_s, and velocity of the fluid relative to the substrate, u_r, as given by Equation 6.38:

$$\theta_d = \cos\theta_s - \frac{\sigma_0}{\sigma}\sinh^{-1}\frac{u_r}{u_0} \tag{6.38}$$

In the equation, σ_0 has units of surface tension and is proportional to thermal energy. The parameter, u_0, has units of velocity and is determined from molecular interactions. These values could not be evaluated for either test solutions or actual solutions. As silicon oil has the same order of viscosity (10 Pa-s) as the BSM, the properties for silicon oil are taken from Popescu et al. [184] and used. For silicon oil, σ_0 = 0.01 N/m and u_0 = 1.35 × 10^{-5} m/s.

The contact angle boundary condition at the substrate is specified using Equation 6.37 for static contact angle case and using Equation 6.38 for dynamic contact angle case. Equation 6.38 is input to the simulation using the UDF option available in FLUENT.

The coating window comparison for BSM at W = 0.30 mm, H = 0.30 mm is shown in Figure 6.8 to compare the static and dynamic contact angle cases (SCA and DCA). Notice that in the plot, the y-axis is volumetric flow rate per unit width, *Q'*, instead of volumetric flow rate, *Q*. This is done to eliminate the dependence of the coating window on the slot width. As shown in Figure 6.8, there is good agreement between the simulations for SCA and DCA. The maximum differences in the corresponding dripping and air entrainment values were found to be within ±3%. The simulations performed using dynamic contact angle was less stable and computationally more expensive than the static contact angle cases. The data for all coating windows presented in this chapter are presented in Appendix D.

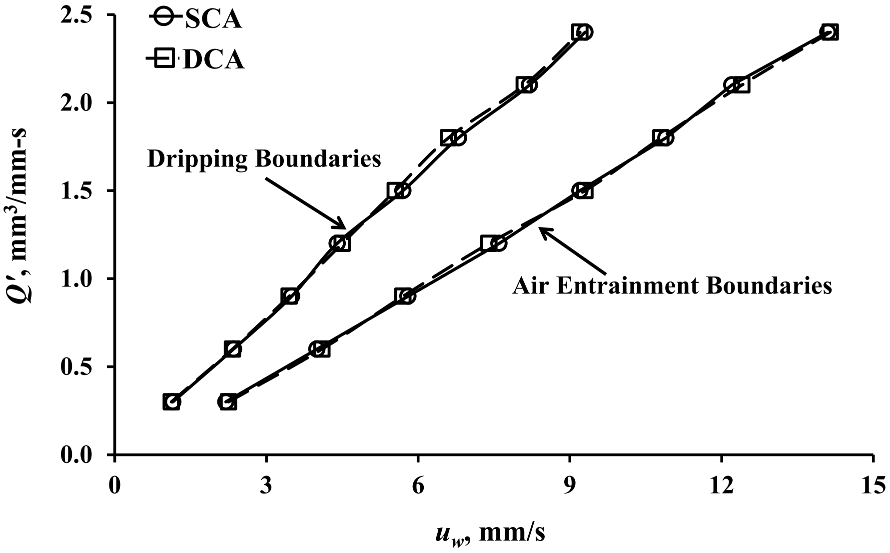

Figure 6.8: Plot showing effect of contact angle type on coating window of BSM for *W* = 0.30 mm, *H* = 0.30 mm.

The contours of the coating solution volume fraction on the PET walls are compared for *Q'* = 1.2 mm^3/mm-s at the point of air entrainment. The air entrainment velocity or maximum coating speed was found to be 7.6 mm/s for the static contact angle case and 7.4 mm/s for the dynamic contact angle case. Figures

6.9 (a) and 6.9 (b) show the top and side (sectional) views, respectively, of the static contact angle case, while Figures 6.9 (c) and 6.9 (d) depict the top and side views, respectively, of the dynamic contact angle case. The die lip boundaries are superimposed on the figures using dashed-black-lines to provide a perspective of contact line location and the sizes of sawteeth and air bubbles. The line X'Y'-X'Y' marked on the top view denotes the location of the side (sectional) view. All the features of the coating process and geometrical boundaries are marked on the figures.

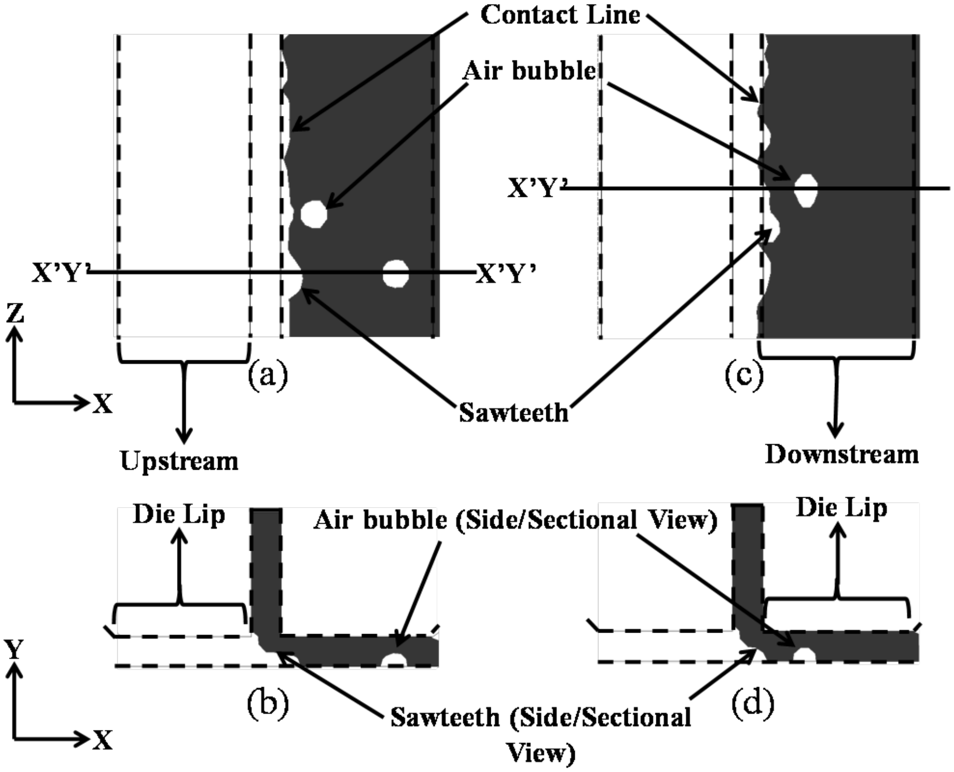

Figure 6.9: (a) Plot showing effect of contact angle type on air entrainment conditions of BSM for $W = 0.30$ mm, $H = 0.30$ mm and $Q' = 1.20$ mm^3/mm-s, dashed lines represent boundaries of die lips (a) Top view for static contact angle case, (b) Side (sectional) view for static contact angle case at location X'Y'-X'Y', (c) Top view for dynamic contact angle case, (d) Side (sectional) view for dynamic contact angle case at location X'Y'-X'Y'.

The air entrainment boundary is chosen as the point of comparison due to the complexity and three-dimensional nature involved. The air entrainment mechanism, as will be shown in the next chapter, is an unsteady process. Hence the contact line shape, the location and size of the sawteeth, and the pinch-off locations of the air bubbles are random. However, there is a distinguishable sawteeth and bubble pattern that falls within a certain range for a given set of geometric and processing parameters. The coating window and the volume fraction comparison indicate that the static contact angle boundary condition would suffice, thereby saving computational time and memory.

6.6 Grid Study

The sensitivity of the mesh size on the coating window is studied using three different meshes for $W = 0.25$ mm, $H = 0.25$ mm and BSM as the coating solution. The coarsest mesh has an interval size of 0.08 mm (86 × 19 × 40), the medium mesh has an interval size of 0.0625 mm (111 × 24 × 50) and the finest mesh has an interval size of 0.05 mm (133 × 30 × 63). The interval sizes for the three meshes (top and sectional views) are presented in Table 6.1.

Table 6.1: Mesh interval sizes.

Mesh Type	**Interval Size (mm), Sectional View (Number of elements in X, Y and Z planes)**	**Interval Size (mm), Top View**
Coarse	0.080 (86 × 19 × 40)	0.13
Medium	0.0625 (111 × 24 × 50)	0.10
Fine	0.050 (133 × 30 × 63)	0.08

For the sake of illustration of a typical mesh distribution, the medium mesh configuration is shown in Figure 6.10. In the sectional plane, the aforementioned interval sizes are used in the slot gap region, the regions between the slot die exit and the substrate, between the upstream die lip and the substrate, between the downstream die lip and the substrate, and for the entire downstream region except the top most volumes. Due to the negligible contribution of the top-most downstream region, a relatively coarser mesh is used. At the upstream end beyond the die lip, a very coarse mesh is used.

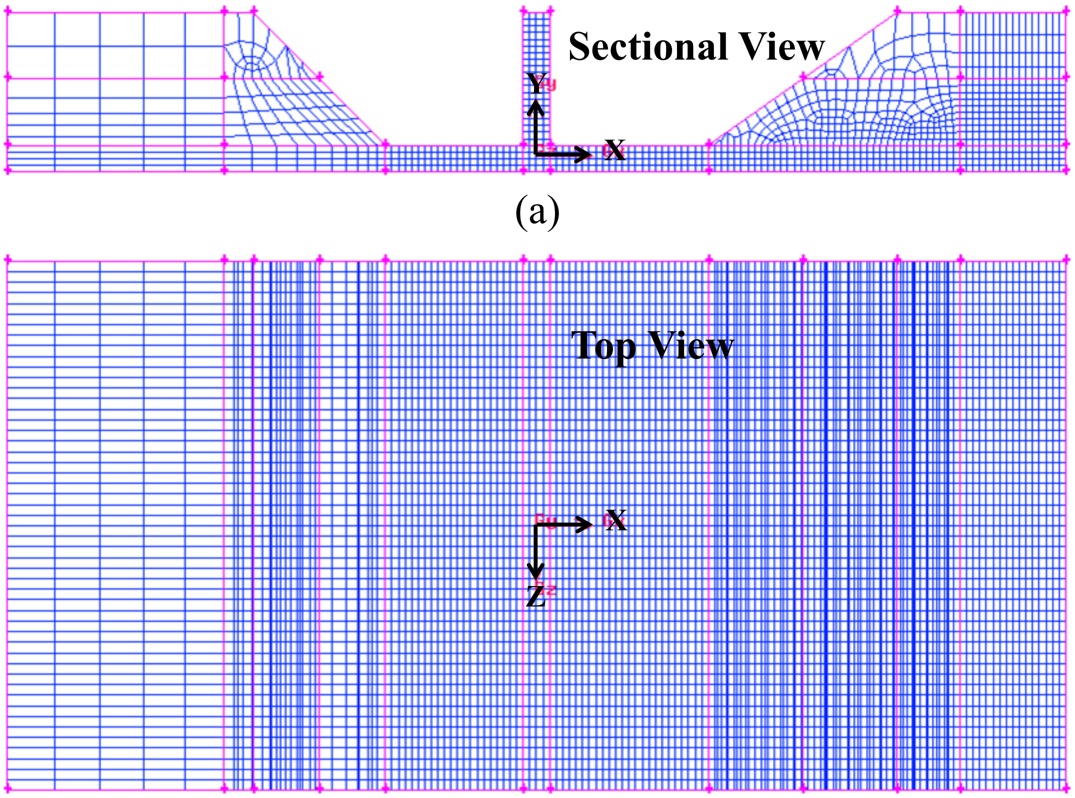

(a)

(b)

Figure 6.10: Medium Mesh (a), Sectional view (b) Top view.

The coating window comparison between the three meshes is shown in Figure 6.11. The difference between coarse and medium mesh predictions is about 7%, while the difference decreased to 4%, when the predictions are compared between the medium and fine meshes. As the mesh size is further reduced, the predictions did not change significantly until an interval size of 0.04 was reached. However, further refinement of the mesh caused the simulation to become unstable. This is a limitation of the VOF model when surface tension forces are dominant [185, 186]. The geo-reconstruct method when used in conjunction with the CSF model causes problems in accurate computation of the curvature. In addition, since the curvature term is obtained from the second-order derivative of volume fraction in space, the curvature term increases significantly as the interval size of the mesh gets smaller resulting in an unstable solution. VOF model also induces spurious velocity currents in the air phase when capillary forces are dominant [187-189]. These spurious currents are further magnified as the mesh becomes smaller resulting in inaccurate results. Nevertheless, within the interval size of 0.04 mm, the current model predicts the experiments within reasonable accuracy as will be shown in Section 6.8.

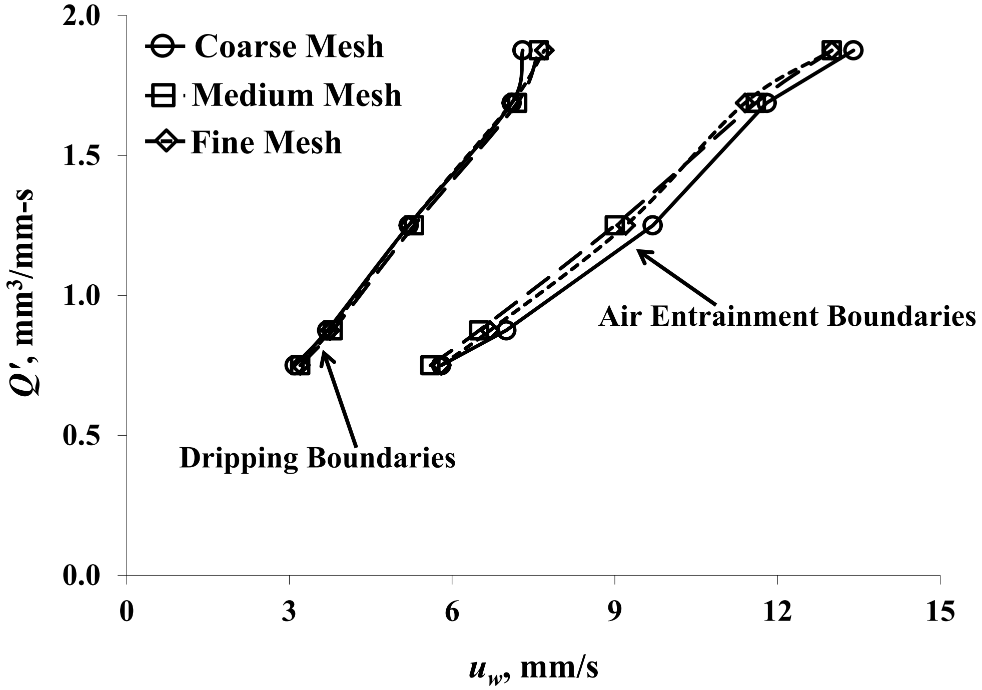

Figure 6.11: Plot showing effect of grid size on coating window of BSM for $W = 0.25$ mm, $H = 0.25$ mm.

The contours of BSM's volume fraction on the PET walls for the three meshes are shown in Figure 6.12. As can be seen from the contours, as the interval size of the mesh is reduced, the sizes of the sawteeth and bubbles reduce, while the number of bubbles per unit width increases. However, the differences are within ±1%.

Due to the higher computational requirement of the fine mesh, medium mesh is used for all the simulations, henceforth. The minimum mesh interval size is however restricted to 0.04 mm.

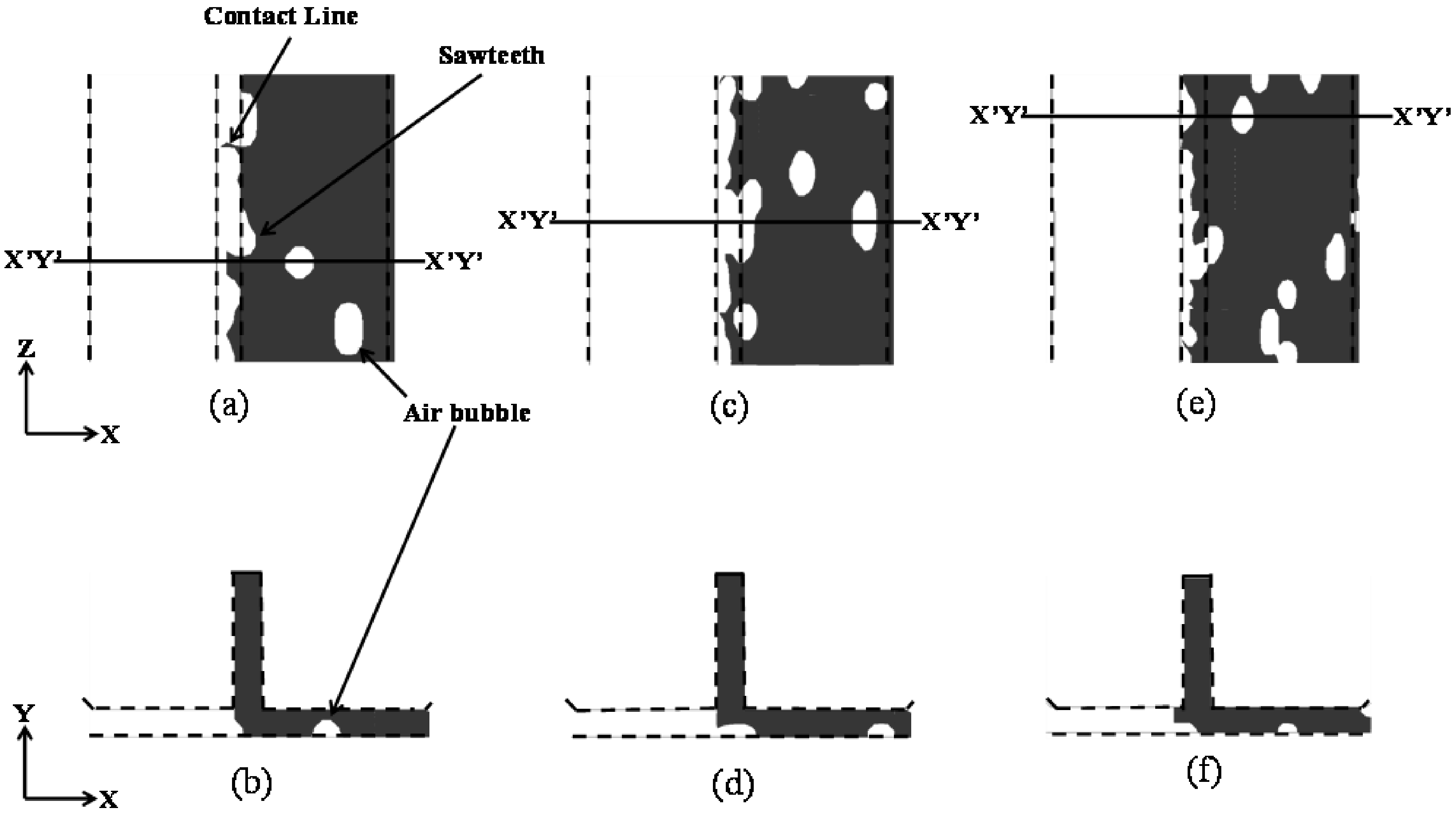

Figure 6.12: Plot showing effect of grid size on air entrainment conditions of BSM for *W* = 0.25 mm, *H* = 0.25 mm and *Q'* = 1.25 mm^3/mm-s, dashed lines represent boundaries of die lips (a) Top view for coarse grid, (b) Side (sectional) view for coarse grid at location X'Y'-X'Y', (c) Top view for medium grid, (d) Side (sectional) view for medium grid at location X'Y'-X'Y', (e) Top view for fine grid, (f) Side (sectional) view for fine grid at location X'Y'-X'Y'.

6.7 2D vs 3D VOF

As mentioned earlier, Harris & Bhamidipati [130] and Bhamidipati & Harris [131-133] used a 2D, transient, VOF model available in FLUENT software to predict air entrainment in the coated film. The use of a 3D VOF model might then seem redundant. This section compares 2D VOF model with 3D VOF model and discusses the need for a 3D model.

All the governing equations are exactly the same for the two models except that as expected, all the variables and derivatives pertaining to the third dimension disappear from the equations for the 2D model. Comparisons are made between coating windows predicted by 2D and 3D model (Figure 6.13) for the DBSM solution at $W = 0.178$ mm and $H = 0.25$ mm. As shown in Figure 6.13, there is a very good agreement between the 2D and 3D predictions.

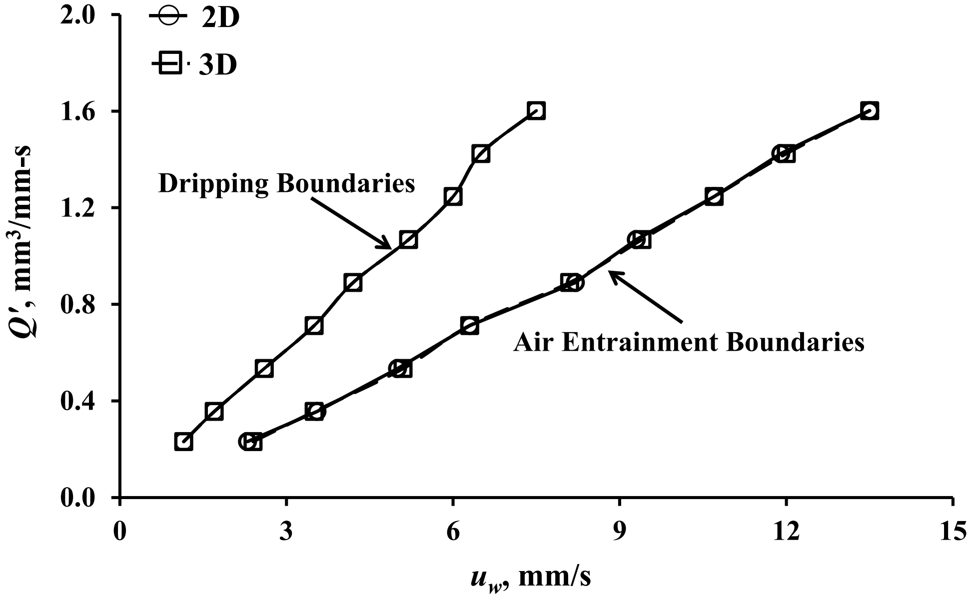

Figure 6.13: Plot showing effect of 2D versus 3D model on coating window of DBSM for $W = 0.178$ mm, $H = 0.25$ mm.

The comparison between 2D and 3D (side/sectional view) model at the point of air entrainment for *W* = 0.178 mm, *H* = 0.25 mm and *Q'* = 1.60 mm^3/mm-s is shown in Figure 6.14. The bubble heights between the two cases is approximately the same.

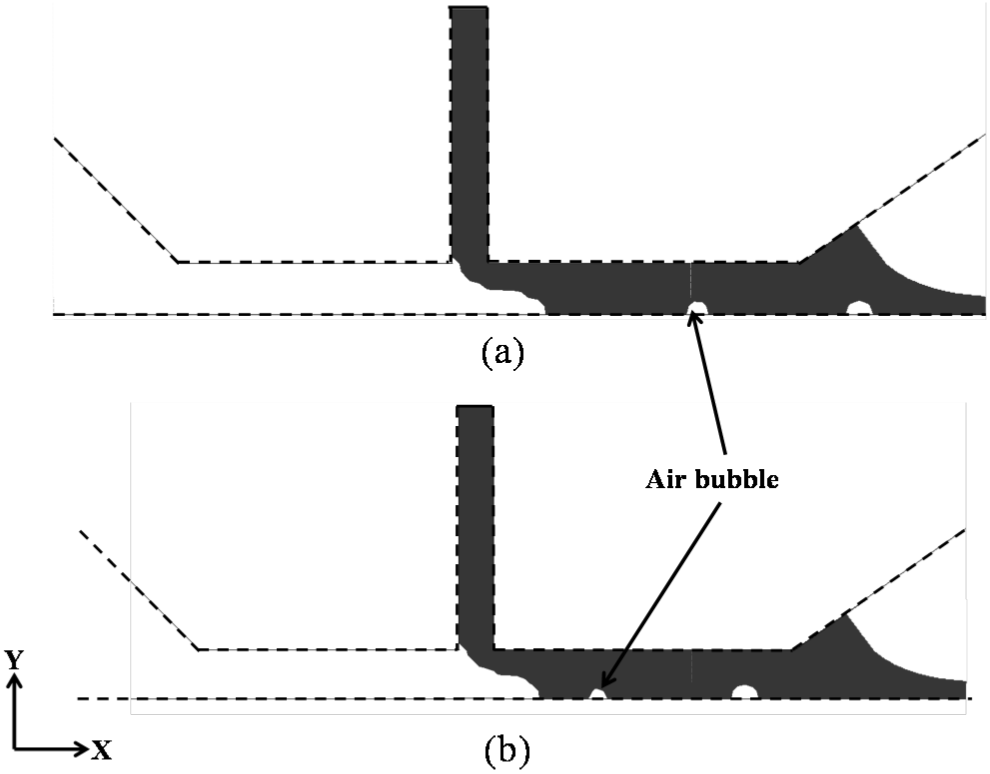

Figure 6.14: Contours of volume fraction of the coating solution for DBSM at *W* = 0.178 mm, *H* = 0.25 mm, *Q'* = 1.60 mm^3/mm-s and u_w = 13.5 mm/s (a) 2D model, (b) 3D model.

Until the point of air entrainment, the flow-field remains two-dimensional, but at and beyond the air entrainment, even though the 2D model can capture the heights of the bubbles comparable to the 3D model, it does not provide any information on the features of sawtooth structures or bubble diameters. Only the 3D model can provide details on the sizes of the sawteeth and the bubble diameters. Therefore, in the current study, the 2D model will be used to obtain the coating window, while the 3D model will be used at and beyond the point of air entrainment to capture more details from the coating process.

6.8 Model Validation with Experiments

The numerical model presented earlier is validated with experiments performed on the test solutions (DBSM, BSM and Polymer Solution) for the slot gap, *W* and coating gap, *H*, listed in Table 6.2. The main study pertaining to PPA/PBI solution is tested for all combinations of three different slot gaps (*W* = 0.178 mm, 0.25 mm and 0.30 mm) and coating gaps (*H* = 0.178 mm, 0.25 mm and 0.30 mm), hence the choice of the parameters chosen for the validation study.

Table 6.2: Details of the geometric conditions and type of solutions used in validation study.

Solution	Slot Gap, *W* (mm)	Coating Gap, *H* (mm)
DBSM	0.178	0.178
BSM	0.250	0.300
Polymer Solution	0.300	0.250

The coating window comparison between simulations and experiments for DBSM and BSM solutions are presented in Figures 6.15 (a) and 6.15 (b). The error bars show the uncertainty in the substrate speed and flow rate per unit width. The simulations compare with the experiments within the uncertainty limits. The percentage differences between simulations and experiments are within 12% and 5% for DBSM and BSM respectively. The higher differences in the DBSM values are because of the higher uncertainties in the

P (*Q'*) values. This is attributed to the higher slope of the *P* versus *Q'* curve for DBSM (Appendix C). The coating window for the Polymer Solution could not be obtained because air entrainment ensued regardless of the processing conditions due to the high solution viscosity.

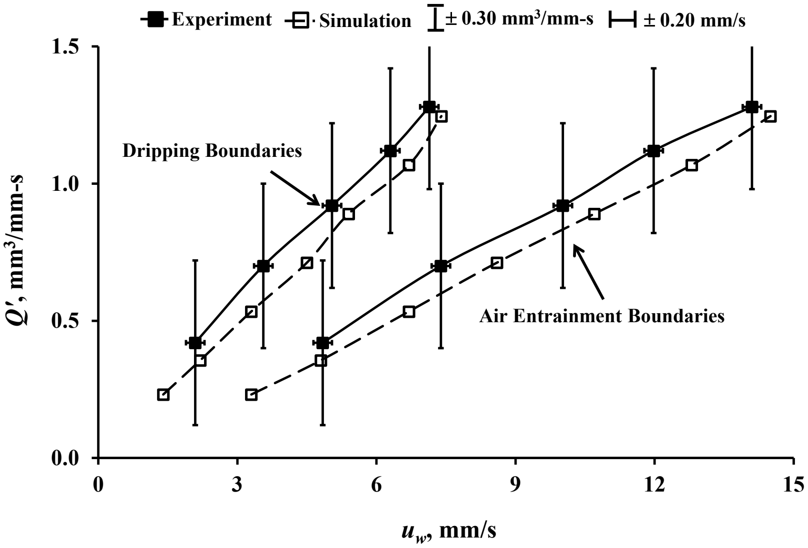

(a)

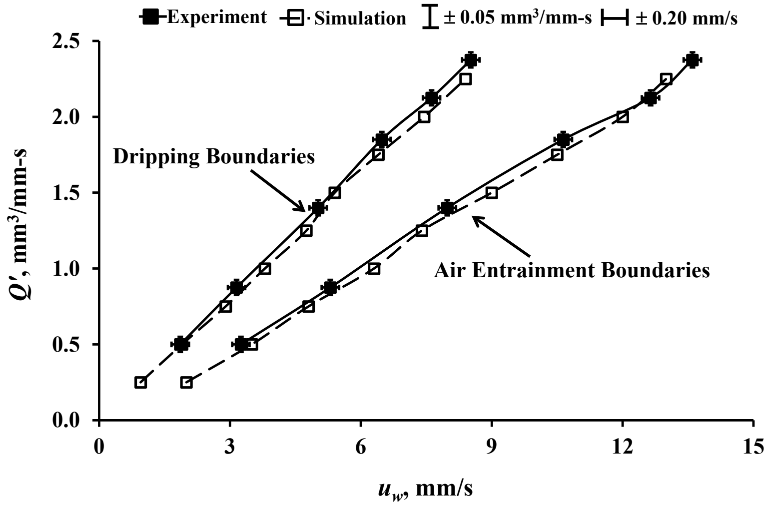

(b)

Figure 6.15: Comparison of experimentally and numerically obtained coating windows (a) DBSM, W = 0.178 mm, H = 0.178 mm, (b) BSM, W = 0.25 mm, H = 0.30 mm.

Comparisons for DBSM at W = 0.178 mm, H = 0.178 mm and Q' = 0.42 mm^3/mm-s (for experiments), and Q' = 0.36 mm^3/mm-s (for simulations) are made between the coating images obtained experimentally and the volume fraction contours of coating solution on the PET walls obtained from the simulations as shown in Figures 6.16 (a) through (f). The boundaries of the die lips are super-imposed on the figures using dotted lines. Three images are shown for each case, dripping boundary, good coating and air entrainment boundary. It can be seen that the interface location compares well before air entrainment occurs. However, at and beyond the air entrainment boundary, the simulations generally under-predict the sawteeth sizes. In addition, the sawteeth are less sharp compared to the experiments. Also, in the simulations, at and beyond the location of pinch-off, the bubbles breakup more readily, hence there is generally a higher number of smaller bubbles in the simulation. These differences are attributed to the averaging of properties and variables used in the VOF model and the approximation of the actual interface by the geo-reconstruct model. The simulations, however, can predict the relative differences between the sawteeth and bubble sizes on the PET walls occurring due to the differences in the geometric and processing conditions as explained in Chapter 8. But, the bubble sizes predicted by the simulation in the sectional view could not be compared either quantitatively or qualitatively with the bubble sizes in the experiments due to the limitation on imaging capabilities. As the model predicts the coating window results accurately, which is the main objective of the study, and the air entrainment phenomenon in this study is only analyzed at a qualitative level, the model is considered to be sufficient for this study.

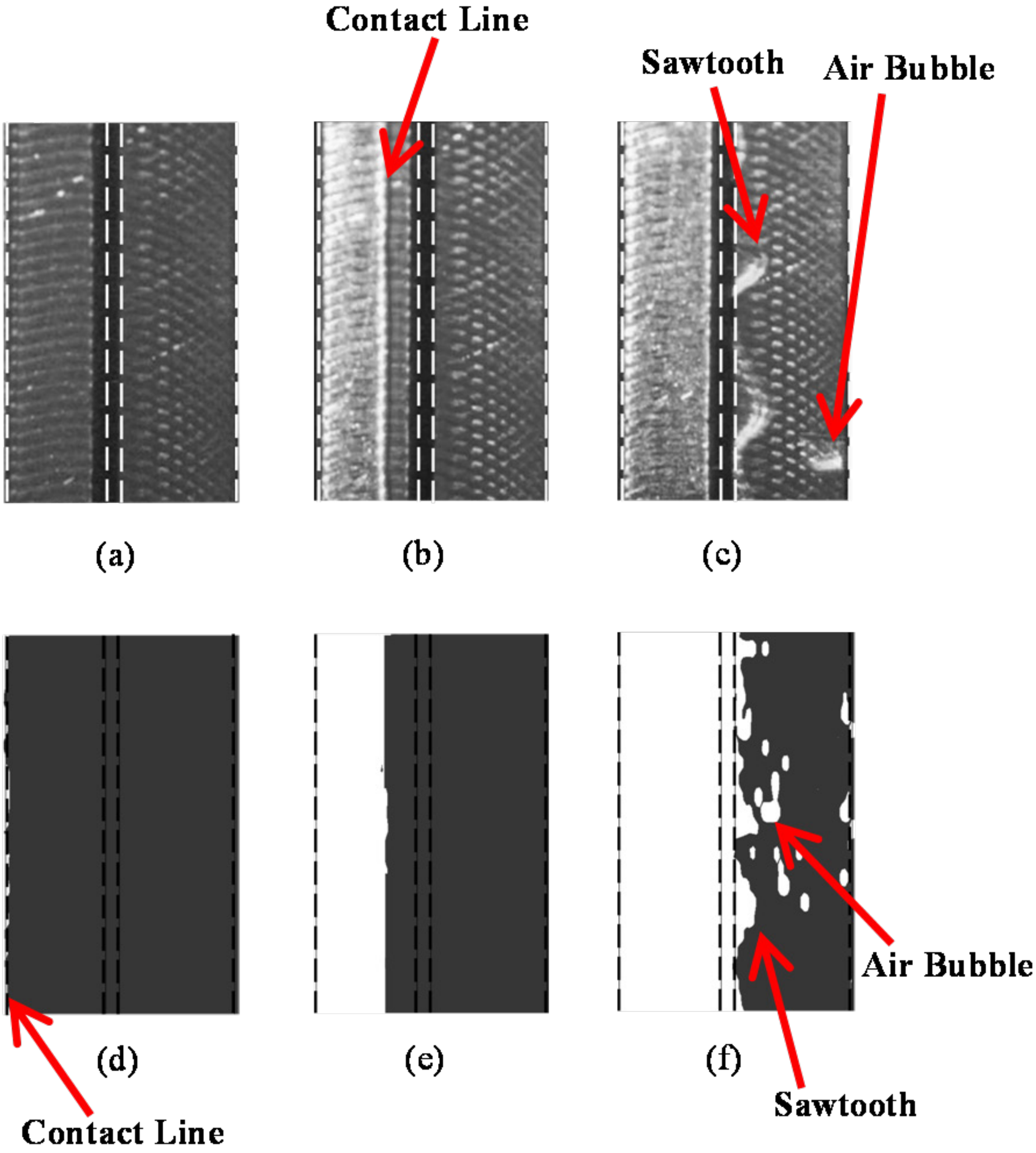

Figure 6.16: Images of coating captured underneath the slot-die, dashed lines represent boundaries of die lips for DBSM at $W = 0.178$ mm and $H = 0.178$ mm (a) Dripping, $u_w = 2.09$ mm/s for $Q' = 0.42$ mm^3/mm-s (Experiment), (b) Good Coating, $u_w = 3.02$ mm/s for $Q' = 0.42$ mm^3/mm-s (Experiment), (c) Air Entrainment & Sawteeth, $u_w = 4.84$ mm/s for $Q' = 0.42$ mm^3/mm-s (Experiment), (d) Dripping, $u_w = 2.2$ mm/s for $Q' = 0.36$ mm^3/mm-s (Simulation), (e) Good Coating, $u_w = 3.10$ mm/s for $Q' = 0.36$ mm^3/mm-s (Simulation), (f) Air Entrainment & Sawteeth, $u_w = 4.80$ mm/s for $Q' = 0.36$ mm^3/mm-s (Simulation).

6.8.1 Illustration of Air Entrainment using Videos from Experiment and Simulation

Snapshots of the videos of sawteeth formation and bubble breakup mechanism, as captured during the experiments and simulations, are presented in Figures 6.17 (a) and 6.17 (b), respectively. The die lips with the mesh are superimposed in the simulation video. The experiments and simulations are made at the air entrainment boundary for BSM at W = 0.30 mm, H = 0.25 mm, and Q' = 0.50 mm^3/mm-s. The time for the experimental video is the actual time, while the video for the simulation is limited to only five seconds, due to the larger computational time and memory requirement needed for longer runs.

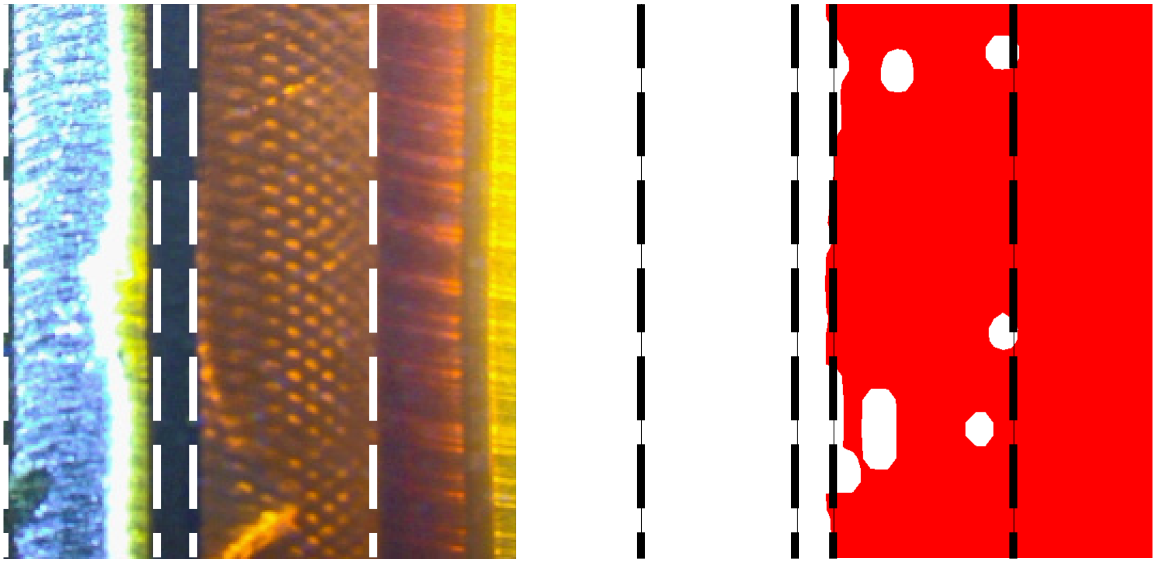

(a) (b)

Figure 6.17: Videos of sawteeth formation and bubble breakup at the point of air entrainment for BSM at W = 0.30 mm, H = 0.25 mm, Q' = 0.50 mm^3/mm-s (a) Experiment, u_w = 3.92 mm/s (bhamidipati_kanthilatha_201105_phd _experiment_air_entrainment.avi, 9.92 MB), (b) Simulation, u_w = 3.75 mm/s (bhamidipati_kanthilatha_201105_phd_simulation_air_entrainment.avi, 29.6 MB).

6.9 Summary

The chapter began by discussing the existing theoretical work for predicting the coating windows and the popular models to solve for the free surface flows. The numerical model and the relevant governing equations that will be used for the current study was then presented in detail. The selection of certain numerical parameters, such as the contact angle, interval size of the mesh, and two-dimensional versus three-dimensional formulation, was then discussed. Finally, the numerical model was validated using the experimental data, which will be used for all numerical case studies presented in subsequent chapters. The effect of geometric parameters and fluid viscosity on air entrainment is presented in the next chapter.

7. AIR ENTRAINMENT STUDIES USING TEST SOLUTIONS

As explained by Higgins and Scriven [59] using the visco-capillary model, instabilities occur resulting in air entrainment when the pressure drop across the coating bead cannot be matched by the externally imposed pressure gradient that drives the coating solution through the slot die. The pressure drop across the coating bead is predominantly due to three factors: (a) Poiseuille contribution at the slot die exit; (b) the Couette flow contribution underneath the upstream and the downstream dies and; (c) the capillary pressure across the upstream and downstream menisci.

From Figures 6.15 (a) and (b), it can be deduced that for a given flow rate, when the maximum coating speed exceeds a certain value, air entrainment occurs. Once the coating speed approaches the maximum value, sawteeth structures form and air bubbles are entrained due to the instabilities at the dynamic contact line (DCL). The overall air entrainment mechanism in pre-metered coating processes can be summarized as follows:

1. As the substrate velocity increases beyond a critical value denoted by the air entrainment velocity, an imbalance occurs between the pressure drop across the coating bead required to maintain a stable coating and the externally imposed pressure gradient driving the flow through the slot die.
2. In conjunction with the pressure imbalance, the inability of the DCL to move beyond the critical velocity results in the formation of a broken DCL containing sawteeth structures or triangular air pocket regions.
3. Due to the three-dimensional nature of the sawteeth structures, there is a finite amount of coating solution present above the air film. Driven by the viscosity and

density differences between the films of air and the solution, instabilities arise at the interface causing air bubble pinch-off and entrainment.

Details of the air entrainment mechanism following the sawteeth formation in a highly viscous, shear-thinning fluid during slot die coating are qualitatively discussed. To the author's knowledge, no such studies currently exist. The detailed physics pertaining to air entrainment are discussed in the following sections.

7.1 Bubble Breakup Mechanism and Air Entrainment

Based on the experimental and numerical observations, the air bubble pinch-off occurs due to two different mechanisms as depicted by Figures 7.1 and 7.2.

Mechanism I: Pinch-off of an air bubble by Mechanism I (Figure 7.1) occurs when solution within the coating gap encloses the air pocket formed by the sawtooth. This mechanism of bubble breakup occurs when the length of the sawtooth is about equal to (Figure 7.1 (a)) or greater than its width (Figure 7.1 (b)). The line X'Y'-X'Y' marked on the top view denotes the location of the side (sectional) view. As the length of the sawtooth compared to its width increases, the pinch-off location of the bubble moves away from the base and closer to the tip of the sawtooth. This mechanism is noticed to some extent by Veverka and Aidun [88] in roll coating of low viscosity solutions.

As the substrate reaches the air entrainment speed, sawteeth or air pockets form. The tip of the sawtooth is subjected to a pulling effect in the direction of the substrate motion due to the viscous nature of the coating solution. This tip exerts a pulling effect on the surrounding coating solution in all directions, thereby bridging the gap between the sawtooth boundaries. Air bubble pinch-off occurs when the solution completely surrounds the sawtooth. Surface tension then draws the bubble closer and the bubble moves downstream and gets entrained in the coated film. Bubble breakup by Mechanism I is depicted using a video file obtained from experiments (Figure 7.1 (c) and Figure 7.1 (d)). While both the videos indicated by Figure 7.1 (c) and Figure 7.1 (d) depict Mechanism I, Figure 7.1 (c) show the pinch-off occurring close to the base of the sawteeth, while in Figure 7.1 (d), the pinch-off is shifted closer to the tip.

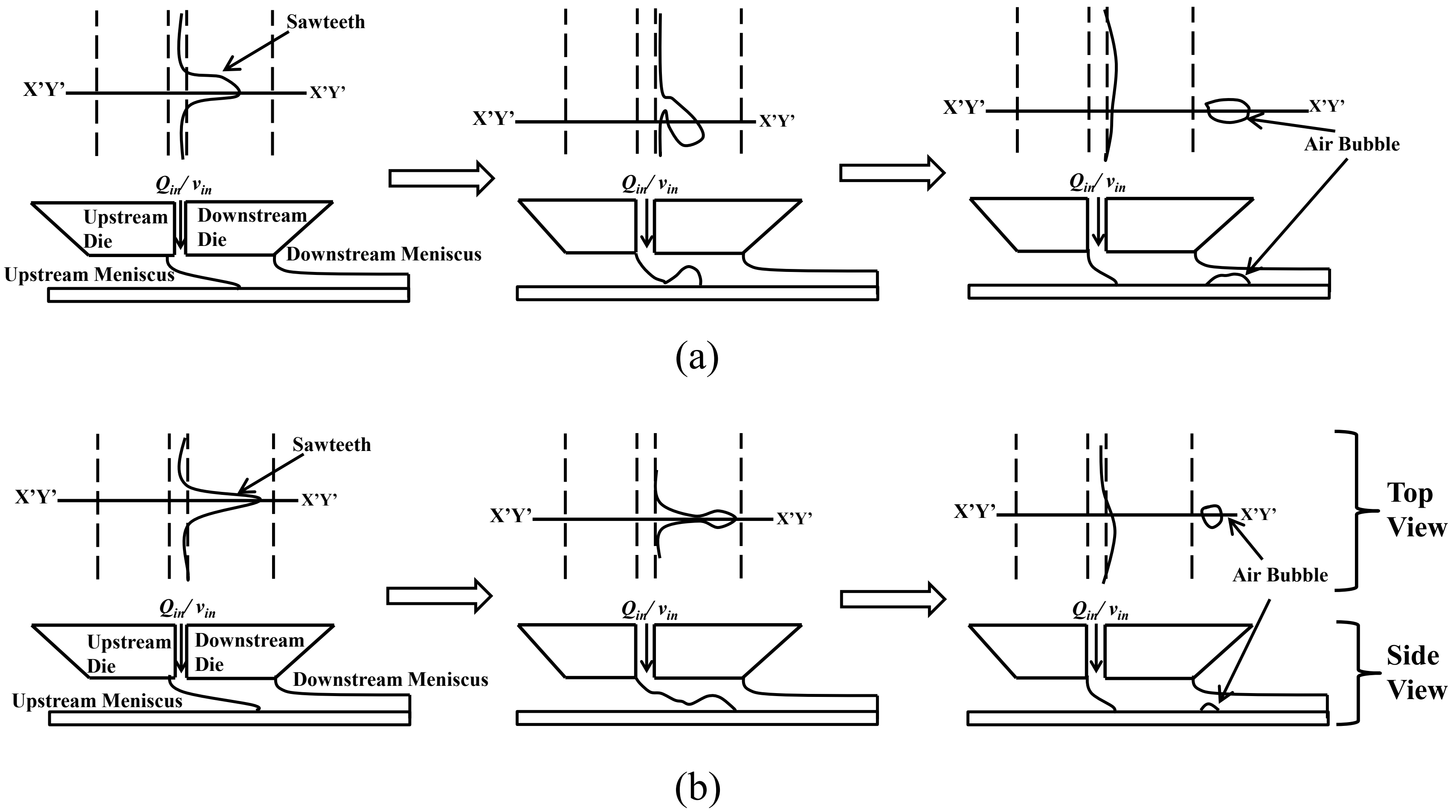

Figure 7.1: Pinch-off of air bubbles by Mechanism I (a) Illustration (air bubble pinch-off closer to the sawtooth base), (b) Illustration (air bubble pinch-off closer to the sawtooth tip).

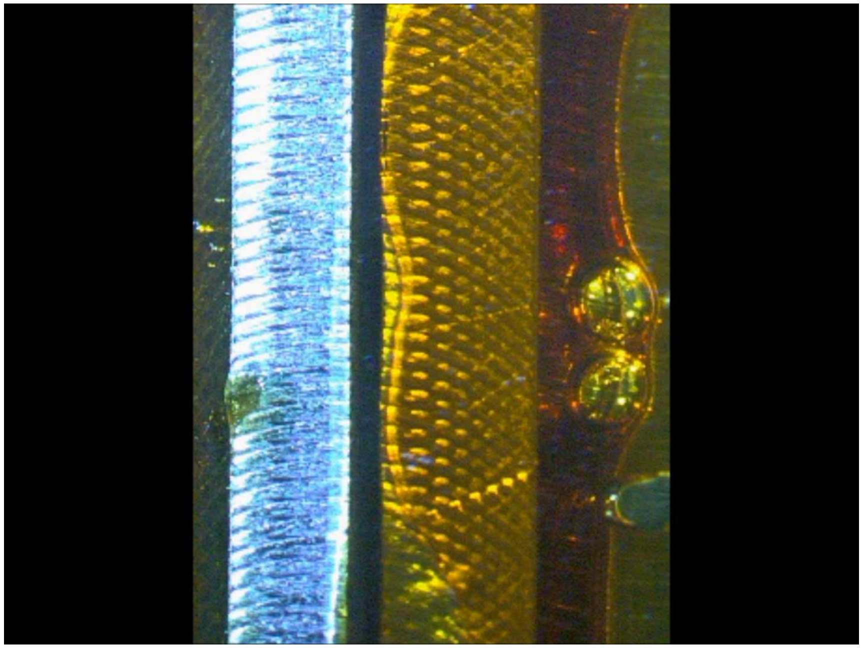

(c)

Figure 7.1: Pinch-off of air bubbles by Mechanism I (c) Snapshot of the video from experiment demonstrating pinch-off closer to the sawtooth base (bhamidipati_kanthilatha_201105_phd_mechanismI_sawtooth_base.avi, 6.65 MB).

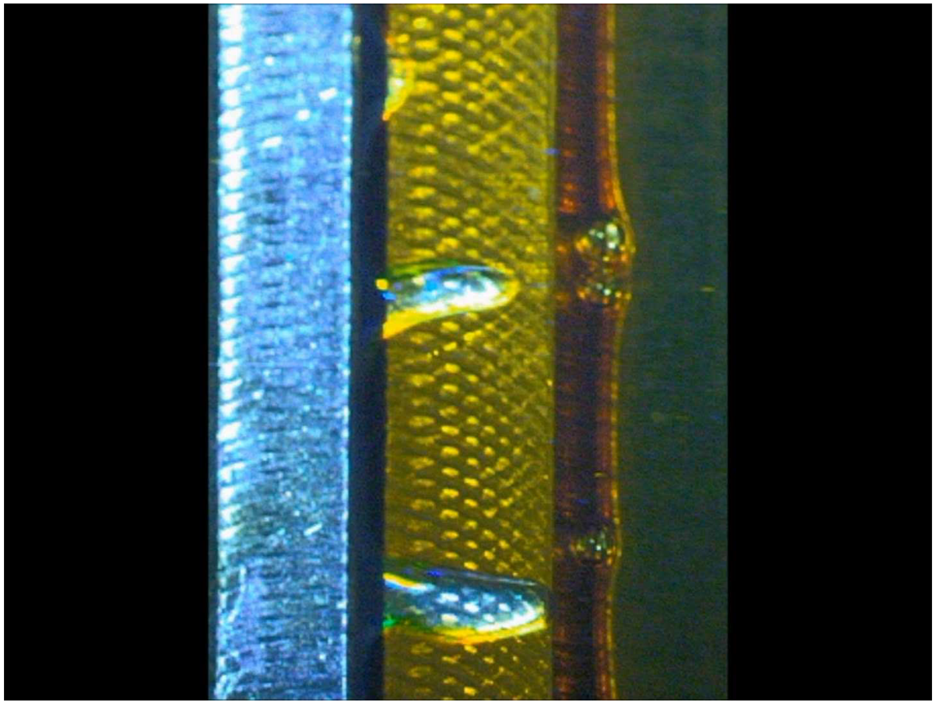

(d)

Figure 7.1: Pinch-off of air bubbles by Mechanism I (d) Snapshot of the video from experiment demonstrating pinch-off closer to the sawtooth tip (bhamidipati_kanthilatha_201105_phd_mechanismI_sawtooth_tip.avi, 4.00 MB).

Mechanism II: In this mechanism, the broken DCL is displaced by a new wave of fluid exiting the slot die. This new fluid assists in enclosing the air pockets formed by the broken DCL as shown in Figure 7.2 (a). A new DCL is then formed in its place. Mechanism II is found to occur when the width of the sawtooth is much greater than its length. In such cases, the solution that is present in the upstream region of the air pocket is incapable of enclosing the air pocket. Instead, the solution exiting the slot die assists in bounding the air pocket, causing pinch-off of the air bubble. Since, the pinch-off is assisted by the new fluid exiting the die, this phenomenon can only be noticed in the pre-metered coating processes.

In the bubble formation by Mechanism II, the pinch-off could extend over a relatively larger area. In such cases, the air bubble looks elongated (in the direction perpendicular to substrate motion) when it pinches-off. Subsequently, the bubble is carried away as a whole or it gets broken into smaller bubbles, which travel independent of each other. The experimental observations are presented using a video file (Figure 7.2 (b)).

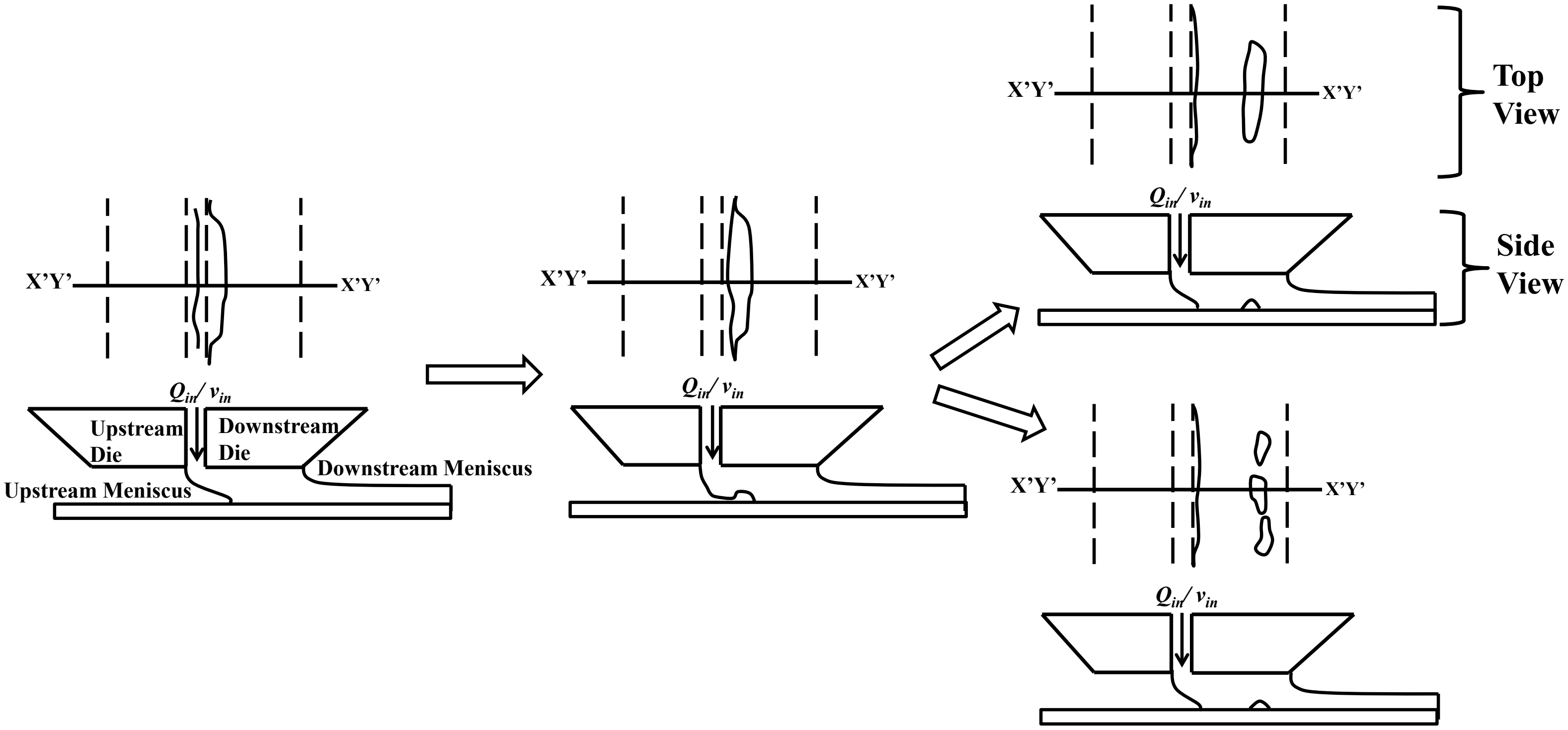

(a)

Figure 7.2: Pinch-off of air bubbles by Mechanism II (a) Illustration.

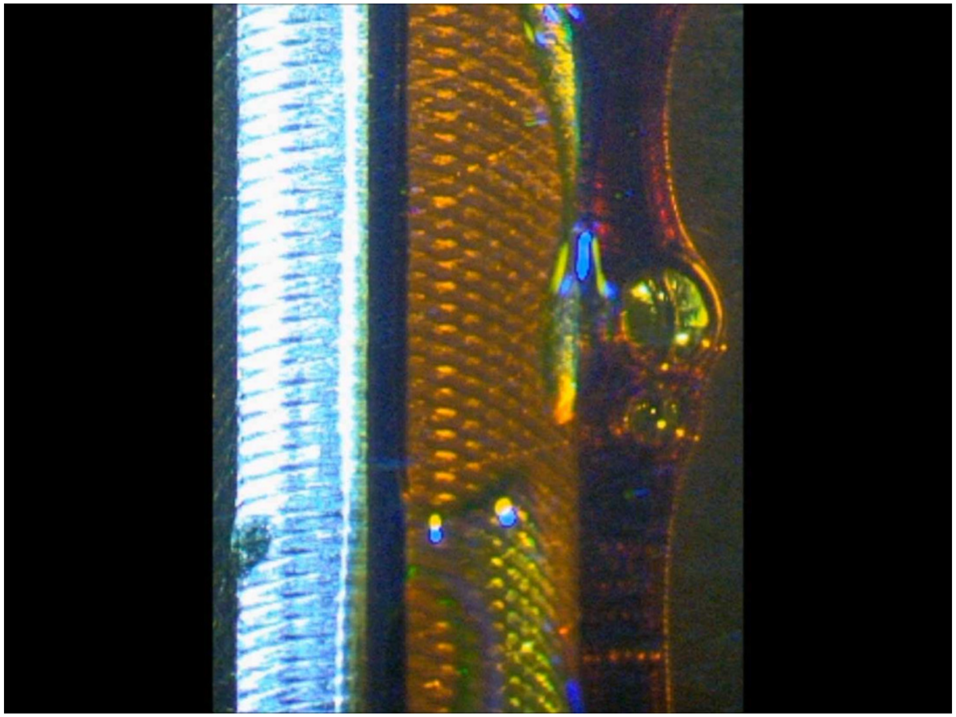

(b)

Figure 7.2: Pinch-off of air bubbles by Mechanism II (b) Snapshot of video from experiment demonstrating Mechanism II (bhamidipati_kanthilatha_201105_phd_mechanismII.avi, 2.74 MB).

In general, regardless of whether the bubble breakup is due to Mechanism I or Mechanism II, at the point of pinch-off, the sizes of the air bubbles are found to be proportional to the sawtooth sizes, unless they are broken into smaller bubbles right away.

7.2 Effect of Geometric Parameters on Sawteeth Sizes

According to the author's knowledge, no studies exist on the effect of geometric parameters on the sawteeth sizes. In this chapter, the effect of slot gap and the coating gap on the sawteeth sizes are investigated and qualitative comparisons are made.

7.2.1 Effect of Slot Gap

The effect of slot gap size on the sawtooth length and width is depicted in Figure 7.3 using BSM at $H = 0.30$ mm. Three slot gaps are considered, $W = 0.178$ mm, 0.25 mm and 0.30 mm, as presented in Figures 7.3 (a) to (c) respectively. The flow rate per unit width, *Q'* is maintained the same between the three cases and the images are obtained at the corresponding air entrainment velocities. For $Q' = 0.53$ mm^3/mm-s, the air entrainment velocities are found to be nearly 3.5 mm/s for all three slot gaps. As the air entrainment mechanism is a random process, four images taken during the coating process for each case are presented. Generally, the sawteeth widths increased with the slot gap, while the differences in the sawteeth lengths were insignificant. This increase in the sawteeth sizes at larger slot gaps possibly occurred due to a reduction in the inlet velocity experienced for the same flow rate. The differences in the substrate speeds and hence the viscous forces between the three cases were negligible. But, the inlet velocities through the slot die and thereby the inertia forces experienced by the fluid decrease as the slot gap increases. This could be the primary reason for the wider sawteeth shapes. Bubble breakup by Mechanism I is more common in smaller slot gaps, while a transition to Mechanism II is noticed as the slot gap increases.

The maximum bubble diameter has been found to be approximately 0.60 mm for W = 0.178 mm, 1.00 mm for W = 0.25 mm and 1.5 mm for W = 0.30 mm. An important conclusion from these results is that, even though the slot-gap does not impact the maximum coating speed, it does have an impact on the size of the entrained bubbles. Therefore, it is advantageous to coat using smaller slot gaps.

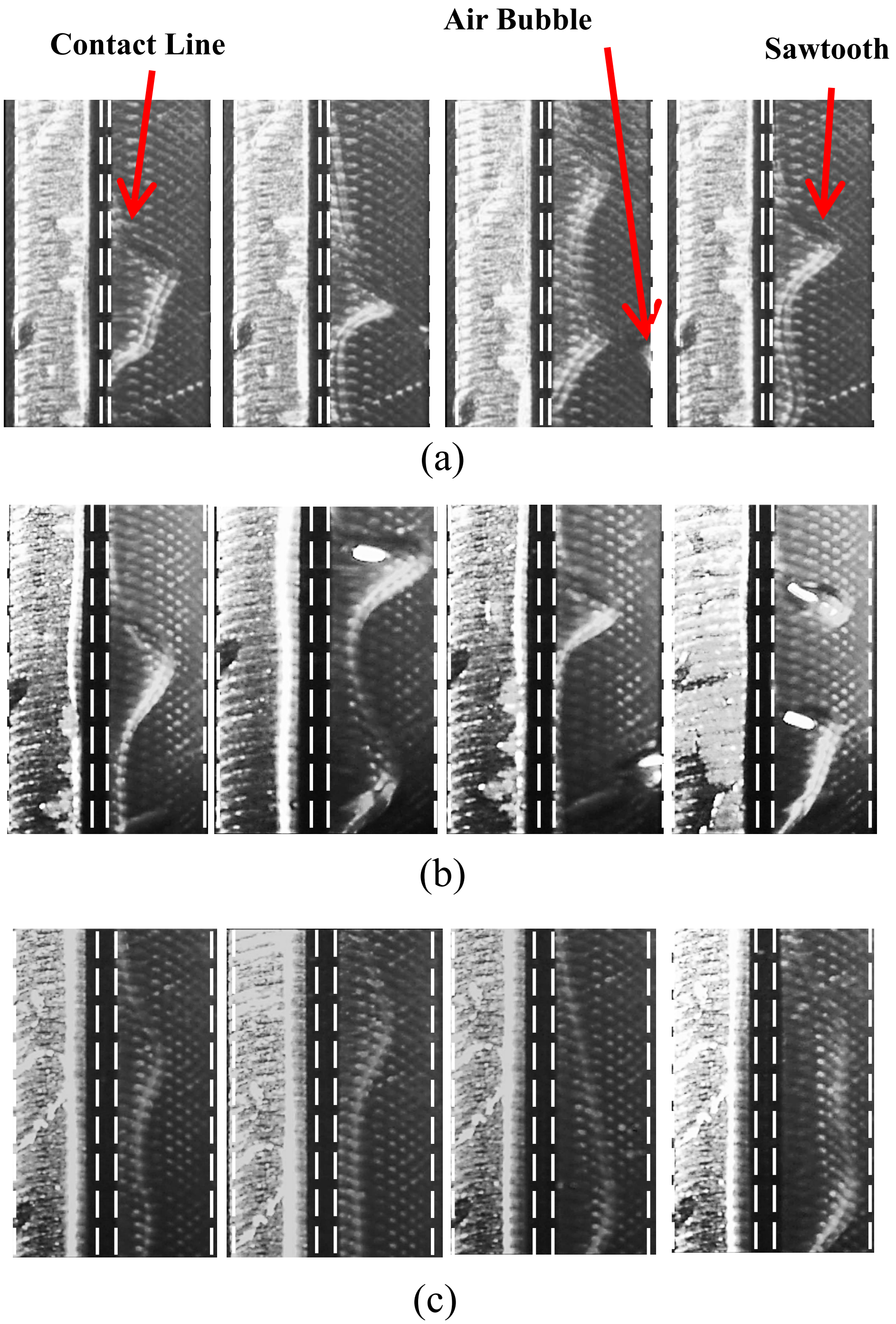

Figure 7.3 : Effect of slot gap, W, on the sizes of the sawteeth at the air entrainment boundary for BSM solution, $H = 0.30$ mm and $Q' = 0.53$ mm^3/mm-s, dashed lines represent boundaries of die lips (a) Images from the experiment for $W = 0.178$ mm at $u_w = 3.54$ mm/s, (b) Images from the experiment for $W = 0.25$ mm at $u_w = 3.5$ mm/s (c) Images from the experiment for $W = 0.30$ mm at $u_w = 3.48$ mm/s.

7.2.2 Effect of Coating Gap

The impact of coating gap on the sawteeth sizes is presented in Figure 7.4 using DBSM at $W = 0.178$ mm. Three coating gaps are selected as $H = 0.178$ mm, 0.25 mm, and 0.30 mm as shown in Figures 7.4 (a) to (c), respectively. For $Q' = 0.62$ mm^3/mm-s, the air entrainment velocities are found to be 7.5 mm/s at $H = 0.178$ mm, 5.5 mm/s at $H = 0.25$ mm and 4.5 mm/s at $H = 0.30$ mm. For $H = 0.178$ mm, it can be seen that in most of the cases, the sawteeth width and length are comparable. Therefore, the pinch-off is expected to follow Mechanism I. With increasing the coating gap, there is a significant increase in the sizes of the sawteeth, both lengthwise and widthwise. Two factors contribute to the larger sawteeth sizes at higher coating gaps:

- The coating speed is lower at larger coating gap. Therefore, the net shear stress experienced by the fluid is smaller. This implies that any stress experienced by the tip of the sawtooth takes longer to propagate towards the solution that is closer to the base of the sawtooth. So, the sawtooth can span a larger area before the upstream elements start experiencing the stresses, at which point, the bubble pinch-off can either follow Mechanism I or Mechanism II.
- If the bubble pinch-off occurs by Mechanism I, the upstream fluid element has to enclose a larger air pocket for pinch-off to occur, allowing even more time for the sawtooth to travel, thereby increasing the size of the sawtooth further. On the other hand, Mechanism II is more likely to occur for larger coating gaps. This is because the inlet velocity is the same for the three cases. Hence, the difference between the inlet and coating speeds

decreases as the coating gap increases. Therefore, there is a higher likelihood for the new solution coming from the slot to cause pinch-off.

In fact, the experiments and simulations show that even though both mechanisms are observed for the three coating gaps, the pinch-off moves from a dominant Mechanism I in smaller coating gaps to a dominant Mechanism II in larger coating gaps.

The maximum bubble sizes are approximately 0.75 mm, 1.00 mm, and 1.80 mm for the three coating gaps, $H = 0.178$ mm, $H = 0.25$ mm, and $H = 0.30$ mm, respectively. This is to be expected because the larger sawteeth generated at higher coating gaps produces bigger bubbles, which is undesirable. Hence, in addition to obtaining larger coating speeds, smaller coating gaps are also advantageous because of the smaller bubble sizes.

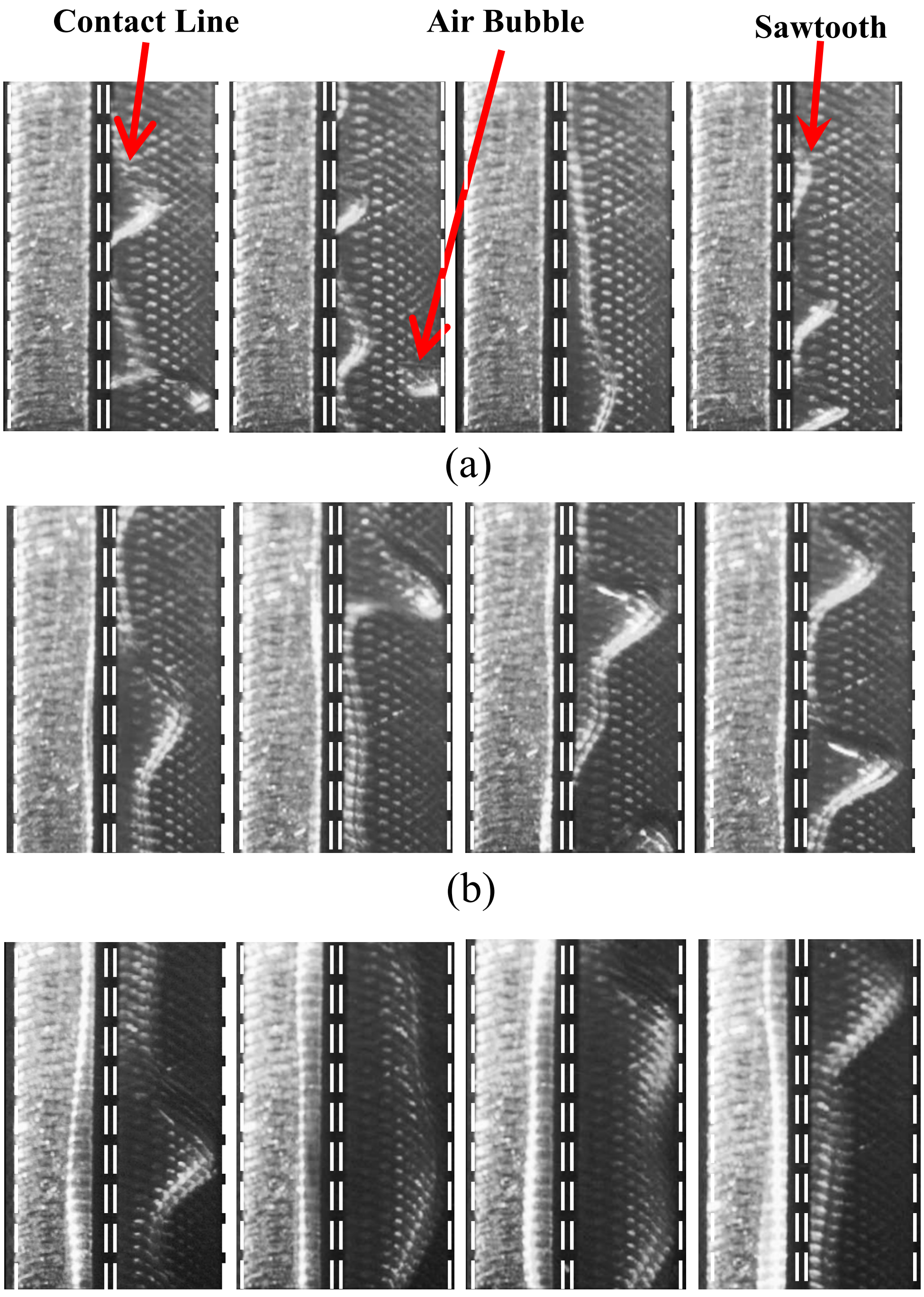

(a)

(b)

(c)

Figure 7.4 : Effect of coating gap, H, on the sizes of the sawteeth and the air bubbles at the air entrainment boundary for DBSM solution, W = 0.178 mm and Q' = 0.62 mm^3/mm-s, dashed lines represent boundaries of die lips (a) Images from the experiment for H = 0.178 mm at u_w = 7.5 mm/s, (b) Images from the experiment for H = 0.25 mm at u_w = 5.5 mm/s, (c) Images from the experiment for H = 0.30 mm at u_w = 4.5 mm/s.

7.3 Effect of Viscosity

The effect of solution viscosity on the sizes of the sawteeth at $W = 0.178$ mm and $H = 0.25$ mm is shown in Figures 7.5 (a) and 7.5 (b) for DBSM and BSM, respectively. For $Q' = 0.55$ mm^3/mm-s, the coating speed corresponding to air entrainment is found to be 7.4 mm/s for DBSM, and 4.3 mm/s for BSM.

From the figures, it is evident that DBSM has longer and wider sawteeth compared to BSM (It implies that lower viscosity solutions have longer and wider sawteeth than higher viscosity solutions). It has to be noticed that similar trends were also noticed by Burley and Kennedy [89] (also depicted in Figure 2.11), even in the case of Newtonian solutions. It can be observed that viscosity has inverse effect on the maximum coating speed (lower viscosity solutions can be processed at higher coating speeds). The reason for the larger sawtooth sizes can be explained as follows: For low-viscosity solutions, the smaller viscosity will reduce the stresses experienced by the fluid, however, the larger air entrainment velocity will increase the stresses. While examining Equation 2.3 (in the current study) obtained by Gutoff and Kendrick [92] and Figure 2.9 (a) in Veverka's thesis [56], it can be observed that the effect of viscosity dominates the effect of air entrainment velocity. Therefore, the stresses follow the same trend as the viscosity of the solution (solutions with lower viscosity experience smaller stresses). In addition, since, for shear-thinning fluids, stresses are proportional to coating speed raised to the power of power-law index (which is less than one for shear-thinning fluids), the impact of the consistency-index further overrides the effect of coating speed causing lower stresses in low-viscosity solutions. Since lower-viscosity solutions experience smaller stresses, the impact felt by the fluid upstream of the sawtooth tip is reduced causing the broken DCL to spread over a larger area.

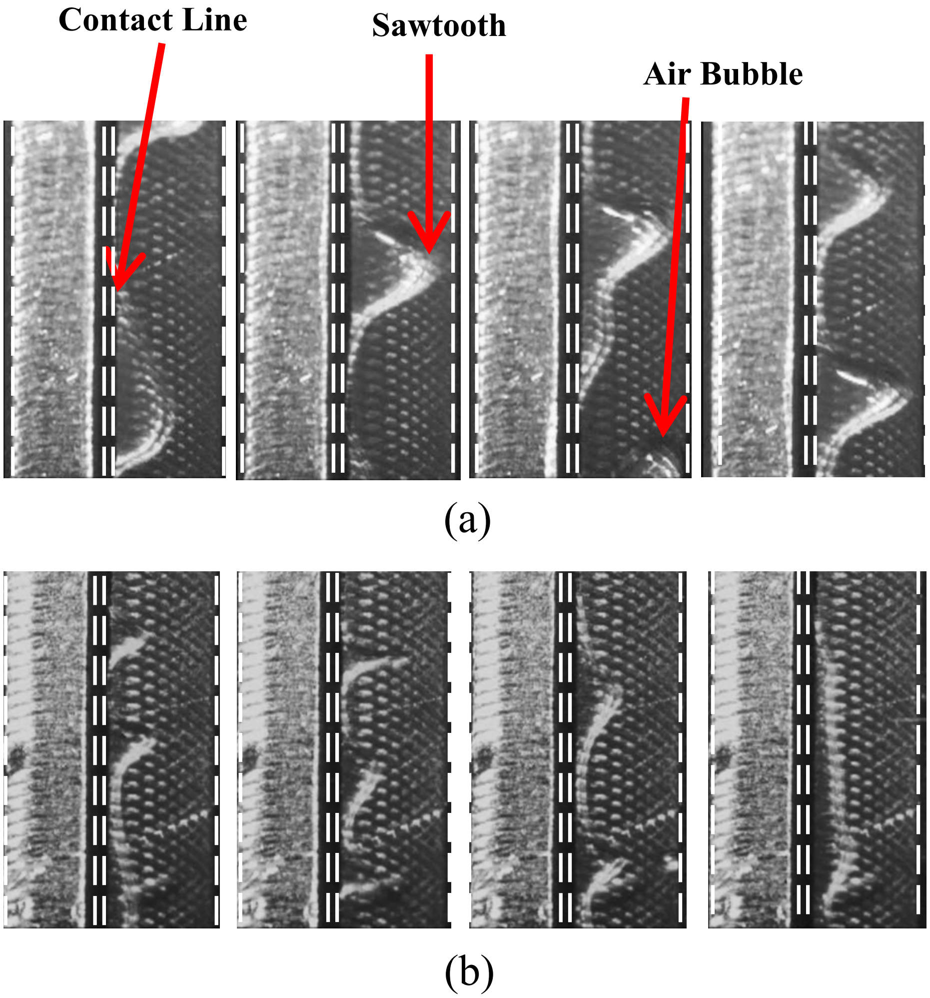

(a)

(b)

Figure 7.5 : Effect of solution viscosity on the sizes of the sawteeth and the air bubbles at the air entrainment boundary for $W = 0.178$ mm, $H = 0.25$ mm and $Q' = 0.55$ mm^3/mm-s, dashed lines represent boundaries of die lips (a) Images from the experiment for DBSM at $u_w = 7.4$ mm/s, (b) Images from the experiment for BSM at $u_w = 4.3$ mm/s.

Based on the previous discussion about the characteristics of the bubble breakup mechanism, low viscosity solutions are expected to exhibit a higher probability of bubble breakup by Mechanism II compared to high-viscosity solutions, which is indeed found to be the case based on the observations from the experiments. Also, the maximum bubble size is approximately 1.00 mm for DBSM and 0.80 mm for BSM.

Another interesting observation is made while coating DBSM at smaller coating speeds. Similar to the observations of Veverka [56], sawteeth formation is observed without the bubble pinch-off. This phenomenon is generally seen while coating low-viscosity solutions at relatively low flow rates and substrate speeds. The DCL is more stable in such cases. For example, a video of DBSM coating at $W = 0.178$ mm, $H = 0.250$ mm, $Q' = 0.35$ mm^3/mm-s and $u_w = 2.9$ mm/s can be found by clicking on Figure 7.6. The air entrainment speed corresponding to these conditions is found to be approximately 3.30 mm/s. However, a major discrepancy between the trends seen in the current study and the study by Veverka is that he found this phenomenon to occur when the ratio of air to liquid viscosity is greater than 2×10^{-4}, while in the current study, the viscosity ratio is nearly 10^{-6}, which is approximately two orders smaller. The discrepancies could be due to the use of a puddle coater in Veverka's study, while the current study is performed using a slot die coater. Therefore, it is important to perform a detailed study to understand the transition in the viscosity ratio value for high-viscosity, shear-thinning fluids in slot die coating and the factors preventing air entrainment. However, it is outside the scope of this study.

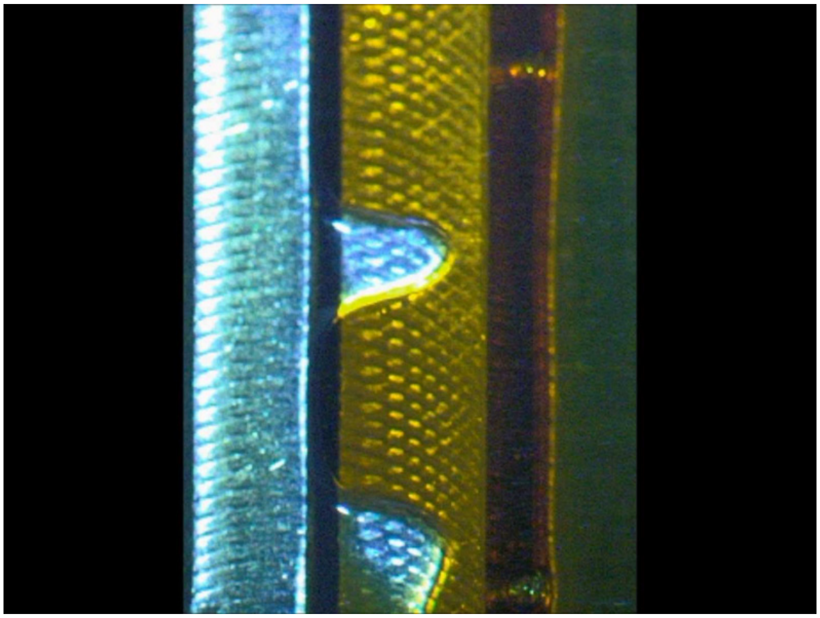

Figure 7.6 : Snapshot of video depicting the presence of sawteeth alone without air entrainment for DBSM at W = 0.178 mm, H = 0.25 mm, Q' = 0.35 mm^3/mm-s and u_w = 2.9 mm/s (bhamidipati_kanthilatha_201105_phd_only_sawteeth_no_air_entrainment.avi, 6.89 MB).

7.4 Summary

A detailed qualitative analysis of the bubble breakup mechanism was carried out in this chapter. Two mechanisms were found to cause bubble pinch-off eventually leading to air entrainment in the coated film. While air entrainment in Mechanism I was found to be driven by the coating solution present in the coating gap, Mechanism II was found to be assisted by the coating solution leaving the slot die exit. Comparative studies between the geometric parameters and processing conditions revealed that Mechanism I is dominant in smaller slot gaps and coating gaps and when processing low viscosity solutions. Mechanism II was found to be dominant when larger sawteeth are present. Bubble sizes were found to vary proportionally with the sawteeth sizes. More detailed studies using Design of Experiments (DOE) for simulations are performed on PPA/PBI solutions as discussed in the next chapter.

8. SLOT DIE COATING STUDIES OF PPA/PBI SOLUTIONS

8.1 PPA/PBI Solution DOE Studies

The primary objective of the current study, as mentioned in Chapter 1 is to improve the durability of the HT-PEMs, which are obtained by slot die coating of PPA/PBI solutions. As discussed in Chapter 2, geometric and processing conditions are found to impact the coating process, therefore, Design of Experiments (DOE) for simulations are performed to study the effects of slot gap (*W*), coating gap (*H*) and processing temperature (*T*). Three values are used for each of the three parameters as listed in Table 8.1. The goals of the study are:

- Obtain a wide range of thicknesses by using the same set of parameters;
- Obtain the conditions that produce maximum coating speed that will assist in manufacturing membranes at a faster rate.

Table 8.1: Parameters used in DOE study for the PPA/PBI solutions.

Name	Units	Level 1	Level 2	Level 3
W	mm	0.178	0.25	0.30
H	mm	0.178	0.25	0.30
T	ºC	120	140	160

A full factorial DOE will generate 27 (3^3) coating windows. As each coating window entails making several simulations for each *Q'*, a full factorial would require a large number of runs. In order to reduce the number of runs, a fractional factorial DOE is performed based on Taguchi’s Robust Design methodology. Taguchi’s Robust Design generated a total of 9 combinations as indicated by Figure 8.1 and listed in Table 8.2.

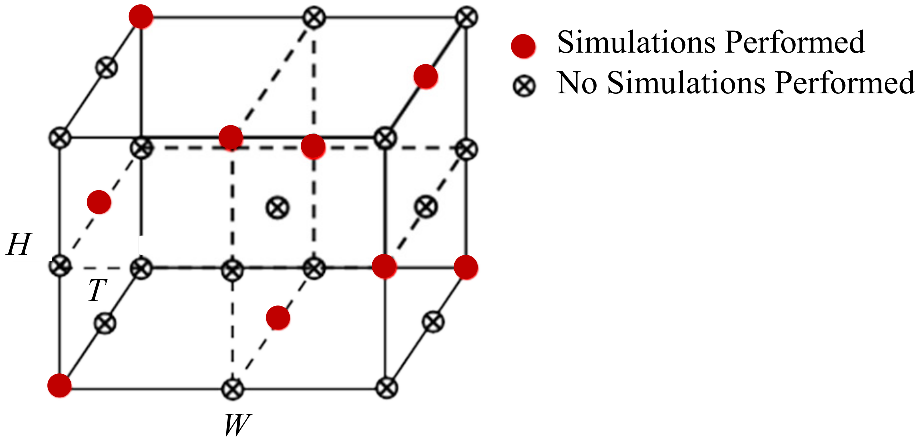

Figure 8.1: Graphical representation of selection criteria for fractional factorial.

Table 8.2: Runs generated for DOE.

Run #	***W*, mm**	***H*, mm**	***T*, ºC**
1	0.178	0.178	120
2	0.178	0.25	140
3	0.178	0.30	160
4	0.25	0.178	140
5	0.25	0.25	160
6	0.25	0.30	120
7	0.30	0.178	160
8	0.30	0.25	120
9	0.30	0.30	140

The coating windows for the nine DOE runs performed using numerical simulations are presented in Figures 8.2 (a) to (c). Each plot shows runs with the same processing temperature. DOE runs 1, 6, and 8 corresponding to T = 120 °C are plotted in Figure 8.2 (a), runs 2, 4, and 9 corresponding to T = 140 °C are presented in Figure 8.2 (b), while runs 3, 5, and 7 corresponding to T = 160 °C are plotted in Figure 8.2 (c). For the sake of comparison, the minimum and maximum values on the axes are kept the same. Unlike the coating windows obtained for the test solutions, DBSM and BSM, the maximum coating speeds for all the runs using PPA/PBI solutions are within the system restrained maximum speed of 15 mm/s, hence there exists the end boundary in the coating window plots. As will be shown in Section 8.3.3.1, this difference in the maximum coating speeds between the test solutions and the PPA/PBI solutions is accredited to the power-law indices, n. On the dripping boundary, it was found that for any given slot die/substrate geometry and coating solution, the ratio of flow rate per unit width, Q' to the dripping velocity, $u_{w,\ min}$ is a constant. Therefore, the dripping boundary is approximately a line with a constant slope. All the values from the DOE runs are presented in Appendix E. The highest coating speed is obtained for Run 5. The runs suggest that coating at higher temperatures is advantageous, which could be attributed to lower viscosities. As discussed in Chapter 2, low viscosity solutions produce larger air entrainment velocities. As for every temperature, different combinations of W and H are studied, it is difficult to predict their impact on the coating window unless the coating windows are plotted in a non-dimensional form and the relationships between the independent and dependent variables are found. The non-dimensional coating windows and the relevant discussion are presented in Section 8.2.

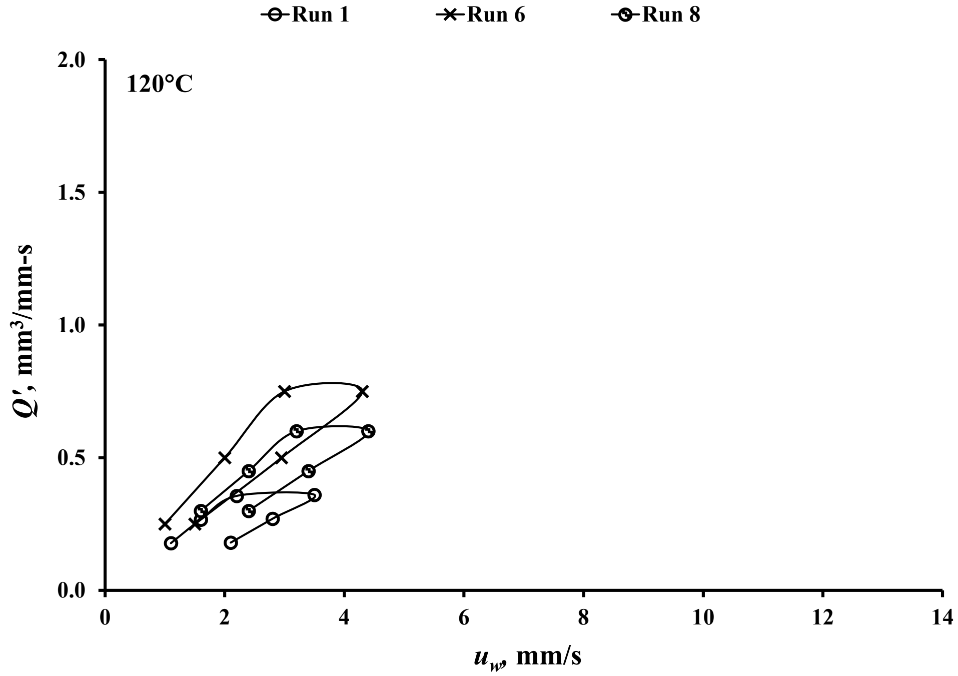

(a)

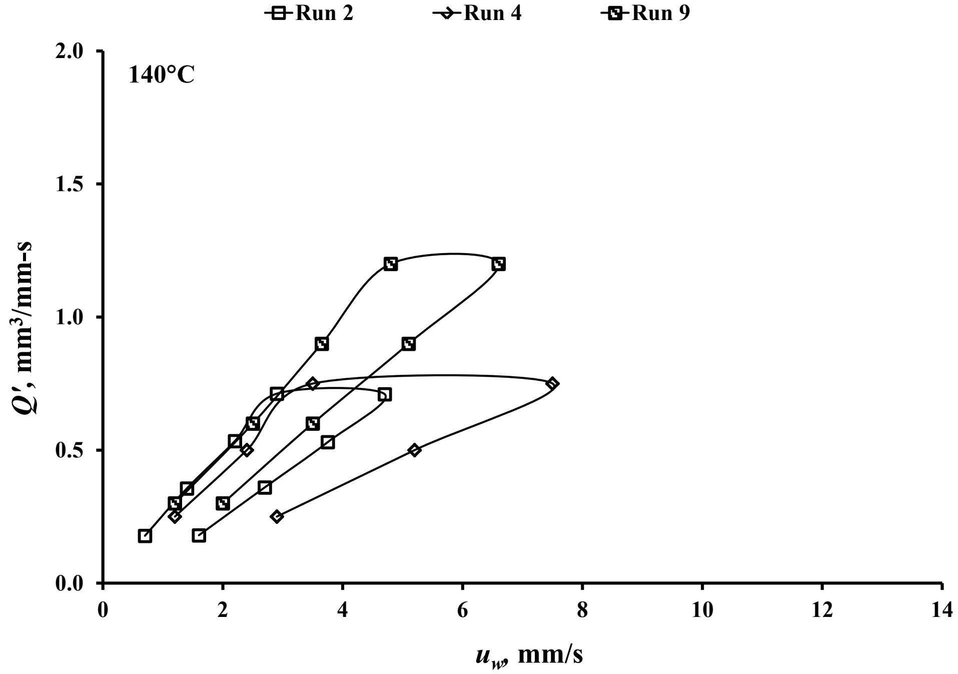

(b)

Figure 8.2: Coating windows obtained for the DOE runs (a) Runs at 120 °C, 1, 6 and 8, (b) Runs at 140 °C, 2, 4 and 9.

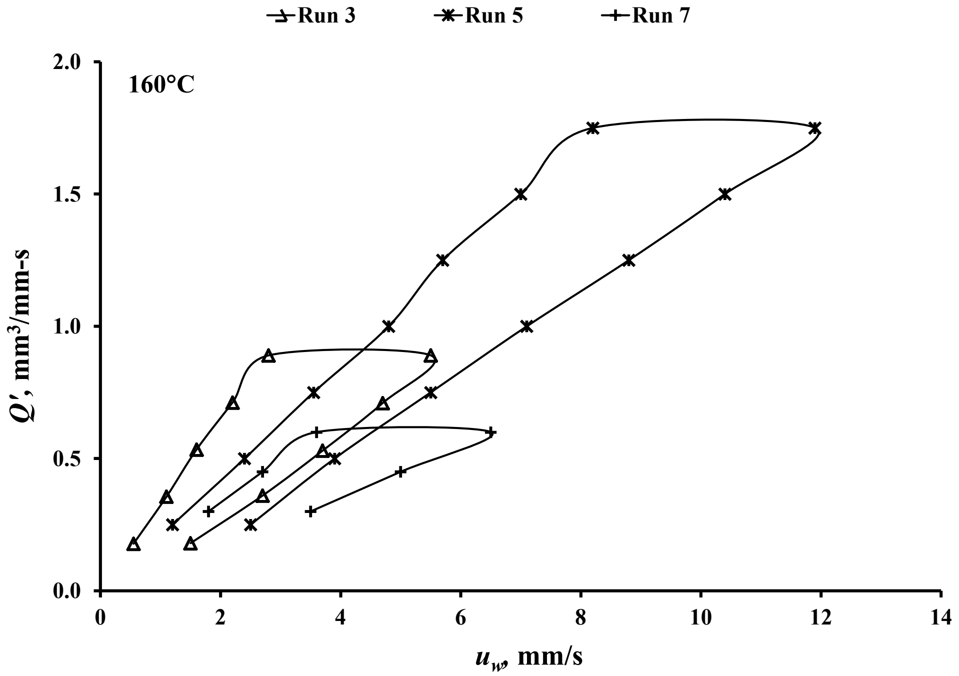

(c)

Figure 8.2: Coating windows obtained for the DOE runs (c) Runs at160 °C, 3, 5 and 7.

As explained previously, one of the goals of the current study is to find a combination of geometric and processing parameters that would give a wide range of wet film thicknesses. A wider range is achieved when the difference between the thickest and the thinnest films that can be obtained for a given set of parameters is the largest. The thickest film is obtained by dividing the flow rate per unit width, *Q'*, by the corresponding dripping velocity, $u_{w,\ min}$. Similarly, the thinnest film is obtained by dividing the flow rate per unit width, *Q'*, by the corresponding air entrainment velocity, $u_{w,\ max}$. As noted before, for a given set of geometric and processing parameters, the ratio of *Q'* to $u_{w,\ min}$ is a constant. So, the maximum wet thickness is independent of the flow rate per unit width. But the minimum wet thickness is obtained for the smallest flow rate per unit width. Thus, for a given set of conditions, the maximum range is obtained at the smallest flow rate possible. Table 8.3 lists the minimum and maximum wet thicknesses for each of the nine runs. It can be observed that increasing the coating gap increases both the maximum and minimum wet thicknesses. This has to be expected because the solution fills the coating gap before it attains the final wet thickness. Among the nine DOE runs, Run 3 demonstrated a wide variety of thicknesses ranging from a minimum of 0.12 mm to 0.33 mm. This is due to the lower viscosity corresponding to the higher PPA/PBI temperature and the larger coating gap. In general, when the processing temperature is high, larger coating gaps produce wider range of thicknesses

Table 8.3: Maximum and minimum wet thicknesses from the DOE runs.

Run #	h_{max}, **mm**	h_{min}, **mm**	$h_{max} - h_{min}$, **mm**
1	0.16	0.09	0.07
2	0.26	0.11	0.15
3	0.33	0.12	0.21
4	0.21	0.09	0.12
5	0.23	0.10	0.13
6	0.25	0.17	0.08
7	0.17	0.09	0.08
8	0.19	0.14	0.05
9	0.25	0.15	0.10

8.2 Non-Dimensionalized Coating/Casting Window

In order to analyze and quantify the effects of slot gap, coating gap and processing temperature on the minimum wet thickness, the dimensionless minimum wet thickness is plotted as a function of all the non-dimensional numbers listed in Table 3.2.

Figure 8.3 shows the variation of non-dimensional minimum wet thickness with capillary number in logarithmic and linear scales. As the capillary number increased, the minimum wet thickness increased. This is consistent with the findings from earlier research [100] that high-viscosity solutions follow Region I (Figure 2.13). The implication of this result is that because the capillary number is a ratio of viscous forces to the surface tension forces, the minimum wet thickness increases as the viscosity of the solution increases or the surface tension of the solution decreases provided all other variables are constant. Regardless of the actual values of the slot gap, coating gap or the processing temperatures, the differences in dimensionless minimum wet thickness at a given capillary number are less significant. These insignificant differences imply that true non-dimensionality exists between the dimensionless minimum wet thickness and the capillary number.

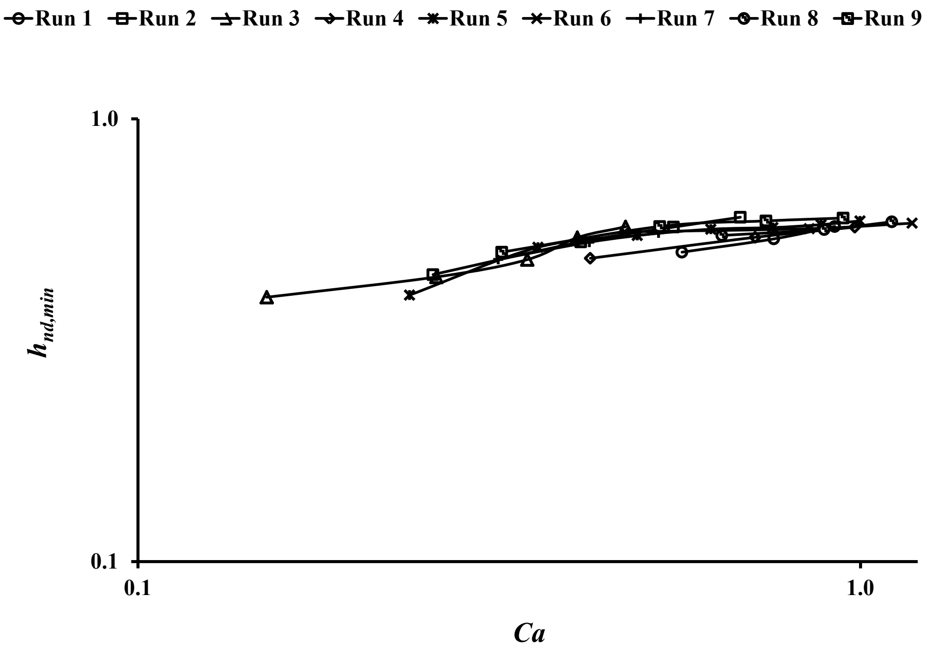

(a)

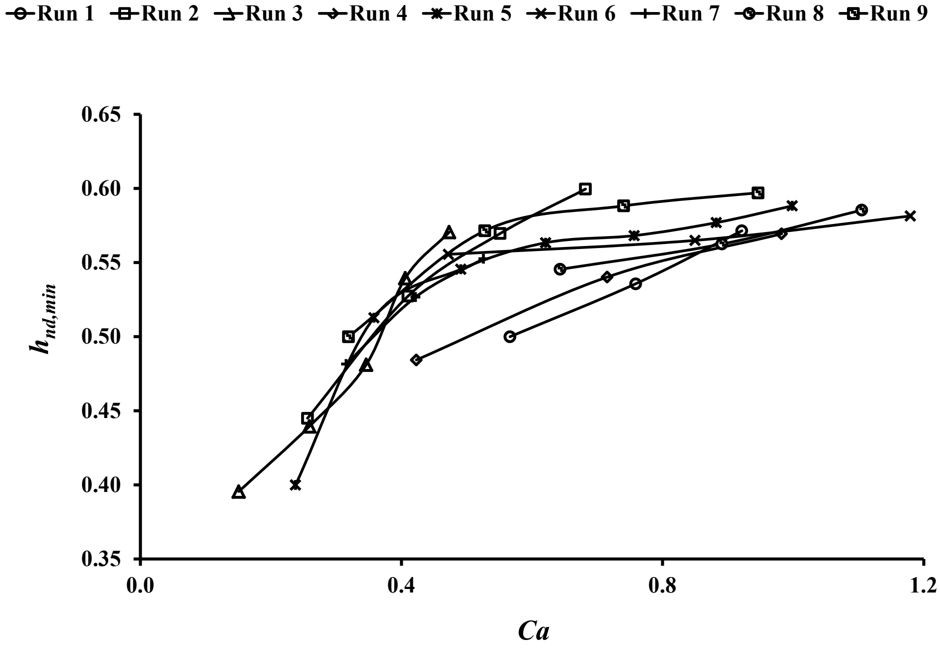

(b)

Figure 8.3: Dimensionless minimum wet thickness versus capillary number (a) Logarithmic scale, (b) Linear scale.

A very interesting observation is made when the dimensional coating window data from Figure 8.2 is compared with dimensionless coating window data from Figure 8.3. The end (right most boundary) of the coating window in Figure 8.2 is obtained when either the dimensionless minimum wet thickness is a value between 0.55 and 0.60 or the capillary number approaches 1.2. In slot-die coating, the restriction on the dimensionless minimum wet thickness is dictated by the downstream die lip, which acts as a doctor blade, preventing the film from getting thicker [69]. Thus, the slot-die coater is also referred to as the metered-knife coater [190]. The capillary number limitation is driven by an imbalance between the viscous and capillary forces. The viscous forces tend to drag the fluid in the direction of the substrate motion, while the capillary forces resulting from the surface tension property of the fluid tend to pull the fluid in the opposite direction. Consequently, as the viscous forces exceed surface tension forces such that the capillary number is greater than 1.2, the upstream meniscus remains unstable for all the substrate speeds. The restriction on the capillary number was also noticed by Wilkinson [191].

In order to obtain a quantitative relation between the dimensionless minimum wet thickness and the capillary number, a curve is fit through all the data points as shown in Figure 8.4. A power-law equation is obtained from the curve fit between the dimensionless minimum wet thickness and the capillary number as given by Equation 8.1:

$$h_{nd,min} = 0.6\, Ca^{0.20} \tag{8.1}$$

The semi-empirical relation given by Equation 8.1 predicts the data from the DOE study within ±10%. This semi-empirical relation between the dimensionless minimum wet thickness and capillary number corresponds to the minimum possible value for the thickness below which defects will originate in the material, e.g., air entrainment or bubbles.

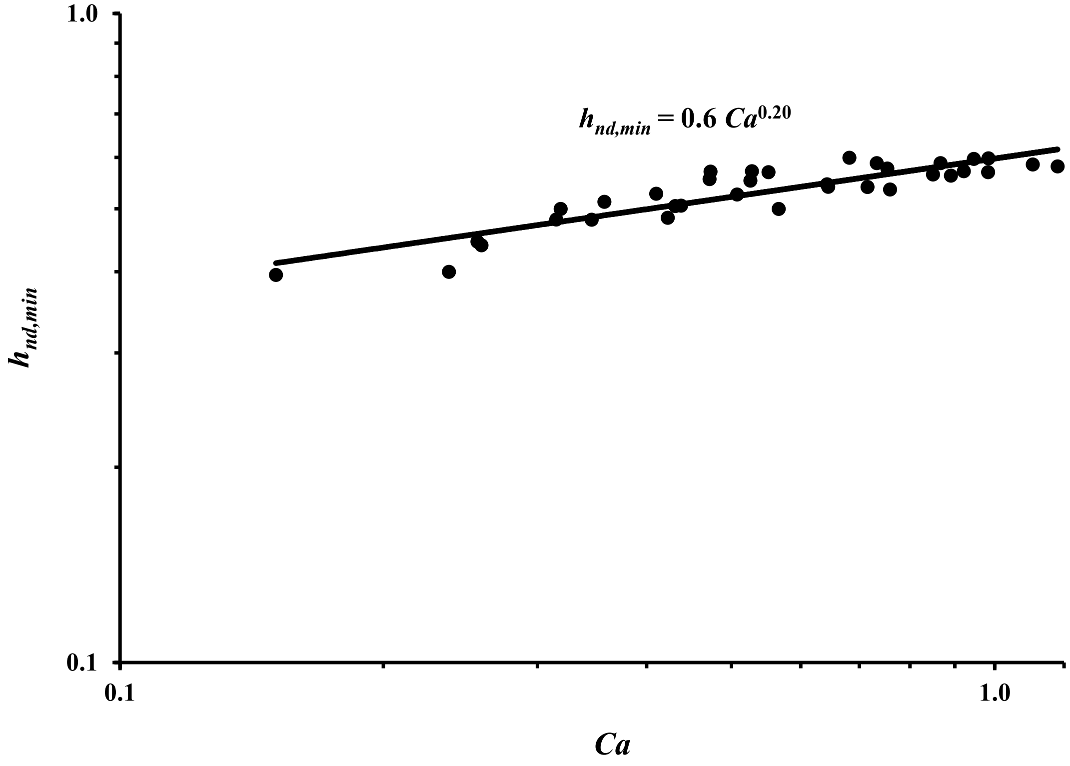

Figure 8.4: Power-law curve-fitting between minimum wet thickness and capillary number.

The predictions by the semi-empirical relation given by Equation 8.1 were compared with the experimental results for BSM and DBSM and results from literature [59, 67, 100], as shown in Figure 8.5. For the numerical study conducted by Lin et al. [67], a Newtonian solution with the following material properties: $\mu = 0.20$ Pa-s and $\sigma =$

0.0665 N/m using a slot die of the following geometry: $W = 0.20$ mm, $H = 0.20$ mm and die lip length of 1.00 mm were used. For the experimental study conducted by Chang et al. [100], a Newtonian solution with the following material properties: $\mu = 0.05$ Pa-s and $\sigma = 0.067$ N/m using a slot die of the following geometry: $W = 0.20$ mm, $H = 0.20$ mm and die lip length of 0.20 mm were used. In both cases, the highest viscosity values from respective figures were used for the comparison, as extracted from Figure 13 [100] and Figure 10 [67]. It is shown in Figure 8.5 that the semi-empirical relation compares within ±10% of the results obtained from experiments using BSM and DBSM solutions. When compared to existing literature results, the semi-empirical model (Equation 8.1) predicts within ±15% of the results by Chang et al. [100] and Lin et al. [67], as shown in Figure 8.5. The relatively higher percentage differences between the predictions by the semi-empirical model and the literature could be due to the differences in the rheology of the solutions. Shear-thinning solutions are used in the current study compared to Newtonian solutions used in the literature. Another important difference between the current study and the literature is that, while the semi-empirical model follows Region I, the data in the literature shows a transition from Region I to Region II. Even though the plot obtained from the curve-fit based on Equation 8.1 qualitatively matches with the plot obtained using the visco-capillary model of Higgins and Scriven [59], the dimensionless minimum wet thickness values are over-predicted for the same capillary number. This is to be expected because in the study by Higgins and Scriven, vacuum is applied behind the upstream die lip resulting in higher coating speeds and smaller wet thicknesses for the same flow rate.

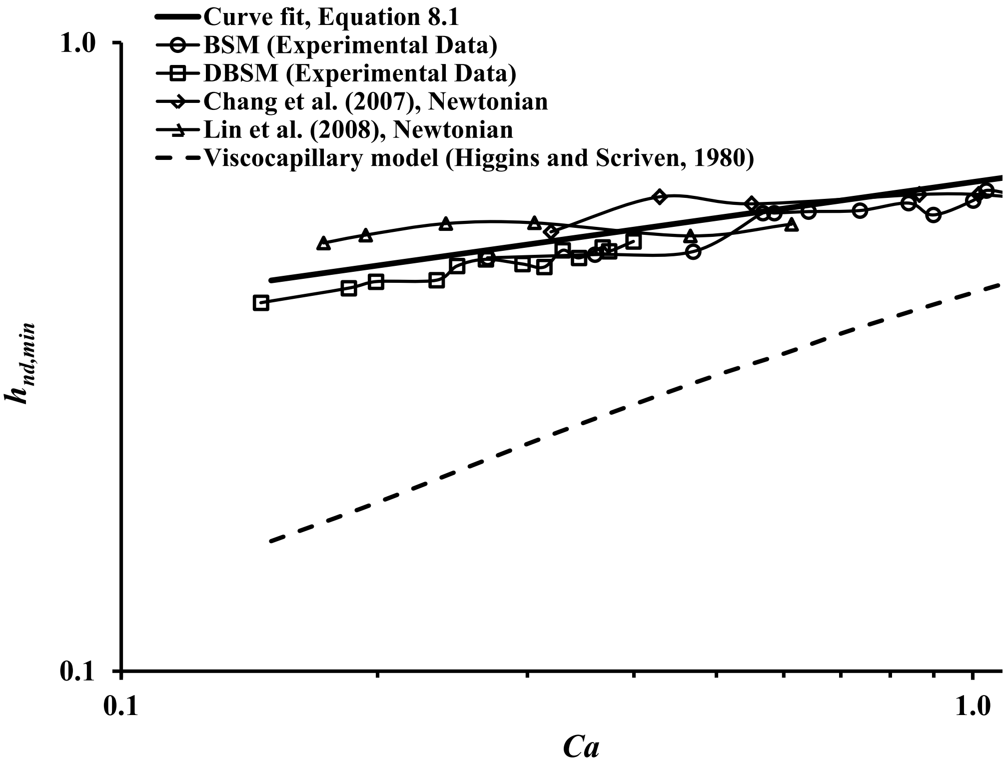

Figure 8.5: Validation of the semi-empirical relation, Equation 8.1, with experiments and literature.

Based on the aforementioned findings, the semi-empirical relation obtained from the DOE (Equation 8.1) can be successfully used to predict the minimum wet thickness. However, the semi-empirical model is subject to the following constraints:

- The maximum value for the dimensionless minimum wet thickness, $h_{nd,min}$ has to be equal to or below a value between 0.55 and 0.6. For instance, due to this constraint, the semi-empirical model under-predicts the data by Lee et al. [69], and Chang et al. [65], who performed experiments using Newtonian solutions and predicted the maximum dimensionless minimum wet thicknesses to occur above 0.6 (curve not explicitly shown here);

- For the entire set of simulations performed using DOE, the minimum capillary number used is 0.15. The validity of the model below this minimum has to be investigated, which is not performed in the current study. The maximum capillary number is 1.2. Thus the capillary number is constrained between 0.15 and 1.2;
- The dimensionless minimum wet thickness, $h_{nd,min}$ either follows Region I or falls in the transition between Region I and Region II.

As discussed in Chapter 2, according to Chang et al. [100], the location of the downstream meniscus dictates the region that the minimum wet thickness follows. For Region I, the downstream meniscus should creep up the downstream die away from the end of the downstream die lip. Similar observations were made in the current study. For example, the contours (shown in Figures 8.6 (a) through 8.6 (c)) of the coating solution volume fraction for $W = 0.25$ mm, $H = 0.25$ mm and $T = 160$ °C and for three different flow rates per unit width, Q', at the limit of air entrainment shows the meniscus creeping up the downstream die lip.

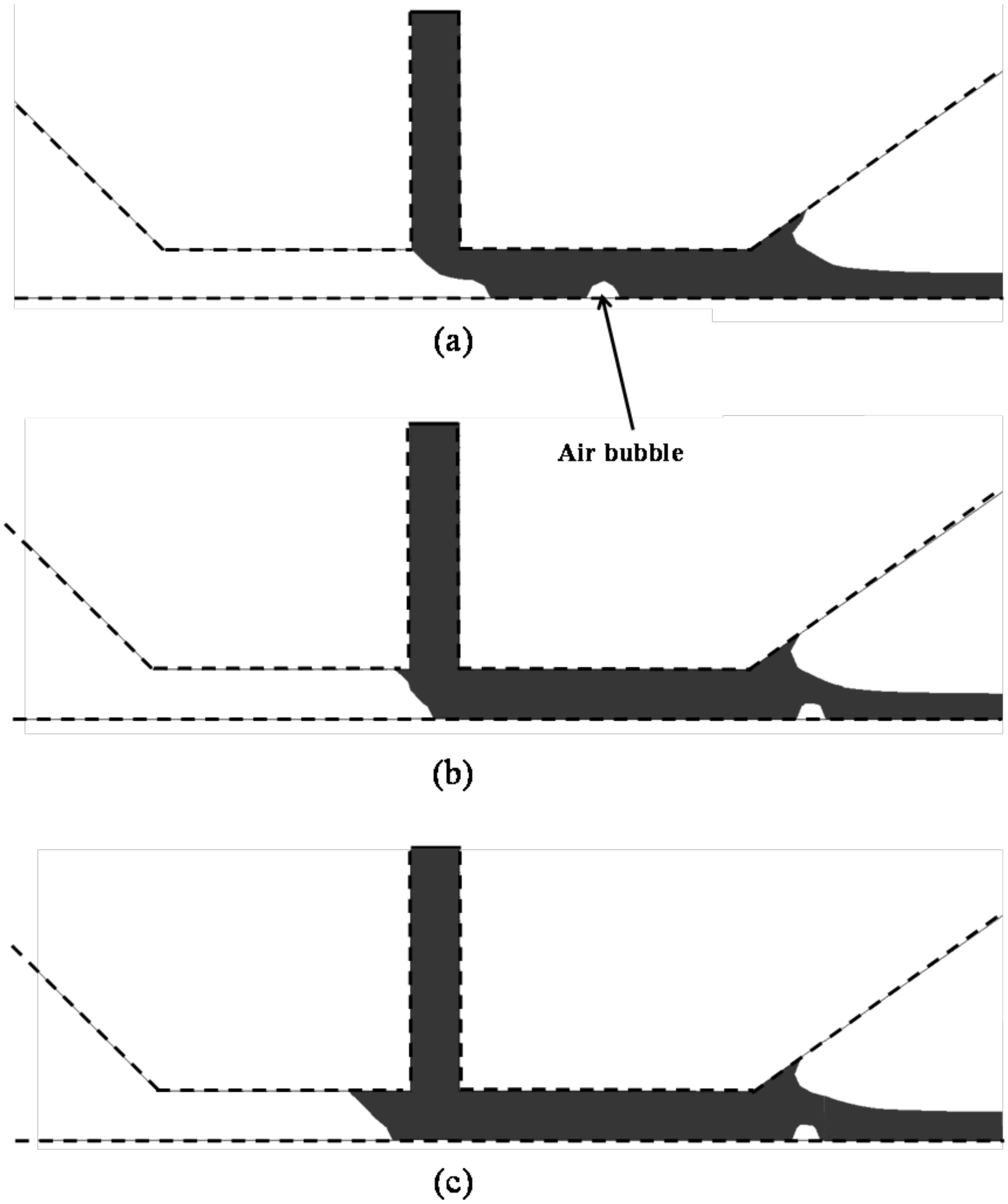

Figure 8.6: Contours of the coating solution volume fraction in the side (sectional) view at W = 0.25 mm, H = 0.25 mm and T = 160 °C (a) Q' = 0.50 mm^3/mm-s, $u_{w, max}$ = 3.9 mm/s, (b) Q' = 1.00 mm^3/mm-s, $u_{w, max}$ = 7.4 mm/s, (c) Q' = 1.50 mm^3/mm-s, $u_{w, max}$ = 10.2 mm/s.

Figure 8.7 presents the variation of dimensionless minimum wet thickness as a function of Reynolds number, *Re* in both logarithmic and linear scale. For a given minimum wet thickness, it is found that the Reynolds number increases as the processing temperature increases (viscosity decreases). This is because in addition to processing at higher substrate speeds, higher flow rates are feasible for low-viscosity solutions as shown in Figure 8.2. In addition, as the Reynolds number is a ratio of the inertial force experienced by the fluid exiting the slot die to the viscous force experienced by the fluid at the moving substrate, relatively lower viscous forces experienced by low viscosity solutions results in higher Reynolds numbers. Therefore, to obtain a desired wet thickness for the coated film, higher flow rates and substrate speeds are needed for low-viscosity solutions. This implies that it is advantageous to work with low-viscosity solutions for faster manufacturing rates. Another means for garnering smaller viscous forces or larger Reynolds numbers is by increasing the coating gap, which is why the runs performed with larger coating gaps are shifted towards the right (higher Reynolds numbers). Based on the observation that the minimum wet thickness increases with increasing *Re*, it can be deduced that for any given solution, the minimum wet thickness increases with decreasing apparent viscosity (lower viscous force) when the inertial force term remains constant.

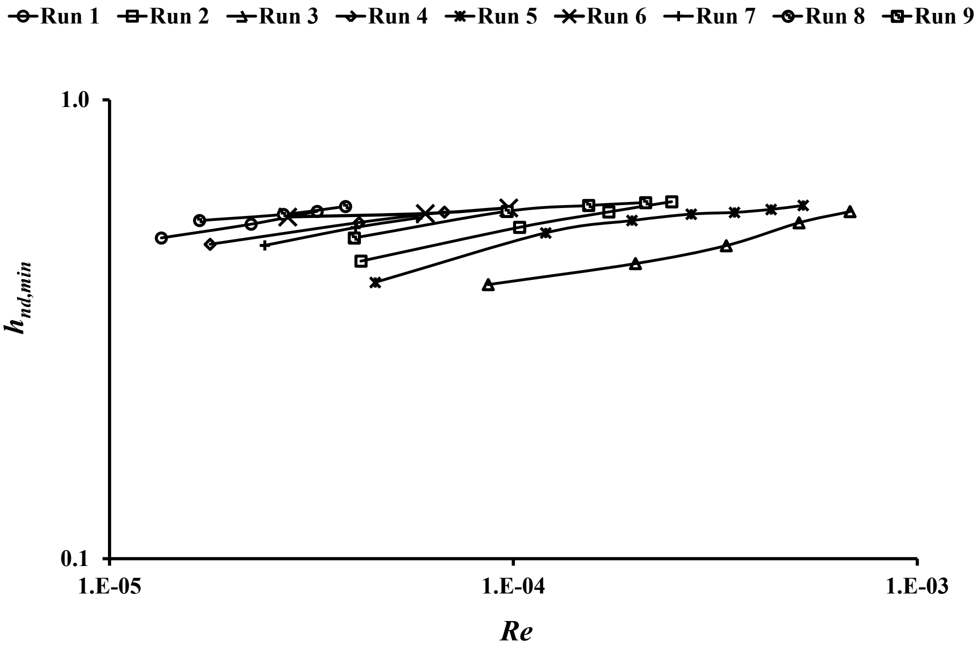

(a)

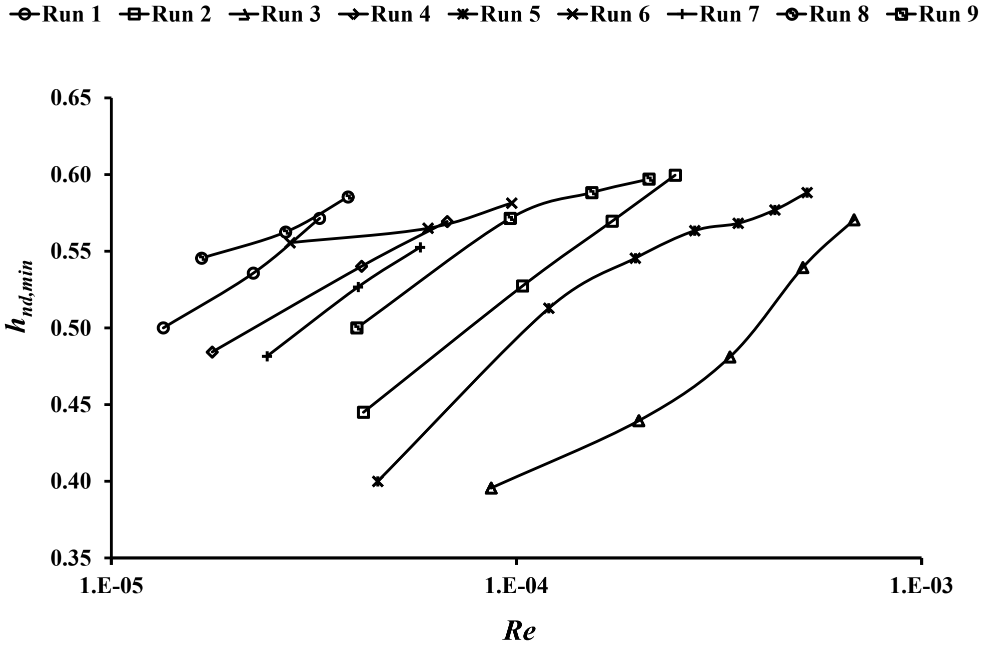

(b)

Figure 8.7: Dimensionless minimum wet thickness versus Reynolds number (a) Logarithmic scale, (b) Linear scale.

True non-dimensionality does not exist between dimensionless minimum wet thickness and the Reynolds number because, from Figure 8.7, it can be seen that the variation of dimensionless minimum wet thickness with Reynolds number is a function of geometric and processing conditions. True non-dimensionality in this study means that if a curve is fitted between two non-dimensional numbers, then the curve-fit equation should be applicable regardless of the actual values of the parameters appearing in the equation as long as the constraints under which the equation is valid are met. This fact regarding the absence of true non-dimensionality can also be deduced from Figure 8.8, which illustrates the comparison between data from the current DOE study and data from experiments on BSM, DBSM, and literature. One set of data points is chosen from each of the studies for comparison. For the numerical data using PPA/PBI solution from the current study, Run 3 is chosen and for experimental data employing BSM and DBSM solutions, the same geometric conditions as Run 3 (W = 0.178 mm, H = 0.25 mm) are chosen. The data for Chang et al._1 [100] corresponds to a viscosity of 0.05 Pa-s and W = H = 0.20 mm and for Chang et al._2 [65] corresponds to a viscosity of 0.3 Pa-s and W = H = 0.20 mm. These selections are chosen such that the geometric and processing parameters from the current study correspond to the maximum Reynolds numbers possible, while the data from literature is chosen pertaining to the minimum Reynolds numbers. In spite of the selection, the lowest Reynolds numbers obtained in the literature is about 3 to 5 orders greater than the Reynolds numbers from the current study. Albeit, the results from Figure 8.8 are consistent with results from Figure 8.7, suggesting that lower viscosity solutions are shifted to higher Reynolds numbers.

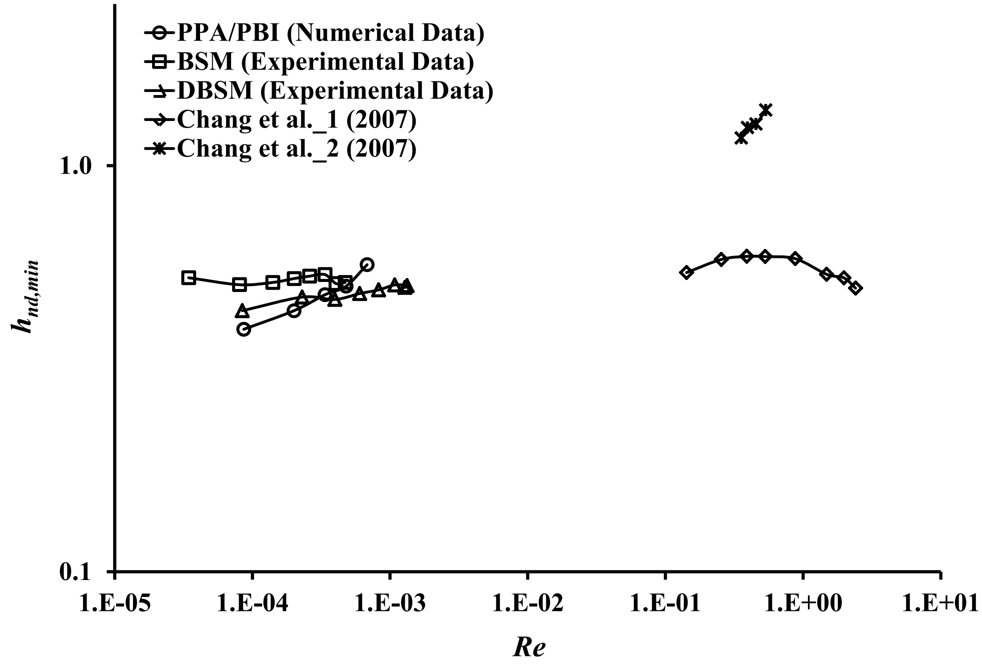

Figure 8.8: Comparison of numerical data for PPA/PBI solution with experiments for DBSM and BSM, and literature.

The other important dimensionless number is the Stokes number, which characterizes the ratio of gravitational force experienced by the coating fluid in the coating gap to the viscous force experienced at the substrate. Figure 8.9 shows that the dimensionless minimum wet thickness decreases with increasing Stokes umber. So, for any given set of geometrical parameters, the minimum wet thickness decreases with decreasing viscosity, if the density of the solution is maintained constant. Similar to Reynolds number, true non-dimensionality between the dimensionless minimum wet thickness and Stokes number does not exist. Again, this conclusion is further confirmed when compared with the results from Chang et al. [65]. In their study, owing to the use of relatively low-viscosity solutions, the Stokes numbers obtained varied between 0.001 and 0.1, which are much higher than the values in the current study.

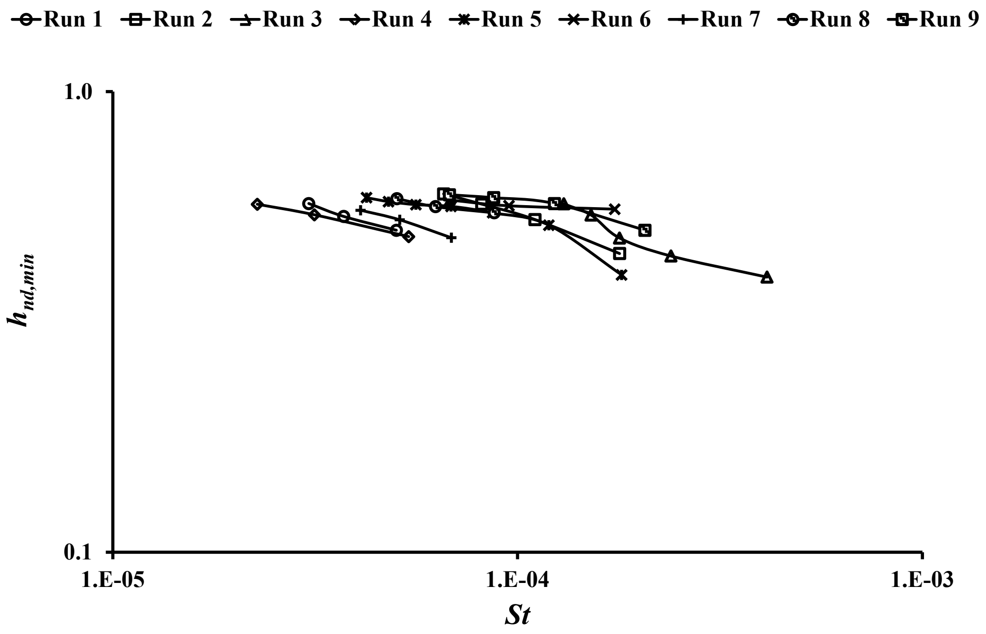

(a)

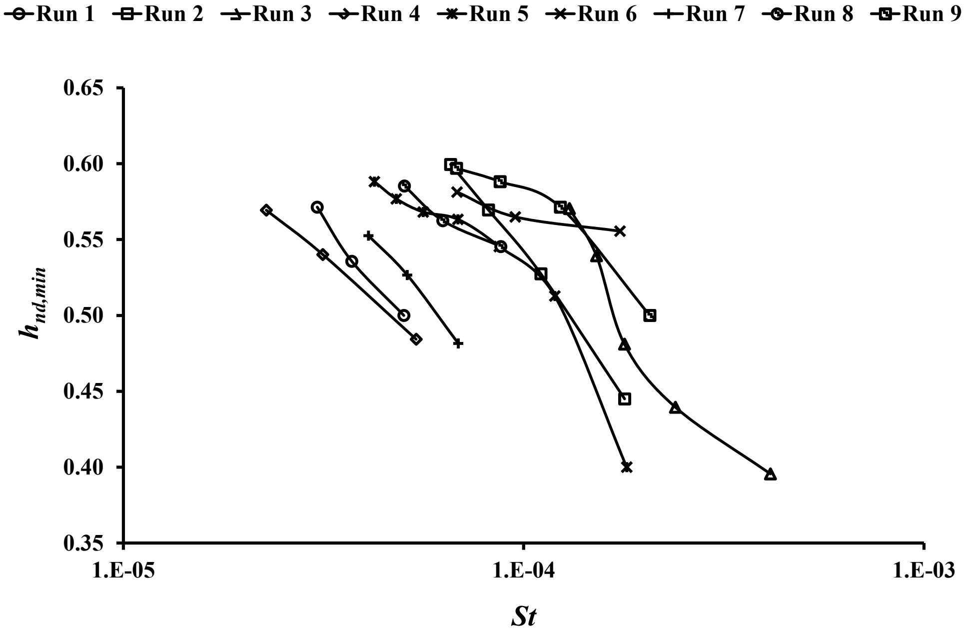

(b)

Figure 8.9: Dimensionless minimum wet thickness versus Stokes number (a) Logarithmic scale, (b) Linear scale.

As depicted in Figures 8.10 through 8.12, the other three dimensionless numbers; Weber number (ratio of inertial forces to surface tension forces), Froude number (ratio of inertial forces to gravitational forces), and Bond number (ratio of gravitational forces to surface tension forces) are found to have no unique relationship with the dimensionless minimum wet thickness. Even though a common correlation that is valid over a wide range of parameters cannot be deduced between the dimensionless minimum wet thickness and the other five dimensionless numbers (all dimensionless numbers listed in Table 3.2 except capillary number), the plots are useful for extracting information pertaining to the effect of various parameters on the dimensionless minimum wet thickness. The following conclusions can be made from the plots:

- The dimensionless minimum wet thickness varies proportionally with the Weber number, which implies that for a solution experiencing a certain inertial force, the dimensionless minimum wet thickness increases by decreasing the surface tension of the solution. A similar effect can be obtained by increasing the coating gap, while keeping the surface tension constant.
- In spite of some minor differences, the variation of the dimensionless minimum wet thickness with the Froude number has characteristics similar to the Weber number plot.
- It can be seen from the Bond number plot (Figure 8.12), that the dimensional minimum wet thickness is independent of the Bond number for a given solution at a given coating gap. This has to be expected because the gravitational force experienced by the solution in the coating gap is independent of the surface tension force acting at the fluid-air interface. In addition, as the Bond number

decreases (when density or coating gap or both decrease or surface tension increases), the variation in dimensionless minimum wet thickness decreases.

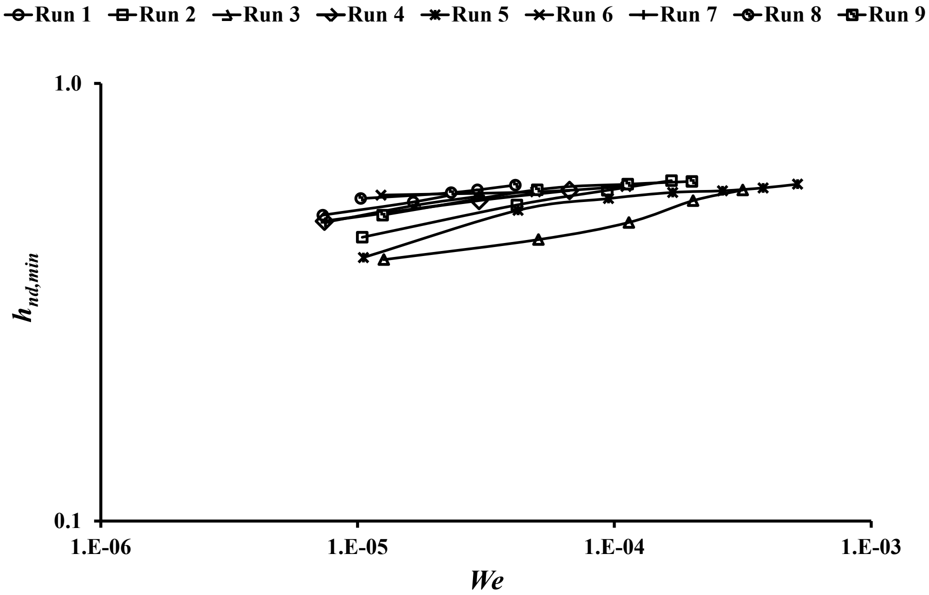

(a)

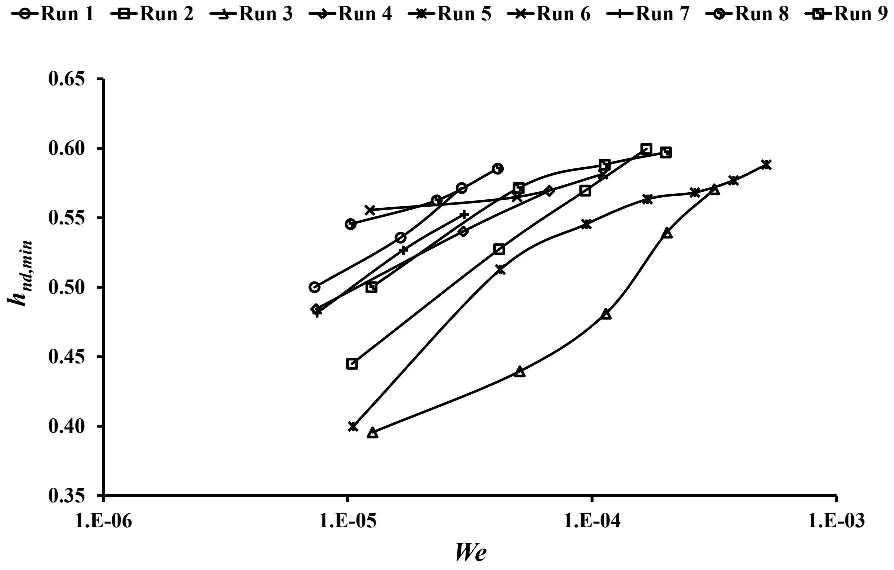

(b)

Figure 8.10: Dimensionless minimum wet thickness versus Weber number (a) Logarithmic scale, (b) Linear scale.

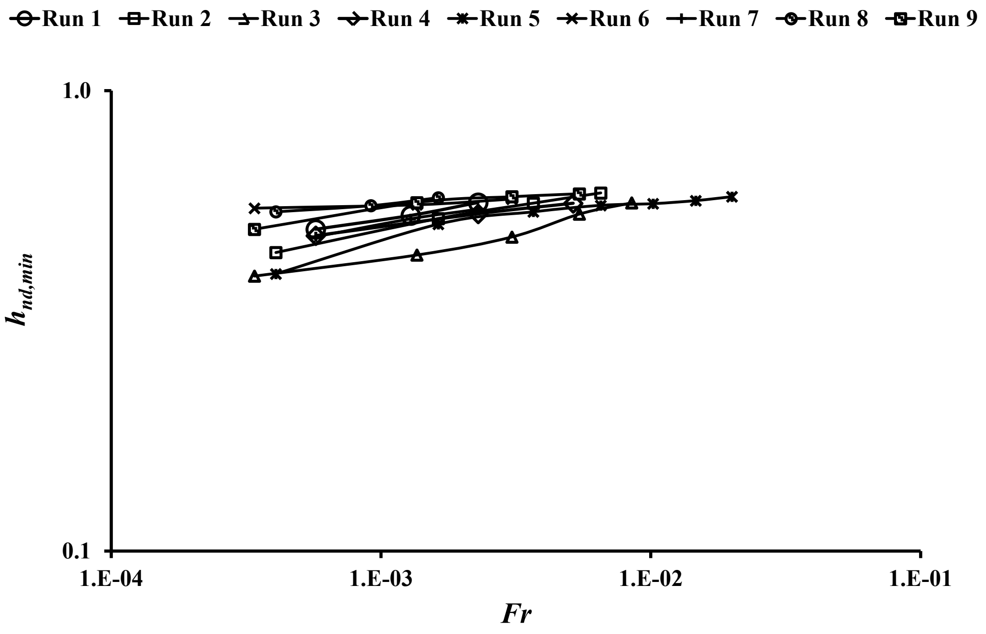

(a)

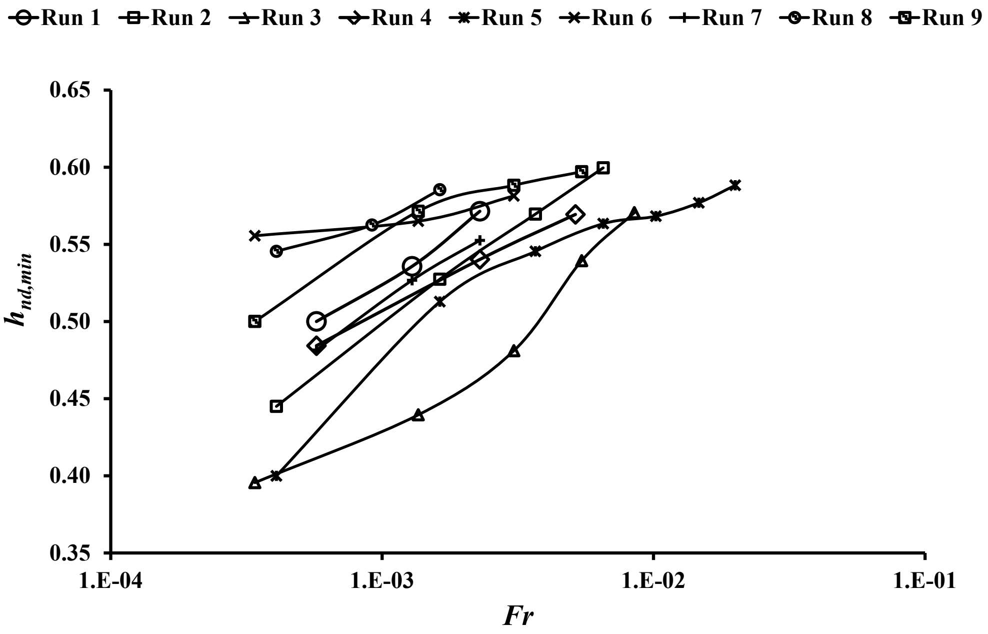

(b)

Figure 8.11: Dimensionless minimum wet thickness versus Froude number (a) Logarithmic scale, (b) Linear scale.

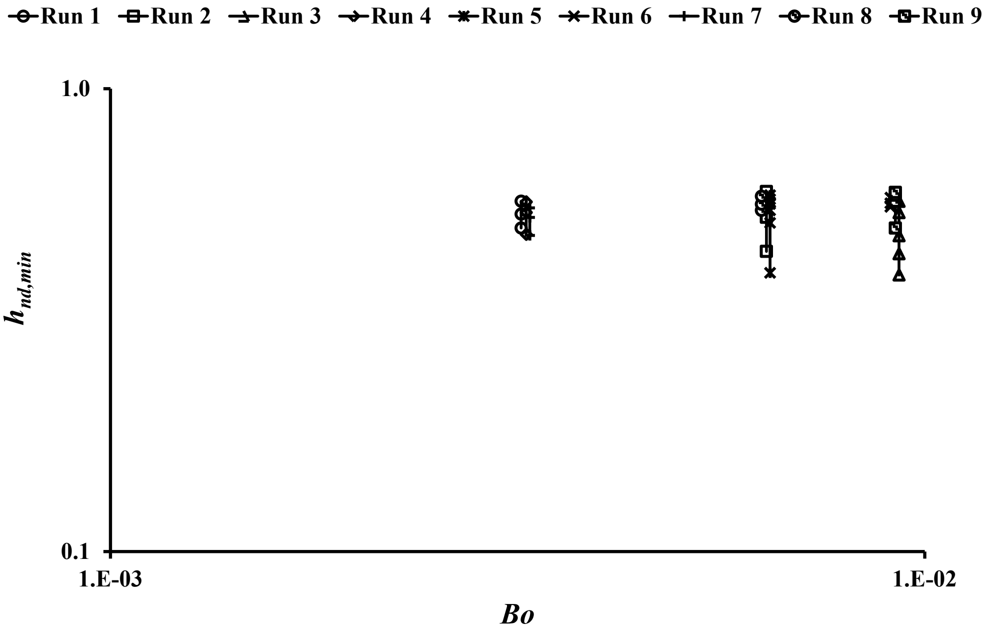

(a)

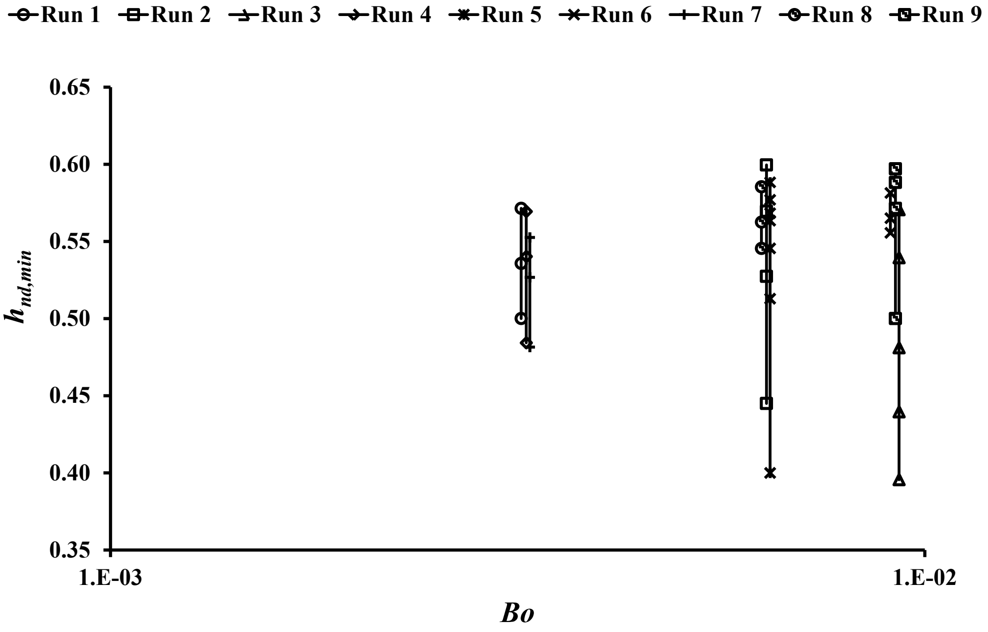

(b)

Figure 8.12: Dimensionless minimum wet thickness versus Bond number (a) Logarithmic scale, (b) Linear scale.

8.3 Effect of Geometric and Processing Parameters on Air Entrainment Velocity of PPA/PBI Solution

Based on the analysis in Section 8.2, within certain constraints, Equation 8.1 can be used to predict the dimensionless minimum wet thickness for a given capillary number within ±10% accuracy for shear-thinning solutions within a viscosity range of 1 to 40 Pa-s. However, Equation 8.1 in its dimensionless form is less desirable. Rather, an equation explicit in maximum coating speed is more appropriate. By substituting $h_{nd,min} = \left(Q^{'}/u_{w,max}\right)/H$, and $Ca = \frac{k(u_w/H)^{n-1}u_w}{\sigma}$ in Equation 8.1 and re-arranging terms, Equations 8.2 and 8.3 (an explicit equation for maximum coating speed, $u_{w,\,max}$) are obtained.

$$\frac{\left(Q^{'}/u_{w,max}\right)}{H} = 0.6\left[\frac{k(u_w/H)^{n-1}u_w}{\sigma}\right]^{0.20} \tag{8.2}$$

$$u_{w,max} = \left[\frac{Q^{'}H^{0.20n-1.20}}{0.6}\left(\frac{\sigma}{k}\right)^{0.20}\right]^{\frac{1}{1+0.20n}} \tag{8.3}$$

Equation 8.3 is a semi-empirical relation deduced from this study to effectively predict the maximum coating speed of a shear-thinning fluid within a viscosity range of 1 - 40 Pa-s and coating speed range of 1 mm/s to 15 mm/s. Beyond these limitations additional work is required to ensure the validity of the model, which is not done in this study. This model is particularly useful for determining the manufacturing processing conditions (e.g., substrate speed, coating gap, or flow rate per unit width) corresponding to a maximum coating limit. In order to use the semi-empirical relation, several parameters must be determined or specified, since the semi-empirical relation is defined by six parameters: $u_{w,max}$, Q', H, k, n and σ. The desired maximum coating speed is generally set by the manufacturer. The material properties, k, n and σ, of the solution used in the coating process can be deduced from the results of data obtained using or measured directly with standard laboratory equipment, e.g., rheometer or goniometer. If the desired maximum coating speed results in material processing behavior that obeys the constraints imposed on the semi-empirical model, as discussed in Section 8.2, then an equation for that given solution can be obtained in terms of Q' or H. Since, both the parameters can be controlled by the manufacturer, if one of the parameters is fixed, then the remaining parameter can be calculated from Equation 8.3 for the solution of interest.

Based on the excellent comparison between the predictions from Equation 8.1 and the data obtained by Chang et al. [100] and Lin et al. [67] using Newtonian solutions, Equation 8.3 might be used in certain cases to even predict the maximum coating speed of Newtonian solutions by substituting power-law index, n equal to1 and the consistency index, k equal to the dynamic viscosity of the coating solution. This is because when the dynamic viscosity of a Newtonian solution is expressed using the power-law form, then n becomes 1 and k equals the dynamic viscosity. However, based on the observations presented in Section 8.2 that Equation 8.1 fails to predict the trends for Newtonian solutions in other cases, the range of parameters within which Equation 8.1 is valid needs to be found. This is not addressed in the current study.

All the parameters are expected to have the opposite effect on the maximum coating speed when compared to their effects on dimensionless minimum wet thickness since for a given Q', the dimensionless minimum wet thickness is inversely proportional to the maximum coating speed as given by Equation 8.2. In the following subsections, the quantitative effect of each of the variables on maximum coating speed along with the qualitative effect on air entrainment phenomenon are discussed. The study is performed by analyzing the variation of maximum coating speed, $u_{w,max}$ with respect to each of the variables (H, W, k, n andσ) for various flow rates, Q'. Since Q' is obtained from the product of average inlet velocity, v_{in}, and the slot gap, W, the effect of flow rate per unit width can also be treated as the effect of average inlet velocity when the slot gap is constant.

8.3.1 Effect of Slot Gap

From Equation 8.3, it is evident that there is no direct correlation between the maximum coating speed, $u_{w,\ max}$, and the slot gap, W. However, the effect of slot gap indirectly enters into the equation through the flow rate per unit width, Q' term, because $Q' = W \times v_{in}$, where v_{in} is the average inlet velocity. Thus, for any given flow rate per unit width, Q', as W changes v_{in} through the slot die adjusts accordingly such that the product of slot gap and average inlet velocity remains constant. Hence, the effect of slot gap on the maximum coating speed should be negligible. To test this hypotheses, simulations are performed at coating gap, $H = 0.30$ mm and the three slot gaps, $W = 0.178$ mm, 0.25 mm, and 0.30 mm using PPA/PBI solution at 160 °C. The flow rate per unit width, Q', is varied from 0.10 mm^3/mm-s to 1.50 mm^3/mm-s. The results are plotted in Figure 8.13. The data obtained using Equation 8.3 (solid black line) are also plotted along with the discrete data points from the simulation.

From Figure 8.13, it can be seen that the maximum coating speed is independent of the slot gap. Similarly, the finding that the effect of slot gap is negligible implies that there is no effect of inertia forces on the maximum coating speed, which is consistent with the findings of Lee et al. [69]. But as higher flow rates are approached, a maximum coating speed exists only for larger slot gaps. At smaller slot gaps, the end of the coating window is reached earlier as dripping begins because the velocity of solution forced out of the slot die is relatively higher.

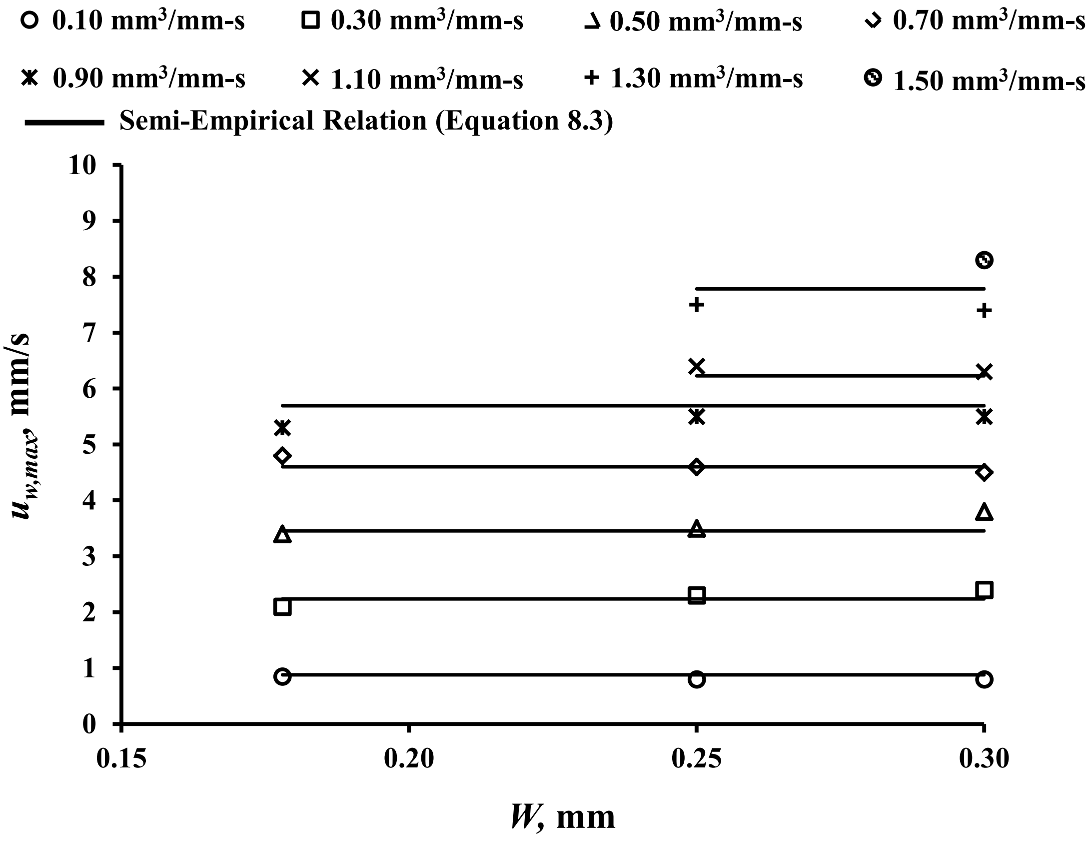

Figure 8.13: Effect of slot gap, *W*, on the maximum coating speed, $u_{w,max}$ for various flow rates per unit width, *Q'* at *H* = 0.30 mm and *T* = 160 °C. The discrete data points represent the simulation results, while the solid lines are obtained from Equation 8.3.

Figure 8.14 shows the contours of PPA/PBI solution's volume fraction at the air entrainment boundary for the three different slot gaps at $Q' = 0.70$ mm^3/mm-s and $T = 160$ °C. For every slot gap, four different images are taken during different times of the coating process. The die lip boundaries are superimposed on the images using dashed lines to show the relative position and size of the sawteeth. The images show that while there is no significant difference in the length of the sawteeth between the three cases, the width of the sawteeth and the average width of the bubbles increased as the slot gap increased. These trends are consistent with the results in Chapter 7, where the test solutions exhibited similar behavior. Therefore, even though the inertia forces have no impact on the maximum coating speed, their effect is realized in the sizes of sawteeth and in turn on the size of the bubbles. As larger bubbles are detrimental to the durability of the membrane; it is beneficial to operate at smaller slot gaps so that even if small bubbles are present, they may be able to more readily dissolve.

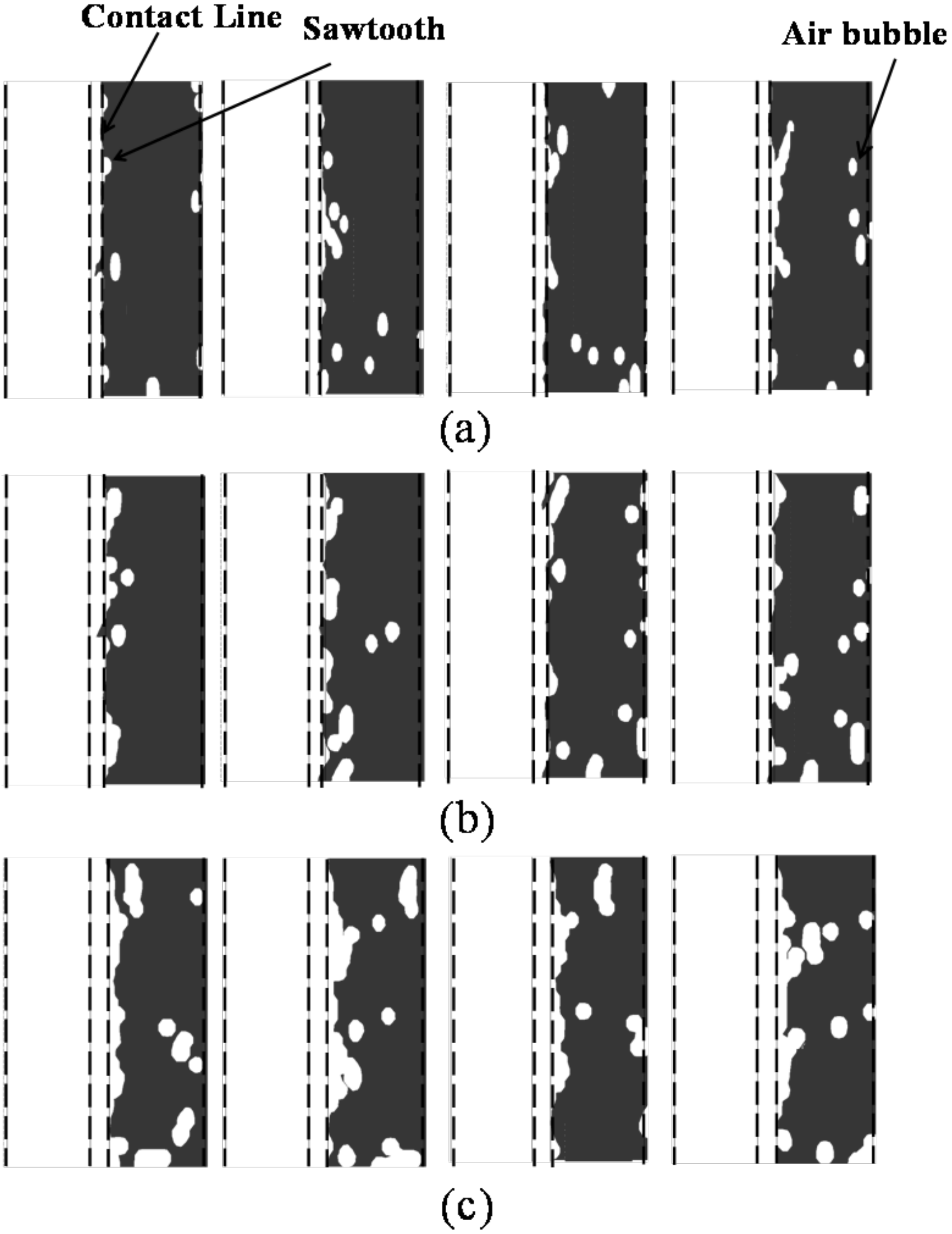

Figure 8.14: Effect of slot gap, *W*, on the sizes of the sawteeth and the air bubbles at the air entrainment boundary for PPA/PBI solution at *T* = 160 °C, *H* = 0.30 mm and *Q'* = 0.70 mm^3/mm-s, dashed lines represent boundaries of die lips (a) Images from the simulation for *W* = 0.178 mm and $u_{w,max}$ = 4.70 mm/s, (b) Images from the simulation for *W* = 0.25 mm and $u_{w,max}$ = 4.65 mm/s, (c) Images from the simulation for *W* = 0.30 mm and $u_{w,max}$ = 4.60 mm/s.

8.3.2 Effect of Coating Gap

The maximum coating speed, $u_{w,\ max}$, varies inversely with the coating gap, H, as shown in Figure 8.15, which is consistent with the results of Lee et al. [69] and Chang et al. [65, 100]. The data in Figure 8.15 are for PPA/PBI solution at W = 0.178 mm, T = 140 °C and Q' ranging from 0.18 mm^3/mm-s to 0.81 mm^3/mm-s. The advantage of using a smaller coating gap on a power-law fluid is two-fold:

- As the fluid is dragged through a smaller coating gap, the power-law behavior of the fluid causes the viscosity of the PPA/PBI solution to decrease, which in turn postpones the air entrainment.
- The capillary forces driven by surface tension are stronger in smaller coating gaps, thus stabilizing the contact line.

On the other hand, as dripping is delayed due to the ability to accommodate more solution, a larger coating gap can be used to operate at higher flow rates. Also, for larger coating gaps, the data from Table 8.3 show that a wide range of thicknesses can be obtained for the same geometric conditions just by changing the flow rate through the slot die. From these observations, the following conclusions can be made:

- If the films must be coated at a faster rate, then one should operate at smaller coating gaps.
- If the priority is to obtain a wide range of thicknesses for the same set of geometrical parameters, then larger coating gaps are desirable.

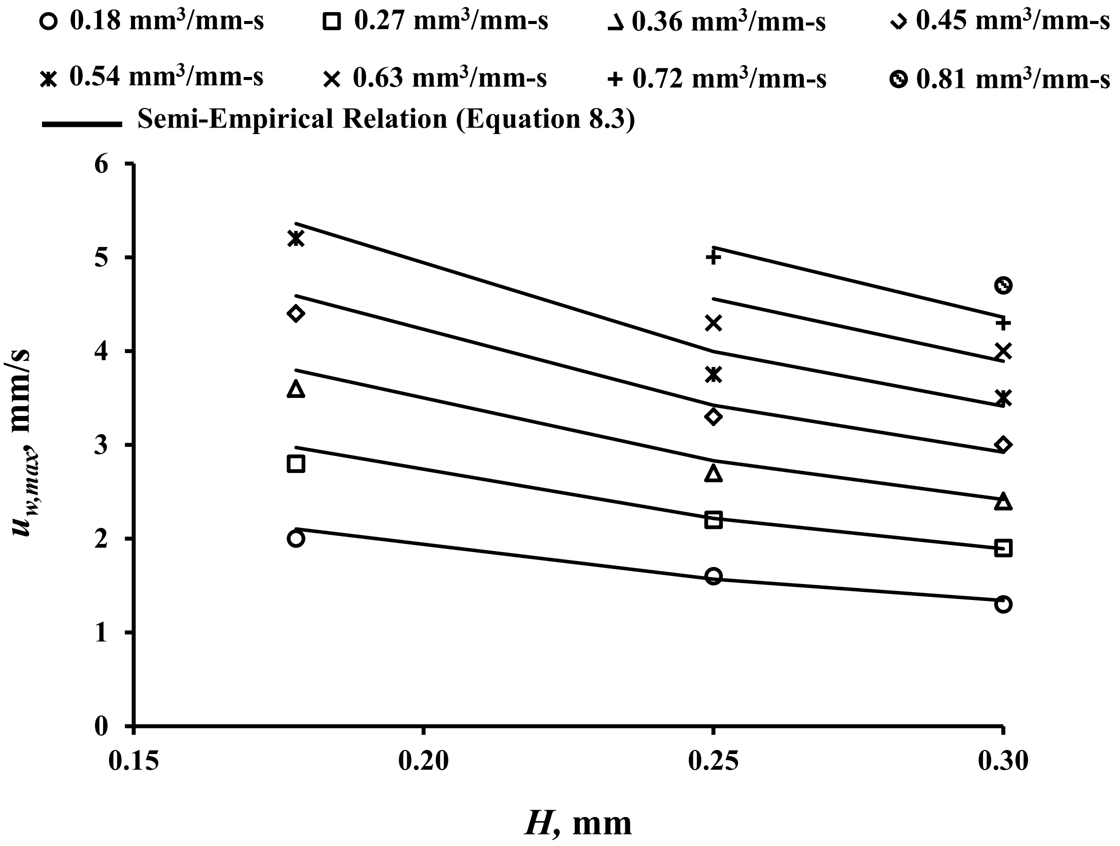

Figure 8.15: Effect of coating gap, *H*, on the maximum coating speed, $u_{w,max}$ for various flow rates per unit width, *Q'* at *W* = 0.178 mm and *T* = 140 °C. The discrete data points represent the simulation results, while the solid lines are obtained from Equation 8.3.

The contours of the volume fraction of PPA/PBI solution at T = 140 °C, W = 0.178 mm, Q' = 0.36 mm^3/mm-s and air entrainment boundary are shown in Figure 8.16. Similar to the trends seen for the test solutions in Chapter 7, as the coating gap increases, the length and width of the sawteeth increase. However, due to the relatively higher viscosity of the PPA/PBI solution at 140 °C compared to DBSM, the sawteeth and the bubbles are not as large. As the coating gap increases, the maximum coating speed decreases causing a reduction in the stresses experienced by the coating solution, which causes a delay in enclosing the air pocket. This results in the spreading of the air pocket over a larger area before pinch-off occurs.

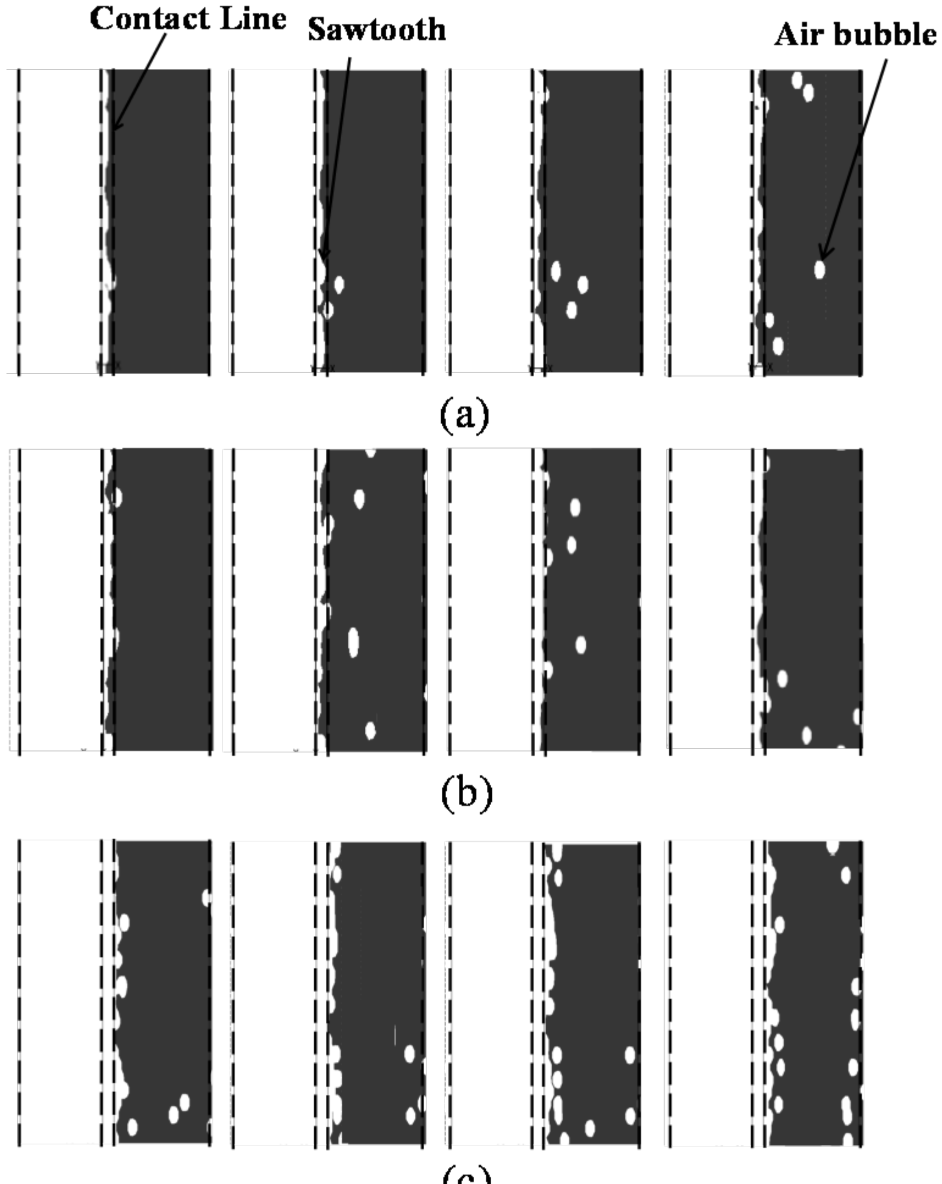

Figure 8.16: Effect of coating gap, *H*, on the sizes of the sawteeth and the air bubbles at the air entrainment boundary for PPA/PBI solution at *T* = 140 °C, *W* = 0.178 mm and *Q'* = 0.36 mm^3/mm-s, dashed lines represent boundaries of die lips (a) Images from the simulation for *H* = 0.178 mm and $u_{w,max}$ = 3.60 mm/s, (b) Images from the simulation for *H* = 0.25 mm and $u_{w,max}$ = 2.70 mm/s, (c) Images from the simulation for *H* = 0.30 mm and $u_{w,max}$ = 2.40 mm/s.

8.3.3 Effect of Temperature

The effect of temperature on the maximum coating speed at various flow rates per unit width (0.18 mm^3/mm-s to 0.81 mm^3/mm-s) for W = 0.178 mm and H = 0.25 mm/s is depicted in Figure 8.17. As the temperature increases, the maximum coating speed increases. This effect is mainly attributed to the lower viscosity characteristics of the high temperature solution. The inverse relationship between the viscosity and maximum coating speed is demonstrated by several researchers [89, 92, 119] in the past. Even though the plot shows a maximum flow rate per unit width of 0.81 mm^3/mm-s, the maximum coating speed for the solution at 160 °C can be extended to 1.25 mm^3/mm-s, and the magnitude of the coating speed at that Q' is equal to 8.4 mm/s. The results imply that it is beneficial to operate at higher temperatures, for larger maximum coating speeds. However, more energy needs to be expended in heating the solution to higher temperatures, which may be seen as a drawback.

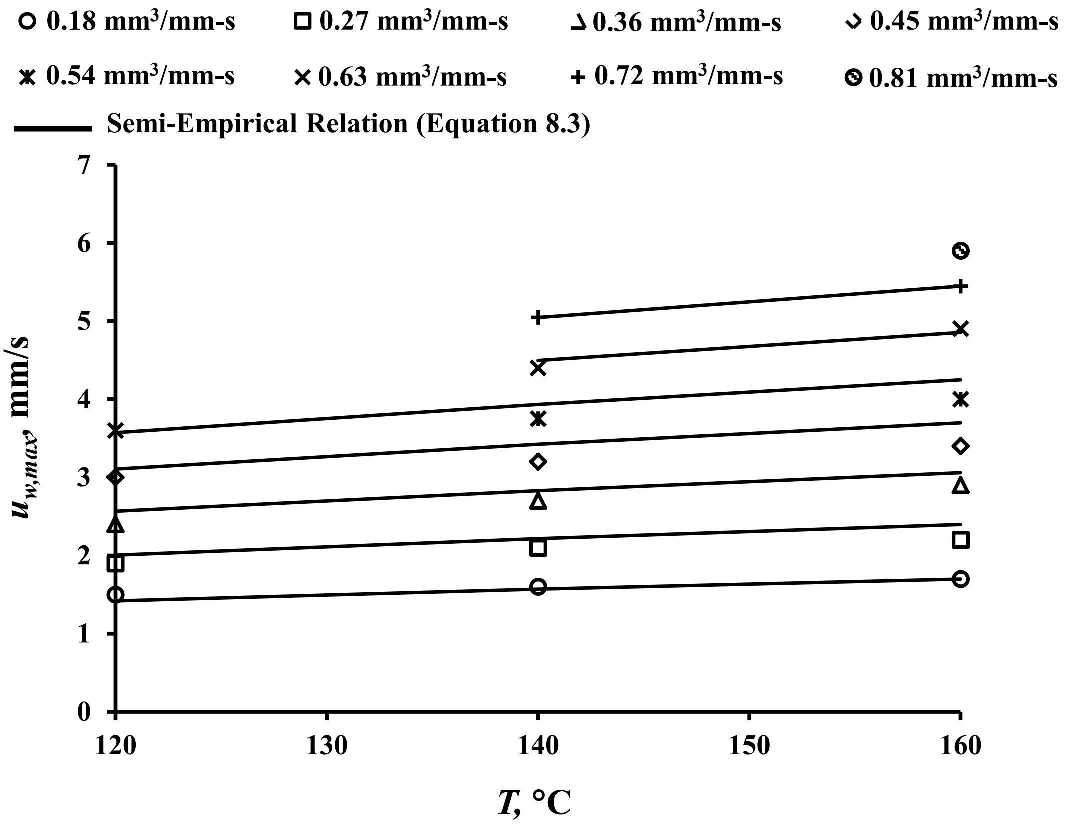

Figure 8.17: Effect of processing temperature, *T*, on the maximum coating speed, $u_{w,max}$ for various flow rates per unit width, *Q'* at *W* = 0.178 mm and *H* = 0.25 mm. The discrete data points represent the simulation results, while the solid lines are obtained from Equation 8.3.

Figure 8.18 presents the contours of PPA/PBI solution's volume fraction at air entrainment boundary for *Q'* = 0.18 mm^3/mm-s. The length and width of the sawteeth increased with the processing temperature similar to the trends seen experimentally in Chapter 7. For lower viscosity solutions, the viscous effects experienced by the air pocket at the tip takes longer to be sensed by the fluid further upstream causing the sawtooth to stretch over a larger area before the bubble pinches off. Another observation from the plots is that the differences in the sawteeth sizes between PPA/PBI solutions at 140 °C and 160 °C are less significant compared to the differences between PPA/PBI solutions at

120 °C and 140 °C. This is due to the reduced differences in the viscosity at higher temperatures.

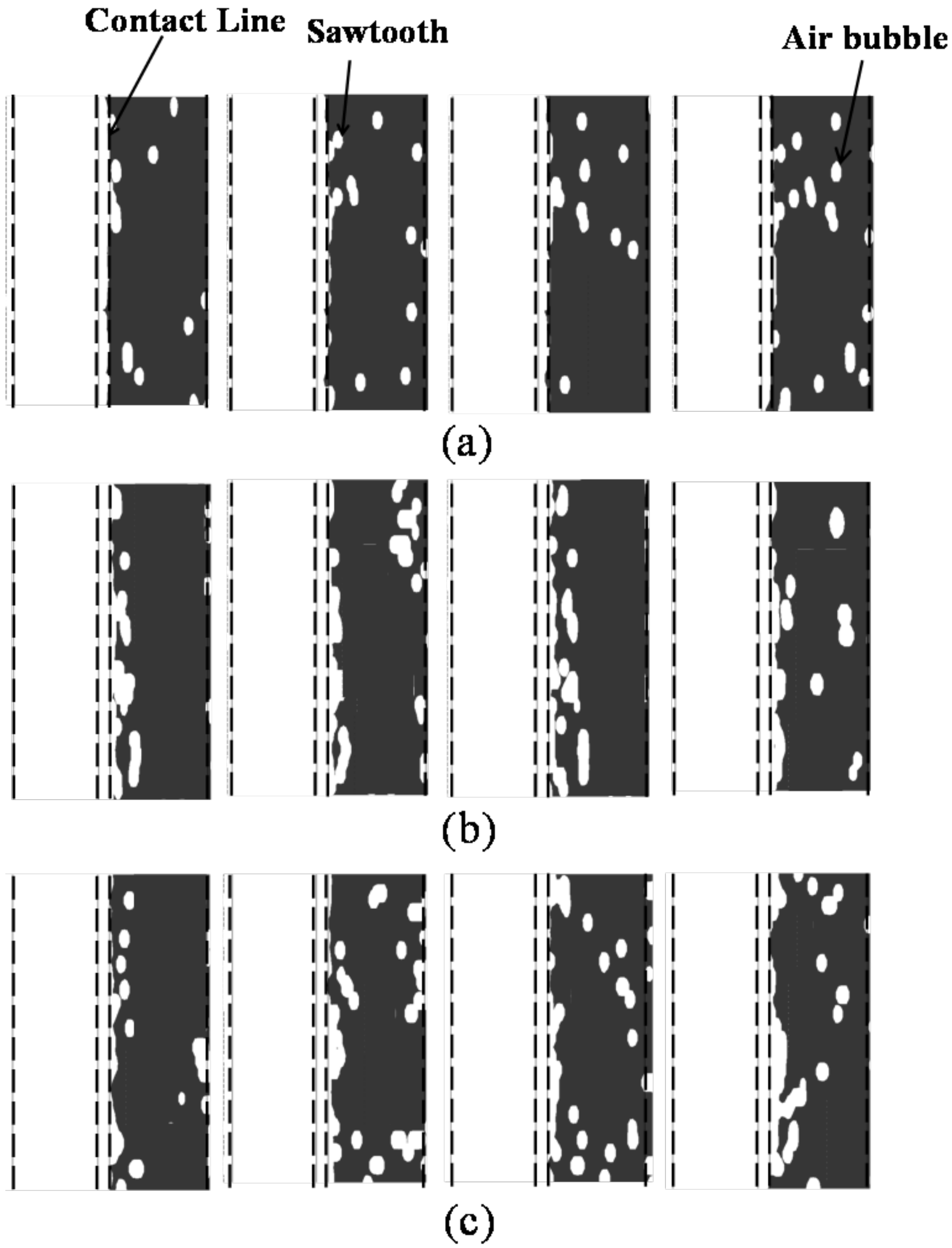

Figure 8.18: Effect of processing temperature, T, on the sizes of the sawteeth and the air bubbles at the air entrainment boundary for PPA/PBI solution at $W = 0.178$ mm, $H = 0.25$ mm and $Q' = 0.18$ mm^3/mm-s, dashed lines represent boundaries of die lips (a) Images from the simulation for $T = 120$ °C and $u_{w,max} = 1.50$ mm/s, (b) Images from the simulation for $T = 140$ °C and $u_{w,max} = 1.60$ mm/s, (c) Images from the simulation for $T = 160$ °C and $u_{w,max} = 1.70$ mm/s.

Based on the findings from this section, solutions processed at higher temperatures are advantageous in terms of achieving higher coating speeds, while the high-temperature solutions experience a setback in terms of larger bubbles arising from larger sawteeth. In addition, extra energy is required to heat the solution. From Chapter 4, it is seen that the temperature of the PPA/PBI solution impacts the properties of the solution. While the changes in the power-law index and surface tension values between the PPA/PBI solutions at 120 °C, 140 °C, and 160 °C are within 5%, significant changes are present between the consistency index values (about 50% between solutions at 120 °C and 140 °C and 40% between 140 °C and 160 °C). Therefore, the effect of the processing temperature on the maximum coating speed as depicted in Figure 8.17 can be treated as the inverse of the impact of consistency index (as temperature increased, the consistency index decreased), which is found to be significant. In the next subsections, the effects of power-law index and surface tension on the maximum coating speed are analyzed.

8.3.3.1 Effect of Power-Law Index

The maximum coating speed varies inversely with the power-law index as shown in Figure 8.19 for W = 0.30 mm, H = 0.30 mm, T = 140 °C and Q' ranging from 0.30 mm^3/mm-s to 2.40 mm^3/mm-s. Three values are considered for power-law indices; 0.50, 0.70 and 0.90. As viscosity varies as a function of $u_{w,max}^n$, the impact of the power-law index is felt more strongly at higher coating speeds corresponding to higher flow rates per unit width. Also, the plot shows that it is advantageous to work with solutions with low power-law index values, as they allow for lower viscosities and higher coating speeds. This explains why the test solutions had much higher maximum coating speeds. The effect of the power-law index on the sizes of the sawteeth structures is similar to the effect of consistency index.

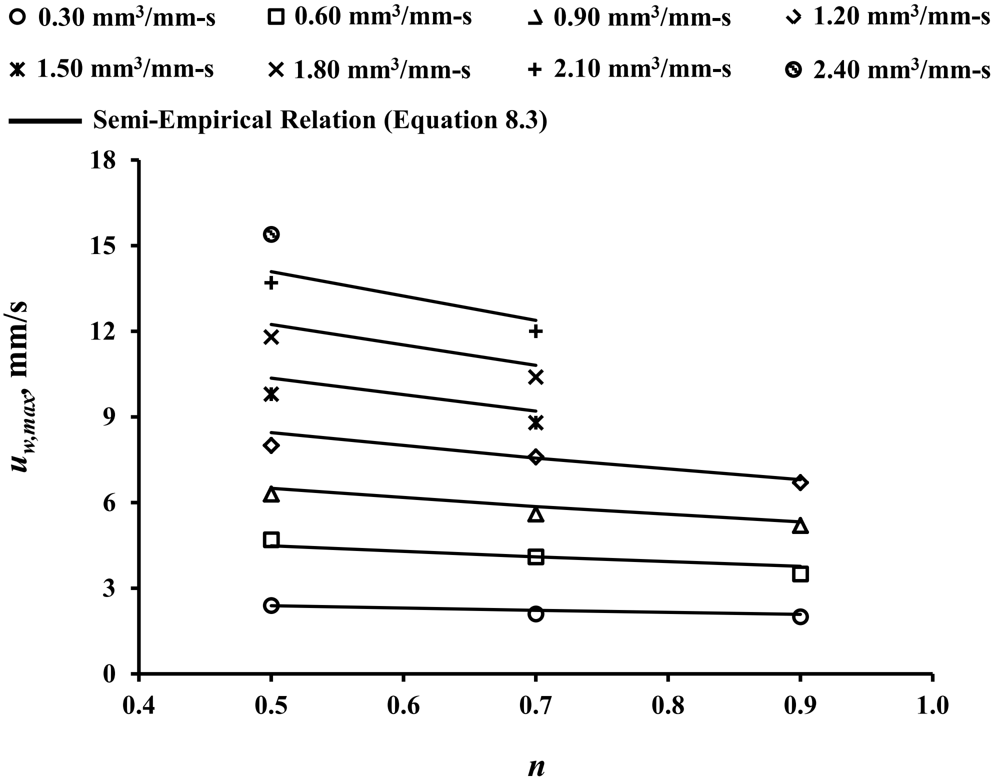

Figure 8.19: Effect of power-law index, *n*, on the maximum coating speed, $u_{w,max}$ for various flow rates per unit width, *Q'* at *W* = 0.30 mm, *H* = 0.30 mm and *T* = 140 °C. The discrete data points represent the simulation results, while the solid lines are obtained from Equation 8.3.

8.3.3.2 Effect of Surface Tension

The plot in Figure 8.20 shows the effect of surface tension on the maximum coating speed for W = 0.25 mm, H = 0.25 mm, T = 160 °C and Q' ranging from 0.25 mm^3/mm-s to 2.00 mm^3/mm-s. It can be seen that solutions with higher surface tension are advantageous since they can be coated at higher flow rates and coating speeds. This further corroborates the finding discussed earlier in Section 8.2 that to produce a stable film, the viscous forces should not dominate the surface tension forces such that the capillary number exceeds 1.2. Therefore, higher surface tension fluids provide the required stability to the film ensuring higher coating speeds. It is found from the simulations that the maximum coating speed corresponding to the fluid with a surface tension of 0.0661 N/m exceeds 15 mm/s, but the plot in Figure 8.20 is restricted to a maximum speed of 15 mm/s. These findings agree with the conclusions made by Chu et al. [70, 77], Tiu et al. [76] and Burley and Kennedy [89] that higher surface tension fluids assist in producing stable films as discussed in Chapter 2. Although, surface tension is found to impact the coating speeds, its effect on the sawteeth and bubble sizes is negligible.

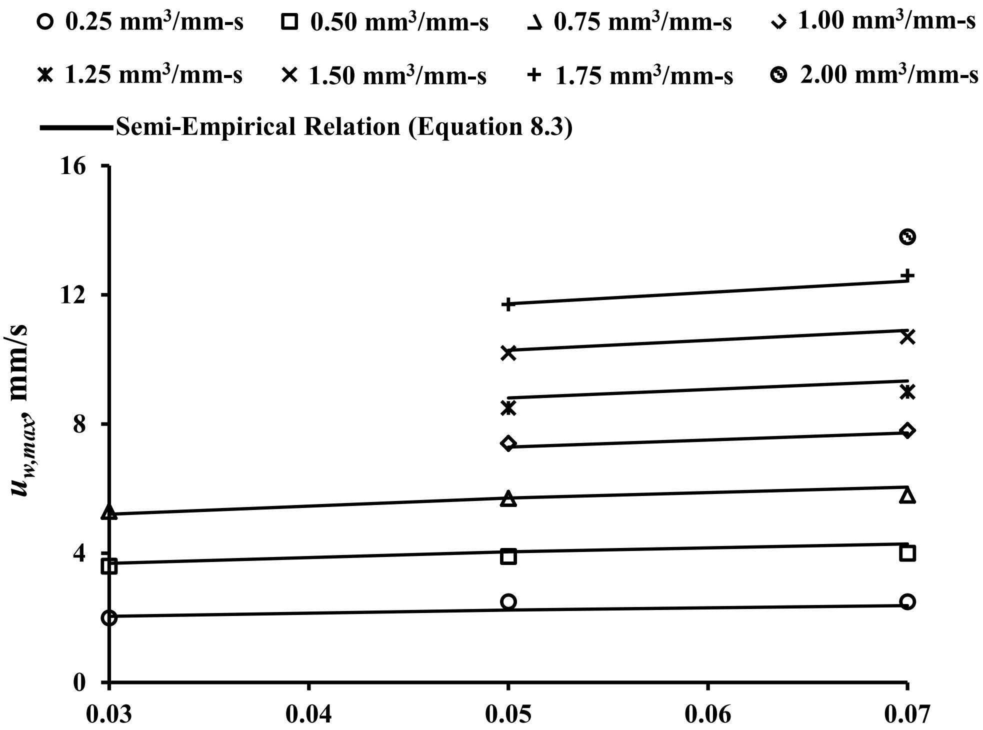

Figure 8.20: Effect of surface tension, σ, on the maximum coating speed, $u_{w,max}$ for various flow rates per unit width, Q' at W = 0.25 mm, H = 0.25 mm and T = 160 °C. The discrete data points represent the simulation results, while the solid lines are obtained from Equation 8.3.

8.3.4 Effect of Density and Slot Die/Substrate Orientation

Density and gravity are present in some of the dimensionless numbers listed in Table 3.2; however, their effects are not captured in Equation 8.3. Simulations are performed to understand the impact of density and gravity on the maximum coating speed. Density effects are studied by considering two other values, one above (2447.5 kg/m^3) and one below (1447.5 kg/m^3) the actual value (1947.5 kg/m^3). The effect of density on maximum coating speed is illustrated in Figure 8.21 for PPA/PBI solution processed at W = 0.25 mm, H = 0.25 mm, T = 140 °C and Q' ranging from 0.25 mm^3/mm-s to 1.25 mm^3/mm-s. It can be observed that density has no impact on the maximum coating speed.

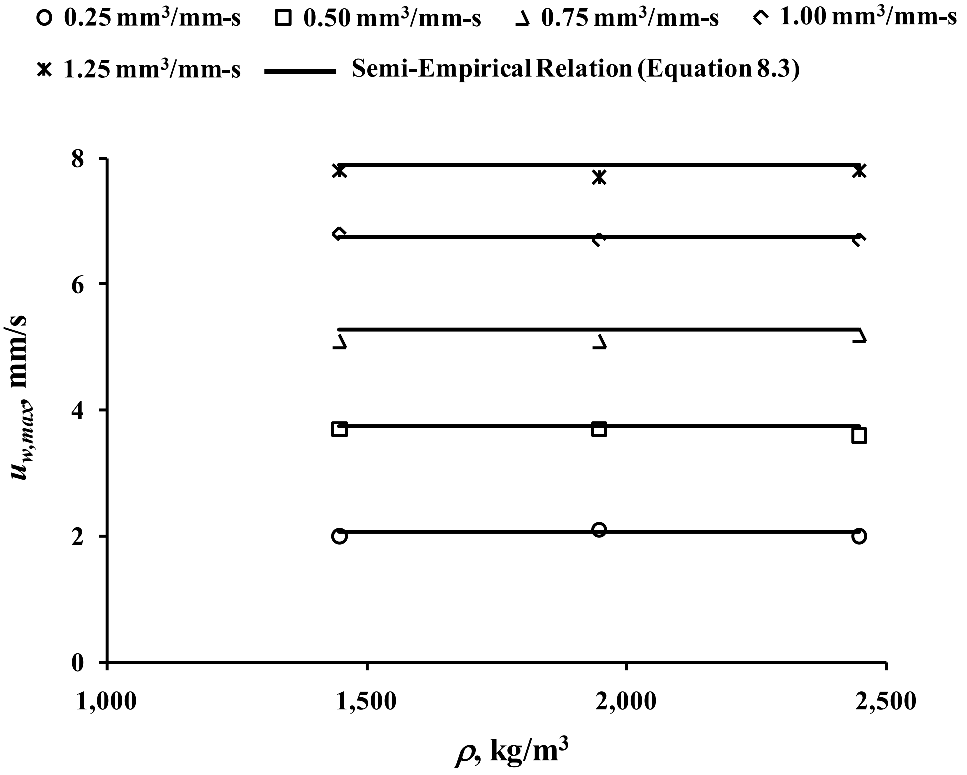

Figure 8.21: Effect of density, ρ, on the maximum coating speed, $u_{w,max}$ for various flow rates per unit width, Q' at W = 0.25 mm, H = 0.25 mm and T = 140 °C. The discrete data points represent the simulation results, while the solid lines are obtained from Equation 8.3.

The effect of gravity (effect of slot die/substrate orientation with respect to gravity) on the maximum coating speed is considered by simulating vertical coating, horizontal coating (shown in Figure 2.15) and no-gravity conditions for PPA/PBI solution processed at W = 0.30 mm, H = 0.30 mm, T = 160 °C and Q' ranging from 0.10 mm^3/mm-s and 1.50 mm^3/mm-s. It can be seen, from Figure 8.22, that gravity does not have any impact on the maximum coating speed.

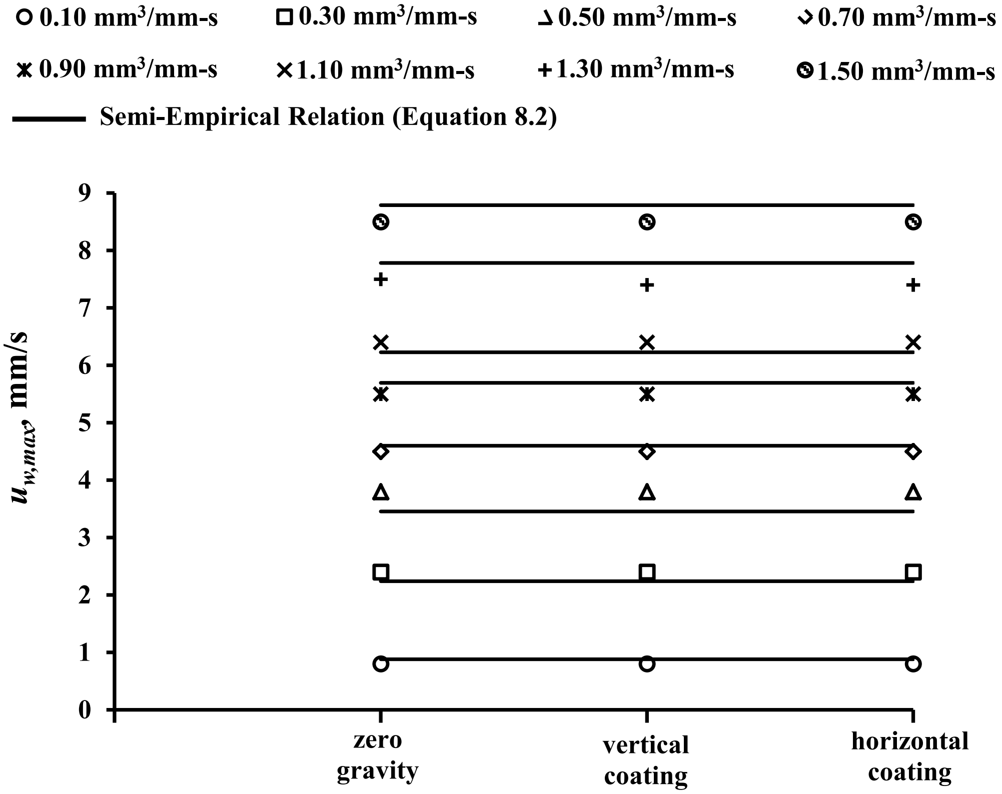

Figure 8.22: Effect of gravity, g, on the maximum coating speed, $u_{w,max}$ for various flow rates per unit width, Q' at W = 0.30 mm, H = 0.30 mm and T = 160 °C. The discrete data points represent the simulation results, while the solid lines are obtained from Equation 8.3.

Based on the results presented in Figures 8.21 and 8.22, the findings discussed in Section 8.2 can be confirmed regarding the lack of true non-dimensionality between the dimensionless minimum wet thickness and the five dimensionless numbers which captured the effect of inertia forces (which is proportional to the density of the solution) or gravitational forces or both.

8.3.5 Validation of the Numerical and Semi-Empirical Model with PPA/PBI Experiment

One set of experiments is performed with the PPA/PBI sample at 120 °C, W = 0.25 mm and H = 0.25 mm. As outlined in Section 5.2.2, the PPA/PBI solution is heated to 120 °C before transferring into the pressure vessel. The pressure vessel, slot die and the PET substrate are all simultaneously heated to the same temperature. Once the solution and all the components reach the desired temperature, the solution is transferred into the pressure vessel and the coating window is obtained by following the first method described in Section 5.2.2. In this method, the pressure is set at a constant value and the substrate speeds corresponding to dripping and air entrainment boundary are recorded, then the next pressure is set and the process is repeated until the boundaries of the coating window are obtained.

The coating window obtained experimentally is compared with the numerical prediction and Equation 8.3 (for maximum coating speed) as shown in Figure 8.23. The differences between the experimental and numerical predictions were within ±4%. The semi-empirical model predicted the maximum coating speed within ±5% of the experimental findings. These predictions are well within the uncertainty limits of the experiments. The uncertainty in Q' is found to be 0.0025 m^3/mm-s, which is negligibly small. So the main uncertainty comes from the coating speed readings.

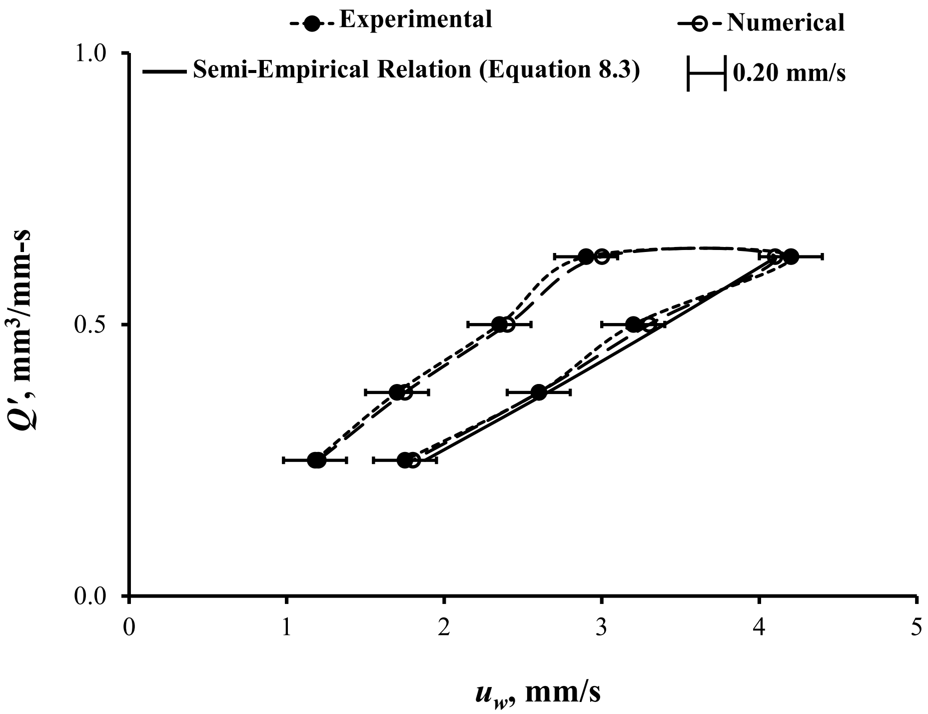

Figure 8.23: Comparison of coating windows obtained experimentally and numerically at $W = 0.25$ mm, $H = 0.25$ mm and $T = 120$ °C. The solid line represents the maximum coating speed obtained from Equation 8.3.

The typical images of the coated PPA/PBI film obtained experimentally at 120 °C are presented in Figure 8.24. The images are captured using the overhead camera. The thin coated films are obtained by keeping the flow rate through the slot die constant (applied pressure is kept constant) and varying the coating speed from a lower value to a higher value. At low coating speeds, dripping occurs accompanied with air entrainment. Past the dripping point, air entrainment begins to ensue only for relatively high-viscosity solutions (PPA/PBI solutions processed at temperatures of 120 °C and 140 °C) due to the inability of the solution to wet the substrate once it creeps up the upstream die. As the coating speed is increased, good coating is obtained in a finite region before air entrainment occurs. As the coating speeds are increased further, break lines, pinholes, and holes appear. It can also be noticed that the image becomes lighter with increasing coating speed due to the reduction in the thickness of the coated film. More holes and break lines are present at higher coating speeds due to the inability of the die to replenish the PPA/PBI solution at the same rate as the substrate takes it away, thus entraining more air. Also, because relatively thinner membranes are obtained at higher substrate speeds owing to mass conservation, the size of the entrained air bubbles is about the same as the thickness of the coated film, giving them the appearance of holes.

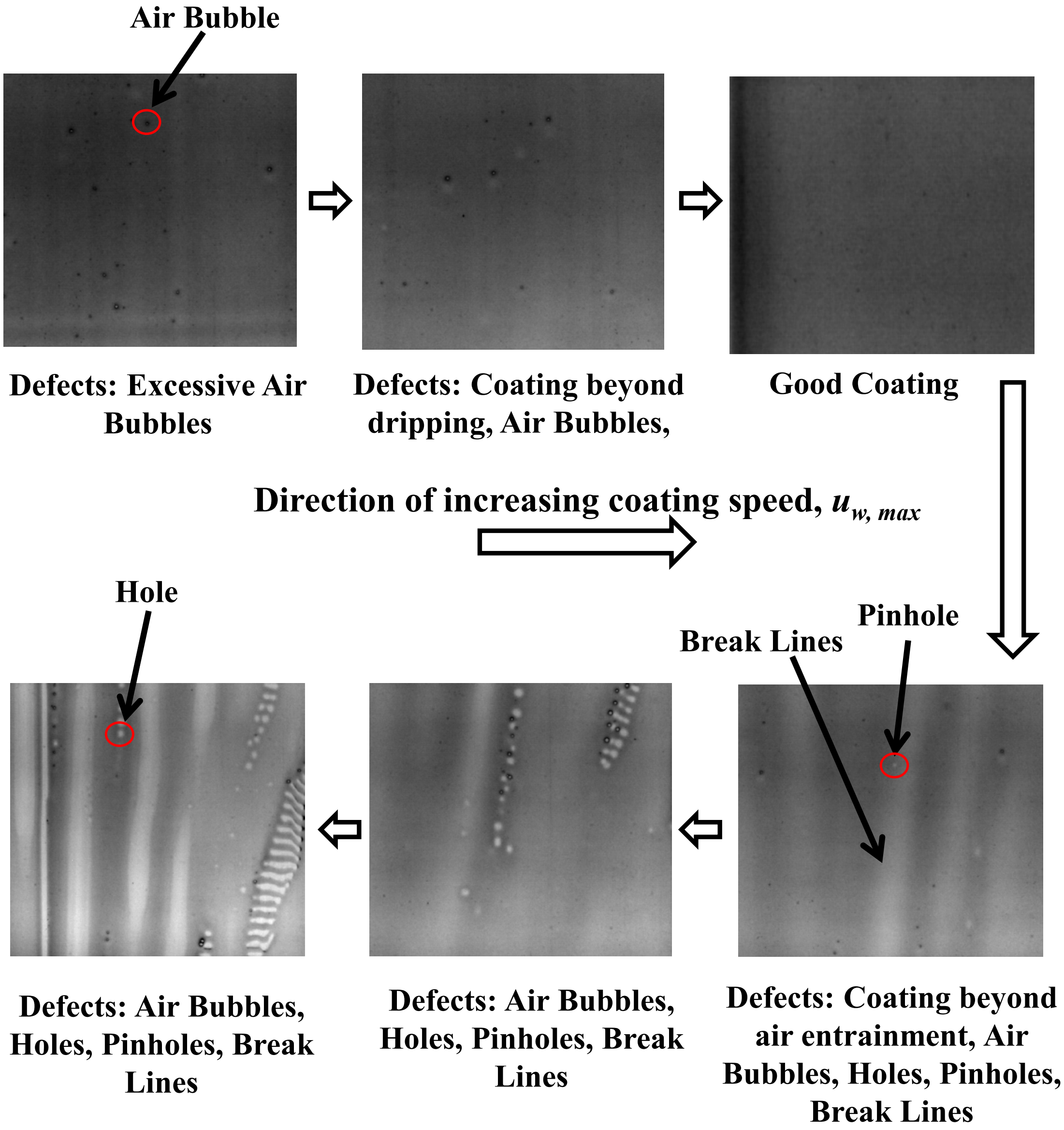

Figure 8.24: Images of the coated film obtained experimentally at W = 0.25 mm, H = 0.25 mm and T = 120 °C.

Based on the previous analysis, it is paramount to control the coating process within the coating window limits.

8.4 Summary

In this chapter, DOE runs were performed to obtain coating windows for PPA/PBI solutions at different geometric and processing conditions. Based on the coating window results, a semi-empirical relation was obtained relating the maximum coating speed to the geometric and processing parameters. Subsequently, the effect of various parameters on the maximum coating speed and sizes of sawteeth structures and bubbles were analyzed. It can be concluded that smaller slot gaps and coating gaps, and larger processing temperatures are beneficial to the coating process in terms of obtaining higher coating speeds and smaller bubble sizes beyond the coating window. If the priority is on obtaining wider range of thicknesses, it has been found that it is better to process using a combination of large coating gaps and higher temperatures. In addition, solutions with higher surface tension were found to produce more stable films. The numerical model and semi-empirical model was finally validated with a set of experiments performed with PPA/PBI solution at 120 °C. The important conclusions and contributions from Chapters 6 through 8 are presented in the next chapter.

9. CONCLUSIONS AND CONTRIBUTIONS

A detailed analysis is performed to understand the effects of geometric parameters and processing conditions during slot die coating of relatively high-viscosity (3 Pa-s to 20 Pa-s), shear-thinning, PPA/PBI solutions. The coating produces PA/PBI membranes used in high-temperature PEMFCs. The primary objective is to find the optimum conditions at which defect-free PA/PBI membranes can be obtained to increase the durability of the membranes by preventing unintended crossover. A certain range of these conditions is found as denoted by the coating window. Even though both experiments and simulations are performed to obtain the coating windows, due to the limited availability of the PPA/PBI solution, simulations are widely used. In order to check the validity of the numerical model and to understand the phenomena of air entrainment, experiments are performed using analogous solutions, referred to as the test solutions in the current study.

9.1 Conclusions

Based on the observations made in the current study, several important conclusions can be drawn regarding the numerical model, air entrainment mechanism, and coating windows.

9.1.1 Features and Limitations of the Numerical Model

As the slot die coating is a wetting process where air is displaced by the coating solution, a two-phase phenomenon arises. Hence, the numerical simulations are performed using VOF, a multiphase model available in FLUENT 6.3.26 and the surface tension forces are captured in the momentum term using the CSF model. A comparative study on the effect of static versus dynamic contact angle boundary conditions at the dynamic contact line showed that while the differences in the coating window predictions are insignificant, the static contact angle boundary condition produced a more stable numerical result.

The grid study performed to understand the sensitivity of the mesh interval size on the numerical predictions showed that there is a narrow range of mesh sizes that can be used. Higher mesh interval sizes resulted in a coarser mesh, which affected the accuracy of the solution, while lower mesh interval sizes suffered from spurious currents or divergence of the solution resulting from very large curvature values arising from the surface tension term.

A two-dimensional VOF model was found to be sufficient for successfully predicting the coating windows and to a certain extent, even the air entrainment phenomenon. However, for more details on the relative sawtooth and bubble sizes along the direction perpendicular to the substrate motion, a three-dimensional VOF model was required.

The numerical coating window predictions were found to compare well within the uncertainty limits of the experiments. At a qualitative level, the simulations captured the bubble entrainment phenomena on the PET walls observed in the experiments. Although, the interface was less sharp in the simulations, the relative differences in the sizes of the sawteeth and bubbles on the PET walls between various geometric/processing conditions as seen in the experiments were also predicted. However, the bubble sizes in the sectional view could not be compared between the experiments and the simulations because of the imaging limitations. Owing to the averaging of the properties and the variables in the VOF model and the approximation of the interface by the geo-reconstruct method, the sawteeth sizes were under-predicted by the simulations. As the focus of the current study is in the defect-free region and only a qualitative comparison is required outside this region, the VOF model is found to be sufficient.

9.1.2 Air Entrainment Mechanism

Two distinct modes of air entrainment were noticed. The first mechanism occurs when the length of a sawtooth was either greater than or equal to the sawtooth's width. The air bubble pinch-off in this mechanism ensued due to the stresses experienced by the solution upstream of the tip of the sawtooth. In the second mechanism, the width of the sawtooth was much wider than its length such that the stresses were not sufficient for the solution in the coating gap to enclose the air pocket; instead the solution exiting the slot die caused the bubble pinch-off.

For a solution flowing through the slot die at a specified flow rate and a given coating gap, the maximum coating speed remained independent of the slot gap. However, the width of the sawtooth was found to increase with the slot gap, while the difference in the sawtooth lengths was insignificant. As the bubble sizes are proportional to the sawteeth sizes, larger bubbles will be form at larger slot gaps. Therefore, it is advantageous to manufacture the membranes using a slot die with a smaller slot gap because smaller bubbles are likely to dissolve, as discussed in Chapter 2 [79].

In the study with varying coating gaps, the maximum coating speed was found to decrease with increasing coating gap, while both the length and width of the sawteeth were found to increase. Therefore, the effect of using smaller coating gaps is two-fold, the processing speeds can be higher and air bubble sizes can be smaller.

The study on viscosity effects showed that both the maximum coating speed and the bubble sizes increase with decreasing solution viscosity. While obtaining higher speeds can be advantageous, there is a disadvantage in working with low viscosity solutions due to the increased bubble sizes. Therefore, if a decision needs to be made between two solutions with varying viscosity, one should consider the other parameters such as slot gap and coating gap. For example, a low-viscosity solution can be used with smaller slot and coating gaps to offset the increase in the bubble sizes due to the low viscosity. Surface tension, on the other hand, did not impact the sawteeth or bubble sizes.

9.1.3 Coating Windows

By employing a fractional factorial DOE, a total of nine runs were performed using PPA/PBI solution for three different slot gaps, coating gaps, and processing temperatures. True non-dimensionalization was found to exist when the data from the DOE runs were plotted in a non-dimensional form with the dimensionless minimum wet thickness on the y-axis and capillary number on x-axis. The coating window reached the extreme boundary, when either the non-dimensional minimum wet thickness approached a value between 0.55 and 0.6 or the maximum capillary number approached 1.2. The constraint on the maximum capillary number means that to obtain a stable coating, the viscous forces should not exceed the surface tension forces such that the capillary number is greater than 1.2. A power-law curve was fit through the data plotted between the dimensionless minimum wet thickness and the capillary number obtained for PPA/PBI solutions. The curve-fit resulted in a semi-empirical relation (Equation 8.3) correlating the maximum coating speed to the geometric parameters, processing parameters, and fluid properties. Equation 8.3 can be used to study the dependence of maximum coating speed on the coating gap and flow rate in addition to the fluid properties of shear-thinning solutions within the viscosity range of 1 to 40 Pa-s.

Even though smaller coating gaps have the advantage of facilitating higher coating speeds, they have a disadvantage in terms of versatility in the thicknesses obtained. In essence, when the coating gap is small, for a given solution and for the same geometrical conditions, a narrow range of thicknesses is obtained by changing the flow rate. It was found that there is no effect of slot gap on either maximum coating speed or the range of thicknesses that can be obtained for a given set of parameters.

Higher consistency indices or power-law indices lead to higher viscosity and lower maximum coating speeds. Also, as the power-law index increases, the extreme end of the coating window was shifted to lower substrate speeds due to the constraint on the dimensionless minimum wet thickness or the capillary number.

Keeping everything else constant, the maximum coating speed can be increased by increasing the surface tension of the solution. Surface tension tends to stabilize the coating bead. On the other hand, density and slot die/substrate orientation did not show any impact on the maximum coating speed.

The effects of various parameters on the maximum coating speed and the sawteeth sizes are summarized in Table 9.1. The symbol ↑ indicates that a proportional relationship exists, ↓ indicates that there is an inverse relationship between the two and N/A indicates that there is no impact.

Table 9.1 Effect of geometric/processing parameters and fluid properties on the coating speeds and sawteeth/bubble sizes.

Parameter	**Maximum coating speed, $u_{w, max}$**	**Sawteeth/Bubble sizes**
Slot gap, W ↑	N/A	↑
Coating gap, H ↑	↓	↑
Consistency index, k ↑	↓	↓
Power-law index, n ↑	↓	↓
Surface tension, σ ↑	↑	N/A

N/A – No impact, ↑- increases, ↓ - decreases

9.2 Key Contributions

In order to achieve the primary objective of obtaining defect-free membranes for operation in PEMFC, the current study is performed. However, several important findings were obtained that can be extended beyond the fuel cell field and have significance at both the fundamental and engineering levels.

9.2.1 Fundamental Contributions

- The experimentally validated VOF model can be used for solving the two-phase flow-field (with very low Reynolds number) that simulates the coating of shear-thinning, relatively high-viscosity solutions, which was not investigated earlier.

- The non-dimensionalized coating windows presented in Chapter 8 demonstrate the effects of interplay between various forces arising during the slot-die manufacturing process and their contribution to the defect formation.
- A semi-empirical model (Equation 8.3) was derived to predict the maximum coating speed, based on fluid properties of the shear-thinning solution, the coating gap and the flow rate. In addition, the relation is not just limited to power-law fluids, but in certain cases can also be used to predict the maximum coating speed of Newtonian fluids by setting the power-law index equal to one and substituting the consistency index with the dynamic viscosity of the Newtonian solution.
- The qualitative analysis dealing with the effect of geometric parameters on air entrainment establishes a correlation between the fundamental forces and the sawteeth/bubble sizes. Prior to this study, even though there was data on the effect of geometric parameters on the coating window sizes, there was no information available pertaining to their effects on sawteeth and bubble sizes.

9.2.2 Engineering Contributions

- The study provides guidelines to manufacturers by setting limits on the processing and geometric conditions, through the data obtained from the coating window and air entrainment study, thereby reducing material waste, cost, and time.
- It provides a robust coating process that will produce highly durable and conductive membranes efficiently and with less turn-around time. As the

defects are curtailed at the manufacturing stage itself, there will be less probability for failure at the application point.

- As thin-film membranes have extensive applications in biomedical, food, pharmaceutical, microelectronics, chemical, and other industries, the findings from the study can be easily extended to these other fields.

9.3 Summary

In this chapter, the important conclusions from the current study and the contributions of the study are discussed. The advantages and limitations of the numerical model are presented. The effect of geometric parameters, processing conditions and fluid properties on the coating windows and air entrainment phenomena are discussed. Finally, the fundamental and engineering contributions of the current study are presented. In the following chapter, details are provided on how the current study can be extended in the future.

10. FUTURE WORK

The future work can be classified into three sections: (1) improving the existing experimental setup and numerical model, (2) studying the effect of other geometric and processing parameters on the coating window and air entrainment, and (3) utilizing the results and data from the current study to understand the future effects of the coating defects.

10.1 Improvements to the Current Experimental Apparatus and Numerical Model

The design of the current experimental apparatus poses certain limitations on the range of geometric and processing parameters used, which limits the data obtained from the research. For example, the maximum substrate speed dictated by the experimental system is 15 mm/s, which is the reason for having open coating windows for the test solutions. The following are some of the suggestions to improve the design of the current experimental setup:

- Isolate the feed roller and take-up roller from the 80-20 frame built to house the other experimental components. Most of the vibrations experienced by the setup are transmitted by the moving rollers, which causes limitation on higher substrate speeds.
- As seen from the validation results in Section 6.8, the uncertainty in the values of flow rate per unit width is huge for DBSM. The uncertainty decreased significantly as the solution viscosity increased, due to the higher pressure

requirement. Therefore, a more precise device such as a flow-meter specially designed for the viscosity range of the solution is desirable.

- The method of setting the coating gap using a feeler gauge can induce errors in the measurement. A more reliable method to control the coating gap could be by replacing the worm gear with a more sophisticated supporting bar, which has a digital reading, such that the gap can be set equal to the reading on the bar.
- The current set up requires that if the slot gap needs to be changed, the entire die system (slot die, pressure vessel, and the connecting pipe along with the valve) needs to be removed. Instead, the system should be redesigned such that the slot die can be removed independent of the pressure vessel and the connecting pipe.
- Based on the images presented in Figure 8.24, if the total number of each of the defects is plotted versus coating speed, the plot depicted in Figure 10.1 is obtained. If all the four defects are present, then decreasing the substrate speed will help to operate within the coating window. However, if dripping and air bubbles are present, the coating speed needs to be increased. This phenomenon noticed while coating high-viscosity solutions provides immense potential to automate the coating process and make the manufacturing more efficient.
- The shapes of upstream and downstream menisci can be investigated using a microscope/camera system placed near the slot die exit to monitor the coating gap region. The information can shed light on the conditions leading to a particular shape of the meniscus.

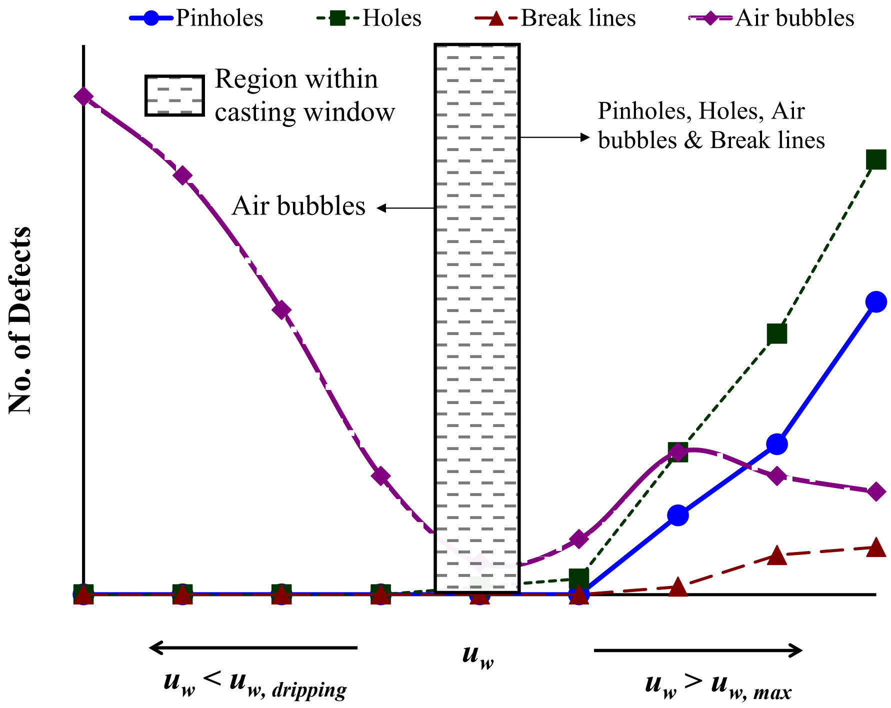

Figure 10.1: Illustration of defect distribution in the coated film of a high-viscosity solution.

The numerical model in the current study was able to capture the coating windows accurately and predict the air entrainment phenomena reasonably well. As discussed earlier, it cannot produce a sharp interface comparable to the ones seen in the experiments and over-predicts the number of bubbles. One of the issues with the numerical model used in the current study is the way the surface tension force is treated. In the CSF model, the surface tension source term is proportional to the volume averaged density as in Equation 6.10. So, if the density difference is large as is the case with the solutions used in the current study, then errors are inherently induced into the results. Also the assumption that the interface is continuous would lead to artificial diffusion of the momentum leading to spurious velocities [192]. To overcome these issues, some of the existing models such as the level-set method [193, 194], the coupled VOF and level-set method [195-197] or any new custom-derived models can be employed.

As discussed in Chapter 8, the semi-empirical model (Equation 8.1) developed for shear-thinning solutions compared within 15% to predictions from literature obtained using Newtonian solutions processed at certain conditions. The current work can be extended to determine the conditions corresponding to processing of Newtonian solutions where Equation 8.1 will be valid.

10.2 Effect of Other Geometrical and Processing Parameters

In lieu of the results obtained in the current study that the slot gap and coating gap have an impact on the coating window or the sizes of sawteeth and bubbles or both, it would be interesting to see how the length of the die lips and die lip angles (shown in Figure 10.2) impact the coating window and air entrainment in shear-thinning solutions. The die lip lengths and angles for the upstream and downstream dies can be different. Earlier studies [58, 59, 100, 198] have discussed the effects of die lip length and die lip angle to a limited extent and hence a more detailed analysis is warranted.

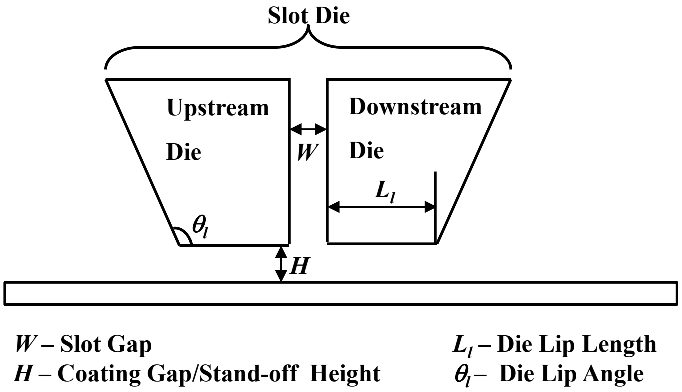

Figure 10.2: Illustration of die lip length, L_l and die lip angle, θ_l, in a slot die.

Based on the discussion in Section 2.6, some researchers have found that angling the substrate with respect to the slot die can have a positive impact on the coating window, while others disagree [199]. It is noteworthy to study the effects of angling the substrate with respect to the slot die on the coating of high-viscosity, shear-thinning solutions.

The effects of geometric and processing parameters on the sawteeth sizes are qualitatively discussed in Chapter 7. A more rigorous analysis is needed to quantify the sizes and correlate the transition from Mechanism I to Mechanism II.

As discussed in Section 2.4, Benkreira and Khan [95] found that higher coating speeds can be obtained while operating under reduced pressure conditions due to the lower air viscosity values. Coating of solutions used in the current study can also be tested under decreased ambient pressure conditions.

The reason for the discrepancies between the current study and Veverka's findings regarding the limit on the viscosity ratio needs to be investigated. According to Veverka's findings, the sawteeth can be present without entraining air when the viscosity ratio between air and the coating solution is greater than 2×10^{-4}, while the current study showed the presence of this phenomenon even at a viscosity ratio as low as 10^{-6}.

10.3 Study of Air Bubbles in the Membrane on PEMFC Performance

The coated films obtained numerically in the current study can be used to study the evolution of the coating defects during the hydrolyzation of PPA/PBI film into PA/PBI membrane. As the film undergoes hydrolyzation, it can either swell or shrink depending on the curing conditions. So, the current numerical study can be extended to simulate the phase-change process.

If the defects are found to remain unchanged during the phase change process, the coated film profile can be directly used for the geometry of PEM to simulate a PEMFC operation and find the correlation between the PEM defects and PEMFC performance and durability.

A study can be performed to understand the time it takes for the entrained bubbles to dissolve and if the dissolution time is a function of the properties of the coated film. Since, Miyamoto and Scriven [79] have shown that smaller bubbles dissolve faster, such studies can be used to find the sizes of the bubbles that can be considered benign and have insignificant impact on the air entrainment.

10.4 Summary

In this chapter, the limitations of the current experimental setup and numerical model are discussed and improvements are proposed. Suggestions are made on studying the effects of other geometric and processing parameters on the slot die coating process. Finally, a discussion is presented on how the data on the air entrainment obtained in the current study can be used to find the threshold on the bubble sizes that are detrimental to PEMFC performance.

APPENDIX A: Derivation of Dimensionless Numbers

The non-dimensional variables for plotting non-dimensional minimum wet thickness are obtained by using the Buckingham $\prod$ theorem. The relevant parameters that define the four forces; viscous, inertia, surface tension and gravity are characteristic velocity, $\mho$, characteristic gap, ℓ, apparent viscosity, η, gravity, g, density, ρ, and surface tension, σ. An implicit function relating all the parameters can be defined as described by Equation A1:

$$f(\mho, \ell, \sigma, \rho, \eta, g) = 0 \tag{A1}$$

In Equation A1, there are a total of six variables, all of which can be defined using three fundamental dimensions; Mass (M'), Length (L'), and Time (T') as given by:

$$[\mho] = \frac{L'}{T'}, [\ell] = L', [\rho] = \frac{M'}{L'^3}, [\eta] = \frac{M'}{L'T'}, [\sigma] = \frac{M'}{T'^2}, [g] = \frac{L'}{T'^2}$$

Using Buckingham $\prod$ theorem, using the six variables defined by three fundamental dimensions, three dimensionless numbers ($\prod_1$ through $\prod_3$) are obtained. The three repeating variables are chosen as; $\mho$, σ, and ℓ. For the first $\prod$ term:

$\prod_1 = \mho \sigma^{a1} \ell^{b1} \rho^{c1}$

$\rightarrow M^0 L^0 T^0 = \left(\frac{L'}{T'}\right)\left(\frac{M'}{T'^2}\right)^{a1} L'^{b1} \left(\frac{M'}{L'^3}\right)^{c1}$

By equating the sum of the powers for a given dimension on the right side of the equation to the power (zero) of the corresponding dimension on the left, a1, b1, and c1 are obtained as:

a1 = -1/2, b1 = 1/2, c1 = 1/2

$$\Pi_1 = \mho\sqrt{\frac{\rho\ell}{\sigma}}$$

The entire Π_1 term can be raised to power 2 without losing the non-dimensionality. Due to the presence of density term, the appropriate characteristic velocity will be v_{in}, which accounts for forces due to inertia, and the appropriate length term for surface tension force would be H, therefore, Π_1 can be rewritten to obtain:

,

$$\Pi_1 = \frac{\rho v_{in}^2 H}{\sigma} \tag{A2}$$

where Π_1 is the ratio of inertia forces to surface tension forces as given by the Weber number (fourth dimensionless number in Table 3.2). For the second Π term:

$$\Pi_2 = \mho\sigma^{a2}\,\ell^{b2}\eta^{c2}$$

$$\rightarrow M^0L^0T^0 = \left(\frac{L'}{T'}\right)\left(\frac{M'}{T'^2}\right)^{a2} L'^{b2}\left(\frac{M'}{L'T'}\right)^{c2}$$

By equating the sum of the powers for a given dimension on the right to the power (zero) of the corresponding dimension on the left, a2, b2, and c2 are obtained as

a2 = -1, b2 = 0, c2 = 1

$$\Pi_2 = \mho\frac{\eta}{\sigma}$$

As, the apparent viscosity term is present, the appropriate characteristic velocity, $\mho$, is set to $u_{w,\ max}$ and η can be rewritten in terms of other fluid properties, i.e., consistency index, k, power-law index, n, characteristic velocity, $u_{w,max}$ and characteristic length, H, as

$$\eta = k\left(\frac{u_{w,max}}{H}\right)^{n} \tag{A3}$$

therefore, Π_2 can be rewritten to obtain

$$\Pi_2 = \frac{\boldsymbol{k}\left(\frac{\boldsymbol{u_{w,max}}}{\boldsymbol{H}}\right)^{\boldsymbol{n-1}} \boldsymbol{u_{w,max}}}{\boldsymbol{\sigma}} \tag{A4}$$

where Π_2 is the ratio of viscous forces to surface tension forces, which is the capillary number (First dimensionless number in Table 3.2). For the third Π term,

$\Pi_3 = \mho\sigma^{a3}\,\ell^{b3}g^{c3}$

$\rightarrow M^0L^0T^0 = \left(\frac{L'}{T'}\right)\left(\frac{M'}{T'^2}\right)^{a3} L'^{b3}\left(\frac{L'}{T'^2}\right)^{c3}$

By equating the sum of the powers for a given dimension on the right to the power (zero) of the corresponding dimension on the left, a3, b3, and c3 are obtained as

a3 = 0, b3 = -1/2, c3 = -1/2

$\Pi_3 = \frac{\mho}{\sqrt{g\ell}}$

The entire Π_3 term can be raised to power 2 without losing the non-dimensionality. If inertia forces are considered, the appropriate characteristic velocity, $\mho$, is set to v_{in} and the appropriate characteristic length for gravitational forces is H. Therefore, Π_3 can be rewritten to obtain:

$$\Pi_3 = \frac{\boldsymbol{v_{in}^2}}{\boldsymbol{gH}} \tag{A5}$$

where $\prod_3$ is the ratio of inertia forces to gravitational forces as given by the Froude number (fifth dimensionless number in Table 3.2). The other three dimensionless numbers can be obtained by performing multiplication or division operations on the existing $\prod$s. It is to be noted that the non-dimensionality will be retained whether multiplication or division is performed on the $\prod$s. To obtain inertia to viscous forces, the ratio of $\prod_1$ to $\prod_2$ is obtained, thus eliminating the effect of surface tension forces, and given by $\prod_4$:

$$\prod_4 = \frac{\prod 1}{\prod 2} = \frac{\left(\frac{\rho v_{in}^2 H}{\sigma}\right)}{\frac{k\left(\frac{u_{w,max}}{H}\right)^{n-1} u_{w,max}}{\sigma}} = \frac{\boldsymbol{\rho v_{in}^2 H^n}}{\boldsymbol{k u_{w,max}^n}} \tag{A6}$$

where $\prod_4$ is the definition for Reynolds number, the second dimensionless number in Table 3.2. Similarly, the ratio of gravitational to viscous forces can be obtained by dividing $\prod_4$ by $\prod_3$, and given by $\prod_5$

$$\prod_5 = \frac{\prod 4}{\prod 3} = \frac{\left(\frac{\rho v_{in}^2 H^n}{k u_{w,max}^n}\right)}{\frac{v_{in}^2}{gH},} = \frac{\boldsymbol{\rho g H^{n+1}}}{\boldsymbol{k u_{w,max}^n}} \tag{A7}$$

where $\prod_5$ is the definition for the Stokes number, the third dimensionless number in Table 3.2. Finally, the ratio of gravitational to surface tension forces can be obtained by multiplying $\prod_2$ and $\prod_5$, and given by $\prod_6$

$$\prod_6 = \prod_2 \prod_5 = \left[\frac{k\left(\frac{u_{w,max}}{H}\right)^{n-1} u_{w,max}}{\sigma}\right]\left[\frac{\rho g\, H^{n+1}}{k u_{w,max}^{n}}\right] = \boldsymbol{\frac{\rho g H^{2}}{\sigma}} \tag{A8}$$

where $\prod_6$ is the definition for Bond number, the sixth dimensionless number in Table 3.2.

APPENDIX B: Fluid Properties of Test Solutions

Properties of DBSM:

Table B1: Apparent viscosity of DBSM

$\dot{\gamma}$, 1/s	η (Run 1), Pa-s	η (Run 2), Pa-s	η (Average), Pa-s
5.00	3.23	3.67	3.45
7.92	3.18	3.42	3.30
12.56	2.62	2.34	2.48
19.91	2.14	1.86	2.00
31.55	1.69	1.78	1.73
50.00	1.38	1.52	1.45

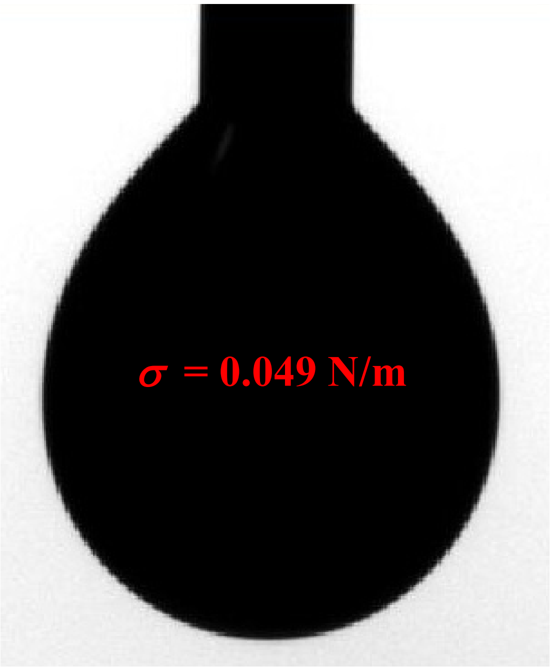

Figure B1: Surface tension of DBSM

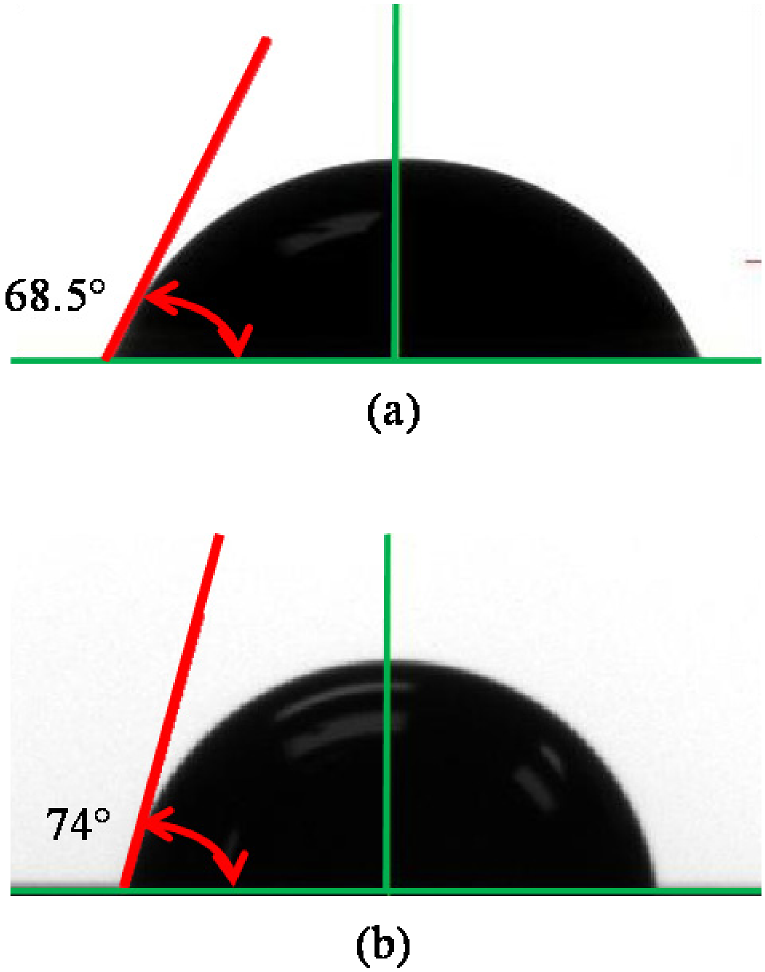

Figure B2: Contact angle made by DBSM on (a) SS 316, (b) PET

Properties of BSM:

Table B2: Apparent viscosity of BSM

$\dot{\gamma}$, 1/s	η (Run 1), Pa-s	η (Run 2), Pa-s	η (Average), Pa-s
0.50	8.02	8.77	8.40
0.79	7.98	8.49	8.24
1.26	7.68	7.37	7.53
1.99	6.98	7.23	7.10
3.15	6.42	6.59	6.51
5.00	6.24	6.17	6.20
7.92	5.96	5.79	5.87
12.56	5.21	5.42	5.32
19.91	5.04	5.22	5.13
31.55	4.43	4.88	4.66
50.00	4.26	4.53	4.40
79.24	4.16	4.24	4.20

Figure B3: Surface tension of BSM

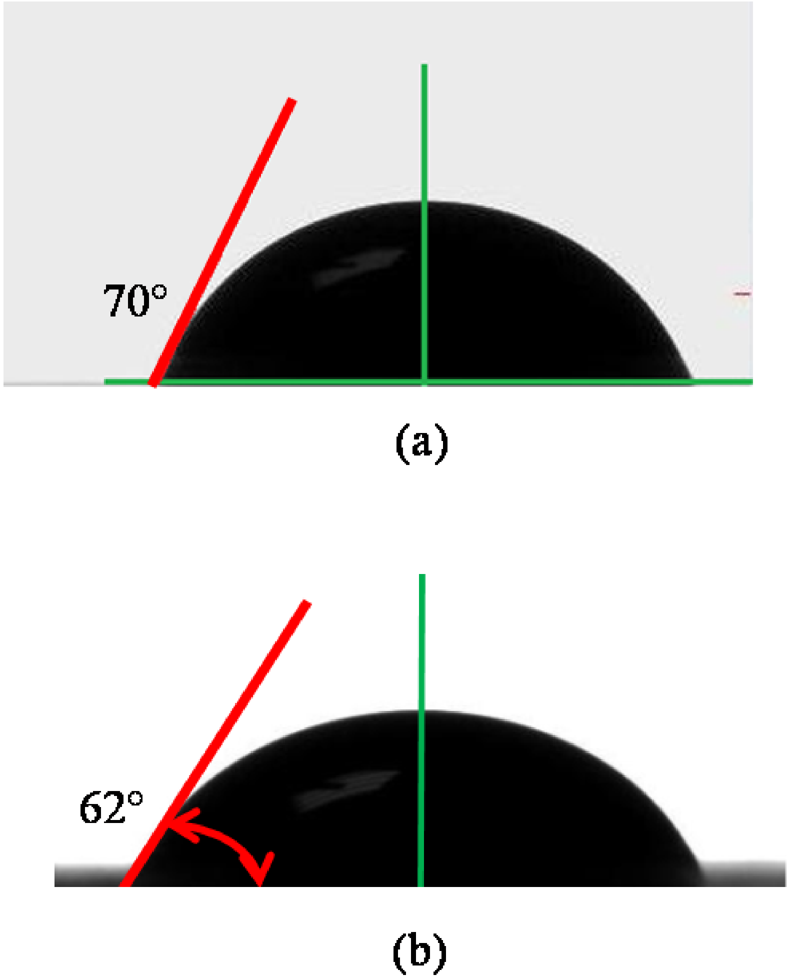

(a)

(b)

Figure B4: Contact angle made by BSM on (a) SS 316, (b) PET

Properties of Polymer Solution:

Table B3: Apparent viscosity of Polymer Solution

$\dot{\gamma}$, 1/s	η (Run 1), Pa-s	η (Run 2), Pa-s	η (Average), Pa-s
0.50	40.54	40.26	40.40
0.79	39.24	40.22	39.73
1.26	38.74	39.82	39.28
1.99	37.67	38.99	38.33
3.15	36.84	35.95	36.40
5.00	34.26	33.38	33.82
7.92	29.67	31.96	30.82
12.56	27.46	26.07	26.77
19.91	21.98	22.69	22.34
31.55	18.01	18.97	18.49
50.00	15.42	14.63	15.03
79.24	11.14	11.91	11.53

Figure B5: Surface tension of Polymer Solution

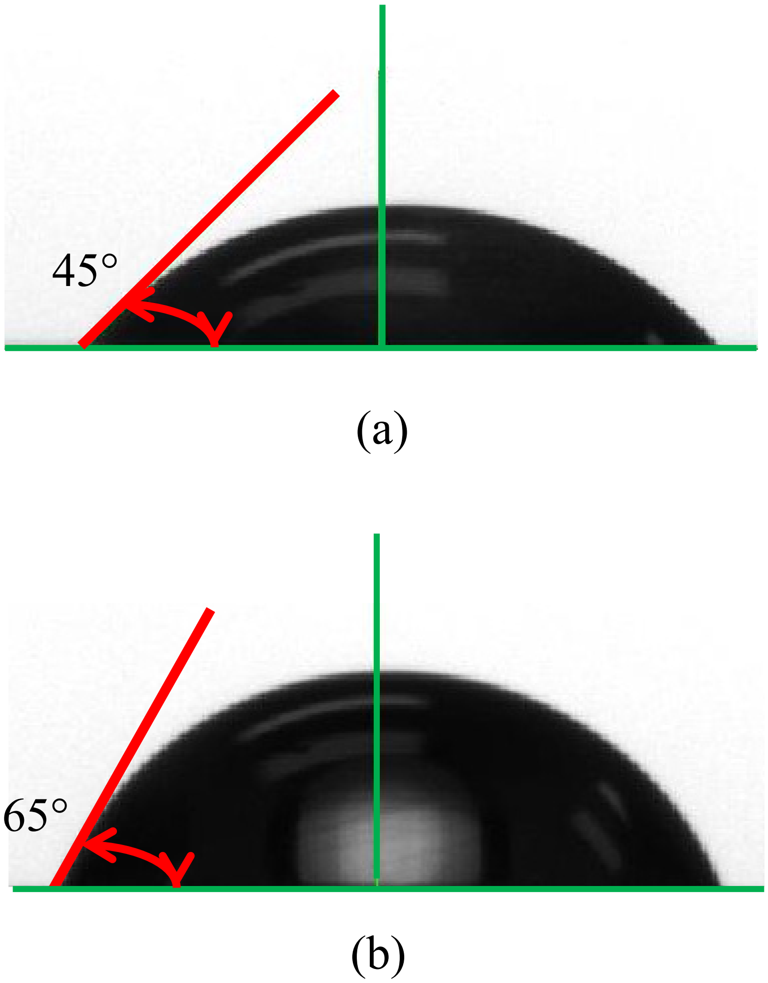

Figure B6: Contact angle made by Polymer Solution on (a) SS 316, (b) PET

APPENDIX C: *Q'* versus *P* Curves

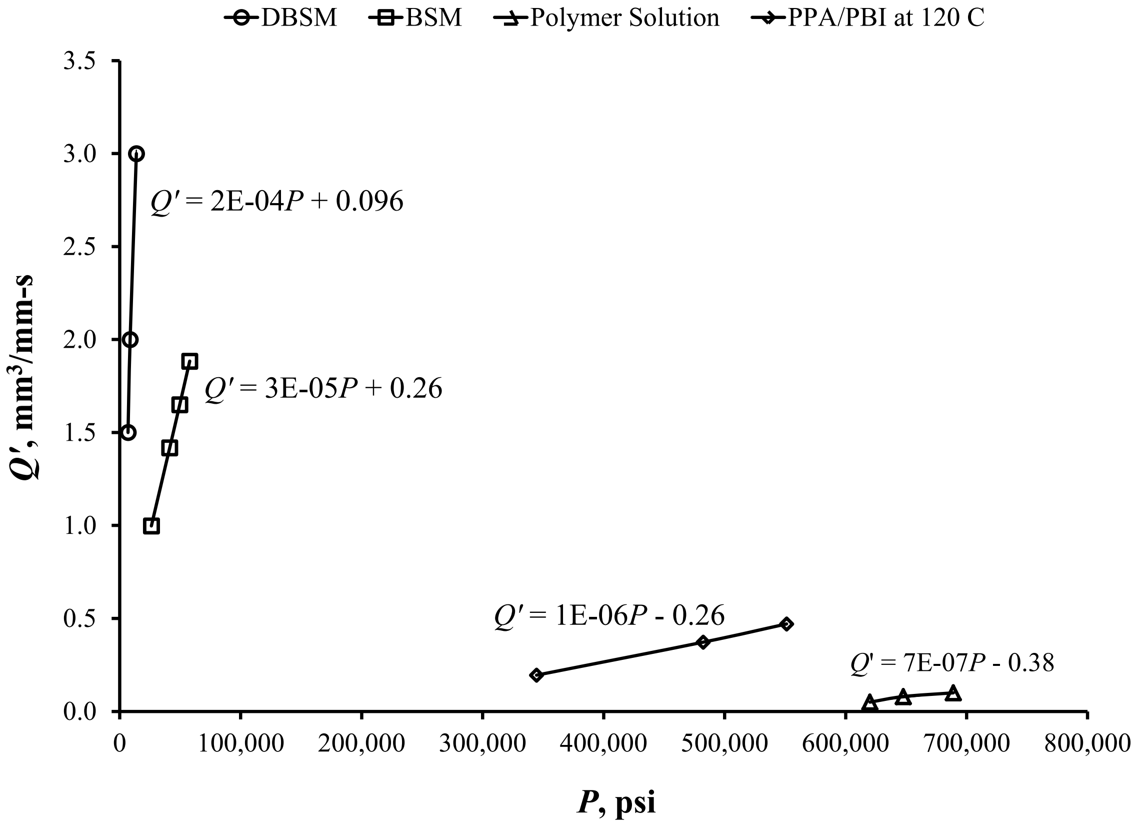

Figure C1: Pressure versus flow rate per unit width

APPENDIX D: Coating Window Results for Test Solutions

Table D1: Coating window data for BSM at $W = 0.30$ mm and $H = 0.30$ mm

Static Contact Angle (SCA)

Q', mm^3/mm-s	$u_{w,\,min}$, mm/s	$u_{w,\,max}$, mm/s	$h_{nd,min}$	Ca
0.30	1.15	2.20	0.45	0.16
0.60	2.35	4.00	0.50	0.29
0.90	3.50	5.80	0.52	0.40
1.20	4.40	7.60	0.53	0.49
1.50	5.70	9.20	0.54	0.60
1.80	6.80	10.90	0.55	0.70
2.10	8.20	12.20	0.57	0.82
2.40	9.30	14.10	0.57	0.91

Dynamic Contact Angle (DCA)

Q', mm^3/mm-s	$u_{w,\,min}$, mm/s	$u_{w,\,max}$, mm/s	$h_{nd,min}$	Ca
0.30	1.12	2.25	0.44	0.16
0.60	2.33	4.10	0.49	0.29
0.90	3.45	5.70	0.53	0.40
1.20	4.50	7.40	0.54	0.50
1.50	5.55	9.30	0.54	0.59
1.80	6.60	10.80	0.56	0.68
2.10	8.10	12.40	0.56	0.81
2.40	9.20	14.15	0.57	0.90

Table D2: Coating window data for BSM at $W = 0.25$ mm and $H = 0.25$ mm

Coarse Mesh

Q', mm^3/mm-s	$u_{w,\ min}$, mm/s	$u_{w,\ max}$, mm/s	$h_{nd,min}$	Ca
0.75	3.10	5.80	0.52	0.35
0.88	3.70	7.00	0.50	0.41
1.25	5.20	9.70	0.52	0.54
1.69	7.10	11.80	0.57	0.70
1.88	7.30	13.40	0.56	0.72

Medium Mesh

Q', mm^3/mm-s	$u_{w,\ min}$, mm/s	$u_{w,\ max}$, mm/s	$h_{nd,min}$	Ca
0.75	3.20	5.60	0.54	0.36
0.88	3.80	6.50	0.54	0.42
1.25	5.30	9.00	0.56	0.55
1.69	7.20	11.60	0.58	0.71
1.88	7.60	13.00	0.58	0.74

Fine Mesh

Q', mm^3/mm-s	$u_{w,\ min}$, mm/s	$u_{w,\ max}$, mm/s	$h_{nd,min}$	Ca
0.75	3.20	5.80	0.52	0.36
0.88	3.75	6.70	0.52	0.41
1.25	5.20	9.20	0.54	0.54
1.69	7.10	11.40	0.59	0.70
1.88	7.70	13.00	0.58	0.75

Table D3: Coating window data for BSM at $W = 0.178$ mm and $H = 0.25$ mm

2D

Q', mm^3/mm-s	$u_{w,\ min}$, mm/s	$u_{w,\ max}$, mm/s	$h_{nd,min}$	Ca
0.23	1.15	2.30	0.40	0.13
0.36	1.70	3.55	0.40	0.21
0.53	2.60	5.00	0.43	0.31
0.71	3.50	6.30	0.45	0.39
0.89	4.20	8.20	0.43	0.46
1.07	5.20	9.30	0.46	0.54
1.25	6.00	10.70	0.47	0.61
1.42	6.50	11.90	0.48	0.65
1.60	7.50	13.50	0.47	0.74

3D

Q', mm^3/mm-s	$u_{w,\ min}$, mm/s	$u_{w,\ max}$, mm/s	$h_{nd,min}$	Ca
0.23	1.15	2.40	0.39	0.14
0.36	1.70	3.50	0.41	0.21
0.53	2.60	5.10	0.42	0.31
0.71	3.50	6.30	0.45	0.39
0.89	4.20	8.10	0.44	0.46
1.07	5.20	9.40	0.45	0.54
1.25	6.00	10.70	0.47	0.61
1.42	6.50	12.00	0.47	0.65
1.60	7.50	13.50	0.47	0.74

Table D4: Coating window data for DBSM at $W = 0.178$ mm and $H = 0.178$ mm

Experiment

Q', mm^3/mm-s	$u_{w,\,min}$, mm/s	$u_{w,\,max}$, mm/s	$h_{nd,min}$	Ca
0.42	2.09	4.84	0.49	0.19
0.70	3.56	7.39	0.53	0.25
0.92	5.04	10.02	0.52	0.30
1.12	6.30	11.98	0.53	0.33
1.28	7.14	14.10	0.51	0.37

Simulation

Q', mm^3/mm-s	$u_{w,\,min}$, mm/s	$u_{w,\,max}$, mm/s	$h_{nd,min}$	Ca
0.23	1.40	3.30	0.39	0.15
0.36	2.20	4.80	0.42	0.19
0.53	3.30	6.70	0.45	0.23
0.71	4.50	8.60	0.47	0.27
0.89	5.40	10.70	0.47	0.31
1.07	6.70	12.80	0.47	0.35
1.25	7.40	14.50	0.48	0.38

Table D5: Coating window data for BSM at $W = 0.25$ mm and $H = 0.30$ mm

Experiment

Q', mm^3/mm-s	$u_{w,\ min}$, mm/s	$u_{w,\ max}$, mm/s	$h_{nd,min}$	Ca
0.50	1.86	3.25	0.51	0.15
0.88	3.15	5.30	0.55	0.20
1.40	5.02	7.98	0.58	0.26
1.85	6.48	10.64	0.58	0.31
2.13	7.62	12.64	0.56	0.34
2.38	8.52	13.60	0.58	0.36

Simulation

Q', mm^3/mm-s	$u_{w,\ min}$, mm/s	$u_{w,\ max}$, mm/s	$h_{nd,min}$	Ca
0.25	0.95	2.00	0.42	0.11
0.50	1.90	3.50	0.48	0.15
0.75	2.90	4.80	0.52	0.19
1.00	3.80	6.30	0.53	0.22
1.25	4.75	7.40	0.56	0.25
1.50	5.40	9.00	0.56	0.28
1.75	6.40	10.50	0.56	0.31
2.00	7.45	12.00	0.56	0.33
2.25	8.4	13.00	0.58	0.35

APPENDIX E: Coating Window Results for PPA/PBI Solutions

Table E1: Coating window data for Run 1

Q', mm^3/mm-s	$u_{w,\,min}$, mm/s	$u_{w,\,max}$, mm/s	$h_{nd,min}$	Ca	Re	Fr	We	St	Bo
0.18	1.10	2.00	0.50	0.57	1.34E-05	5.73E-04	7.32E-06	5.02E-05	3.19E-03
0.27	1.60	2.80	0.54	0.76	2.24E-05	1.29E-03	1.65E-05	3.72E-05	3.19E-03
0.36	2.20	3.50	0.57	0.92	3.27E-05	2.29E-03	2.93E-05	3.05E-05	3.19E-03

Table E2: Coating window data for Run 2

Q', mm^3/mm-s	$u_{w,\,min}$, mm/s	$u_{w,\,max}$, mm/s	$h_{nd,min}$	Ca	Re	Fr	We	St	Bo
0.18	0.70	1.60	0.45	0.26	4.19E-05	4.08E-04	1.04E-05	1.79E-04	6.39E-03
0.36	1.40	2.70	0.53	0.41	1.04E-04	1.63E-03	4.17E-05	1.10E-04	6.39E-03
0.53	2.20	3.75	0.57	0.55	1.72E-04	3.67E-03	9.38E-05	8.16E-05	6.39E-03
0.71	2.90	4.75	0.60	0.68	2.47E-04	6.52E-03	1.67E-04	6.57E-05	6.39E-03

Table E3: Coating window data for Run 3

Q', mm^3/mm-s	$u_{w,\ min}$, mm/s	$u_{w,\ max}$, mm/s	$h_{nd,min}$	*Ca*	*Re*	*Fr*	*We*	*St*	*Bo*
0.18	0.55	1.50	0.40	0.15	8.66E-05	3.40E-04	1.26E-05	4.13E-04	9.30E-03
0.36	1.10	2.70	0.44	0.26	2.01E-04	1.36E-03	5.06E-05	2.39E-04	9.30E-03
0.53	1.60	3.70	0.48	0.35	3.37E-04	3.06E-03	1.14E-04	1.79E-04	9.30E-03
0.71	2.20	4.40	0.54	0.41	9.70E-04	5.09E-04	5.44E-03	2.02E-04	1.52E-04
0.89	2.80	5.20	0.57	0.47	6.81E-04	8.49E-03	3.16E-04	1.30E-04	9.30E-03

Table E4: Coating window data for Run 4

Q', mm^3/mm-s	$u_{w,\ min}$, mm/s	$u_{w,\ max}$, mm/s	$h_{nd,min}$	*Ca*	*Re*	*Fr*	*We*	*St*	*Bo*
0.25	1.20	2.90	0.48	0.42	1.77E-05	5.73E-04	7.42E-06	5.39E-05	3.24E-03
0.50	2.40	5.20	0.54	0.72	4.15E-05	2.29E-03	2.97E-05	3.15E-05	3.24E-03
0.75	3.50	7.40	0.57	0.98	6.75E-05	5.15E-03	6.68E-05	2.27E-05	3.24E-03

Table E5: Coating window data for Run 5

Q', mm^3/mm-s	**$u_{w, min}$, mm/s**	**$u_{w, max}$, mm/s**	**$h_{nd,min}$**	***Ca***	***Re***	***Fr***	***We***	***St***	***Bo***
0.25	1.10	2.50	0.40	0.24	4.55E-05	4.08E-04	1.05E-05	1.81E-04	6.46E-03
0.50	2.20	3.90	0.51	0.36	1.20E-04	1.63E-03	4.21E-05	1.20E-04	6.46E-03
0.75	3.35	5.50	0.55	0.49	1.96E-04	3.67E-03	9.48E-05	8.68E-05	6.46E-03
1.00	4.50	7.10	0.56	0.62	2.75E-04	6.52E-03	1.69E-04	6.85E-05	6.46E-03
1.25	5.40	8.80	0.57	0.76	3.53E-04	1.02E-02	2.63E-04	5.61E-05	6.46E-03
1.50	6.50	10.40	0.58	0.88	4.35E-04	1.47E-02	3.79E-04	4.80E-05	6.46E-03
1.75	7.90	11.90	0.59	1.00	5.22E-04	2.00E-02	5.16E-04	4.24E-05	6.46E-03

Table E6: Coating window data for Run 6

Q', mm^3/mm-s	**$u_{w, min}$, mm/s**	**$u_{w, max}$, mm/s**	**$h_{nd,min}$**	***Ca***	***Re***	***Fr***	***We***	***St***	***Bo***
0.25	1.00	1.50	0.56	0.47	2.76E-05	3.40E-04	1.23E-05	1.74E-04	9.07E-03
0.50	2.00	2.95	0.56	0.85	6.05E-05	1.36E-03	4.93E-05	9.52E-05	9.07E-03
0.75	3.00	4.30	0.58	1.18	9.74E-05	3.06E-03	1.11E-04	6.81E-05	9.07E-03

Table E7: Coating window data for Run 7

Q', mm^3/mm-s	$u_{w,\,min}$, mm/s	$u_{w,\,max}$, mm/s	$h_{nd,min}$	Ca	Re	Fr	We	St	Bo
0.30	1.80	3.50	0.48	0.32	2.42E-05	5.73E-04	7.50E-06	6.86E-05	3.27E-03
0.45	2.70	4.80	0.53	0.42	4.07E-05	1.29E-03	1.69E-05	5.12E-05	3.27E-03
0.60	3.60	6.10	0.55	0.53	5.78E-05	2.29E-03	3.00E-05	4.09E-05	3.27E-03

Table E8: Coating window data for Run 8

Q', mm^3/mm-s	$u_{w,\,min}$, mm/s	$u_{w,\,max}$, mm/s	$h_{nd,min}$	Ca	Re	Fr	We	St	Bo
0.30	1.60	2.20	0.55	0.64	1.67E-05	4.08E-04	1.03E-05	8.76E-05	6.30E-03
0.45	2.40	3.20	0.56	0.89	2.69E-05	9.17E-04	2.31E-05	6.28E-05	6.30E-03
0.60	3.20	4.10	0.59	1.11	3.84E-05	1.63E-03	4.11E-05	5.03E-05	6.30E-03

Table E9: Coating window data for Run 9

Q', mm^3/mm-s	$u_{w,\,min}$, mm/s	$u_{w,\,max}$, mm/s	$h_{nd,min}$	Ca	Re	Fr	We	St	Bo
0.30	1.20	2.00	0.50	0.32	4.04E-05	3.40E-04	1.25E-05	2.07E-04	9.20E-03
0.60	2.50	3.50	0.57	0.53	9.65E-05	1.36E-03	5.00E-05	1.23E-04	9.20E-03
0.90	3.65	5.10	0.59	0.74	1.54E-04	3.06E-03	1.13E-04	8.73E-05	9.20E-03
1.20	4.80	6.70	0.60	0.95	2.12E-04	5.44E-03	2.00E-04	6.79E-05	9.20E-03

REFERENCES

[1] Ogden, J. M., Williams, R. H., and Larson, E. D., 2004, "Societal lifecycle costs of cars with alternative fuels/engines," Energy Policy, 32, pp. 7-27.

[2] 1998, "Confronting energy insecurity," Mining Voice, 4, pp. 40-40.

[3] Bishop, J. D. K., Amaratunga, G. A. J., and Rodriguez, C., 2010, "Linking energy policy, electricity generation and transmission using strong sustainability and co-optimization," Electric Power Systems Research, 80, pp. 633-641.

[4] MacKenzie, J. J., "Climate change, air pollution, and oil insecurity. The linked issues," Proceedings - 82nd A&WMA Annual Meeting, June 25, 1989 - June 30, 1989, Publ by Air & Waste Management Assoc.

[5] U.S. Energy Information Administration, 2010, "Annual Energy Outlook 2010."

[6] U.S. Energy Information Administration, June 2009, "Annual Energy Review 2008, DOE/EIA-0384(2008)." Projections: AEO2010 National Energy Modeling System, run AEO2010R. D111809A., Washington, DC.

[7] Deutch, J., Schlesinger, J., and Victor, D., October 12, 2006, "U.S. Energy Dependence Undercutting U.S. National Security, Council Task Force Warns," Council on Foreign Relations.

[8] U.S. Energy Information Administration, 2009, "Petroleum Supply Annual 2008." Projections: AEO2010 National Energy Modeling System, run AEO2010R.D111809A. , Washington, DC.

[9] AEO2010 National Energy Modeling System, 2009, "run AEO2010R.D111809A."

[10] Musti, S., Kortum, K., and Kockelman, K. M., 2011, "Household energy use and travel: Opportunities for behavioral change," Transportation Research Part D: Transport and Environment, 16, pp. 49-56.

[11] Oliveira, A. R. M., Amorim, J. C. C., and Pereira, C. R., "Analysis of the major world strategies for reducing the emission of greenhouse gases generated by public and

private transport," 2010 13th International IEEE Conference on Intelligent Transportation Systems (ITSC 2010), 19-22 Sept. 2010, IEEE, pp. 54-59.

[12] Hawkins, T. R., and Dente, S. M. R., 2010, "Greenhouse gas emissions driven by the transportation of goods associated with French consumption," Environmental Science and Technology, 44, pp. 8656-8664.

[13] Wang, Y., Chen, K. S., Mishler, J., Cho, S. C., and Adroher, X. C., 2010, "A review of polymer electrolyte membrane fuel cells: Technology, applications, and needs on fundamental research."

[14] Barbir, F., and Gómez, T., 1996, "Efficiency and economics of proton exchange membrane (PEM) fuel cells," International Journal of Hydrogen Energy, 21(10), pp. 891-901.

[15] Larminie, J., and Dicks, A., Fuel Cell Systems Explained (2nd Edition), John Wiley & Sons.

[16] Silberstein, M. N., and Boyce, M. C., 2010, "Constitutive modeling of the rate, temperature, and hydration dependent deformation response of Nafion to monotonic and cyclic loading," Journal of Power Sources, 195, pp. 5692-5706.

[17] Chupin, S., Colinart, T., Didierjean, S., Dube, Y., Agbossou, K., Maranzana, G., and Lottin, O., 2010, "Numerical investigation of the impact of gas and cooling flow configurations on current and water distributions in a polymer membrane fuel cell through a pseudo-two-dimensional diphasic model," Journal of Power Sources, 195, pp. 5213-5227.

[18] Bunmark, N., Limtrakul, S., Fowler, M. W., Vatanatham, T., and Gostick, J., 2010, "Assisted water management in a PEMFC with a modified flow field and its effect on performance," International Journal of Hydrogen Energy, 35, pp. 6887-6896.

[19] Meng, H., 2010, "Numerical studies of liquid water behaviors in PEM fuel cell cathode considering transport across different porous layers," International Journal of Hydrogen Energy, 35, pp. 5569-5579.

[20] Davey, J. R., Mukundan, R., Spendelow, J. S., Mukherjee, P., Hussey, D. S., Jacobson, D. L., Arif, M., and Borup, R. L., "Wetting and drying responses of gas diffusion layers and proton exchange membrane to current transients," 9th Proton Exchange Membrane Fuel Cell Symposium (PEMFC 9) - 216th Meeting of the

Electrochemical Society, October 4, 2009 - October 9, 2009, Electrochemical Society Inc., pp. 971-983.

[21] Antoine, O., Bultel, Y., and Durand, R., 2001, "Oxygen reduction reaction kinetics and mechanism on platinum nanoparticles inside Nafion," Journal of Electroanalytical Chemistry, 499(Compendex), pp. 85-94.

[22] Song, C., Tang, Y., Zhang, J. L., Zhang, J., Wang, H., Shen, J., McDermid, S., Li, J., and Kozak, P., 2007, "PEM fuel cell reaction kinetics in the temperature range of 23-120 C," Electrochimica Acta, 52, pp. 2552-2561.

[23] Parthasarathy, A., Srinivasan, S., Appleby, A. J., and Martin, C. R., 1992, "Temperature dependence of the electrode kinetics of oxygen reduction at the platinum/nafion(R) interface - a microelectrode investigation," Journal of the Electrochemical Society, 139, pp. 2530-2537.

[24] Yongchao, S., Ruichun, J., Jung-Chou, L., Kunz, H. R., and Fenton, J. M., 2004, "CO tolerance of carbon-supported platinum-ruthenium catalyst at elevated temperature and atmospheric pressure in a PEM fuel cell," Journal of the Electrochemical Society, 151, pp. 1820-1824.

[25] Meland, A. K., and Kjelstrup, S., 2007, "Three steps in the anode reaction of the polymer electrolyte membrane fuel cell. Effect of CO," Journal of Electroanalytical Chemistry, 610, pp. 171-178.

[26] Pitois, A., Pilenga, A., Pfrang, A., Tsotridis, G., Abrams, B. L., and Chorkendorff, I., 2010, "Temperature dependence of CO desorption kinetics at a novel Pt-on-Au/C PEM fuel cell anode," Chemical Engineering Journal, 162, pp. 314-321.

[27] Hussaini, I. S., and Wang, C. Y., 2010, "Dynamic water management of polymer electrolyte membrane fuel cells using intermittent RH control," Journal of Power Sources, 195, pp. 3822-3829.

[28] He, R., Li, Q., Jensen, J. O., and Bjerrum, N. J., 2007, "Doping phosphoric acid in polybenzimidazole membranes for high temperature proton exchange membrane fuel cells," Journal of Polymer Science, Part A: Polymer Chemistry, 45(14), pp. 2989-2997.

[29] Li, Q., He, R., Jensen, J. O., and Bjerrum, N. J., 2004, "PBI-based polymer membranes for high temperature fuel cells - Preparation, characterization and fuel cell demonstration," Fuel Cells, 4(3), pp. 147-159.

[30] Mustarelli, P., Quartarone, E., Grandi, S., Carollo, A., and Magistris, A., 2008, "Polybenzimidazole-based membranes as a real alternative to nafion for fuel cells operating at low temperature," Advanced Materials, 20(7), pp. 1339-1343.

[31] Savadogo, O., and Xing, B., 2000, "Hydrogen/oxygen polymer electrolyte membrane fuel cell (PEMFC) based on acid-doped polybenzimidazole (PBI)," Journal of New Materials for Electrochemical Systems, 3(4), pp. 343-347.

[32] Li, Q., He, R., Berg, R. W., Hjuler, H. A., and Bjerrum, N. J., 2004, "Water uptake and acid doping of polybenzimidazoles as electrolyte membranes for fuel cells," Solid State Ionics, 168(1-2), pp. 177-185.

[33] Litt, M., Ameri, R., Wang, Y., Savinell, R., and Wainwright, J., 1999, "Polybenzimidazoles/phosphoric acid solid polymer electrolytes: mechanical and electrical properties," Materials Research Society Symposium - Proceedings, 548, pp. 313-323.

[34] Noye, P., Li, Q., Pan, C., and Bjerrum, N. J., 2008, "Cross-linked polybenzimidazole membranes for high temperature proton exchange membrane fuel cells with dichloromethyl phosphinic acid as a cross-linker," Polymers for Advanced Technologies, 19(9), pp. 1270-1275.

[35] Xiao, L., Zhang, H., Scanlon, E., Ramanathan, L. S., Choe, E.-W., Rogers, D., Apple, T., and Benicewicz, B. C., 2005, "High-temperature polybenzimidazole fuel cell membranes via a sol-gel process," Chemistry of Materials, 17(21), pp. 5328-5333.

[36] Harris, T. A. L., and Walczyk, D. F., 2006, "Development of a casting technique for membrane material used in high-temperature PEM fuel cells," Journal of Manufacturing Processes, 8(1), pp. 8-20.

[37] Mecerreyes, D., Grande, H., Miguel, O., Ochoteco, E., Marcilla, R., and Cantero, I., 2004, "Porous Polybenzimidazole Membranes Doped with Phosphoric Acid: Highly Proton-Conducting Solid Electrolytes," Chemistry of Materials, 16(4), pp. 604-607.

[38] Xiao, L., Zhang, H., Jana, T., Scanlon, E., Chen, R., Choe, E. W., Ramanathan, L. S., Yu, S., and Benicewicz, B. C., 2005, "Synthesis and characterization of pyridine-based polybenzimidazoles for high temperature polymer electrolyte membrane fuel cell applicationsx," Fuel Cells, 5(2), pp. 287-295.

[39] Hu, J., Zhang, H., Zhai, Y., Liu, G., and Yi, B., 2006, "500 h Continuous aging life test on PBI/H3PO4 high-temperature PEMFC," International Journal of Hydrogen Energy, 31(13), pp. 1855-1862.

[40] Liu, G., Zhang, H., Hu, J., Zhai, Y., Xu, D., and Shao, Z.-g., 2006, "Studies of performance degradation of a high temperature PEMFC based on H3PO4-doped PBI," Journal of Power Sources, 162(1), pp. 547-552.

[41] Yu, S., Xiao, L., and Benicewicz, B. C., 2008, "Durability studies of PBI-based high temperature PEMFCs," Fuel Cells, 8(3-4), pp. 165-174.

[42] Zhai, Y., Zhang, H., Liu, G., Hu, J., and Yi, B., 2007, "Degradation study on MEA in H2 P O2 PBI high-temperature PEMFC life test," Journal of the Electrochemical Society, 154(1), pp. 72-76.

[43] Lobato, J., Canizares, P., Rodrigo, M. A., and Linares, J. J., 2007, "PBI-based polymer electrolyte membranes fuel cells. Temperature effects on cell performance and catalyst stability," Electrochimica Acta, 52(12), pp. 3910-3920.

[44] Ma, Y. L., Wainright, J. S., Litt, M. H., and Savinell, R. F., 2004, "Conductivity of PBI membranes for high-temperature polymer electrolyte fuel cells," Journal of the Electrochemical Society, 151(1), pp. 8-16.

[45] Schechter, A., Savinell, R. F., Wainright, J. S., and Ray, D., 2009, "H1 and P31 NMR study of phosphoric acid-doped polybenzimidazole under controlled water activity," Journal of the Electrochemical Society, 156(2), pp. 283-290.

[46] Liu, D., Kyriakides, S., Case, S. W., Lesko, J. J., Yanxiang, L. I., and McGrath, J. E., 2006, "Tensile behavior of Nafion and sulfonated poly(arylene ether sulfone) copolymer membranes and its morphological correlations," Journal of Polymer Science, Part B: Polymer Physics, 44(10), pp. 1453-1465.

[47] Mathias, M. F., Makharia, R., Gasteiger, H. A., Conley, J. J., Fuller, T. J., Gittleman, C. J., Kocha, S. S., Miller, D. P., Mittelsteadt, C. K., Xie, T., Van, S. G., and Yu, P. T., 2005, "Two fuel cell cars in every garage?," Electrochemical Society Interface, 14(3), pp. 24-35.

[48] Liu, D., Hickner, M. A., Case, S. W., and Lesko, J. J., 2006, "Relaxation of proton conductivity and stress in proton exchange membranes under strain," Journal of Engineering Materials and Technology, Transactions of the ASME, 128(4), pp. 503-508.

[49] Stanic, V., and Hoberecht, M., "Mechanism of pin-hole formation in membrane electrode assemblies for PEM fuel cells," Electrochemical Society Inc., p. 1891.

[50] Suvorov, A. P., Elter, J., Staudt, R., Hamm, R., Tudryn, G. J., Schadler, L., and Eisman, G., 2008, "Stress relaxation of PBI based membrane electrode assemblies," International Journal of Solids and Structures, 45(24), pp. 5987-6000.

[51] Zhang, J., Tang, Y., Song, C., and Zhang, J., 2007, "Polybenzimidazole-membrane-based PEM fuel cell in the temperature range of 120-200 °C," Journal of Power Sources, 172(1), pp. 163-171.

[52] Fowler, M. W., Kundu, S., Simon, L. C., and Grot, S., 2006, "Morphological features (defects) in fuel cell membrane electrode assemblies," Journal of Power Sources, 157(2), pp. 650-656.

[53] Ramaswamy, S., Greenberg, A. R., and Peterson, M., 2007, "Ultrasonic detection of defects in highly porous polymeric membranes," Insight: Non-Destructive Testing and Condition Monitoring, 49(11), pp. 651-656.

[54] Vente, J. F., van Veen, H. M., and Pex, P. P. A. C., 2007, "Microporous sol-gel membranes for molecular separations," Annales de Chimie (Science des Materiaux), 32(2), pp. 231-244.

[55] Lü, W., Liu, Z., Wang, C., Mao, Z., and Zhang, M., 2011, "The effects of pinholes on proton exchange membrane fuel cell performance," International Journal of Energy Research, 35(1), pp. 24-30.

[56] Veverka, P. J., 1995, "An investigation of interfacial instability during air entrainment," Doctor of Philosophy, Georgia Institute of Technology, Atlanta.

[57] Beguin, A. E., 1954, "U. S. Patent 2, 681, 694."

[58] Lin, F.-H., Liu, C.-M., Liu, T.-J., and Wu, P.-Y., 2008, "A macroscopic mathematical model for tensioned-web slot coating," Polymer Engineering and Science, 48(2), pp. 307-315.

[59] Higgins, B. G., and Scriven, L. E., 1980, "Capillary pressure and viscous pressure drop set bounds on coating bead operability," Chemical Engineering Science, 35, pp. 673-682.

[60] Ruschak, K. J., 1976, "Limiting flow in a pre-metered coating device," Chemical Engineering Science, 31(11), pp. 1057-1060.

[61] Landau, L. D., and Levitch, V. G., 1942, Acta Physicochim URSS, 17.

[62] Carvalho, M. S., and Kheshgi, H. S., 2000, "Low-flow limit in slot coating: Theory and experiments," AIChE Journal, 46(10), pp. 1907-1917.

[63] Romero, O. J., Suszynski, W. J., Scriven, L. E., and Carvalho, M. S., 2004, "Low-flow limit in slot coating of dilute solutions of high molecular weight polymer," Journal of Non-Newtonian Fluid Mechanics, 118(2-3), pp. 137-156.

[64] Romero, O. J., Scriven, L. E., and Carvalho, M. S., 2006, "Slot coating of mildly viscoelastic liquids," Journal of Non-Newtonian Fluid Mechanics, 138(2-3), pp. 63-75.

[65] Chang, H.-M., Chang, Y.-R., Lin, C.-F., and Liu, T.-J., 2007, "Comparison of vertical and horizontal slot die coatings," Polymer Engineering and Science, 47, pp. 1927-1936.

[66] Chin, C.-P., Wu, H.-S., and Wang, S. S., 2010, "Improved coating window for slot coating," Industrial and Engineering Chemistry Research, 49, pp. 3802-3809.

[67] Lin, C.-F., Wong, D. S. H., Liu, T.-J., and Wu, P.-Y., 2010, "Operating windows of slot die coating: Comparison of theoretical predictions with experimental observations," Advances in Polymer Technology, 29, pp. 31-44.

[68] Gutoff, E. B., and Kendrick, C. E., 1987, "Low flow limits of coatability on a slide coater," AIChE Journal, 33(1), pp. 141-145.

[69] Lee, K.-Y., Liu, L.-D., and Ta-Jo, L., 1992, "Minimum wet thickness in extrusion slot coating," Chemical Engineering Science, 47(7), pp. 1703-1713.

[70] Chu, W.-B., Yang, J.-W., Wang, Y.-C., Liu, T.-J., Tiu, C., and Guo, J., 2006, "The effect of inorganic particles on slot die coating of poly(vinyl alcohol) solutions," Journal of Colloid and Interface Science, 297(1), pp. 215-225.

[71] Yamamura, M., Miura, H., and Kage, H., 2005, "Postponed air entrainment in dilute suspension coatings," AIChE Journal, 51, pp. 2171-2177.

[72] Lin, Y.-T., Chu, W.-B., and Liu, T.-J., 2009, "Slot die coating of dilute suspensions," Asia-Pacific Journal of Chemical Engineering, 4, pp. 125-132.

[73] Chu, V., Tsai, M.-Z., Chang, Y.-R., Liu, T.-J., and Tiu, C., 2010, "Effects of the molecular weight and concentration of poly(vinyl alcohol) on slot die coating," Journal of Applied Polymer Science, 116, pp. 654-662.

[74] Ning, C.-Y., Tsai, C.-C., and Liu, T.-J., 1996, "Effect of polymer additives on extrusion slot coating," Chemical Engineering Science, 51(12), pp. 3289-3297.

[75] Hamers, C., Schatl, M., Krumbacher, E., Birkert, O., Frohlich, U., Tietz, M., and Gerteiser, N., 2005, "Curtain coating for graphical papers offers better coverage, printability," Pulp and Paper, 79, pp. 49-51.

[76] Tiu, C., Wang, L., and Liu, T.-J., 1999, "Non-Newtonian effects on pre-metered reverse roll coating," Journal of Non-Newtonian Fluid Mechanics, 87, pp. 247-261.

[77] Chu, W.-B., Yang, J.-W., Liu, T.-J., Tiu, C., and Guo, J., 2007, "The effects of pH, molecular weight and degree of hydrolysis of poly(vinyl alcohol) on slot die coating of PVA suspensions of TiO2 and SiO2," Colloids and Surfaces A (Physicochemical and Engineering Aspects), 302, pp. 1-10.

[78] Yang, C. K., Wong, D. S. H., and Liu, T. J., 2004, "The effects of polymer additives on the operating windows of slot coating," Polymer Engineering and Science, 44, pp. 1970-1976.

[79] Miyamoto, K., and Scriven, L. E., "Breakdown of air film entrained by liquid coated on web," 1982 Annual Meeting - American Institute of Chemical Engineers., AIChE, pp. AIChE, New York, NY, USA.

[80] Teletzke, G. F., Davis, H. T., and Scriven, L. E., 1988, "Wetting hydrodynamics," HAL - CCSD.

[81] Deryagin, B. V., and Kusakov, M. M., 1939, Acta Physicochim, 10(25).

[82] Kim, H. I., Mate, C. M., Hannibal, K. A., and Perry, S. S., 1999, "How disjoining pressure drives the dewetting of a polymer film on a silicon surface," Physical Review Letters, 82, pp. 3496-3499.

[83] Derjaguin, B. V., and Churaev, N. V., 1974, "Structural component of disjoining pressure," Journal of Colloid and Interface Science, 49(2), pp. 249-255.

[84] Kistler, S. F., 1993, Wettability, M. Dekker, New York :.

[85] Miyamoto, K., 1993, "On the mechanism of air entrainment," Fuji Film research & development, pp. 105-122.

[86] Ablett, R., 1923, "An investigation of the angle of contact between paraffin wax and water," Philosophical Magazine Series 6, 46(272), pp. 244 - 256.

[87] Deryagin, B. V., and Levi, S. M., 1959, Film Coating Theory, Focal Press, London.

[88] Veverka, P. J., and K., A. C., "Flow visualization of air entrainment and dynamic contact line instability in low-speed roll coating," 1991 TAPPI Engineering Conference Proceedings,, Atlanta TAPPI Press, pp. 719-725.

[89] Burley, R., and Kennedy, B. S., 1976, "An experimental study of air entrainment at a solid/liquid/gas interface," Chemical Engineering Science, 31(10), pp. 901-911.

[90] Kennedy, B. S., and Burley, R., 1977, "Dynamic fluid interface displacement and prediction of air entrainment," Journal of Colloid and Interface Science, 62(1), pp. 48-62.

[91] Blake, T. D., and Ruschak, K. J., 1979, "A maximum speed of wetting," Nature, 282(5738), pp. 489-491.

[92] Gutoff, E. B., and Kendrick, C. E., 1982, "Dynamic contact angles," AIChE Journal, 28(3), pp. 459-466.

[93] Cohu, O., and Benkreira, H., 1998, "Air entrainment in angled dip coating," Chemical Engineering Science, 53, pp. 533-540.

[94] Cohu, O., and Benkreira, H., 1998, "Entrainment of air by a solid surface plunging into a non-newtonian liquid," AIChE Journal, 44(11), pp. 2360-2368.

[95] Benkreira, H., and Khan, M. I., 2008, "Air entrainment in dip coating under reduced air pressures," Chemical Engineering Science, 63, pp. 448-459.

[96] Benkreira, H., and Ikin, J. B., 2010, "Dynamic wetting and gas viscosity effects," Chemical Engineering Science, 65, pp. 1790-1796.

[97] Veverka, P. J., 1991, "Dynamic Contact Line Instability and Air Entrainment in Coating Systems," A-190 Master's Project, Georgia Institute of Technology, Atlanta.

[98] Veverka, P. J., and K., A. C., 1991, Using high-speed cinematography to obtain visual evidence on air entrainment in low-speed roll coating, TAPPI, Norcross, GA, ETATS-UNIS.

[99] Severtson, Y. C., and Aidun, C. K., 1996, "Stability of two-layer stratified flow in inclined channels: applications to air entrainment in coating systems," Journal of Fluid Mechanics, 312(-1), pp. 173-200.

[100] Chang, Y.-R., Chang, H.-M., Lin, C.-F., Liu, T.-J., and Wu, P.-Y., 2007, "Three minimum wet thickness regions of slot die coating," Journal of Colloid and Interface Science, 308(1), pp. 222-230.

[101] Chang, Y.-R., Lin, C.-F., and Liu, T.-J., 2009, "Start-up of slot die coating," Polymer Engineering & Science, 49(6), pp. 1158-1167.

[102] Yamamura, M., 2007, "Assisted dynamic wetting in liquid coatings," Colloids and Surfaces A: Physicochemical and Engineering Aspects, 311, pp. 55-60.

[103] Romero, O. J., and Carvalho, M. S., 2008, "Response of slot coating flows to periodic disturbances," Chemical Engineering Science, 63(8), pp. 2161-2173.

[104] Romero, O. J., Scriven, L. E., and Carvalho, M. d. S., 2006, "Effect of curvature of coating die edges on the pinning of contact line," AIChE Journal, 52(2), pp. 447-455.

[105] Benkreira, H., and Cohu, O., 1998, "Angling the wetting line retards air entrainment in premetered coating flows," AIChE Journal, 44(5), pp. 1207-1209.

[106] Scriven, L. E., "How does air entrain at wetting lines?," A.I.Ch.E. Winter National Meeting.

[107] Buonopane, R. A., Gutoff, E. B., and Rimore, M. M. T., 1986, "Effect of plunging tape surface properties on air entrainment velocity," AIChE Journal, 32(4), pp. 682-683.

[108] Benkreira, H., 2004, "The effect of substrate roughness on air entrainment in dip coating," Chemical Engineering Science, 59(13), pp. 2745-2751.

[109] Blake, T. D., Clarke, A., and Ruschak, K. J., 1994, "Hydrodynamic assist of dynamic wetting," AIChE Journal, 40, pp. 229-242.

[110] Blake, T. D., Dobson, R. A., and Ruschak, K. J., 2004, "Wetting at high capillary numbers," Journal of Colloid and Interface Science, 279, pp. 198-205.

[111] Blake, T. D., Clarke, A., and Stattersfield, E. H., 2000, "Investigation of electrostatic assist in dynamic wetting," Langmuir, 16, pp. 2928-2935.

[112] Fermin, R. J., and Scriven, L. E., "Electrostatically Assisted Coating Flows," Proc. of 3rd European Coating Symposium pp. 91-95.

[113] Fermin, R. J., and Scriven, L. E., "Electrostatically assisted slot coating," Proceedings of the Ninth International Coating Science and Technology Symposium, pp. 149-152.

[114] Iuliano, S. G., "Using simulations to predict coating characteristics of a slot die system," 2004 TAPPI PLACE - Polymers, Laminations, Adhesives, Coatings, and Extrusions Division Conference, August 29, 2004 - September 2, 2004, Technical Assoc. of the Pulp and Paper Industry Press, pp. 715-731.

[115] Harris, T. A. L., 2006, "Design methodology, science, and technology to manufacture high temperature polymer electrolyte membranes for fuel cells," Doctor of Philosophy, Rensselaer Polytechnic Institute, Troy.

[116] Clegg, C., Mar 27, 2009, "How to Measure Surface Tension:with ramé-hart DROPimage Advanced," http://knol.google.com/k/carl-clegg/how-to-measure-surface-tension/1lfb9vuvh4x3s/5.

[117] Johnson, J., 2009, "Defect and thickness inspection system for cast thin films using machine vision and full-field transmission densitometry," Master of Science, Georgia Institute of Technology, Atlanta.

[118] "LabVIEW. 2009,"National Instruents: Austin, TX.

[119] Burley, R., and Jolly, R. P. S., 1984, "Entrainment of air into liquids by a high speed continuous solid surface," Chemical Engineering Science, 39(9), pp. 1357-1372.

[120] Hartman, R., L., 1987, "High speed curtain coating process and apparatus," International Patent.

[121] Johnson, J., and Harris, T., 2010, "Full-field optical thickness profilometry of semitransparent thin films with transmission densitometry," Applied Optics, 49(15), pp. 2920-2928.

[122] Coleman, H. W., and Steele, W. G., 2009, Experimentation, Validation, and Uncertainty Analysis for Engineers.

[123] Saito, H., and Scriven, L. E., 1981, "Study of coating flow by the finite element method," Journal of Computational Physics, 42(1), pp. 53-76.

[124] Kheshgi, H. S., 1989, "Profile equations for film flows at moderate Reynolds numbers," AIChE Journal, 35(10), pp. 1719-1727.

[125] Pasquali, M., and Scriven, L. E., 2002, "Free surface flows of polymer solutions with models based on the conformation tensor," Journal of Non-Newtonian Fluid Mechanics, 108(1-3), pp. 363-409.

[126] Bajaj, M., Ravi Prakash, J., and Pasquali, M., 2008, "A computational study of the effect of viscoelasticity on slot coating flow of dilute polymer solutions," Journal of Non-Newtonian Fluid Mechanics, 149(1-3), pp. 104-123.

[127] Lee, A. G., Shaqfeh, E. S. G., and Khomami, B., 2002, "A study of viscoelastic free surface flows by the finite element method: Hele-Shaw and slot coating flows," Journal of Non-Newtonian Fluid Mechanics, 108(1-3), pp. 327-362.

[128] TopCoat, "RheoLogic Ltd.,"Leeds, UK.

[129] Hirt, C. W., and Richardson, J. E., 1997, "Simulation of Transient and Three-Dimensional Coating Flows Using a Volume-of-Fluid Technique," 50th Annual Conference of the Society for Imaging and Science TechnologyBoston.

[130] Harris, T. A. L., and Bhamidipati, K. L., 2008, "Computational Modeling of a Polymer Electrolyte Membrane Fabrication Process," ECS Transactions, 12(1), pp. 251-262.

[131] Bhamidipati, K. L., and Harris, T. A. L., 2010, "Numerical Simulation of a High Temperature Polymer Electrolyte Membrane Fabrication Process," Journal of Fuel Cell Science and Technology, 7(6), p. 061005.

[132] Bhamidipati, K. L., and Harris, T. A. L., 2009, "Numerical Analysis of the Effects of Processing Conditions on the Casting of High Temperature PEMFC Membrane Solutions," ASME Conference Proceedings, 2009(48814), pp. 695-702.

[133] Bhamidipati, K. L., and Harris, T. A. L., 2010, "Numerical analysis of defect formation during fabrication of high temperature polymer electrolyte membrane solutions," Polymer Engineering & Science (Article online in advance of print).

[134] Hirt, C. W., Cook, J. L., and Butler, T. D., 1970, "A lagrangian method for calculating the dynamics of an incompressible fluid with free surface," Journal of Computational Physics, 5(1), pp. 103-124.

[135] Preisig, M., and Zimmermann, T., 2011, "Free-surface fluid dynamics on moving domains," Computer Methods in Applied Mechanics and Engineering, 200, pp. 372-382.

[136] Ramaswamy, B., and Kawahara, M., 1987, "Lagrangian finite element analysis applied to viscous free surface fluid flow," International Journal for Numerical Methods in Fluids, 7(9), pp. 953-984.

[137] Harlow, F., and Welch, E., 1965, "Numerical Calculation of Time-Dependent Viscous Incompressible Flow of Fluid with Free Surface," Physics of Fluids, 8(12), pp. 2182-2189.

[138] Nakayama, T., and Mori, M., 1996, "An Eulerian finite element method for time-dependent free surface problems in hydrodynamics," International Journal for Numerical Methods in Fluids, 22(3), pp. 175-194.

[139] Cheng, S. I., and Lu, Y., 1986, "An Eulerian method for transient nonlinear free surface wave problems," Journal of Computational Physics, 62, pp. 429-440.

[140] Hirt, C. W., and Nichols, B. D., 1981, "Volume of fluid /VOF/ method for the dynamics of free boundaries," Journal of Computational Physics, 39, pp. 201-225.

[141] Braess, H., and Wriggers, P., 2000, "Arbitrary Lagrangian Eulerian finite element analysis of free surface flow," Computer Methods in Applied Mechanics and Engineering, 190, pp. 95-109.

[142] Hsu, M. H., Chen, C. H., and Teng, W. H., 2001, "An Arbitrary Lagrangian-Eulerian finite difference method for computations of free surface flows," Journal of Hydraulic Research/De Recherches Hydrauliques, 39, pp. 481-491.

[143] Nithiarasu, P., 2005, "An arbitrary Lagrangian Eulerian (ALE) formulation for free surface flows using the characteristic-based split (CBS) scheme," International Journal for Numerical Methods in Fluids, 48, pp. 1415-1428.

[144] Ramaswamy, B., and Kawahara, M., "Arbitrary Lagrangian-Eulerian finite element method for unsteady, convective, incompressible viscous free surface fluid flow," Sixth International Symposium on Finite Element Methods in Flow Problems, 16-20 June 1986, pp. 1053-1075.

[145] Soulaimani, A., and Saad, Y., 1998, "An arbitrary Lagrangian-Eulerian finite element method for solving three-dimensional free surface flows," Computer Methods in Applied Mechanics and Engineering, 162, pp. 79-106.

[146] Souli, M., and Zolesio, J. P., 2001, "Arbitrary Lagrangian-Eulerian and free surface methods in fluid mechanics," Computer Methods in Applied Mechanics and Engineering, 191, pp. 451-466.

[147] Glimm, J., Grove, J. W., Li, X. L., Oh, W., and Sharps, D. H., 2001, "A critical analysis of Rayleigh-Taylor growth rates," Journal of Computational Physics, 169(2), pp. 652-677.

[148] Tryggvason, G., Bunner, B., Esmaeeli, A., Juric, D., Al-Rawahi, N., Tauber, W., Han, J., Nas, S., and Jan, Y.-J., 2001, "A front-tracking method for the computations of multiphase flow," Journal of Computational Physics, 169(2), pp. 708-759.

[149] Oran, E. S., and Boris, J. P., 1987, Numerical Simulation of Reactive Flow, Elsevier, New York.

[150] Shopov, P. J., Minev, P. D., Bazhlekov, I. B., and Zapryanov, Z. D., 1990, "Interaction of a deformable bubble with a rigid wall at moderate Reynolds numbers," Journal of Fluid Mechanics, 219, pp. 241-271.

[151] Feng, J., Hu, H. H., and Joseph, D. D., 1994, "Direct simulation of initial value problems for the motion of solid bodies in a Newtonian fluid Part 1. Sedimentation," Journal of Fluid Mechanics, 261, pp. 95-134.

[152] Feng, J., Hu, H. H., and Joseph, D. D., 1994, "Direct simulation of initial value problems for the motion of solid bodies in a Newtonian fluid. Part 2. Couette and Poiseuille flows," Journal of Fluid Mechanics, 277, pp. 271-301.

[153] Fukai, J., Shiiba, Y., Yamamoto, T., Miyatake, O., Poulikakos, D., Megaridis, C. M., and Zhao, Z., 1995, "Wetting effects on the spreading of a liquid droplet colliding with a flat surface. Experiment and modeling," Physics of Fluids, 7, pp. 236-236.

[154] McKibben, J. F., and Aidun, C. K., 1993, "A volume-of-fluid computational technique for free surface flow problems," Georgia Institute of Technology, Atlanta.

[155] Young, D. L., 1982, "Time-dependent multi-material flow with large fluid distortion," Numerical Methods for Fluid Dynamics, pp. 273-285.

[156] FLUENT, 2006, "User Guide Fluent 6.3.,"Lebanon, NH.

[157] van Leer, B., 1973, "Towards the ultimate conservative difference scheme I. The quest of monotonicity," Proceedings of the Third International Conference on Numerical Methods in Fluid Mechanics, H. Cabannes, and R. Temam, eds., Springer Berlin / Heidelberg, pp. 163-168.

[158] Brackbill, J. U., Kothe, D. B., and Zemach, C., 1992, "A continuum method for modeling surface tension," Journal of Computational Physics, 100(2), pp. 335-354.

[159] Michael, D. H., 1958, "The separation of a viscous liquid at a straight edge," Mathematika, 5(01), pp. 82-84.

[160] Huh, C., and Scriven, L. E., 1971, "Hydrodynamic model of steady movement of a solid/liquid/fluid contact line," Journal of Colloid and Interface Science, 35(1), pp. 85-101.

[161] Moffatt, H. K., 1964, "Viscous and resistive eddies near a sharp corner," Journal of Fluid Mechanics, 18(01), pp. 1-18.

[162] 2007, "Moving contact lines," Capillary Flows with Forming Interfaces, Chapman & Hall.

[163] Kistler, S. F., 1983, "The fluid mechanics of curtain coating and related viscous free surface flows with contact lines," PhD, University of Minnesota.

[164] Dussan V., E. B., and Davis, S. H., 1974, "On the motion of a fluid-fluid interface along a solid surface," Journal of Fluid Mechanics, 65(01), pp. 71-95.

[165] Dussan V., E. B., 1976, "The moving contact line: the slip boundary condition," Journal of Fluid Mechanics, 77(04), pp. 665-684.

[166] Dussan, E. B., 1979, "On the Spreading of Liquids on Solid Surfaces: Static and Dynamic Contact Lines," Annual Review of Fluid Mechanics, 11(1), pp. 371-400.

[167] Kafka, F. Y., and Dussan, E. B., 1979, "On the interpretation of dynamic contact angles in capillaries," Journal of Fluid Mechanics, 95(03), pp. 539-565.

[168] Silliman, W. J., 1979, "Viscous film flows with contact lines : finite element simulation, a basis for stability assessment and design optimization," PhD, University of Minnesota.

[169] Lowndes, J., 1980, "The numerical simulation of the steady movement of a fluid meniscus in a capillary tube," Journal of Fluid Mechanics, 101(03), pp. 631-646.

[170] de Gennes, P. G., 1985, "Wetting: statics and dynamics," Reviews of Modern Physics, 57(3), p. 827.

[171] Cox, R. G., 1986, "The dynamics of the spreading of liquids on a solid surface. Part 1. Viscous flow," Journal of Fluid Mechanics, 168, pp. 169-194.

[172] Thompson, P. A., and Robbins, M. O., 1989, "Simulations of contact-line motion: Slip and the dynamic contact angle," Physical Review Letters, 63(7), p. 766.

[173] Brochard, F., and De Gennes, P. G., 1992, "Shear-dependent slippage at a polymer/solid interface," Langmuir, 8(12), pp. 3033-3037.

[174] Renardy, M., Renardy, Y., and Li, J., 2001, "Numerical Simulation of Moving Contact Line Problems Using a Volume-of-Fluid Method," Journal of Computational Physics, 171(1), pp. 243-263.

[175] Weidner, D. E., and Schwartz, L. W., 1994, "Contact-line motion of shear-thinning liquids," Physics of Fluids, 6, pp. 3535-3538.

[176] Blake, T. D., and Ruschak, K. J., 1997, "Wetting: static and dynamic contact lines," Liquid Film Coating, S. F. K. a. P. M. Schweizer, ed., Chapman & Hall, London.

[177] Hocking, L. M., 1981, "Sliding and spreading of thin two-dimensional drops," Quarterly Journal of Mechanics and Applied Mathematics, 34, pp. 37-55.

[178] Hocking, L. M., 1983, "The spreading of a thin drop by gravity and capillarity," Quarterly Journal of Mechanics and Applied Mathematics, 36, pp. 55-69.

[179] Hocking, L. M., and Rivers, A. D., 1982, "The spreading of a drop by capillary action," Journal of Fluid Mechanics, 121, pp. 425-442.

[180] Huh, C., and Mason, S. G., 1977, "The steady movement of a liquid meniscus in a capillary tube," Journal of Fluid Mechanics, 81(03), pp. 401-419.

[181] Silliman, W. J., and Scriven, L. E., 1980, "Separating how near a static contact line: Slip at a wall and shape of a free surface," Journal of Computational Physics, 34(3), pp. 287-313.

[182] Benny, D. J., and Timson, W. J., 1980, "The rolling motion of a viscous fluid on and off a rigid surface," Studies in Applied Mathematics, 63, pp. 93-98.

[183] Blake, T. D., and Haynes, J. M., 1969, "Kinetics of liquid/liquid displacement," Journal of Colloid and Interface Science, 30(3), pp. 421-423.

[184] Popescu, M. N., Ralston, J., and Sedev, R., 2008, "Capillary Rise with Velocity-Dependent Dynamic Contact Angle," Langmuir, 24(21), pp. 12710-12716.

[185] Afkhami, S., and Bussmann, M., 2009, "Height functions for applying contact angles to 3D VOF simulations," International Journal for Numerical Methods in Fluids, 61(8), pp. 827-847.

[186] Sujatha, K. S., Matallah, H., Banaai, M. J., and Webster, M. F., 2006, "Computational predictions for viscoelastic filament stretching flows: ALE methods and free-surface techniques (CM and VOF)," Journal of Non-Newtonian Fluid Mechanics, 137(1-3), pp. 81-102.

[187] Scardovelli, R., and Zaleski, S., 1999, "Direct numerical simulation of free-surface and interfacial flow," Annual Review of Fluid Mechanics, 31(1), pp. 567-603.

[188] Williams, M. W., Kothe, D. B., and Puckett, E. G., 1998, Accuracy and convergence of continuum surface tension models, Cambridge Univ. Press, Cambridge, UK.

[189] Zacharioudaki, M., Kouris, C., Dimakopoulos, Y., and Tsamopoulos, J., 2007, "A direct comparison between volume and surface tracking methods with a boundary-fitted coordinate transformation and third-order upwinding," Journal of Computational Physics, 227(2), pp. 1428-1469.

[190] Scharenberg, R. T., 1985, Encyclopedia of Polymer Science and Technology, Wiley-Interscience, New York.

[191] Wilkinson, W. L., 1975, "Entrainment of air by a solid surface entering a liquid/air interface," Chemical Engineering Science, 30(10), pp. 1227-1230.

[192] Bohacek, J., 2010, "Surface Tension Model for High Viscosity Ratios Implemented in VOF Model," ILASS – Europe 2010, 23rd Annual Conference on Liquid Atomization and Spray SystemsBrno, Czech Republic.

[193] Shepel, S. V., Smith, B. L., and Paolucci, S., 2005, "Implementation of a Level Set Interface Tracking Method in the FIDAP and CFX-4 Codes," Journal of Fluids Engineering, 127(4), pp. 674-686.

[194] Deganello, D., Williams, A. J., Croft, T. N., Lubansky, A. S., Gethin, D. T., and Claypole, T. C., 2011, "Level-set method for the modelling of liquid bridge formation and break-up," Computers and Fluids, 40, pp. 42-51.

[195] Jia, W., 1997, "Computing surface tension by a hybrid VOF and LS algorithm," Fifteenth International Conference on Numerical Methods in Fluid Dynamics, P. Kutler, J. Flores, and J.-J. Chattot, eds., Springer Berlin / Heidelberg, pp. 504-509.

[196] Wang, Z., Yang, J., Koo, B., and Stern, F., 2009, "A coupled level set and volume-of-fluid method for sharp interface simulation of plunging breaking waves," International Journal of Multiphase Flow, 35(3), pp. 227-246.

[197] Yang, X., James, A. J., Lowengrub, J., Zheng, X., and Cristini, V., 2006, "An adaptive coupled level-set/volume-of-fluid interface capturing method for unstructured triangular grids," Journal of Computational Physics, 217(2), pp. 364-394.

[198] Nam, J., and Carvalho, M. S., 2010, "Flow in tensioned-web-over-slot die coating: Effect of die lip design," Chemical Engineering Science, 65(13), pp. 3957-3971.

[199] Bolton, B., and Middleman, S., 1980, "Air entrainment in a roll coating system," Chemical Engineering Science, 35(3), pp. 597-601.